/N-35
33860
P. 240

Laser-Induced Fluorescence Measurements and Modeling of Nitric Oxide in High-Pressure Premixed Flames

John R. Reisel and Normand M. Laurendeau
Purdue University
West Lafayette, Indiana

December 1994

TABLE OF CONTENTS

LIST OF TABLES

Appendix
Table

LIST OF FIGURES

Figure

Figure   Page

Figure   Page

LIST OF SYMBOLS

English Symbols

Symbol	Description	Units
a	Voigt profile parameter	--
A	Frequency factor for bimolecular reaction	$cm^3/(mol{\cdot}s)$
A_{ul}	Einstein A coefficient for spontaneous emission	s^{-1}
B_{lu}	Einstein B coefficient for absorption	$cm^2{\cdot}cm^{-1}{\cdot}J^{-1}$
B_{ul}	Einstein B coefficient for stimulated emission	$cm^3{\cdot}cm^{-1}{\cdot}J^{-1}{\cdot}s^{-1}$
$\hat{B}_{ul}$	Einstein B coefficient for stimulated emission	$cm^3{\cdot}J^{-1}{\cdot}s^{-2}$
c	Speed of light	cm/s
E_a	Activation energy	cal/mol
E	Total molecular energy	cm^{-1}
e	Electronic charge	C
f_B	Boltzmann fraction for rotational level	--
$f_{v''v'}$	Band oscillator strength	--
g	Degeneracy of the electronic level	--
$G(v)$	Laser spectral lineshape function	--
G	Photomultiplier gain	(V/W)
h	Planck constant	$J{\cdot}s$
I_L	Laser irradiance	W/cm^2
I_v^0	Peak spectral laser irradiance	$W/cm^2{\cdot}cm^{-1}$
J	Rotational quantum number	--

Symbol	Description	Units
k	Boltzmann constant	J/K
k_f	Bimolecular rate coefficient	$cm^3/(mol \cdot s)$
m_e	Electron rest mass	g
n	Temperature exponent in rate equation	--
n_i	Index of refraction	--
N	Population in rotational level	cm^{-3}
N	Number density	cm^{-3}
N_1^0	Total population in system	cm^{-3}
P	Pressure	atm, kPa
Q	Electronic quenching rate coefficient	s^{-1}
Q_e	Electronic quenching rate coefficient	s^{-1}
Q_r	Rotational relaxation rate coefficient	s^{-1}
Q_v	Vibrational relaxation rate coefficient	s^{-1}
Q_{ul}	Electronic quenching rate coefficient	s^{-1}
R	Ideal gas constant	$cal/(K \cdot mol)$
$S_{J''J'}$	Hönl-London factor (relative rotational line strength)	--
S	Rayleigh scattering signal	W
t	Time	s^{-1}
T	Temperature	K
T_L	Laser temporal distribution function	--
V	Fluorescence voltage	V
$\overline{V}$	Average fluorescence voltage	V
$V(\xi,a)$	Voigt function	--

Symbol	Description	Units
$\dot{V}$	Volumetric flow rate	l/min
V_c	Fluorescence collection volume	cm^3
V_f	Fluorescence voltage	V
W_{lu}	Rate coefficient for stimulated absorption	s^{-1}
W_{ul}	Rate coefficient for stimulated emission	s^{-1}
X_i	Mole fraction	--
$Y(\nu)$	Absorption spectral lineshape	cm
Z_e	Electronic partition function	--
Z_r	Rotational partition function	--
Z_v	Vibrational partition function	--

Greek Symbols

Symbol	Description	Units
$\alpha(\nu)$	Spectral absorption coefficient	cm^{-1}
β	Detection efficiency of collection optics	--
Γ_{lu}	Fractional overlap integral	--
$\Delta\nu_C$	Collisionally broadened linewidth	cm^{-1}
$\Delta\nu_D$	Doppler broadened linewidth	cm^{-1}
$\Delta\nu_L$	Laser spectral linewidth	cm^{-1}
ε_f	Fluorescence emission	$W/(cm^3 \cdot sr)$
ζ	Grouping constant	--
λ	Wavelength	nm
μ_i	Reduced mass	g
ν_f	Wavenumber of fluorescence	cm^{-1}
ν_L	Wavenumber of laser radiation	cm^{-1}

Symbol	Description	Units
ξ	Voigt function parameter	--
ρ_v	Depolarization ratio	--
σ	Standard deviation	V
σ	One-photon absorption cross-section	cm^2
σ_i	Quenching cross-section of species i	cm^2
σ_i	Photoionization cross-section	cm^2
υ	Grouping constant	--
ϕ	Equivalence Ratio	--
ψ	Dilution Ratio	--
Ω_c	Solid collection angle of detection optics	sr

Subscripts

Symbol	Description	Units
BG	Background	--
cal	Refers to the calibration flame	--
f	Fluorescence	--
$flame$	Refers to the measurement flame	--
He	Helium	--
j, m	Refers to levels of excited state	--
J'	Upper rotational state quantum number	--
J''	Lower rotational state quantum number	--
l	Refers to lower rovibronic level	--
L	Laser	--
NO	Nitric Oxide	--
N_2	Molecular nitrogen	--

Symbol	Description	Units
O_2	Molecular oxygen	--
u	Refers to upper rovibronic level	--
v'	Upper vibrational state quantum number	--
v''	Lower vibrational state quantum number	--
0	Reference measurement	--

Superscripts

Symbol	Description	Units
$''$	Refers to the ground electronic state	--

ABSTRACT

Laser-induced fluorescence (LIF) has been applied to the quantitative measurement of nitric oxide (NO) in premixed, laminar, high-pressure flames. The chemistry of these flames was also studied using three current chemical kinetics schemes so as to determine the predictive capabilities of each mechanism with respect to NO concentrations. The flames studied were low-temperature (1600<T<1850 K) $C_2H_6/O_2/N_2$ and $C_2H_4/O_2/N_2$ flames, and high-temperature (2100<T<2300 K) $C_2H_6/O_2/N_2$ flames. The NO formed in the low-temperature flames was predominantly prompt-NO, while the NO formed in the high-temperature flames was predominantly thermal-NO.

It was initially desired to use laser-saturated fluorescence (LSF) to measure the NO concentrations. However, while the excitation transition was well saturated at atmospheric pressure, the fluorescence behavior was basically linear with respect to laser power at pressures above 6 atm. It has been demonstrated through measurements and calculations that the fluorescence quenching rate variation is negligible for a set of LIF measurements of NO at a given pressure. Therefore, linear LIF could be used to perform quantitative measurements of NO concentration in these high-pressure flames.

For the low-temperature flames, it was found that the equivalence ratio corresponding to the peak [NO] at a given pressure shifted towards leaner conditions with increasing pressure. Chemical kinetics calculations using the coupled species-energy equations gave generally acceptable NO predictions for the ethane flames, but less acceptable results for the ethylene flames. The LIF measurements of [NO] in the high-temperature flames were also compared to NO predictions using the energy solution;

however, the input temperature profile found from the energy solution was scaled to a post-flame temperature measured using Rayleigh scattering. These results showed acceptable agreement between the measurements and predictions, but demonstrated the need for more precise temperature measurements.

The transportability of a calibration factor from one set of flame conditions to another also was investigated by considering changes in the absorption and quenching environment for different flame conditions. Finally, the feasibility of performing LIF measurements of [NO] in turbulent flames was studied; the single-shot detection limit was determined to be 2 ppm.

CHAPTER 1

INTRODUCTION

1.1 Background

Nitric oxide (NO) is a major atmospheric pollutant which contributes to a variety of environmental problems, including the destruction of the stratospheric ozone layer [Johnston, 1971], the formation of acid rain [Miller and Fisk, 1987], and the production of smog in urban environments [Mortimer, 1983]. NO is formed in every practical combustion application, many of which (such as internal combustion engines and gas-turbine combustors) are operated at high pressure. With the increasingly stringent environmental regulations being enacted worldwide, it has become a goal of combustion designers to reduce NO emissions from practical combustors. To do this, a more thorough understanding of the chemical kinetics of NO formation at high pressure is needed. In turn, this requires accurate *in situ* measurements of NO concentrations in practical combustion environments.

Quantitative measurements of NO concentration can be obtained using both physical techniques, such as probe-sampling [Heberling, 1977; Leonard and Correa, 1990; Drake *et al.*, 1991], and optical techniques, such as laser-induced fluorescence (LIF) [Morley, 1981, 1982; Chou *et al.*, 1983; Cattolica *et al.*, 1989; Heard *et al.*, 1992; Reisel *et al.*, 1993]. Probe-sampling combined with chemiluminescent detection is advantageous since it possesses a lower detection limit, is easier to use, and is less expensive than laser-based methods. However, a physical probe can disrupt the flow field, potentially altering the concentrations of radical species; moreover, such probes may not be able to withstand the

harsh conditions of practical combustion environments [Miller and Fisk, 1987]. These disadvantages can be overcome by employing optical techniques. Optical procedures allow for remote sensing of numerous species in a variety of environments. Unlike sampling probes, optical methods generally do not alter the combustion process; in addition, many combustors are more readily adaptable to optical access than to physical sampling probes. Finally, precise spatial resolution is achievable through the use of optical methods.

Previous LIF measurements of NO have been performed in both subatmospheric- and atmospheric- pressure flames. When performing a linear LIF measurement, one must be concerned with the effects of electronic quenching on the fluorescence signal. There are several possible techniques which can be used to account for the influence of a variable quenching environment on the LIF signal. First, changes in electronic quenching can be simply ignored [Morley, 1981; Chou et al., 1983]. This tactic should only be considered after it has been determined that the quenching environment is nearly constant for the flame conditions studied. A second approach is to measure the quenching rate coefficient in each flame, and adjust the LIF signal accordingly [Cattolica et al., 1989; Heard et al., 1992]. This procedure requires additional measurements, and may introduce further uncertainties into the results. A third approach is to calculate the quenching rate coefficient for each flame. This method requires knowledge of the major species concentrations and quenching cross-sections for these species. Finally, laser-saturated fluorescence (LSF) can be used to eliminate the effects of quenching on the fluorescence signal. LSF has been used previously, in a narrowband detection scheme, to measure OH [Salmon and Laurendeau, 1985; Carter et al., 1992], CH [Kohse-Höinghaus et al., 1984], and NH [Salmon et al., 1984] concentrations. A broadband LSF detection scheme has also been developed and applied to NO concentration measurements at atmospheric pressure [Reisel et al., 1993]. Of these four approaches, broadband LSF may be the most straightforward

and accurate approach. However, a broadband LSF technique may not be applicable to NO at high pressure, due to the compactness of the NO spectrum and the increased collisional broadening of the spectral lines at high pressure.

Nitric oxide is produced through three main reaction pathways [Drake and Blint, 1991]. These mechanisms are the Zeldovich, or thermal-NO, mechanism [Zeldovich, 1946], the N_2O-intermediate mechanism [Malte and Pratt, 1974], and the prompt-NO mechanism [Fenimore, 1971]. The amount of NO formed through each of these pathways depends on temperature, pressure, equivalence ratio, and fuel type [Drake $et\ al.$, 1991]. For instance, the thermal-NO mechanism will form very little NO at temperatures below 1900 K, but becomes the dominant NO formation pathway for lean flames at temperatures above 2000 K. Similarly, Bachmaier $et\ al.$ [1973] found that the amount of prompt-NO produced in a flame at a given equivalence ratio depends on the fuel type.

Most of the relevant chemical kinetics models have been developed using low-pressure measurements. The applicability of such a chemical kinetics scheme is unclear for high-pressure flames. Drake $et\ al.$ [1991] found that one proposed mechanism [Drake and Blint, 1991] could be used with some certainty to predict flame front NO production in lean, low-temperature (T < 1800 K), premixed $C_2H_6/O_2/N_2$ flames up to 9 atm. However, work is still required in rich flames, high-temperature flames, flames using other fuel types, and even in lean flames to thoroughly evaluate the ability of the kinetics models with respect to NO predictions at high pressure. Other proposed chemical kinetics schemes also exist which require systematic evaluation at high pressure.

1.2 Contents of Thesis

In this work, the LIF method is employed for the measurement of NO concentrations in a variety of atmospheric- and high-pressure flames. These flames include laminar, high-pressure (P < 15 atm), low-temperature (1600 < T < 1850 K) $C_2H_6/O_2/N_2$ and C_2H_4 $/O_2/N_2$ flames, and laminar, high-temperature (2100 < T < 2300 K) $C_2H_6/O_2/N_2$ flames.

Because of its quenching-independent nature, the feasibility of the LSF method is assessed for these measurements. The measured results are compared to the predictions of several chemical kinetics models to determine their capability for predicting high-pressure NO concentrations. While thermocouples can be used to measure temperatures in the low-temperature flames, a Rayleigh scattering thermometric technique is developed and utilized to measure temperatures in the high-temperature flames. The LSF method is also applied, in a preliminary fashion, to a few atmospheric-pressure turbulent flames to assess the capability for single-pulse measurements. The above work can be used to determine the accuracy of current chemical kinetics schemes. More importantly, this investigation demonstrates the feasibility of applying LIF to the measurement of NO concentrations in practical combustion environments.

In Chapter 2, a review is presented of the basic theory for laser-induced fluorescence (LIF). Owing to the importance of chemical kinetic modeling, a summary is also presented of the formation mechanisms for NO. Following this, previous studies which employed LIF to make quantitative measurements of NO are reviewed. Finally, a few other techniques available for obtaining quantitative measurements of NO are briefly discussed; these techniques include probe sampling and resonantly enhanced multiphoton ionization (REMPI). In Chapter 3, the experimental apparatus and methods used for the LIF measurements are described. The procedures used for making the theoretical calculations of the flame chemistry are also presented.

The results of LIF measurements of NO in flat, laminar, $C_2H_6/O_2/N_2$ flames at pressures up to 14.6 atm are presented in Chapter 4. In addition, to evaluate the utility of current chemical kinetics models at high pressure, the flames are modeled using two different reaction mechanisms: the GMK-DB mechanism [Drake and Blint, 1991], and the MB mechanism [Miller and Bowman, 1989]. Comparisons between the predicted results and the LIF measurements provide a test of the ability of these mechanisms to predict the

effects of high pressure on NO emissions. The similarity of the predicted and measured pressure trends also indicates that the trends are real and not an artifact of the measurement technique. A primary result found from this study is that the equivalence ratio corresponding to the peak NO concentration at a given pressure shifts towards leaner conditions as the pressure increases for these low-temperature flames.

In Chapter 5, this work is extended by presenting LIF measurements of NO in flat, laminar, $C_2H_4/O_2/N_2$ flames at pressures up to 11.9 atm. By comparing the NO measurements obtained from two different excitation lines, the internal consistency of the LIF procedure is verified. These measurements also seek to determine whether the shifting behavior is limited to paraffinic fuels (like ethane), or if, as anticipated, this trend is a more universal phenomenon. By again modeling the flames using two different reaction mechanisms, the ability of current chemical kinetics schemes to predict [NO] is evaluated in high-pressure $C_2H_4/O_2/N_2$ flames. One of these is the GMK-DB model; the other is the hydrocarbon scheme of Miller and Melius [1992] combined with the nitrogen kinetics of the GMK-DB model (MIME-DB). Comparisons between the predicted results and the LIF measurements provide a test of the ability of these mechanisms to predict the effects of high pressure on NO emissions from low-temperature premixed ethylene flames.

The theoretical transportability of the calibration factor is investigated for linear LIF measurements of [NO] in Chapter 6. In particular, comparisons are made between predicted fluorescence signals for a fixed NO mole fraction at calibration and measurement conditions for several calibration schemes. The flames considered are laminar, premixed, high-pressure $C_2H_6/O_2/N_2$ flames. Many of the same concepts would apply to other types of flames, as well. Finally, a discussion is given of some practical problems that would arise when attempting to use the same calibration factor at considerably different operating conditions.

The technique used to measure temperatures using Rayleigh scattering is developed and explained in Chapter 7. An approach similar to that of Namer and Schefer [1985] is taken; the technique used is an iterative scheme which involves correcting for the scattering cross-section based upon the species concentrations predicted using a comprehensive chemical kinetics model. Instead of assuming that the minor species are insignificant (as done by Namer and Schefer [1985]), the GMK-DB mechanism is used to provide a more accurate description of the flame chemistry. This should provide a more accurate representation of the flame composition, particularly through the flame front. Having calculated the gas composition, effective Rayleigh scattering cross-sections can be determined at each point in the flame. The Rayleigh scattering signal can then be corrected to give an accurate temperature measurement.

In Chapter 8, the low-temperature, laminar flame work is extended by presenting LIF measurements of NO concentrations in lean, laminar, high-temperature ($2100 \leq T_{max} \leq 2300$ K) $C_2H_6/O_2/N_2$ flames at equivalence ratios of 0.7 to 0.95 and pressures of 1.0 and 3.05 atm. The flames studied exhibit a steady rise in NO concentration with increasing height above the burner, indicating that significant thermal-NO production occurs in the burnt-gas region. To evaluate the predictive capability of current chemical kinetics models with respect to the NO production in these flames, the flames are also modeled using the GMK-DB model.

Preliminary results of [NO] measurements in a turbulent flame are presented in Chapter 9. A single-shot detection limit is also determined. Because the measurements are performed at 1 atm, broadband laser-saturated fluorescence (LSF) [Reisel et al., 1993] is employed for the measurements. LSF has been used previously to measure [OH] in turbulent flames [Lucht et al., 1984; Drake and Pitz, 1985]. The LSF signal is independent of the fluorescence quenching environment; therefore, the variable quenching environ-

ment of a turbulent flame will not affect the measurement. Finally, Chapter 10 contains conclusions reached from the entire investigation. Recommendations are also made for further work.

CHAPTER 2

THEORY AND LITERATURE REVIEW

2.1 Introduction

Nitric oxide (NO) is a major atmospheric pollutant which contributes to a variety of environmental problems, including the destruction of the stratospheric ozone layer [Johnston, 1971], the production of photochemical smog [Mortimer, 1983], and the formation of acid rain [Miller and Fisk, 1987]. Combustion processes, ranging from boilers in power plants to gas turbine engines on aircraft, are a primary source of NO. The above problems could be lessened by reducing NO emissions from various combustors into the atmosphere. To reduce NO emissions, an understanding is needed of the chemical kinetics involved in combustion processes.

Miller and Fisk [1987] argue that while some kinetics research can be conducted with physical sampling probes, improved measurements are more likely to arise from the use of optical measurement techniques. Physical sampling probes disrupt the flow field near the probe, and this disruption along with internal probe reactions may cause the concentration of the species under investigation to change. Optical measurement techniques are less likely to disturb the combustion process, as these remote measurements do not physically affect the flame; the result is more accurate measurements of the concentrations of minor flame species such as NO. In addition, optical techniques are more easily applied to practical combustion processes, whereas a physical probe may not withstand the harsh (high-pressure and high-temperature) conditions in such devices.

In this chapter, a review is presented of the basic theory for laser-induced fluorescence (LIF). Owing to the importance of chemical kinetic modeling, a summary of the formation mechanisms for NO is also presented. Following this, previous studies which employed LIF to make quantitative measurements of NO are reviewed. Finally, a few other techniques available for obtaining quantitative measurements of NO are briefly discussed; these techniques include probe sampling and resonantly enhanced multiphoton ionization (REMPI).

2.2 Theory

For this investigation, an understanding is needed of both the laser-induced fluorescence technique and the chemical kinetics controlling NO formation. The basic theory behind these two subjects is presented below.

2.2.1 Laser-Induced Fluorescence Theory

Laser-induced fluorescence is an optical technique which can be used for the detection and measurement of various radical species in a combustion environment. A basic understanding of the physical processes important to LIF can be gained through the use of a two-level electronic model. This model does not represent completely the physical situation controlling the broadband LIF measurements of NO discussed below. However, the two-level model is presented first so that the general behavior of an LIF system can be more readily understood. Following the discussion of the two-level model, the model is extended to include other features important in LIF measurements of NO.

In the two-level model, the number density (cm^{-3}) for the ground level is designated by N_l and that for the excited level by N_u. As discussed by Laurendeau and Goldsmith [1989], there are four basic assumptions that must be made when using this model. First, the laser beam employed for excitation should be uniform and linearly polarized. Second, all of the population must be in the ground level before laser excitation ($N_l = N_l^0$). Third,

the fluorescence signal is measured only when the population in the excited level reaches steady state conditions. Fourth, the fluorescence signal occurs at one wavelength, corresponding to a single electronic transition.

There are four transitions between the two electronic levels, each represented by a different rate coefficient (s^{-1}). The four processes are absorption (represented by W_{lu}), stimulated emission (W_{ul}), spontaneous emission (A_{ul}), and collisional quenching (Q_{ul}). While absorption requires the absorption of one photon (if the process is single-photon LIF), stimulated emission and spontaneous emission result in the emission of one photon. Two rate equations can be written for the population in each electronic level with time. These equations are

$$\frac{dN_l}{dt} = -N_l W_{lu} + N_u(W_{ul} + A_{ul} + Q_{ul}) \quad , \tag{2.1}$$

and

$$\frac{dN_u}{dt} = N_l W_{lu} - N_u(W_{ul} + A_{ul} + Q_{ul}) \quad . \tag{2.2}$$

Under steady-state conditions, Eqs. (2.1) and (2.2) are both equal to zero. Noting that $N_l^0 = N_l + N_u$, the population in the excited state can then be related to the total population, N_l^0, through

$$N_u = \frac{N_l^0}{\{(W_{ul} + A_{ul} + Q_{ul})/W_{lu}\} + 1} \quad . \tag{2.3}$$

Both the absorption and stimulated emission rate coefficients depend on the laser irradiance. Thus, under non-saturated conditions (i.e., when the laser irradiance is small) both W_{lu} and W_{ul} are small. In this case, Eq. (2.3) can be written as

$$N_u = \left\{ \frac{W_{lu}}{A_{ul} + Q_{ul}} \right\} N_l^0 \quad . \tag{2.4}$$

The fluorescence emission ε_f (W/cm^3•sr) can be related to N_u through [Laurendeau and Goldsmith, 1989]

$$\varepsilon_f = \frac{hc\nu_f A_{ul}}{4\pi} N_u \quad , \tag{2.5}$$

where ν_f (cm^{-1}) represents the wavenumber at which the fluorescence occurs. The signal obtained from the fluorescence emission depends on the collection optics and the detection electronics, i.e.,

$$V_f = \beta G \Omega_c V_c \varepsilon_f \quad , \tag{2.6}$$

where V_f is the fluorescence voltage, G is the photomultiplier gain (V/W), V_c is the fluorescence collection volume (cm^3), Ω_c is the solid collection angle of the optics (sr), and β is a term accounting for the detection efficiency of the collection optics. Combining Eqs. (2.4), (2.5), and (2.6), the fluorescence voltage for linear fluorescence can be determined from

$$V_f = \beta hc\nu_f G V_c \left(\frac{\Omega_c}{4\pi}\right) \left\{\frac{A_{ul}}{A_{ul} + Q_{ul}}\right\} N_l^0 W_{lu} \quad . \tag{2.7}$$

As mentioned above, the rate coefficient for absorption depends on the laser irradiance. For single-photon LIF, this rate coefficient can be found from

$$W_{lu} = \frac{\sigma I_L}{hc\nu_L} \quad , \tag{2.8}$$

where σ is the one-photon cross-section (cm^2), I_L is the laser irradiance (W/cm^2), and ν_L represents the wavenumber of the laser irradiance (cm^{-1}). From Eqs. (2.7) and (2.8), it is easy to see that, for small laser irradiances, the LIF signal depends on both the quenching environment and the laser power.

Under saturation conditions, the laser irradiance is large, which results in large values for W_{lu} and W_{ul}. For this case, Eq. (2.3) can be written as

$$N_u = \frac{W_{lu}}{W_{lu} + W_{ul}} N_l^0 \quad .$$

(2.9)

The two rate coefficients for absorption and stimulated emission are related by $g_l W_{lu} = g_u W_{ul}$, where g_l and g_u are the degeneracies of the ground and excited levels, respectively. After substitution, Eq. (2.9) becomes

$$N_u = \left\{ \frac{g_u}{g_l + g_u} \right\} N_l^0 \quad .$$

(2.10)

Using Eqs. (2.5) and (2.6), the signal for laser-saturated fluorescence (LSF) can then be written as

$$V_f = \beta h c \nu_f G V_c \left(\frac{\Omega_c}{4\pi} \right) \left\{ \frac{g_u}{g_l + g_u} \right\} A_{lu} N_l^0 \quad .$$

(2.11)

By comparing Eqs. (2.11) and (2.7), it can be seen that the LSF method is inherently independent of electronic quenching and laser power, while linear LIF measurements depend on both of these quantities. This often makes LIF more difficult to use than LSF for quantitative measurements of species concentrations.

The above discussion applies to narrowband detection, for which one transition is monitored exclusively. However, for LSF and LIF measurements of NO in flames, it has been previously shown that broadband detection is required to enhance the fluorescence signal [Reisel et al., 1993]. This requirement is due to both the compactness of the NO spectrum and the small NO concentration present in many flames. Previously, broadband detection has not been necessary for LSF measurements of flame radicals; on the other hand, standard LIF measurements are routinely performed using broadband detection. The basic analysis of the LSF or LIF signal remains unchanged for broadband detection. However, the effects of rotational population transfer must now be considered. In addition, the influence of photoionization should be included for NO. These details have been covered in depth by Reisel et al. [1993], and only the highlights are summarized here.

By including photoionization and rotational energy transfer, five types of transition can now occur between two electronic levels, and one can occur within a single electronic level. Each of these is represented by a different rate coefficient (s^{-1}). The five inter-electronic processes are absorption (W_{lu}), stimulated emission (W_{ul}), spontaneous emission ($A(j,k)$), collisional quenching (Q_e), and photoionization (W_i). In addition, rotational relaxation ($Q_r(m,n)$) can occur within each electronic level. In the following equations, j will be used to represent a rovibronic level in the excited electronic state, and k a rovibronic level in the ground electronic state. A diagram of the process is shown in Figure 2.1. As seen in Fig. 2.1, after excitation (which occurs through one rovibronic transition), the molecule may experience either stimulated emission, electronic quenching, vibrational or rotational relaxation, spontaneous emission (fluorescence), or photoionization. If a molecule first undergoes vibrational or rotational relaxation, it may still fluoresce, be photoionized, or be electronically quenched. In addition, after returning to the X-state, vibrational and rotational relaxation will almost certainly occur. (A further complication is that more than one rovibronic transition can often be excited, which leads to more than one pair of laser-coupled levels. For simplicity, however, only one set of laser-coupled levels is considered in the present analysis.)

Rate equations can now be written for the population in each laser-coupled level. These two equations are

$$\frac{dN_l}{dt} = -N_l W_{lu} - \sum_{k \neq l} N_l Q_r(l,k) + N_u W_{ul} + \sum_j N_j A(j,l) + \sum_{k \neq l} N_k Q_r(k,l) \quad , \tag{2.12}$$

and

$$\frac{dN_u}{dt} = N_l W_{lu} - N_u \{ W_{ul} + Q_e + W_i \} - \sum_{j \neq u} N_u Q_r(u,j)$$

$$- \sum_k N_u A(u,k) + \sum_{j \neq u} N_j Q_r(j,u) \quad . \tag{2.13}$$
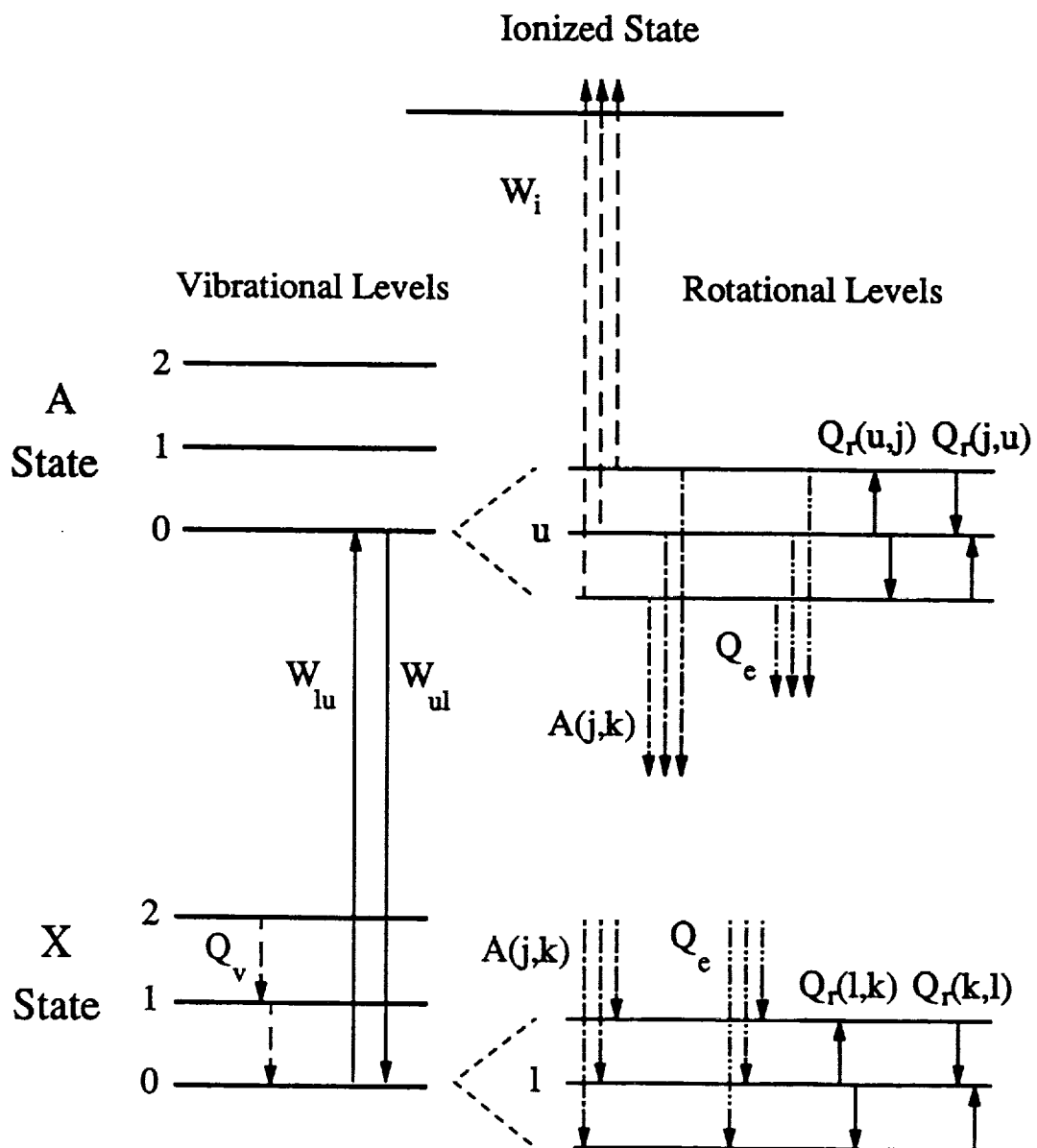
Figure 2.1   Example excitation scheme used in LIF studies. Shown are the rate coefficients for electronic quenching (Q_e), vibrational (Q_v) and rotational (Q_r) relaxation, absorption (W_{lu}) and emission (W_{ul}), spontaneous emission ($A(j,k)$), and photoionization (W_i).

A rate equation for the population in each of the collisionally populated levels within the excited electronic state can also be written:

$$\frac{dN_j}{dt} = \sum_{m \neq j} \{N_m Q_r(m,j) - N_j Q_r(j,m)\} - \sum_k N_j A(j,k) - N_j(Q_e + W_i) \quad , \qquad (2.14)$$

where m is a rovibronic level in the excited electronic state not corresponding to the level of interest. Under steady-state conditions, Eqs. (2.12), (2.13), and (2.14) are each equal to zero.

The influence of photoionization can be assessed by considering the ratio of the rate coefficient for photoionization to that for stimulated emission [Salmon and Laurendeau, 1987], i.e.,

$$\frac{W_i}{W_{ul}} = \frac{\sigma_i I_L/(h\nu_o c)}{2 I_L B_{ul}/(\pi \Delta \nu_L c)} \quad , \qquad (2.15)$$

where σ_i is the photoionization cross section (cm^2), I_L is the laser irradiance (W/cm^2), ν_o is the transition wavenumber (cm^{-1}), $\Delta \nu_L$ is the laser spectral width (cm^{-1}), c is the speed of light (cm/s), and B_{ul} is the Einstein coefficient for stimulated emission (cm$^3 \cdot$cm^{-1}/J$\cdot$s). In this expression, the following assumptions have been made: (1) the laser linewidth is much greater than the absorption linewidth, (2) the laser linewidth is described by a Lorentzian lineshape, and (3) the laser line is centered on the molecular transition. Equation (2.15) can be reduced to

$$\frac{W_i}{W_{ul}} = \frac{\pi \sigma_i (\Delta \nu_L/\nu_o)}{2(\hat{B}_{ul}/c)h} \quad , \qquad (2.16)$$

where $\hat{B}_{ul}$ is the Einstein coefficient for stimulated emission (cm^3/J$\cdot$s^2), as tabulated by

Reisel et al. [1992]. For the LIF measurements of NO considered by Reisel et al. [1993], $\sigma_i \approx 7.0 \times 10^{-19}$ cm^2 [Zacharias et al., 1980] and $\Delta \nu_L = 0.3$ cm^{-1}; hence, for the $Q_2(26.5)$ line of NO in the $\gamma(0,0)$ band, $W_i/W_{ul} \approx 0.001$. An estimate of $W_{ul} \approx 5 \times 10^{11}$ s^{-1} at the peak of the laser pulse can be made by considering a beam energy of 2 mJ/pulse, a Gaussian spatial

profile with a spot size of 250 μm, and a typical temporal profile. Therefore, the photo-ionization rate coefficient is found to be $W_i \approx 5 \times 10^8$ s^{-1} along the laser centerline. This value of the rate coefficient for photoionization is comparable to that for electronic quenching at atmospheric pressure [Drake and Ratcliffe, 1993]. Thus, in regions of high laser irradiance, fluorescence is inhibited by photoionization as well as electronic quenching.

Besides noting the effects of photoionization on the fluorescence signal, it is important to determine the effects of rotational energy transfer. As discussed by Reisel *et al.* [1993], after excitation the population rapidly redistributes over the different rovibronic levels within the excited electronic state. Fluorescence is then detected from each of these rovibronic levels back to the ground electronic state. By comparison to Eq. (2.5), the total fluorescence emission, $\varepsilon_{f,T}$, for broadband LIF can be found from

$$\varepsilon_{f,T} = \frac{hc}{4\pi}\left\{ v_f(u,k)A(u,k)N_u + \sum_{j\neq u} v_f(j,k)A(j,k)N_j \right\} \quad , \tag{2.17}$$

where, from Eqs. (2.13) and (2.14) under steady-state conditions,

$$N_u = \frac{N_l W_{lu} + \sum_{j\neq u} N_j Q_r(j,u)}{W_{ul} + Q_e + W_i + \sum_{j\neq u} Q_r(u,j) + \sum_k A(u,k)} \quad , \tag{2.18}$$

and

$$N_j = \frac{\sum_{m\neq j} N_m Q_r(m,j)}{Q_e + W_i + \sum_{m\neq j} Q_r(j,m) + \sum_k A(j,k)} \quad . \tag{2.19}$$

In Eq. (2.17), $v_f(j,k)$ is the wavenumber of the fluorescence transition and N_j is the population in rovibronic level j of the excited electronic state. As can be seen from Eq. (2.17), broadband detection will offer a much larger signal than narrowband detection, for if narrowband detection were to be used, only fluorescence from the directly excited rovibronic level would be detected.

If one desired to analytically determine the population in each excited rovibronic level, one would need to know the rotational transfer coefficients, Q_r. However, there is very little data available on these rate coefficients [Crosley, 1992]. Therefore, the above expressions are more valuable for demonstrating the increase in available signal when using broadband detection than for computing the actual distribution in population among the rovibronic levels in the upper electronic state.

2.2.2 Nitric Oxide Chemical Kinetics

NO is produced through three main reaction mechanisms [Drake and Blint, 1991]: (1) the Zeldovich, or thermal-NO, mechanism [Zeldovich, 1946], (2) the N_2O-intermediate mechanism [Wolfrum, 1972; Malte and Pratt, 1974], and (3) the prompt-NO mechanism [Fenimore, 1971]. The amount of NO formed through each of these mechanisms depends on the temperature, pressure, and equivalence ratio of the flame.

There are three primary reactions in the thermal-NO mechanism. These are [Miller and Bowman, 1989]

$$O + N_2 \leftrightarrow NO + N , \tag{Z1}$$

$$N + O_2 \leftrightarrow NO + O , \tag{Z2}$$

and

$$N + OH \leftrightarrow NO + H . \tag{Z3}$$

The thermal-NO mechanism principally involves the breaking of strong molecular bonds; hence, the mechanism is very temperature dependent. For low temperature flames, the amount of NO produced through this mechanism is small, but for high temperature flames, the thermal-NO mechanism becomes the dominant pathway for NO production [Corr *et al.*, 1992]

The N_2O-intermediate mechanism has four primary reactions [Malte and Pratt, 1974]. These are

$$N_2 + O + M \leftrightarrow N_2O + M \ , \tag{MP1}$$

$$N_2O + O \leftrightarrow NO + NO \ , \tag{MP2}$$

$$N_2O + O \leftrightarrow N_2 + O_2 \ , \tag{MP3}$$

and

$$N_2O + H \leftrightarrow N_2 + OH \ . \tag{MP4}$$

As can be seen, the N_2O-intermediate mechanism involves the production of nitrous oxide, and the subsequent attack of N_2O by the atomic flame radicals O and H. These reactions can lead to either the production of NO, or the reforming of N_2.

The third main pathway for NO formation is the prompt-NO mechanism. This mechanism does not directly form NO; rather the prompt-NO mechanism involves the reaction of hydrocarbon species with N_2 to form cyano compounds (such as HCN) and atomic nitrogen which then react to form NO. The dominant reaction in this mechanism is now thought to be [Corr et al., 1992]

$$CH + N_2 \leftrightarrow HCN + N \ . \tag{F1}$$

In addition, three other reactions are frequently considered for modeling prompt-NO production; however, the first two of these are considered insignificant, and the last one is considered minor when compared to Reaction F1 [Miller and Bowman, 1989]. These are

$$CH_2 + N_2 \leftrightarrow HCN + NH \ , \tag{F2}$$

$$CH_2 + N_2 \leftrightarrow H_2CN + N \ , \tag{F3}$$

and

$$C + N_2 \leftrightarrow CN + N \ . \tag{F4}$$

It has been found [Bachmaier, 1973] that the prompt-NO mechanism depends on the type of fuel used in the combustion process. This is due to the various rates at which different fuels will break into the required smaller hydrocarbons. In addition, the prompt-NO

mechanism depends strongly on the equivalence ratio. This mechanism also tends to produce much more NO under moderately fuel-rich conditions than under fuel-lean conditions. However, prompt-NO production is significantly curtailed for highly fuel-rich flames.

Another source of NO in practical combustion processes is the NO formed from fuel-bound nitrogen. Unlike the ideal "clean" fuels that are frequently used in laboratory experiments, many practical fuels, such as coal, contain nitrogen. For these fuels, it is important to study the chemical kinetics involved in producing NO from fuel-bound nitrogen. However, because this conversion does not apply to the fuels used in this study, the pertinent reactions will not be reviewed here. Miller and Bowman [1989] discuss the kinetics of fuel-bound nitrogen in considerable detail.

Over the years, computer modeling of various flames has produced information concerning the relative importance of each of the above mechanisms. As mentioned previously, the thermal-NO mechanism is very temperature dependent. To minimize the amount of thermal-NO formed, the temperature of the flame must be reduced. This, however, will tend to decrease the efficiency of combustion devices. It has also been found that production of NO through the thermal-NO and the N_2O-intermediate paths can be enhanced by superequilibrium concentrations of OH and O [Drake et al., 1991].

Glarborg et al. [1986] found that for methane combustion in well-stirred reactors, the thermal-NO contribution, because it is temperature dependent, is greatest in near-stoichiometric flames. However, prompt-NO formation peaks in rich flames, thereby pushing peak NO emissions to richer conditions for low-temperature flames. Corr et al. [1992] claim that all three mechanisms should be considered for lean, premixed combustion. Unlike diffusion flames, which are dominated by thermal-NO production, premixed flames are not necessarily stoichiometric, and thus the lower temperature of these flames tends to enhance the influence of the prompt and N_2O mechanisms.

Miller and Bowman [1989] performed a thorough chemical kinetics modeling study to determine the relative importance of the various reaction paths. They found that, in general, the thermal-NO reactions need to be coupled with those reactions involving oxidation of the fuel. This is necessary because of the presence of O and OH radicals in the thermal-NO mechanism. Frequently, equilibrium concentrations of O, O_2, N_2, and OH had been used in previous thermal-NO calculations; this procedure however, leads to an inaccurate prediction of the NO formation rates. As mentioned previously, Miller and Bowman [1989] also determined that Reactions (F2) and (F3) are insignificant in the prompt-NO production process, and that Reaction (F1) dominates the process. Reaction (F4) does contribute a minor amount of prompt-NO. Their work also suggests that the rapid drop-off of prompt-NO production in rich flames is due to a rapid decrease in the HCN concentration. This would correspondingly indicate a lack of N atoms being produced through Reaction (F1).

Part of this work is concerned with high-pressure, low-temperature premixed flames. Reisel et al. [1993] found that most of the NO is formed in the flamefront for atmospheric-pressure versions of these flames. Modeling the flamefront NO in such flames requires consideration of all three reaction mechanisms [Drake and Blint, 1991; Corr et al., 1992]. However, the prompt-NO mechanism does not contribute to post-flame NO production, owing to a lack of necessary radicals in the post-flame gases. Drake et al. [1991] found that for high-pressure, low-temperature, lean, premixed $C_2H_6/O_2/N_2$ flames, all three mechanisms (with the thermal-NO and N_2O-intermediate mechanisms enhanced by superequilibrium O concentrations) contribute to flamefront NO production.

In summary, previous work has found that the thermal-NO mechanism dominates at high temperatures, and that all three mechanisms are important in low-temperature flames. However, the prompt-NO mechanism tends to dominate in moderately rich low-temperature flames. As the flames become more fuel-rich, prompt-NO production peaks,

and then rapidly decreases. In low-temperature flames, most of the NO is formed in the flamefront, while in high-temperature flames, significant NO production will occur in the post-flame zone. These results suggest that for low NO production, combustion designers should keep flame temperatures low, and either use very lean or very rich combustion.

2.3 Previous Quantitative NO Measurements

Previously, quantitative NO measurements have been made through a variety of techniques, including laser-induced fluorescence, probe sampling, and absorption spectroscopy. Below, the previous studies of NO using LIF are thoroughly reviewed; a brief discussion is also provided of two other useful techniques for obtaining quantitative measurements of NO, REMPI and probe sampling. A summary of other NO-measuring techniques, such as absorption spectroscopy, can be found in Reisel [1991].

2.3.1 LIF Measurements of NO

There have been several laser-induced fluorescence studies which have provided semi-quantitative NO measurements in combustion environments. Most of these [Morley, 1981, 1982, Chou, et al. 1983, Cattolica et al. 1989, and Heard et al., 1992] have used linear LIF. Consequently, these studies employed various strategies to account for variations in the quenching rate coefficient.

Morley [1981] used LIF measurements to study the reaction mechanism which produces NO from fuel nitrogen. He utilized flat, rich, $H_2/O_2/Ar$ flames at 1790-2200 K, doped with varying amounts of CH_3CN, as the environment for the NO concentration measurements. The range of NO concentrations which he measured was 180 to 1600 ppm. For excitation, the region containing the P_1 bandhead in the $\gamma(0,0)$ band was used, while for detection, the fluorescence was monitored in the spectral region between and including the $\gamma(0,1)$ and $\gamma(0,5)$ bands [Morley, 1982]. Calibration was achieved by doping NO into each flame, and obtaining the fluorescence signal for this known amount of NO. This technique assumes that there is no NO destruction in these $H_2/O_2/Ar$ flames; Morley

[1981] felt that this was an acceptable technique, for the NO signal was constant in the burnt gas region and was proportional to the amount of NO originally doped into the flame. For small amounts of CH_3CN, the NO concentration increased throughout the post-flame region. Large amounts of CH_3CN doping produced a maximum point of NO concentration early in the post-flame region, with the NO concentration decreasing downstream from this point. Morley [1981] determined from this result that the NO-producing reaction is initially faster than the NO-consuming reaction, but that this trend reverses further downstream in the flame.

Chou et al. [1983] utilized the LIF technique to determine NO concentration profiles in flat, atmospheric-pressure $NH_3/O_2/N_2$ and $CH_4/air/O_2$ flames. They determined absolute concentrations for all their flames by using absorption measurements to determine the NO concentration in a lean $NH_3/O_2/N_2$ flame. They then scaled the fluorescence signal of interest to that from this flame, assuming a linear relationship between the LIF signal and the absolute concentration. Hence, their calibration method assumes that the quenching environment is the same in all flames. They were unsuccessful at calibrating the signal by doping NO into rich NH_3 flames, because the NO was consumed in these rich flames. The results they present were all for rich $NH_3/O_2/N_2$ and $CH_4/air/O_2$ flames, which they believed should have a higher NO concentration than comparable lean flames. However, as described by Reisel [1991], there is reason to doubt their absolute concentration measurements, for there is a strong possibility that part of the LIF signal they measured was attributable to another polyatomic molecule.

For their measurements, Chou et al. [1983] utilized a laser energy of 1 μJ/pulse, which was low enough, based on previous calculations [Eckbreth et al., 1979], to avoid saturation. Chou et al. [1983] also determined that NH_3 quasi-continuum absorption in the NO $\gamma(0,0)$-band region could provide considerable interference to the NO measurements. To reduce this problem, they used a combination of the $Q_2(7.5)$, $^QR_{12}(7.5)$, $P_2(14.5)$,

$^{P}Q_{12}(14.5)$, and $^{O}P_{12}(24.5)$ lines of the (0,1) band for NO excitation, even though this choice lowered the LIF signals by a factor of 2.5 (due to the lower initial population in the $v'' = 1$ vibrational level). Detection was performed using the $\gamma(0,3)$ band. They reported measured concentrations down to ~13 ppm, and felt that NO could be detected with LIF at concentrations less than 1 ppm. Finally, they detected the evolution of prompt-NO in a variety of $CH_4/air/O_2$ flames.

Cattolica *et al.* [1989] used LIF to perform quantitative NO concentration measurements in flat, low-pressure (76 torr) $H_2/O_2/NO$ flames. They utilized both lean and rich flames with two different levels of NO-doping. The NO was excited using the $Q_2(25.5)$ transition in the $\gamma(1,0)$-band, as this transition is well separated from nearby main-branch transitions, and has a ground state population which varies by only ±3% over a temperature range from 1000 to 1700 K. The fluorescence was detected in the $\gamma(1,4)$-band, as that band has a favorable branching ratio and is sufficiently spectrally separated from the excitation wavelength to allow for rejection of Rayleigh scattering. They found a rapid reduction in NO concentration in the first 10 mm above the burner, beyond which the NO concentration remained constant for each flame. The concentration in the post-flame region was proportional to the amount of NO added. These results indicated that some (~10-30%) destruction of NO was occurring in the flame, but that the amount of destruction was smaller than Seery and Zabielski [1981] had observed through use of a molecular-beam mass spectroscopy experiment. To obtain absolute NO concentrations, Cattolica *et al.* [1989] measured the local collisional quenching rate coefficient by determining the time constant of the fluorescence decay via a temporally-resolved fluorescence measurement.

Heard *et al.* [1992] performed LIF measurements of NO in low-pressure (30-120 torr) CH_4/air flames. For excitation, they utilized the $Q_1(17.5)$ line of the $\gamma(0,0)$ band, while detection was accomplished using either the $\gamma(0,1)$ band or the $\gamma(0,2)$ band. To

avoid saturation effects, the NO measurements were taken with a laser energy of ~1 µJ/pulse. Heard *et al.* [1992] calibrated the NO fluorescence signals by obtaining LIF measurements of known amounts of NO in He/Ar mixtures at room temperature. The difference in quenching environment between the calibration mixture and the flames was accounted for by the measurement of fluorescence decay times. The change in Boltzmann fraction of the ground level owing to the temperature difference between the calibration mixture and the flame conditions was also incorporated into the analysis.

As discussed in Section 2.1, linear fluorescence is complicated by the dependence of the signal on both the laser power and the quenching environment in the flame. Variations in laser power can be quantitatively corrected by using laser-energy normalization. Collisional effects must be handled by either assuming a constant quenching rate coefficient or determining the actual value of this rate coefficient. The four studies discussed above handled the quenching problem in different ways; Morley [1981, 1982] and Chou *et al.* [1983] related their fluorescence signal to that in a flame with a known NO concentration, thus making the assumption of a constant quenching environment, while Cattolica *et al.* [1989] and Heard *et al.* [1992] monitored the quenching rate coefficient directly to correct the fluorescence signals.

One way to essentially avoid the dependence on laser power and quenching rate coefficient is to employ laser-saturated fluorescence (LSF) [Daily, 1977]. To achieve saturation of the NO transition of interest, the laser irradiance must be large enough to ensure that the laser excitation rate is much greater than the collisional quenching rate. When this condition is met, the population in the excited level is equal to that in the ground level to within a ratio of the degeneracies of the two levels. Because the LSF signal is unaffected by the quenching environment, quantitative measurements are more easily made with LSF than with linear LIF. A drawback of LSF is that saturation cannot be maintained in the wings of the beam where the irradiance is low. Previously, laser-

saturated fluorescence has been used for successful quantitative measurements of OH [Salmon and Laurendeau, 1985; Carter *et al.*, 1992], NH [Salmon *et al.*, 1984], and CH [Kohse-Höinghaus *et al.*, 1984]. In addition, a broadband version of LSF has been applied to quantitative measurements of NO [Reisel *et al.*, 1993].

Reisel *et al.* [1993] used LSF to perform quantitative NO measurements in a series of laminar, flat, atmospheric-pressure, $C_2H_6/O_2/N_2$ flames. In this study, they measured [NO] vs. height above the burner for six different flames, using both linear LIF and LSF. In addition, they measured the NO concentration in the post-flame zone in a series of flames with different equivalence ratios. The NO concentrations were calibrated by doping three different known quantities of NO into a lean (ϕ=0.80) flame, and measuring the respective fluorescence signals. The resulting data were fit to a straight line through a least-squares procedure, and the slope of the line was used as a calibration factor for [NO] vs. the fluorescence signal. This factor was then applied to each flame of interest to obtain the relevant NO concentrations. The data from the post-flame zone (8 mm above the burner surface) in the various flames is reproduced from Reisel *et al.* [1993] in Fig. 2.2. The temperatures of these flames were 1600-1800 K. The linear LIF measurements were performed with a laser energy of ~25 μJ/pulse, and the laser energy for the LSF measurements was ~1 mJ/pulse.

Figure 2.2 shows that the results obtained using linear LIF and LSF are almost identical, thus indicating that the effects of fluorescence quenching on the LIF signal can be neglected. Further analysis, involving the calculation of the quenching rate coefficient based on the calculated major species concentrations and existing quenching cross-sections [Drake and Ratcliffe, 1991], verifies that the quenching rate coefficient does not vary significantly over the range of equivalence ratios studied (see Chapter 4). This result shows that for these flames, quantitative measurements of NO can be made using linear LIF, without the normally requisite corrections for quenching rate variations.
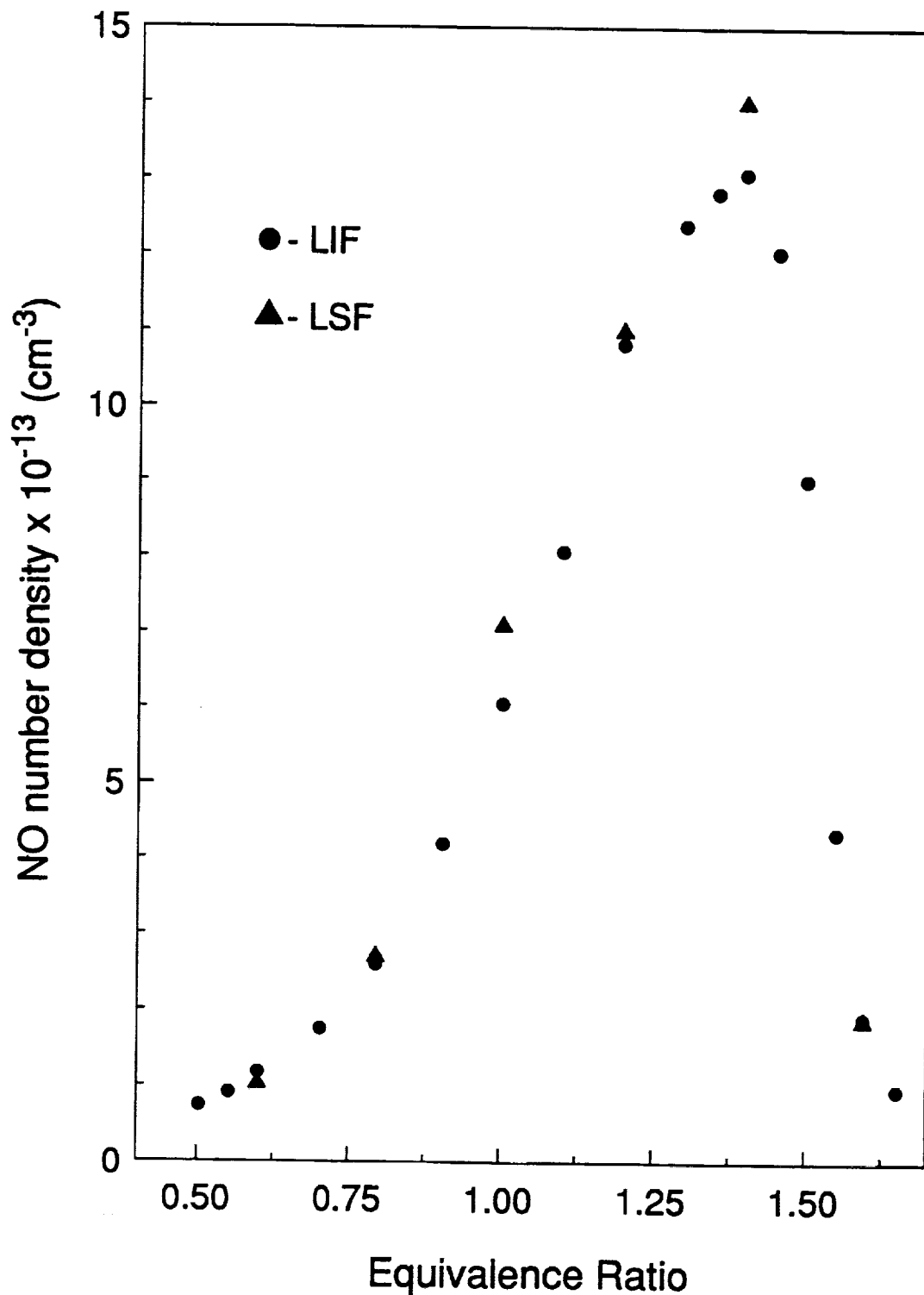
Figure 2.2   Measurement of NO number density vs. equivalence ratio in the post-flame zone of $C_2H_6/O_2/N_2$ flames at atmospheric pressure. The total flow rate and dilution ratio were held constant at ~17.7 slpm and 3.1, respectively. [Reisel *et al.*, 1993]

Reisel *et al.* [1993] also determined that the NO was produced predominantly in the flamefront of these low-temperature flames. The NO concentration did not vary with height above ~3 mm, indicating that the NO produced was primarily prompt-NO. The temperatures obtained in these flames were not high enough to produce significant amounts of thermal-NO. Finally, Reisel *et al.* [1993] estimated a detection limit of ~1 ppm of NO for the flames of their investigation.

Recently, Battles *et al.* [1994] attempted to obtain quantitative planar laser-induced fluorescence (PLIF) images of NO in lean, high-pressure, CH_4/air flames. Excitation was performed using the $Q_1(14.5)$ + $Q_2(20.5)$ + $P_1(23.5)$ lines of the $\gamma(0,0)$ band, and the broadband fluorescence was detected after passing through a UG5 Schott glass filter. The excitation region was chosen to minimize interference with O_2, which has spectral features in the same region as the $\gamma(0,0)$ band of NO. In addition, the wide spectral region encompassing UG5 detection increases the possibility of interference from O_2 fluorescence. The excitation region is also fairly sensitive to temperature, which leads to additional uncertainty when interpreting relative fluorescence signals from a flowfield. To make the images quantitative, a measurement of the [NO] was obtained with a chemiluminescent analyzer at a single point in the flow field, and then applied over the remainder of the flowfield. A procedure was also developed to apply the same calibration in other flames. This procedure involves correcting the fluorescence signal for changes in the quenching environment and for variations in the spectrum resulting from temperature changes and from pressure broadening of the spectral lines. Using this procedure, Battles *et al.* [1994] calibrated the NO fluorescence signal in a 1 atm flame, and then applied the calibration at higher pressures. To successfully use the atmospheric-pressure calibration at higher pressures, precise positioning of the laser wavelength at different pressures and accurate knowledge of the laser and spectral linewidths are needed.

2.3.2 REMPI Measurements of NO

Resonantly enhanced multiphoton ionization (REMPI) is an optical diagnostic technique which involves ionization, through multiphoton absorption, of the species under investigation. The ionized particles are then detected with a physical probe located above the point of laser excitation. REMPI provides high sensitivity, and has excellent spatial resolution [Rockney et al., 1982]. In addition, REMPI allows for NO measurements which are independent of quenching [Cattolica et al., 1989].

Two studies using REMPI to detect NO in flames appeared almost simultaneously. Rockney et al. [1982] used REMPI to detect nascent NO in an atmospheric-pressure, laminar, premixed, CH_4/air flame. They measured a REMPI spectrum of the (0,0) and (1,0) A-X bands, and determined the absolute NO concentration in the flames. The signals were calibrated by using a linear relationship between concentration and signal, based upon a measurement of the REMPI signal at a known NO concentration. Mallard et al. [1982] used REMPI to detect NO in an atmospheric-pressure H_2/air/N_2O flame. In this study, Mallard et al. [1982] presented a REMPI spectrum of the A-X transition between 270 and 317 nm and noted that the spectrum was very similar to the single-photon absorption spectrum in atmospheric-pressure flames. This prompted them to develop a new model for REMPI, which accounts for both the collisional repopulation of the state depleted by laser excitation and the collisional removal of molecules from the directly excited state, to explain this behavior. Mallard et al. [1982] also determined that the detectability limit of NO by REMPI is ~1 ppm. Jacobs [1986] used REMPI to determine the population of NO in the ground electronic state. They reported that REMPI has more sensitivity than LIF for detecting low concentrations of NO.

Howard et al. [1992] used REMPI to measure relative NO concentrations in low-pressure C_2H_4/O_2/Ar and H_2/NO_2 flames. These measurements were taken as part of a study comparing measured O, H, OH, CH_3, HCO, NO and NO_2 measurements to kinetic

predictions. The ions produced from the REMPI process were detected on a 0.5-mm diameter platinum rod located just above the focus of the laser beam. Using REMPI, the relative NO concentration as a function of height above the burner was measured. These values could have easily been converted to quantitative measurements with a suitable calibration.

2.3.3 Probe Sampling Measurements of NO

The description "probe sampling techniques" encompasses several measurement processes which all involve the insertion of a physical probe into the flame, withdrawing a sample of gas from the flame, and analyzing the sample to measure the concentrations of various species. Two of the more commonly used techniques currently used to measure [NO] are probe sampling with chemiluminescent detection and molecular beam-mass spectrometry (MBMS).

The chemiluminescent detection concept was first proposed by Fontijn, *et al.* [1970]. In the proposed scheme, NO reacts with O or O_3, emitting light in the process. The light is detected by a phototube, and the resulting intensity is directly equated to the NO concentration through an appropriate calibration. Such a technique is useful for detection of NO down to ppb levels, and has been implemented in commercially available devices. This technique has been used in numerous studies for the detection of NO. Frequently, the NO is measured in conjunction with NO_2 and reported as NO_x; however, most of the NO_x in a flame will be in the form of NO. To give an idea as to some of the applications of this technique, a sampling of relevant studies is presented below.

Heberling [1977] used chemiluminescent detection to determine prompt NO formation in high pressure, premixed, C_2H_4/air flames. To do this, gas samples from the flames were collected with a 1/4-inch water-cooled stainless steel probe from various locations in the post-flame zone. The data were then extrapolated back to a height of zero, and the resulting intercept was termed the prompt NO. Such an analysis includes the NO

formed from other paths besides the Fenimore path; therefore, many investigators may not consider this result to give only prompt-NO. Total NO_x was measured, which led to added difficulties near the flamefront, where the ratio of $[NO_2]/[NO]$ was high. This meant that the [NO] measured in the flamefront was also too high. However, this problem was not as great in the post-flame zone, where most of the measurements were taken.

Leonard and Correa [1990] used chemiluminescent detection to measure NO_x in lean, premixed, high-pressure methane flames. A 1/8-inch uncooled quartz sampling probe was used to remove gas samples from the post-flame zone of the different flames. The samples were then directed to a NO_x analyzer, as well as to CO, CO_2, and O_2 analyzers. Using the probe, NO_x was measured, down to ppm levels, as a function of equivalence ratio for different pressures (up to 10.3 atm) and different inlet temperatures. They found that the $[NO_x]$ at a given equivalence ratio in these lean flames was greater at higher pressures and at higher inlet temperatures.

Drake *et al.* [1991] measured [NO] as a function of height above the burner for several high-pressure, lean, $C_2H_6/O_2/N_2$ flames. An uncooled, 100-μm quartz sampling probe was used to remove the gas sample, and the sample was transported to the chemiluminescent analyzer through water-cooled quartz and Teflon lines so as to minimize surface reactions. The chemiluminescence was generated using a surface reaction of NO_2 with an organic liquid. These features improved the sensitivity and spatial resolution of the technique. Almost all of the measured NO_x was found to occur in the form of NO. The measured profiles of [NO] were found to rise rapidly, and then to flatten in the post-flame zone of these low-temperature flames. The distance above the burner over which the [NO] increased varied inversely with pressure. However, the spatial resolution of the technique remained adequate to resolve the NO production region up to 6.1 atm.

Molecular beam-mass spectrometry is a technique in which a sample of gas is removed from the flame and sent in a narrow stream into a mass spectrometer. A

molecular beam is a very low-pressure, narrow beam of neutral molecules which is designed to minimize collisions with other molecules in the beam and with the walls [Ramsey, 1985]. Such a beam should retain the species concentrations it possessed when the sample was originally removed from the flame. The beam is then directed through a mass spectrometer. In such a device, the molecules are first turned into ions, often through electron bombardment. The ions are then separated into different beams corresponding to a ratio of mass to charge [Shrader, 1971]. This separation is done either with a steady magnetic field (magnetic deflection spectrometry) or with a pulsating magnetic field (time-of-flight spectrometry) [Fristrom and Westenberg, 1965]. For the former, the ions are deflected by varying amounts based upon the mass of the ion. For the latter, a constant kinetic energy from the magnetic field is imparted onto a group of ions, resulting in different velocities for the ions based on the mass of the ion. The time necessary to reach a detector is then recorded, allowing for the determination of the concentration of the ions. While the analysis of the resulting signals can be more involved than with chemilumi-nescent detection, the MBMS system offers simultaneous measurement of many species. The sensitivity of the MBMS technique depends on the sensitivity of the detector used. To give a flavor of the type of work which can be done with MBMS, two MBMS studies involving NO are discussed below.

Seery and Zabielski [1981] performed MBMS with a time-of-flight mass spectrometer to study low-pressure $H_2/O_2/Ar/NO$ flames. A quartz probe with a diameter of 350 μm was used to remove the gas samples from different heights above the burner. The major species H_2O, H_2, and O_2 were measured, in addition to the NO, as a function of height above the burner. Garo et al. [1992] used MBMS to measure NO and other species concentrations in low-pressure, premixed, laminar, CH_4/O_2 flames with added NH_3 and NO. A small quartz probe was used to remove the gas sample and begin the formation of the molecular beam. They used the samples to obtain profiles of H_2O, OH, O, CO, CO_2,

H, HCN, CH$_3$, and NO as a function of height above the burner. The data were then used to evaluate chemical kinetics models for the flames. As can be seen from these examples, MBMS allows for simultaneous measurement of many flame species, which is convenient for chemical kinetic evaluations.

Physical probe techniques allow for the spatially resolved measurement of NO, often coupled with the measurement of other species. However, care must be taken to minimize perturbation of the flowfield and to ensure that the reactions in the gas sample are frozen as it is removed from the flame. If these are not done, the probe may alter the chemistry of the flame or products, resulting in inaccurate concentration measurements.

2.4 Summary

In summary, laser-induced fluorescence in an accurate, sensitive, non-intrusive diagnostic technique which can be used to measure NO. Unlike other quantitative techniques such as REMPI and probe sampling, LIF allows for measurements to be made without use of any physical probe which could disturb the flame. This disturbance could alter the actual NO concentrations. The theory for LIF has been summarized, both for a simple two-level model of NO, and for broadband LIF measurements.

The basic chemical kinetics of NO formation have also been reviewed. There are three main reaction paths for NO formation which are of concern in the combustion of non-nitrogen containing fuels. The Zeldovich mechanism dominates NO production at high-temperatures (> 2000 K). The N$_2$O-intermediate mechanism is important in lean flames in the flamefront, and the prompt-NO mechanism is especially important in the flamefront of rich flames.

CHAPTER 3

EXPERIMENTAL APPARATUS AND COMPUTER MODELING

3.1 Introduction

Combustion environments can be studied both experimentally and theoretically. Experimentally, the concentration of certain radical species can be determined by both optical techniques and with physical sampling probes [Miller and Fisk, 1987]. These measurements can then be compared to theoretically predicted concentrations which can be calculated from comprehensive chemical kinetics models. A comparison of this type can be beneficial in one of two ways. First, if the chemical kinetics are well understood for a given flame, the results predicted by the computer programs can be used to determine the accuracy of an experimental technique. Conversely, if the accuracy of the measurement technique is well known, the measurements can be used to determine the validity of the proposed chemical kinetics.

In this study, an experimental technique, laser-induced fluorescence (LIF), is applied to the detection of nitric oxide (NO) in high-pressure flames. Previously, LIF had not been applied to the detection of NO at high pressure; however, based on the accuracy of LIF ($\pm$ 25%) in the determination of the NO concentration at atmospheric-pressure [Reisel et al., 1993] and the success of LIF (in the form of laser-saturated fluorescence) for the measurement of [OH] at high-pressure [Carter et al., 1992], LIF is expected to be an accurate technique for the determination of NO concentration in high-pressure flames. The NO measurements obtained using LIF will then be used to check the accuracy of the chemical kinetics models for laminar, premixed, flat, high-pressure $C_2H_6/O_2/N_2$ and $C_2H_4/O_2/N_2$

flames.

In this chapter, the apparatus used for the LIF measurements is described. An explanation of the procedure used in making the theoretical calculations of the flame structure is then presented.

3.2 Experimental Apparatus

For the majority of the LIF measurements of NO, the $Q_2(26.5)$ line of the $\gamma(0,0)$ band ($\lambda \approx 225.6$ nm) was used for excitation of NO. The laser system producing this wavelength is composed of a Quanta-Ray DCR-3G Nd:YAG laser, with a PDL-2 dye laser and a WEX-1 wavelength extender. The second harmonic ($\lambda=532$ nm) of the Nd:YAG laser was used to pump the dye laser, which was configured for transverse pumping of the oscillator and longitudinal pumping of the amplifier. The dye laser output ($\lambda \approx 572$ nm) was frequency doubled, and the resulting ultraviolet beam was mixed with the residual infrared beam (1064 nm) to produce radiation at $\lambda \approx 225.6$ nm. A Pellin-Broca prism was used to disperse the colinear beams (with wavelengths of 1064, 572, 286, and 225.6 nm), and the desired beam (225.6 nm) was raised in height with a prism assembly inside the WEX. The maximum energy obtained for the mixed beam leaving the WEX assembly was ~6.5 mJ/pulse (corresponding to an energy of ~330 mJ/pulse for the $\lambda=532$ nm beam).

A schematic diagram of the experimental apparatus is shown in Fig. 3.1. After the beam left the WEX, a portion was directed to a UV-sensitive photodiode, which produced a triggering pulse for the electronics. The main beam was then focussed with a 1000-mm focal length lens, giving an ~250 µm spot size over the burner. To block any scattered radiation, an aperture was placed before the burner. The beam was directed towards the burner and raised in height with a two-mirror beam steering assembly. After passing over the burner, the beam was directed towards a beam dump, with a portion of the beam split off with a fused silica plate and directed towards a photodiode. This photodiode was used to monitor the beam energy.

FROM LASER
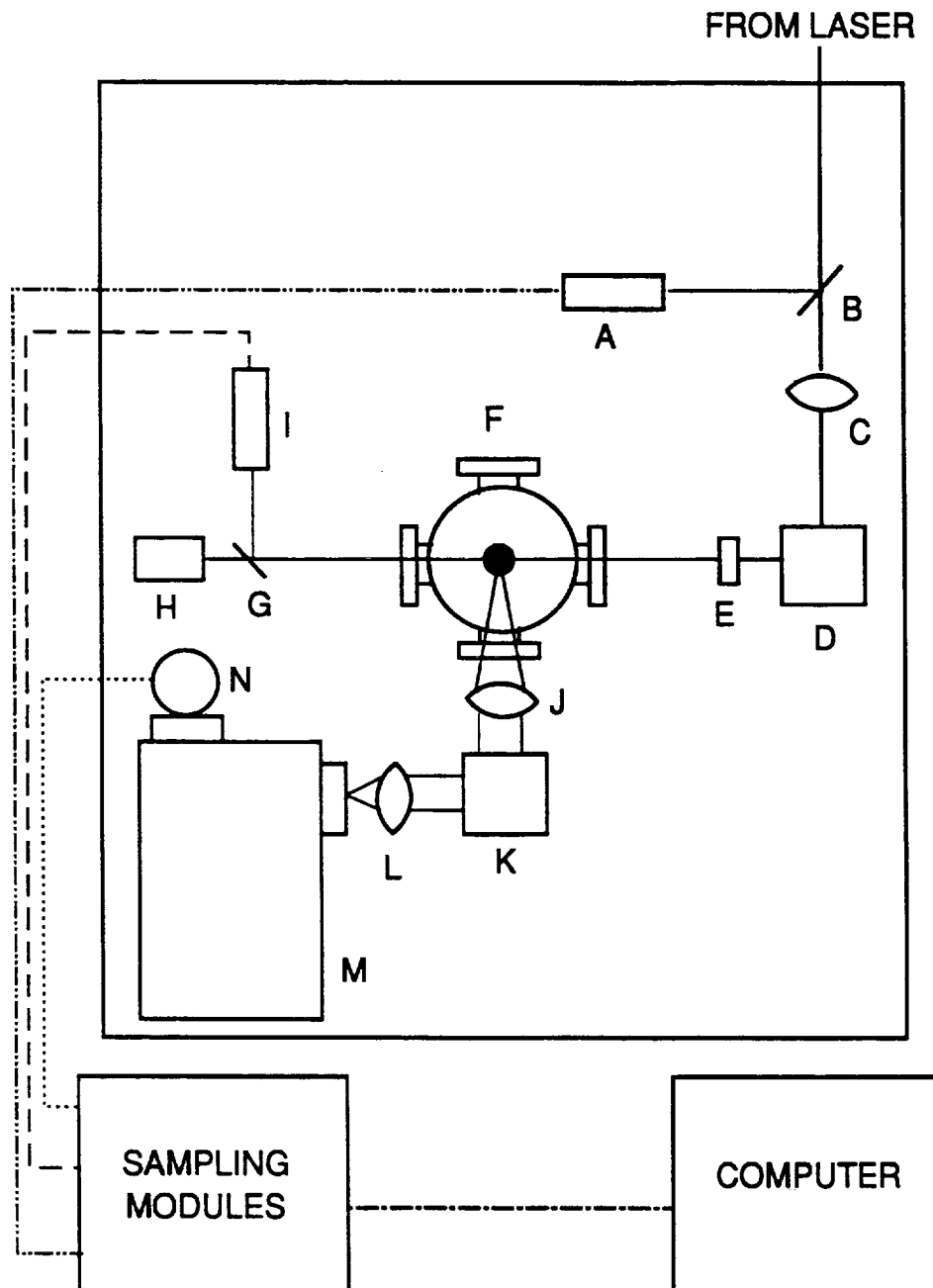
Figure 3.1:   Schematic diagram of experimental apparatus: A-trigger photodiode; B,G-beam-splitter; C-1000-mm focal-length lens; D,K-beam steering assembly; E-aperture; F-pressure vessel; H-beam dump; I-power-monitoring photodiode; J-200-mm focal length lens; L-300-mm focal-length lens; M-1/2 m monochromator; N-PMT.

Fluorescence, typically from the $\gamma(0,1)$ band of NO at 234 - 237 nm, was collected at a 90° angle to the incident laser radiation. The fluorescence was collimated with a 200-mm focal-length fused silica lens. A mirror assembly rotated the fluorescence by 90°, after which the fluorescence was focused by a 300-mm focal-length fused silica lens onto the entrance slit of a 1/2-m monochromator. The detector located after the exit slit was an RCA 1P28B photomultiplier tube (PMT), specially wired for temporal resolution of the fluorescence signal [Harris *et al.*, 1976].

For the LIF measurements of NO number density, the entrance slit width of the 1/2-m monochromator was 120 µm and the entrance slit height was set at 1 cm. With a magnification factor of 1.5 in the collection optics, the resulting image of the entrance slit was 80 µm × 6.67 mm. In an attempt to achieve laser-saturated fluorescence (LSF), which would have resulted in a natural independence of the fluorescence signal from quenching and laser power fluctuations, it was desired to minimize the collection of fluorescence from the wings of the laser beam. To achieve this, the image of the entrance slit (80 µm) was chosen to be smaller than the width of the focused laser beam (250µm) and was positioned at the center of the beam.

The PMT and photodiode signals were recorded with Stanford Research Systems equipment. For the LIF experiments, the PMT signal was resolved with an SR255 fast sampler using a 500-ps sampling gate, which was centered on the peak of the fluorescence pulse using an SR200 gate scanner. An SR250 gated integrator was used to capture signals from the photodiode monitoring the UV-beam energy. The output voltages from the fast sampler and the gated integrator were digitized and stored with the SR245 computer interface module and the SR265 software package, respectively. For the measurements of NO number density, the fluorescence signal was normally averaged over 600 laser shots.

Two burners were used for the laminar flame experiments. For the low-temperature flames, the burner used was a 2.5-cm diameter, water-cooled, sintered-bronze McKenna

flat-flame burner. For the high-temperature measurements, the burner was a 1.3×1.3 cm premixed Hencken burner, which consists of densely packed, 0.5-mm diameter, stainless steel tubes. In both cases, the burner is located inside the high-pressure combustion facility described by Carter et al. [1989]. The pressure vessel has four optical ports, two of which are used for directing the laser beam through the facility. Mass flow controllers were employed in the gas delivery system for the fuel, O_2, diluent N_2, and N_2 guard flows, and rotameters were used for the NO/N_2 flow with which NO was doped into the flame for fluorescence signal calibration. Calibration of the mass flow controllers and rotameters was performed through use of a dry-test volumetric flowmeter and a bubble meter.

Temperatures were measured in two ways: with a Pt-Pt/10%Rh, radiation-corrected, uncoated thermocouple (bead diameter ≈ 0.2 mm), and with Rayleigh scattering. For the thermocouple measurements, the measured temperatures were corrected for radiative heat loss using the corrections found in Bradley and Matthews [1968]. For the Rayleigh scattering measurements, the experimental apparatus used for the LIF measurements was utilized with the following modifications. The power monitoring photo-diode was moved to a location before the pressure vessel. For the McKenna burner, the image of the entrance slit was reduced to 67μm × 6.7 mm by reducing the entrance slit width to 100μm. For the Hencken burner, the height of the entrance slit was also reduced to 2 mm, resulting in an entrance slit image of 67μm × 1.3 mm. The excitation frequency was changed to v=44355 cm^{-1}; this frequency does not cause significant interference from NO fluorescence. The monochromator was also tuned for maximum detection of the Rayleigh scattering signal at λ≈225.4 nm. Finally, the Rayleigh scattering signal was processed with a Stanford Research System SR250 boxcar averager and gated integrator, using a 6-ns temporal gate width.

3.3 Chemical Kinetics Modeling

Most of the experimental laminar flames, as well as a number of variations on these flames, were investigated through computer modeling. The modeling of the chemical kinetics was performed using the Sandia steady, laminar, one-dimensional, premixed flame code [Kee et al., 1985]. This is a standard Fortran program that solves the species conservation equations for the concentration of each species under consideration, the density of the combustion products, and the flow velocity as a function of position above the burner. If an energy equation solution is also desired, the code solves for the temperature profile of the flame, considering conductive heat loss to the burner, but not considering radiative heat losses. The program uses Newton's method and time-stepping procedures to solve the boundary value problem. In addition, the CHEMKIN-II computer program library was used to process the chemical kinetics into a form which is appropriate for use by the Sandia flame code [Kee et al., 1989]. The thermodynamic and transport properties, required by the Sandia flame code for calculation of the species concentration profiles, were provided by two reports from Sandia National Laboratories: Kee et al. [1987] provided the thermodynamic property data base and Kee et al. [1986] provided the transport property data base.

Three different elementary reaction mechanisms have been used as the chemical kinetics input into the computer model. All three mechanisms are based on the mechanism assembled by Glarborg et al. [1986] and are listed in Appendix A . The first mechanism used is taken from the set of elementary reactions listed by Drake and Blint [1991], and will be referred to as "GMK-DB". This reaction mechanism considers 49 species and over 200 elementary reactions. In their reaction mechanism, Drake and Blint [1991] adopted most of the reaction mechanism in Glarborg et al. [1986]; however, they made a few changes. These modifications include a change in the $N_2O + M \leftrightarrow N_2 + O + M$ rate parameters, which were altered based on the results of Hanson and Salimian [1984]. Also,

the rate parameters for the $CH + N_2 \leftrightarrow HCN + N$ reaction were taken from Dean *et al.* [1988] based on measurements in a high temperature shock tube. (New rate parameters have since been proposed by Dean *et al.* [1991]. However, these new rate parameters lead to a substantial increase in the [NO] calculated with the GMK-DB model. The [NO] calculated with the new rate parameters was a factor of ~7 times greater than that calculated with the Dean *et al.* [1988] parameters.) In addition, a propane reaction mechanism was included [Drake *et al.*, 1991; Blint, 1986]. Finally, pressure dependencies were added for four reactions. The reaction rates for these were computed through Troe corrections [Gardiner and Troe, 1984] for 3 hydrocarbon recombination reactions, and a Lindemann-Hinshelwood correction [Kee *et al.*, 1989] for the $N_2O + M = N_2 + O + M$ reaction. The rate parameters for pressures of 0.98, 3.1, 6.1, and 9.2 atm are given by Drake *et al.* [1991]. The rate parameters for 11.9 and 14.6 atm were provided by Drake and Blint [1992], and the rates for these four reactions are listed for all pressures in Table 3.1. These were incorporated directly into the chemical kinetics, and were used to model the flames at 1.0, 3.05, 6.10, 9.15, 11.9 and 14.6 atm. The GMK-DB model was used for the modeling of the high- and low-temperature $C_2H_6 / O_2 / N_2$ flames and the low-temperature $C_2H_4 / O_2 / N_2$ flames, and for the prediction of scattering coefficients for the Rayleigh scattering measurements.

The second mechanism used was assembled by Miller and Bowman [1989], and will be referred to as "MB". This mechanism is, for the most part, a revision of the Glarborg *et al.* [1986] mechanism, and includes the modification of many reaction rate coefficients. The updated mechanism accounts for the pressure dependencies of five different reactions; in addition, convenient formulations are provided for the Troe, SRI, and Lindemann-Hinshelwood correction parameters. The SRI technique is very similar to the Troe approach, but uses a different form for the "center-broadening" parameter. These correction parameters can be input directly into the CHEMKIN program, and the flame

Table 3.1   Reaction rates of pressure-dependent reactions in the GMK-DB mechanism. The coefficients listed are for the formula $k = A \cdot T^n \cdot \exp(-E_a/RT)$.

Reaction	A (s^{-1})	n	E_a (cal/mole)
1.0 atm.			
$CH_4 \leftrightarrow CH_3 + H$	4.4E+30	-5.158	104290.0
$C_2H_6 \leftrightarrow CH_3 + CH_3$	3.9E+31	-4.810	91908.0
$C_2H_5 \leftrightarrow C_2H_4 + H$	3.1E+23	-3.384	42121.0
$N_2O \leftrightarrow N_2 + O$	1.2E+21	-3.313	65200.0
3.05 atm.			
$CH_4 \leftrightarrow CH_3 + H$	3.2E+30	-5.016	104599.0
$C_2H_6 \leftrightarrow CH_3 + CH_3$	3.2E+33	-5.346	92810.0
$C_2H_5 \leftrightarrow C_2H_4 + H$	3.2E+24	-3.577	42892.0
$N_2O \leftrightarrow N_2 + O$	1.7E+20	-2.880	64115.0
6.1 atm.			
$CH_4 \leftrightarrow CH_3 + H$	5.0E+30	-5.020	104853.0
$C_2H_6 \leftrightarrow CH_3 + CH_3$	8.3E+30	-4.532	92034.0
$C_2H_5 \leftrightarrow C_2H_4 + H$	1.4E+24	-3.116	42588.0
$N_2O \leftrightarrow N_2 + O$	1.2E+19	-2.474	63527.0
9.15 atm.			
$CH_4 \leftrightarrow CH_3 + H$	7.9E+30	-5.048	105030.0
$C_2H_6 \leftrightarrow CH_3 + CH_3$	1.7E+29	-4.003	91510.0
$C_2H_5 \leftrightarrow C_2H_4 + H$	6.7E+21	-2.693	42218.0
$N_2O \leftrightarrow N_2 + O$	1.4E+18	-2.169	63075.0
11.9 atm.			
$CH_4 \leftrightarrow CH_3 + H$	9.2E+30	-5.049	105120.0
$C_2H_6 \leftrightarrow CH_3 + CH_3$	3.6E+29	-3.493	91201.0
$C_2H_5 \leftrightarrow C_2H_4 + H$	8.8E+20	-2.414	41961.0
$N_2O \leftrightarrow N_2 + O$	3.2E+17	-1.962	62765.0
14.6 atm.			
$CH_4 \leftrightarrow CH_3 + H$	8.9E+30	-5.030	105166.0
$C_2H_6 \leftrightarrow CH_3 + CH_3$	1.4E+29	-3.360	91082.0
$C_2H_5 \leftrightarrow C_2H_4 + H$	1.8E+20	-2.197	41756.0
$N_2O \leftrightarrow N_2 + O$	9.4E+16	-1.794	62509.0

code then computes the unimolecular reaction rate coefficients at any given pressure. This form is more useful than the information provided by Drake and Blint [1991] and Drake et al. [1991], which while usable over a range of pressures, is only truly applicable at a few specific pressures. Finally, to allow utilization of the thermodynamic property and transport property databases, two of the species in the Miller and Bowman mechanism were renamed: C_3H_3 was changed to H_2CCCH, and C_4H_3 was changed to H_2CCCCH [Miller, 1992]. The MB model was used to model the low-temperature $C_2H_6/O_2/N_2$ flames.

The third model used was a combination of the model for the H-C-O kinetics proposed by Miller and Melius [1992] and the nitrogen kinetics from the GMK-DB model, and will be known as "MIME-DB". This mechanism extends the MB model with the inclusion of higher hydrocarbon chemistry. It was designed to model the rich combustion of aliphatic fuels. While the model was also designed with sooting conditions in mind, the mechanism is still applicable in rich, non-sooting flames [Miller et al., 1991]. We have added the nitrogen kinetics from the GMK-DB model, based upon the success that was achieved in the NO modeling with this mechanism. The MIME-DB model was used for modeling the low-temperature $C_2H_4/O_2/N_2$ flames.

There have been some comparisons to [NO] measurements of the Glarborg et al. [1986] model, the GMK-DB model, and the MB model. Glarborg et al. [1986] compared their model to the measurements of Bartok et al. [1972] and Duterque et al. [1981] in stirred reactors. These two studies made measurements of NO_x formation as a function of equivalence ratio for CH_4/air combustion. Very good agreement was found between these measurements and the chemical kinetics modeling of NO_x. Drake et al. [1991] compared measurements of NO in lean, laminar, premixed $C_2H_6/O_2/N_2$ flames at high pressure to the NO concentrations calculated using the GMK-DB model. Overall, the agreement between measured and calculated profiles was qualitatively correct, but there tended to be

some underprediction of [NO] below 6.1 atm, and overprediction of [NO] at 9.2 atm. Drake and Blint [1991] also compared the GMK-DB model with the data of Heberling [1977] in high-pressure C_2H_4/air flames. The results of this study showed that the GMK-DB model predicted the flamefront NO to within a factor of two, and followed the correct qualitative trends. The MB model has been compared by Miller and Bowman [1989] to the NO_x measurements of Bartok et al. [1972]. The agreement between the two was found to be good, although the model tended to underpredict the NO_x in very rich CH_4/air combustion. However, Garo et al. [1992] found that the MB mechanism generally underpredicted measured NO concentrations in low-pressure CH_4/O_2/NH_3 flames. A review of some comparisons of the model predictions to experimental results for various other species can be found in Appendix B.

Table 3.2 lists the important keywords used in the solutions of the computer model for each flame. A keyword is a tool used to specify the procedure to be employed by the computer in the solution. A brief description of each is also provided in Table 3.2, and a more thorough description of each can be found in Kee et al. [1985]. Typically, some of the values of these variables were varied for different flames, in attempts to obtain convergence of the solution. However, some values were fairly standard. The value of XEND was always set at 5.0 cm or 10.0 cm, and was held constant for a specific fuel and pressure. The four tolerances were typically set at 10^{-4}. GRAD and CURV were usually set at 0.20 and 0.40, respectively. These values remained fairly constant, with few exceptions, for all the flames. Most of the time, the program was run to solve the coupled energy-species equations (ENRG) for a burner stabilized flame (BURN), utilizing multi-component diffusion (MULT). As an initial guess, the flame was estimated to be thin and near the burner.

Table 3.2 Important keywords used in computer modeling.

Keyword	Description
BURN	Solve problem as a burner-stabilized flame.
TGIV	Solve fixed temperature case.
ENRG	Solve coupled energy-species equations.
USTG	Solve using specified temperature profile in keyword file.
RSTR	Solve using a previous solution as the initial guess.
TIME	Set the parameters for time integration (s).
XEND	Set position of the end of the computation interval (cm).
XCEN	Set estimate of the position of the center of the flame zone (cm).
WMIX	Set estimate of the width of the flame zone (cm).
PRES	Set the pressure at which the flame is burning (atm).
FLRT	Set the cold gas flow rate flux ($g/cm^2 \cdot sec$).
GRAD	Controls number of grid points placed in regions of high gradient.
CURV	Controls number of grid points placed in regions of high curvature.
MOLE	Report results in mole fractions.
ATOL	Set absolute tolerance for termination of Newton integration.
RTOL	Set relative tolerance for termination of Newton integration.
ATIM	Set absolute tolerance for termination of time stepping.
RTIM	Set relative tolerance for termination of time stepping.
MULT	Set use of multicomponent diffusion.
VCOR	Transport option which corrects velocity formalism.

While a solution of the coupled species-energy equations could be found, theoretically, for each flame by running an isolated case starting with the full reaction mechanism, this procedure would be very time consuming. Obtaining a solution from scratch is difficult, for success requires accurate guesses of the temperature profile and species concentrations. To counteract these problems, an alternative solution method was developed. While different techniques were occasionally implemented in attempts to encourage solution convergence, the basic outline of the method is as follows.

1. Run a case for the flame of interest utilizing the reaction mechanism without nitrogenous species. For instance, this eliminates 17 species and over 60 reactions in the GMK-DB mechanism. Consider a fixed temperature (keyword TEMP) case, using as accurate an estimate of the temperature profile as possible (keyword USTG), and beginning with a small number of grid points. The majority of the grid points should be near the burner surface. This allows the first solution to be found without considering the energy equation, which the computer code has more difficulty solving. Step 1 is typically only performed for the first lean and first rich flame at a given pressure for a particular fuel.

2. Use the output from step 1 as the input for a combined energy-species equation solution. Replace TEMP with ENRG, eliminate USTG, and insert RSTR (for a restart file input). In addition, refine the solution by increasing the number of grid points in the solution by decreasing the size of "GRAD" and "CURV".

3. Modify the solution file (restart file) from step 2 to contain the additional nitrogeneous species and reactions; these species will have an initial concentration of zero throughout the entire flame. Use this to find the solution of the combined energy-species equations for the full mechanism. Due to

the size of the reaction mechanism, the complete MIME-DB mechanism was usually only solved with a fixed temperature profile for this step, instead of the full energy solution. A test case was run, and the temperature profile from a full energy solution and the energy solution using the reduced mechanism was found to differ by only 2-3 K.

4. Use the output from step 2 as the initial guess for the energy solution for a flame with a similar stoichiometry. It is best if the equivalence ratio changes by only 0.05 or 0.1. Once this is found, the full mechanism can be solved as in step 3. In addition, when starting a new pressure, a flame with the same equivalence ratio from a different pressure can be used as the initial guess at a new pressure.

For this work, the modification of the solution file required in step 3 was performed with a computer program written by Inbody [1990]. A satisfactory number of grid points was considered to be between 60 and 80, depending on the complexity of the flame.

The above solution technique was found to be adequate for obtaining a computer-generated model of the flame structure. A flame could often be solved in several hours using steps 2 and 3 and an appropriate previous solution as the initial guess. However, several days were often needed to obtain the solutions of the first lean and rich flame at a new pressure. Certain characteristics of the program were noticed, and solution strategies were developed based on these. For instance, when beginning solutions at a new pressure, the program usually preferred to go from a lower pressure to a higher pressure. So, for a solution at 6.1 atm, convergence was more easily obtained by using a solution from a 3.05 atm flame than from a 9.15 atm flame as the restart file. In addition, when finding a temperature profile via an energy solution, the program converged more easily if the new temperature was higher than the initial guess (for changes of more than a few degrees). Thus, lean flames could be solved in order of increasing equivalence ratio rather easily,

but it was then very difficult to progress from a $\phi=1.0$ flame to a $\phi=1.05$ flame. It was found to be easier to use a $\phi=0.80$ flame solution as the initial guess for a rich flame than to proceed to rich flames from a stoichiometric flame (which would require a drop in temperature). Also, if one wished to find a $\phi=0.70$ solution from a $\phi=0.80$ flame, it was usually best to provide an initial temperature guess 50-100 K lower than that calculated for the $\phi=0.80$ flame. To induce solution, it was occasionally necessary to temporarily modify the size of the tolerances. Often, the number of grid points from one solution needed to be reduced to form a coarser grid for the next solution to be achieved.

The computer modeling was performed on both a Sun Sparcstation 1, and on a Gould PN9080 computer. Both computers gave identical results for a tested simulation. Due to the relative speed of the machines, most of the modeling was done using the Gould computer.

3.4 Summary

In this chapter, the apparatus used for LIF measurements of NO and for temperature measurements have been described. In addition, a description has been presented of the NO modeling technique utilized in this study. A summary of the different reaction mechanisms used for the modeling has also been presented. The combination of both an experimental and a theoretical study can prove very useful in the determination of the current understanding of a combustion process. In this case, the experimental NO data allow assessment of the NO profiles predicted by the currently postulated chemical kinetics for high-pressure, laminar, $C_2H_6/O_2/N_2$ and $C_2H_4/O_2/N_2$ flames.

CHAPTER 4

LASER-INDUCED FLUORESCENCE MEASUREMENTS AND MODELING

OF NITRIC OXIDE IN HIGH-PRESSURE, LOW-TEMPERATURE

LAMINAR $C_2H_6/O_2/N_2$ FLAMES

4.1 Introduction

High-pressure combustion applications, such as gas-turbine engines, are a major

source of nitric oxide (NO) emissions. An important goal is to minimize the NO produced

through combustion, for NO is a pollutant which contributes to a variety of environmental

problems. The achievement of this goal by combustion designers requires, among other

things, a thorough understanding of the chemical kinetics involved in the production of

NO at high-pressure. Such understanding, in turn, mandates accurate *in situ* measure-

ments of NO concentration.

Quantitative measurements of NO concentration can be obtained using both physical

techniques, such as probe-sampling [Heberling, 1977; Leonard and Correa, 1990; Drake

et al., 1991], and optical techniques, such as laser-induced fluorescence (LIF) [Morley,

1981, 1982; Chou *et al.*, 1983; Cattolica *et al.*, 1989; Heard *et al.*, 1992; Reisel *et al.*,

1993]. Probe-sampling combined with chemiluminescent detection is advantageous since

it possesses a lower detection limit, is easier to use, and is less expensive than laser-based

methods. However, a physical probe can disrupt the flow field, potentially altering the

concentrations of radical species; moreover, such probes may not be able to withstand the

harsh conditions of practical combustion environments [Miller and Fisk, 1987]. These

disadvantages can be overcome by employing optical techniques. Optical procedures

allow for remote sensing of numerous species in a variety of environments. Unlike sampling probes, optical methods generally do not alter the combustion process; in addition, many combustors are more readily adaptable to optical access than to physical sampling probes. Finally, precise spatial resolution is achievable through the use of optical methods.

In this chapter, LIF measurements of NO in flat, laminar, $C_2H_6/O_2/N_2$ flames at pressures up to 14.6 atm are presented. In addition, to evaluate the utility of current chemical kinetics models at high pressure, the flames are modeled using two different reaction mechanisms [Miller and Bowman, 1989; Drake and Blint, 1991]. Comparisons between the modeling results and the LIF measurements provide a test of the ability of these mechanisms to predict the effects of high pressure on NO emissions. The similarity of the predicted and measured pressure trends also indicates that the trends are real and not an artifact of the measurement technique.

4.2 Laser-Induced Fluorescence Methodology

The laser system and optical layout used in performing the LIF measurements of NO are described in Chapter 3. The burner used for the measurements was a 2.5-cm diameter, water-cooled, sintered-bronze McKenna flat-flame burner. The burner was located inside the high-pressure combustion facility described by Carter *et al.* [1989].

When performing a linear LIF measurement, one must be concerned with the effects of both laser power fluctuations and quenching variations on the fluorescence signal. Corrections for laser power variation can be made by normalizing the fluorescence signal using the measured laser power. Quenching variations can be handled in a similar manner; however, measurement of the quenching rate coefficient is not a trivial task. By comparing measurements obtained using both LIF and laser-saturated fluorescence (LSF), it has previously been found that the quenching variation over the flame conditions is not significant at a given pressure [Reisel *et al.*, 1993]. To develop a better appreciation of

the flame conditions over which the NO fluorescence signal is not susceptible to significant errors due to quenching variations, quenching rate coefficients in the post-flame zone have been calculated using equilibrium concentrations and the quenching cross-sections from Drake and Ratcliffe [1993]. The quenching rate coefficient per unit pressure, Q/P, can be calculated from

$$\frac{Q}{P} = \frac{1}{kT}\left(\frac{8kT}{\pi}\right)^{0.5}\sum_i \frac{X_i\sigma_i}{\sqrt{\mu_i}} \quad , \tag{4.1}$$

where k is Boltzmann's constant, T is the temperature, X_i is the mole fraction of quenching species i, σ_i is the quenching cross-section of NO with species i, and μ_i is the reduced mass between species i and NO. A plot of the results of this calculation for a variety of C_2H_6 /O_2/N_2 flames (with a volumetric dilution ratio of 3.1) is shown in Fig. 4.1. In these calculations, only the species studied by Drake and Ratcliffe [1993] were considered in the calculations (N_2, O_2, H_2O, CO_2, CO, C_2H_6, H_2, NO, H, OH, and O); these include the dominant quenching species in the post-flame zone.

As can be seen from Fig. 4.1, the quenching variation over most temperatures for this range of equivalence ratios in C_2H_6/O_2/N_2 flames is relatively small. However, if LIF measurements were to be made in flames at the extremes of this region, the fluorescence signal would need to be corrected for quenching variations. For instance, if the measured fluorescence ratio between two flames at $\phi=1.0$, T=1500 K and $\phi=1.4$, T=2100 K was x, then the actual fluorescence ratio (after quenching corrections) would be $1.55x$. This suggests that significant errors due to quenching variations could appear under some LIF measurement conditions. However, for the range of the flame conditions in this investigation, the quenching fluctuations after calibration at $\phi=0.80$, T=1700 K are less than ±15%, which is within the accuracy of the LIF measurements.
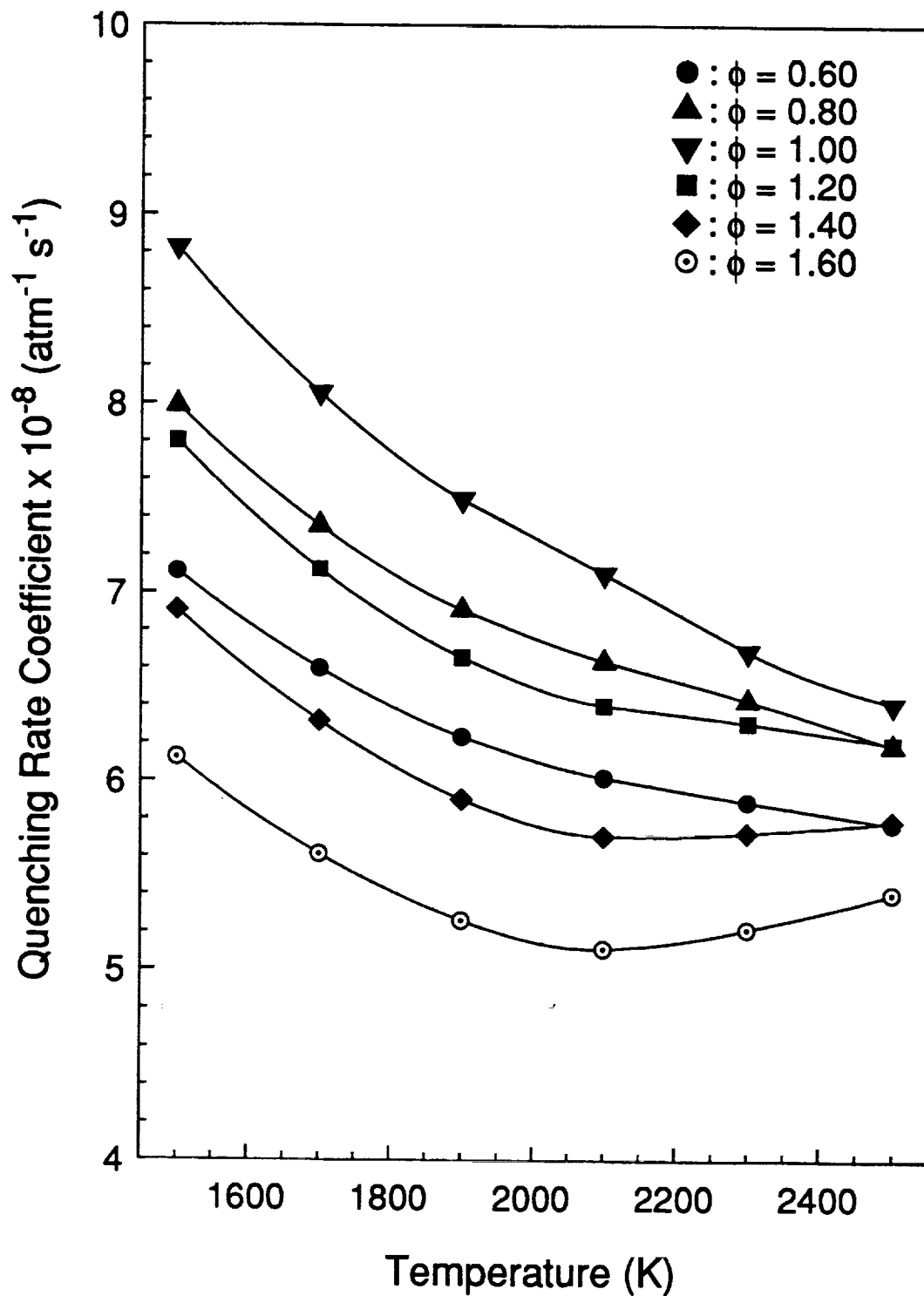
Figure 4.1: Calculated quenching rate coefficient per unit pressure (atm^{-1}•s^{-1}) in the post-flame region for a series of $C_2H_6/O_2/N_2$ flames at $\dot{V}_{N_2}/\dot{V}_{O_2} = 3.1$.

4.3 Chemical Kinetics Modeling Calculations

NO is produced through three main reaction mechanisms [Drake and Blint, 1991]:
(1) the Zeldovich, or thermal-NO, mechanism [Zeldovich, 1946], (2) the N_2O-intermediate mechanism [Wolfrum, 1972; Malte and Pratt, 1974], and (3) the prompt-NO mechanism [Fenimore, 1971]. The amount of NO formed through each of these mechanisms depends on the temperature, pressure, and equivalence ratio of the flame. The details of these paths can be found in Chapter 2.

Most of the experimental flames in this study, as well as a number of variations on these flames, were investigated through computer modeling. The modeling of the chemical kinetics was performed using the Sandia steady, laminar, one-dimensional, premixed flame code [Kee et al. , 1985]. The details of the modeling can be found in Chapter 3.

Two different mechanisms have been used as the chemical kinetics input into the computer model. Both are based on the comprehensive mechanism assembled by Glarborg et al. [1986]. The first mechanism (GMK-DB) is taken from the set of elementary reactions listed by Drake and Blint [1991]. This reaction mechanism considers 49 species and over 200 reactions. Drake and Blint [1991] adopted most of the reaction mechanism from Glarborg et al. [1986]; however, they made a few modifications. These include the introduction of pressure dependency into four unimolecular reactions, the addition of a C_3H_8 reaction mechanism, and the introduction of rate parameters for $CH + N_2 \leftrightarrow HCN + N$ based on measurements in a high temperature shock tube [Dean et al. , 1988]. The unimolecular rate parameters for pressures of 3.05, 6.1, 9.15, 11.9 and 14.6 atm are listed in Table 3.1.

The second mechanism (MB) was assembled by Miller and Bowman [1989]. This mechanism is a revision of the Glarborg et al. [1986] mechanism, and includes the modification of many reaction rate coefficients. To allow utilization of the thermody-

namic property and transport property data bases, two of the species in the Miller and Bowman mechanism were renamed: C_3H_3 was changed to H_2CCCH, and C_4H_3 was changed to H_2CCCCH [Miller, 1992].

This work is concerned with high-pressure, low-temperature premixed flames. Reisel *et al.* [1993] found that most of the NO is formed in the flamefront for atmospheric-pressure versions of these flames. As mentioned in Chapter 3, modeling the flamefront NO in such flames generally requires consideration of all three reaction mechanisms. In particular, while the prompt-NO mechanism does not contribute to NO production in the post-flame zone (where the measurements are taken), its inclusion remains necessary, as almost all of the NO production in these flames occurs in the flame-front, where the prompt-NO reaction path is important. The primary goal of the kinetics modeling effort is to assess the ability of the kinetics models to predict the effects of pressure on NO concentration. To do this, the solution of the coupled species-energy equations is employed to determine the temperature profile in these flames. A burner surface temperature of 300 K is used as a boundary condition to mimic heat loss to the burner. While the calculated temperature profile will not agree precisely with the actual temperature profile (leading to potential errors in quantitative agreement), the calculated temperatures agree sufficiently with the measured temperatures to allow for accurate assessment of the pressure trends.

4.4 Results and Discussion

Using the experimental apparatus described in Chapter 3, quantitative LIF measurements of NO were performed in flat, laminar, high-pressure $C_2H_6/O_2/N_2$ flames. Data were obtained at five pressures over a range of 3.05-14.6 atm. The temperatures of these flames, as measured with radiation-corrected Pt-Pt/10%Rh thermocouples in the post-flame region, ranged from 1600 to 1850 K (precision ±30 K, accuracy ±75 K). All of the

flames had a dilution ratio ($\dot{V}_{N_2}/\dot{V}_{O_2}$) of 3.1. The total flow rates were held constant at each pressure, and were as follows: 6.18 slpm (3.05 atm), 9.10 slpm (6.10 atm), 10.95 slpm (9.15 atm), 12.75 slpm (11.9 atm), and 14.5 slpm (14.6 atm).

Originally it was intended to perform laser-saturated fluorescence (LSF) measurements at high-pressure, as had been successfully demonstrated for the hydroxyl radical [Carter et al. , 1992]. This approach was desired so that the effects of changes in the quenching environment could be neglected [Laurendeau and Goldsmith, 1989]. To determine the extent of saturation of the $Q_2(26.5)$ line of NO, the fluorescence signal was measured as a function of laser power at each flame pressure. The laser power was attenuated through the use of quartz plates, a borosilicate glass reflector (replacing one turning mirror) and neutral density filters. The attenuation factor of each combination was determined through Rayleigh scattering measurements.

Previously, a similar saturation curve was obtained for the $R_1(16.5)$ line of NO at atmospheric pressure. This atmospheric data indicated that the transition is well saturated [Reisel et al. , 1993]; however, saturation was found to become more difficult with increasing pressures. Plots of the relative fluorescence signal vs. the relative laser power are presented in Fig. 4.2 for pressures up to 6.1 atm. The atmospheric-pressure curve is taken from Reisel et al. [1993] for the $R_1(16.5)$ line, and the other two curves are for the $Q_2(26.5)$ line. Partial saturation still occurs at 3 atm, but at higher pressures, the fluorescence signal varies nearly linearly with laser power. The lack of saturation at high pressures is most likely due to increased line broadening [Carter, 1992] as shown in Fig. 4.3. Figure 4.3 presents laser excitation scans over the same spectral region for a $\phi=0.80$ flame at three pressures. The apparent increase in background signal as the pressure is increased is due to increased NO spectral line-broadening as opposed to increased fluorescence from another species. The line-broadening, coupled with the compactness of the NO spectrum
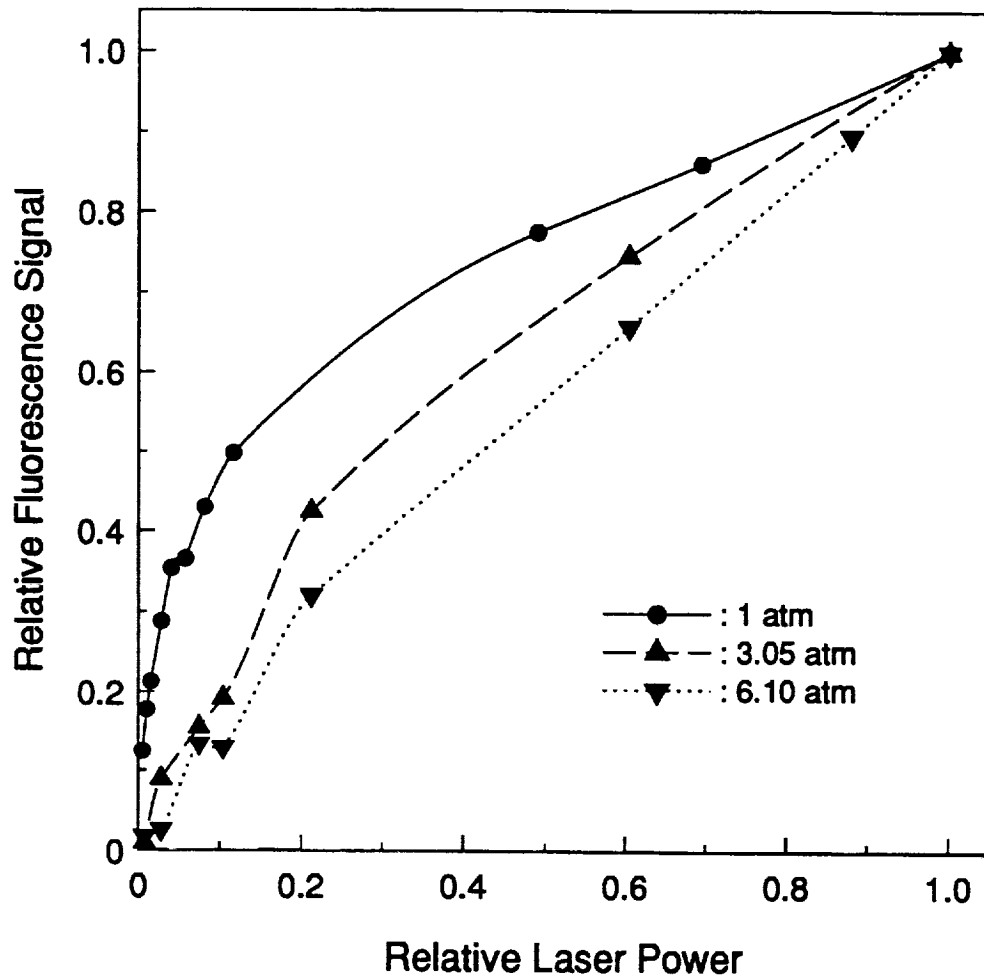
Figure 4.2:   Plots of relative fluorescence signal vs. relative laser power for NO in three $C_2H_6/O_2/N_2$ flames at different pressures. The equivalence ratio of each flame was $\phi=0.80$. Note that significant saturation behavior exists at 1 atm, and some saturation occurs at 3.05 atm. However, the relationship is basically linear for 6.1 atm and higher pressures.
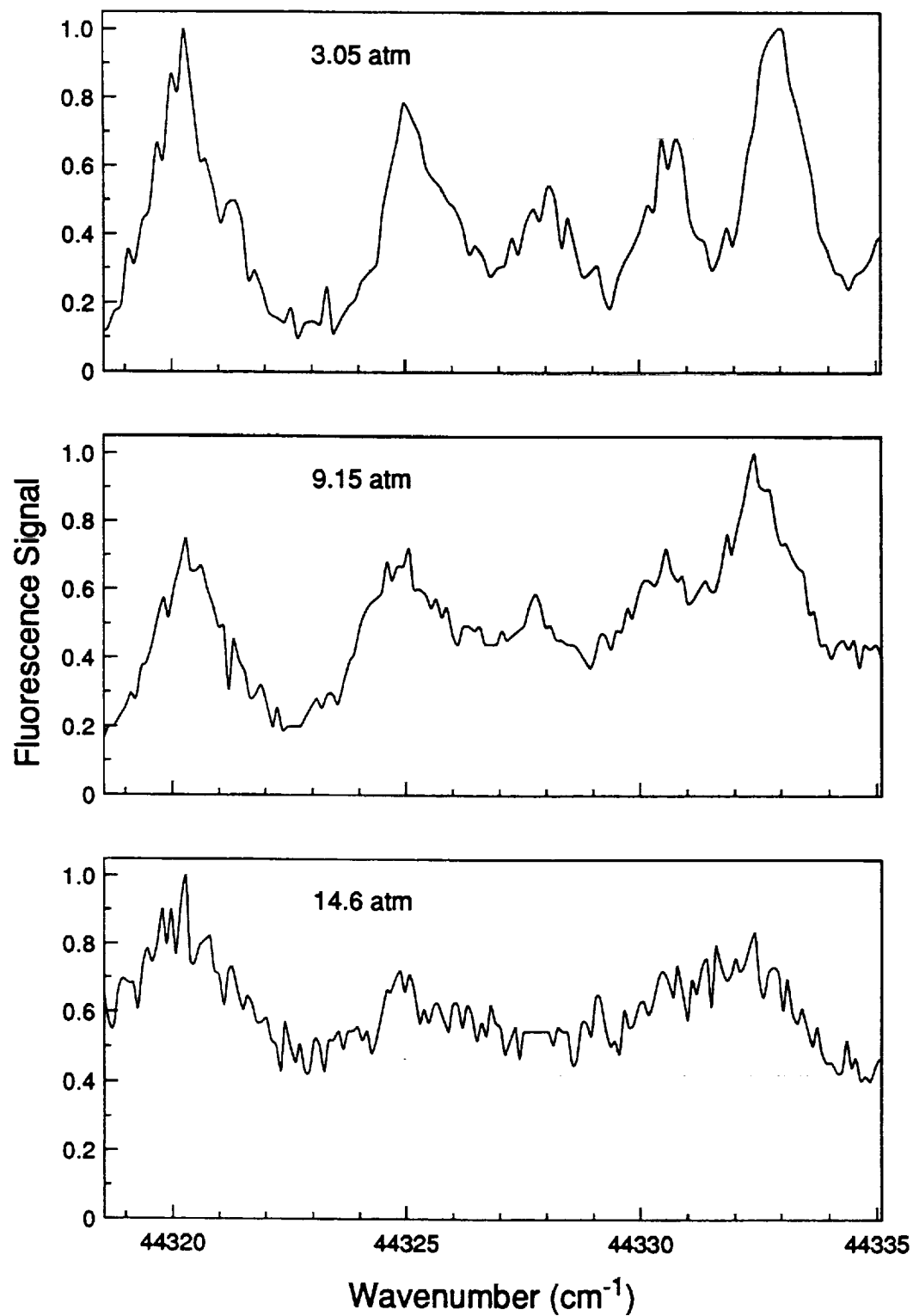
Figure 4.3:   Series of excitation scans in a φ=0.80 flame at three different pressures for
a region which includes the Q₂(26.5) transition (v≈44330.6 cm⁻¹).

[Reisel *et al.* , 1993], causes the wings of neighboring lines to be excited along with the primary line. It is difficult to maintain saturation in the wings of these lines, and therefore the addition of neighboring lines drives the broadband fluorescence towards linear behavior. Although the primary line is still experiencing saturation, the broadband detection scheme monitors the additional linear behavior of neighboring lines, and thus brings the whole fluorescence behavior towards linearity.

Since the quenching environment for the flames at a given pressure is relatively constant (Fig. 4.1), the linear fluorescence signal should be fairly insensitive to changes in stoichiometry. Thus, the ratio of fluorescence signals for any two flames should give approximately the ratio of NO number densities. This conclusion has been verified at atmospheric pressure by demonstrating the excellent agreement between NO number densities determined via LSF and LIF [Reisel, *et al.* , 1993]. On this basis, the fluorescence signals at a given pressure were calibrated using the following procedure. Measurements of the fluorescence voltage from the burnt-gas region of the $\phi=0.80$ flame were obtained for three different levels of doped NO. It is assumed that the doped NO does not react through the flame, and that the amount of NO found in this flame is small compared to the amount of doped NO. The former assumption is supported by computer modeling, which indicates that the burnt-gas NO concentration is equal to the doped NO concentration to within 5% for these lean flames.

The data from the three doping conditions, when plotted as fluorescence signal vs. doped [NO], form a straight line. The slope of this line was used to obtain a fluorescence voltage calibration, which was then applied to the fluorescence signal measured in the undoped $\phi=0.80$ flame. The observed linear relationship further indicates that the NO undergoes little reaction in this flame. NO concentrations in the other flames at the same pressure were determined from the measured fluorescence signal using the NO concen-

tration vs. signal voltage calibration determined in the ϕ=0.80 flame. With the nearly constant quenching environment, corrections for any variation in quenching between flames was deemed unnecessary.

By calibrating at each pressure, no corrections are required for both changes in the quenching environment (due to pressure changes) and changes in the optical alignment which results from maximizing the NO fluorescence signal at each pressure. This calibration procedure also does not require corrections originating from changes in the spectral linewidth due to pressure broadening, variations in spectral line overlap with pressure, and changes in rotational energy transfer with pressure.

Table 4.1 presents, for a representative sample of the flames studied, a comparison of the corrected thermocouple measurements with the flame temperatures found through computer modeling for both the GMK-DB and the MB mechanisms. The results in Table 4.1, when coupled with previous thermocouple measurements and modeling of atmospheric-pressure flames [Reisel, 1991], indicate that the temperatures calculated using the GMK-DB reaction mechanism are fairly close to the measured temperatures, particularly at lower pressures. However, due to an increase with pressure of the temperatures calculated by the GMK-DB model, the temperatures calculated by the MB model are closer to the experimentally measured temperatures at higher pressures. Due to the differences between the measured and modeled temperatures, it will be important to determine the sensitivity of the modeling results to small changes ($\pm$50 K) in temperature. The temperatures calculated from the MB mechanism are consistently 50-100 K below those determined from the GMK-DB mechanism. This may be due to the fact that the MB mechanism predicts a flame-front location slightly closer to the burner than the GMK-DB mechanism; this would lead to a larger heat loss to the burner for the MB mechanism.

Figures 4.4 - 4.6 present NO number density as a function of equivalence ratio at five different pressures as found through LIF measurements (Fig. 4.4), the GMK-DB model

Table 4.1:   Comparison of the post-flame temperatures found through thermocouple measurements and through computer modeling, using the GMK-DB (1991) and the MB (1989) reaction mechanisms, for various flames. All temperatures are in K.

Flame		Source of Temperature		
Pressure	ϕ	Thermocouple	Drake-Blint	Miller-Bowman
3.05	0.80	1730	1716	1666
3.05	1.00	1860	1835	1788
3.05	1.20	1790	1716	1681
6.10	0.80	1710	1714	1652
6.10	1.00	1830	1825	1774
6.10	1.20	1780	1707	1685
9.15	0.80	1700	1756	1647
9.15	1.00	1800	1859	1756
9.15	1.20	1750	1736	1678
11.9	0.80	1680	1778	1653
11.9	1.00	1790	1866	1764
14.6	0.80	1690	1802	1661
14.6	1.00	1800	1888	1767

(Fig. 4.5), and the MB model (Fig. 4.6). The results are for 3 mm above the burner surface for the flames up to 9.15 atm, and 2.5 mm above the burner for the flames at 11.9 and 14.6 atm. Profiles of [NO] vs. height above the burner were measured in several flames, and the NO number density was found to be constant from 1.0 mm to 5.0 mm, indicating that most of the NO was formed in the flamefront. Figure 4.7 presents examples of these profiles, taken in $\phi=0.80$ flames at four different pressures.

The LIF measurements of the post-flame zone [NO] shown in Fig. 4.4 have also been tabulated in Table 4.2. The laser energy above the burner was ~1 mJ/pulse. The LIF measurements were corrected for laser power fluctuations; linearly for the flames at P $\geq$ 6.10 atm, and non-linearly based on the results of the saturation experiments for the flames at 3.05 atm. The estimated detection limit is ~1 ppm. This limit could probably be increased by using a larger slit width and/or a longer temporal detection window. Statistical uncertainties (95% confidence level) in the relative measurements have been found to be less than ±7.5%. The propagation of errors analysis which is used to determine the statistical uncertainties is described in Appendix C. However, estimated uncertainties in the calibration procedure (due primarily to the repeatability of the NO calibration and secondarily to the assumption of no NO destruction through the flame) lead to an uncertainty in the accuracy of the quantitative measurements of ±25%.

Note that all of the curves in Fig. 4.4 maintain the same basic shape; i.e., the NO number density steadily increases with increasing equivalence ratio, peaks in a slightly rich flame, and then rapidly decreases. However, as the pressure is increased, the equivalence ratio corresponding to the point of peak NO shifts towards leaner conditions. This can also be seen in Fig. 4.8, which shows the equivalence ratio at peak NO concentration as a function of pressure, and also the variation with pressure of the points of half-peak NO concentration.
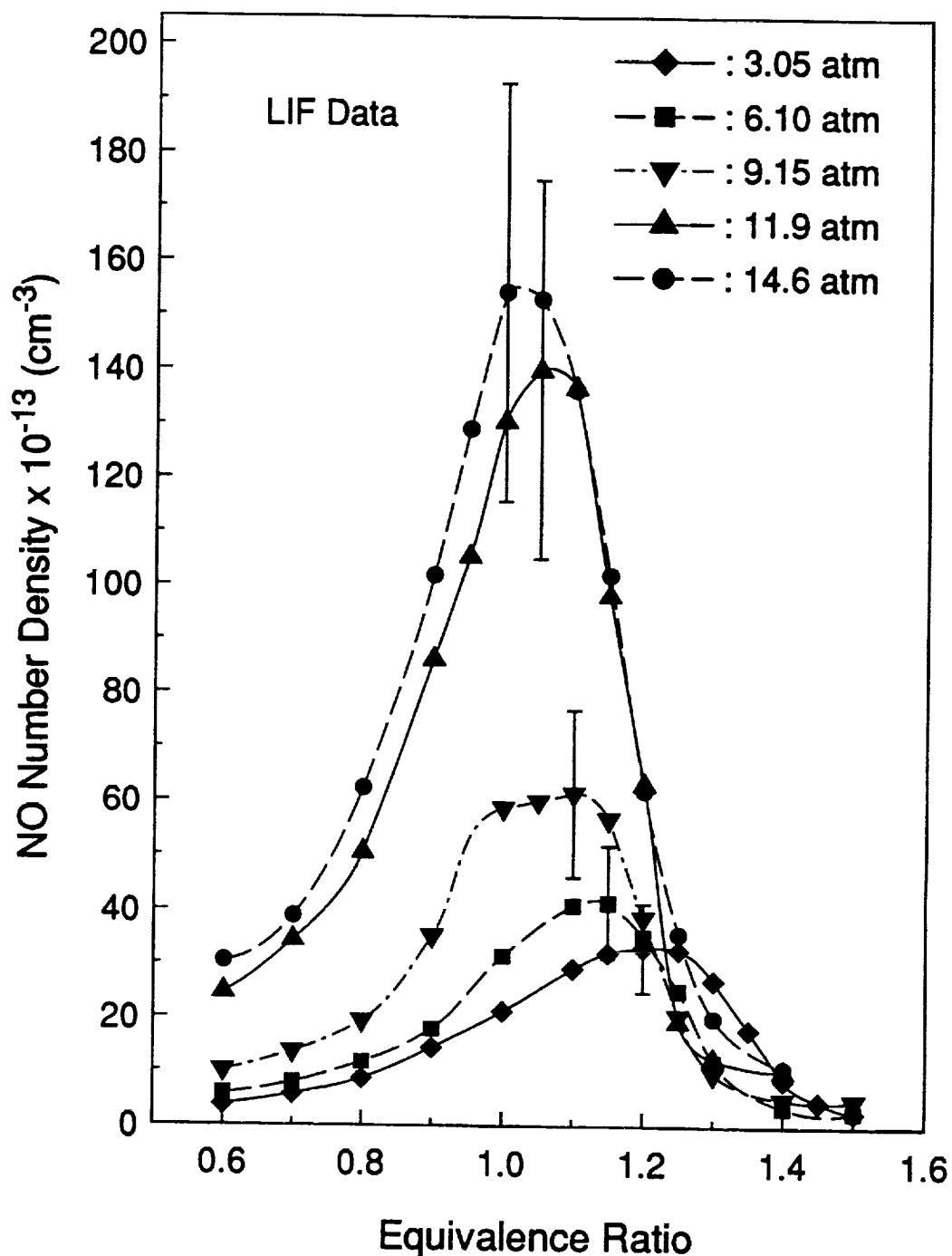
Figure 4.4:   LIF measured NO concentrations in high-pressure C_2H_6 /O_2 /N_2 flames. The measurements were taken 3 mm above the burner for the 3.05, 6.10 and 9.15 atm flames, and 2.5 mm above the burner for the 11.9 atm and 14.5 atm flames. The dilution ratio was 3.1 for all flames, and the total flow rates were 6.18 slpm (3.05 atm), 9.1 slpm (6.10 atm), 10.95 slpm (9.15 atm), 12.75 slpm (11.9 atm), and 14.5 slpm (14.6 atm). The uncertainty shown is the accuracy of ± 25%. The precision of the measurements is <7.5%.
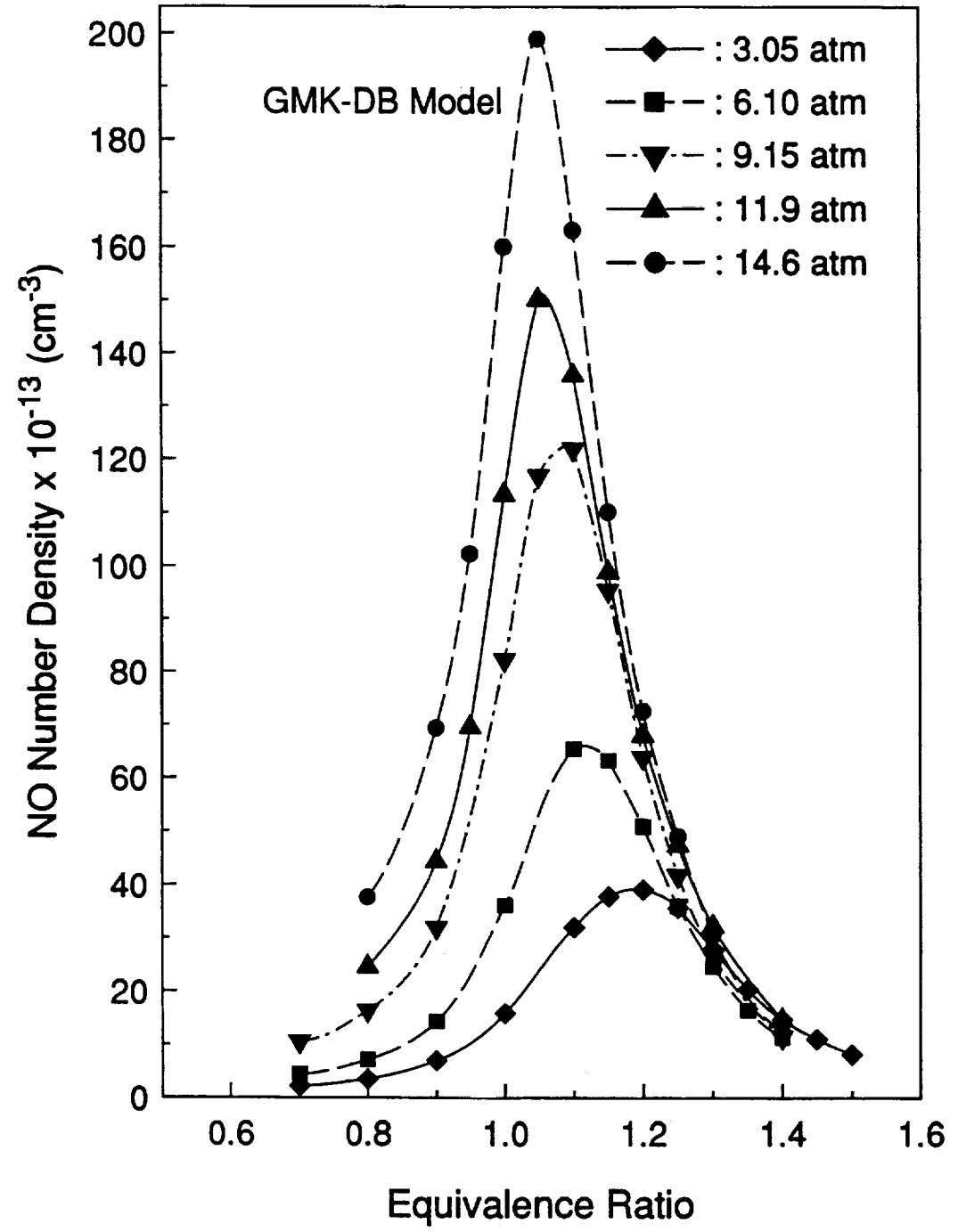
Figure 4.5: NO concentrations found for the experimental flames by solving the coupled species-energy equations using the GMK-DB reaction mechanism. The concentrations are at the same heights as the measurements shown in Fig. 4.4.
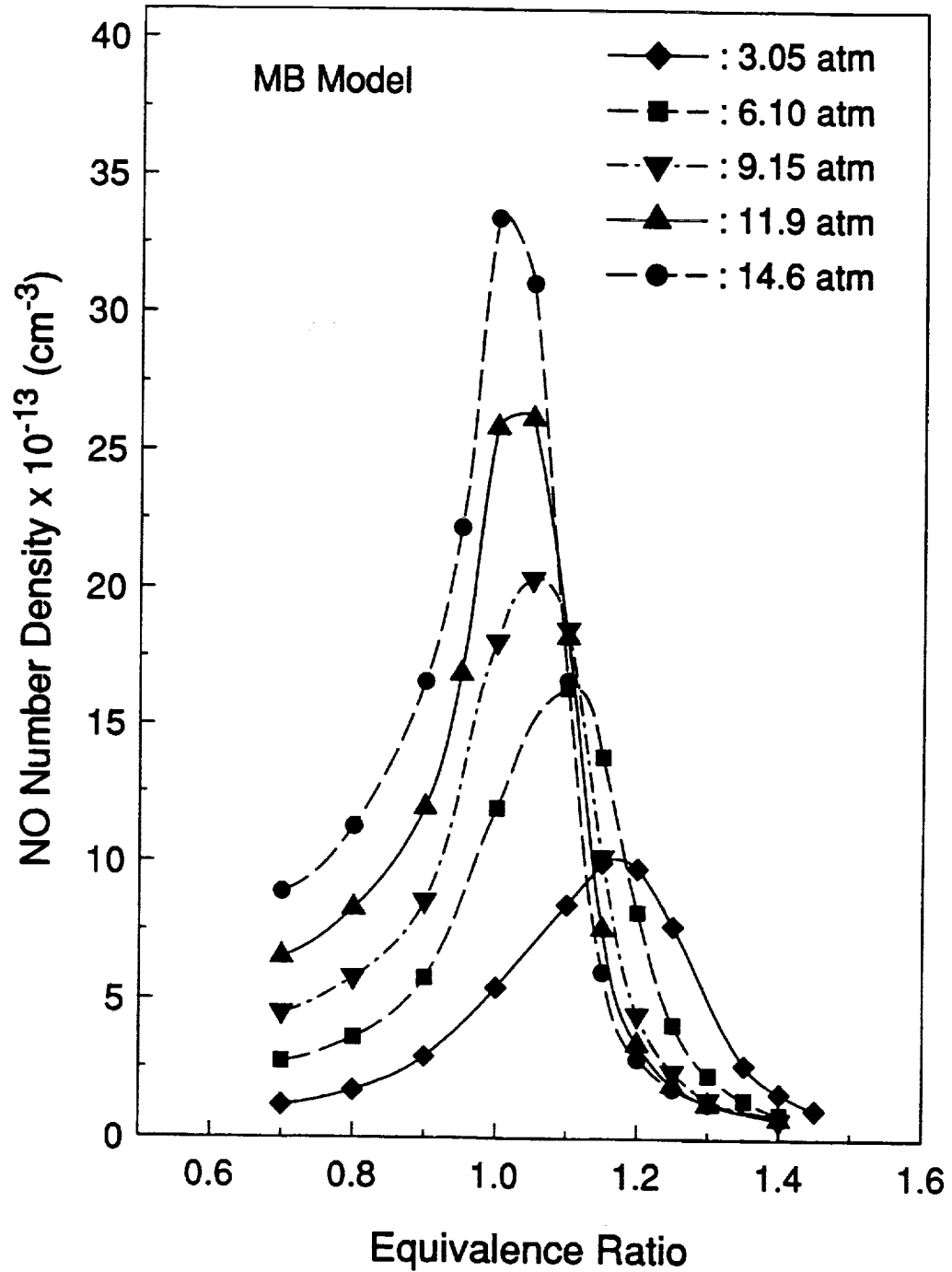
Figure 4.6:   NO concentrations found for the experimental flames by solving the coupled species-energy equations using the MB reaction mechanism. The concentrations are at the same heights as the measurements shown in Fig. 4.4. Note that the NO concentration scale is 1/5 the size presented in Figs. 4.4 and 4.5.
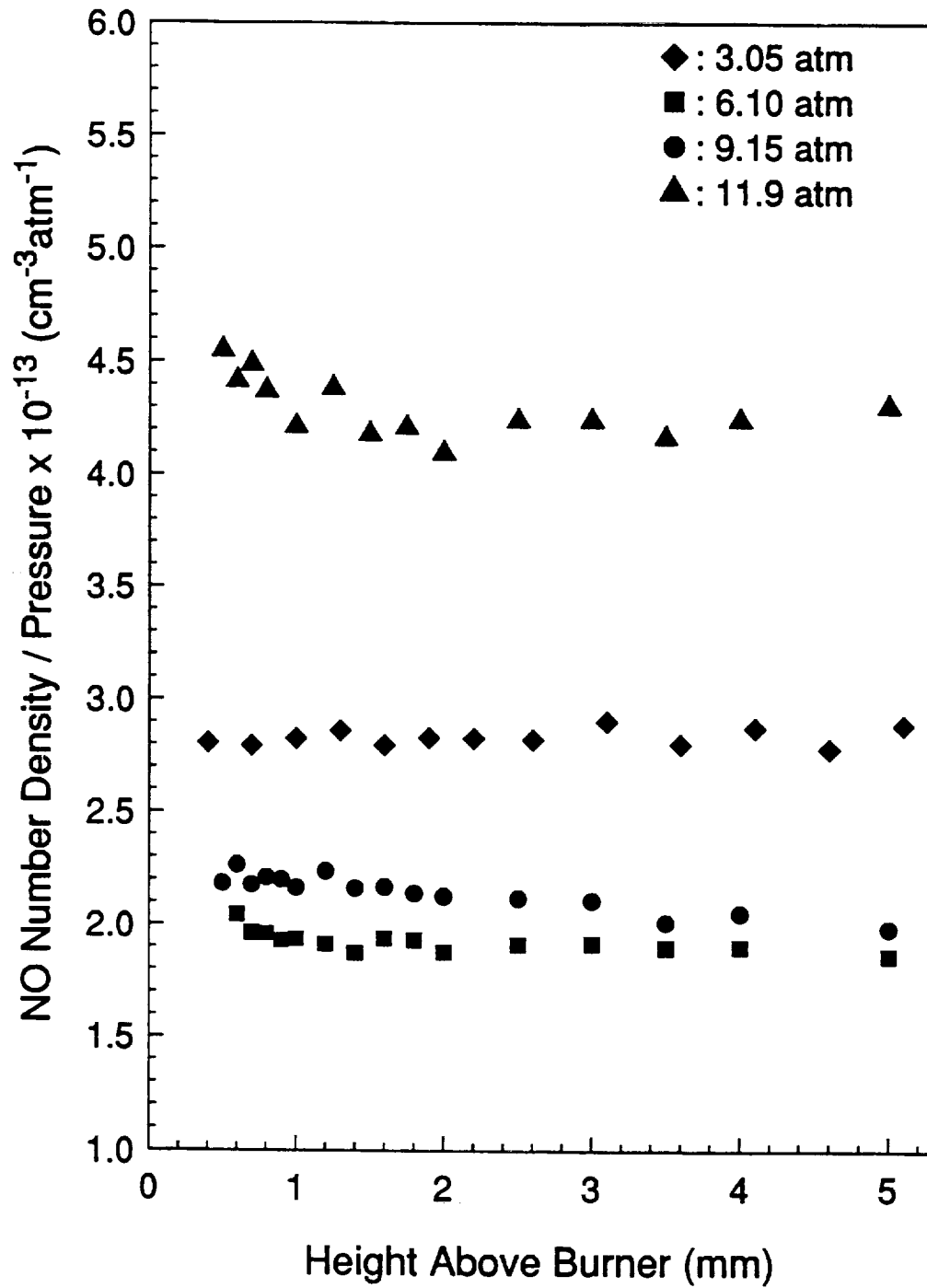
Figure 4.7   Measured NO concentrations vs. height above the burner for the φ=0.80 flame at four pressures. Note that the NO concentration is constant as a function of height above the burner.

Table 4.2: Measured NO number densities ($\times 10^{-13}$ cm^{-3}) in the $C_2H_6/O_2/N_2$ flames of this study. (NM indicates no measurement at this condition.)

ϕ	Pressure (atm)				
	3.05	6.10	9.15	11.9	14.6
0.60	3.7	5.7	10.0	24.6	30.5
0.70	5.7	7.8	13.6	34.4	38.9
0.80	8.5	11.7	19.9	50.5	62.4
0.90	14.4	17.9	35.2	86.2	102
0.95	NM	NM	NM	105	129
1.00	21.1	31.5	58.7	131	154
1.05	NM	NM	60.0	140	153
1.10	29.2	40.9	61.5	137	136
1.15	32.1	41.4	56.7	98.1	102
1.20	33.1	35.2	56.7	63.1	62.0
1.25	32.7	25.2	38.7	19.3	35.7
1.30	27.0	11.9	20.5	12.3	20.1
1.35	17.9	NM	NM	NM	NM
1.40	8.4	3.5	4.9	10.1	10.7
1.45	4.6	NM	NM	NM	NM
1.50	2.6	2.7	4.8	NM	NM

Figure 4.5 indicates that the GMK-DB reaction mechanism predicts with good accuracy the post-flame NO concentrations under most conditions. The plots of NO concentration vs. equivalence ratio found through computer modeling follow the same general trends as the experimentally measured NO concentration with pressure; i.e., the equivalence ratio corresponding to the peak NO concentration shifts towards leaner conditions with increasing pressure. In addition, at each pressure, the predictions show a rising NO concentration with increasing equivalence ratio, through a peak value in slightly rich flames, followed by a rapid drop-off in NO concentration. However, the results found using the GMK-DB mechanism also display a few inconsistencies with the measurements. While the quantitative agreement appears to be quite good in the lean flames, the predictions tend to be higher than the measurements near the peak NO concentrations, especially at 6.10 and 9.15 atm. In addition, the drop-off from the peak NO concentration appears to occur more slowly in the predictions than in the measurements under rich conditions, and more quickly under lean conditions. The quantitative inconsistencies at 6.10 and 9.15 atm are significant, but perhaps should be taken as anomalies in the generally good agreement, rather than an indication of a serious problem in the under-standing of the chemical kinetics. As will be seen, small errors in the modeling temperature can lead to significant variations in the predicted results. In fact, due to the general increase in calculated flame temperatures with pressure (as compared to the fairly consistent measured temperatures listed in Table 4.1), the predicted increase in NO number density with pressure may be slightly greater than that actually occurring. This feature, coupled with the uncertainties in the measurements, may place the measurements and modeling in better agreement than shown in Figs. 4.4 and 4.5. However, the remaining inconsistencies, such as the underprediction of the NO concentrations in lean flames, appear at each pressure, and thus indicate that work may be needed on the kinetics under these conditions.

The results for the MB mechanism are shown in Fig. 4.6. The predicted pressure trends follow the expected behavior, and the equivalence ratio corresponding to the peak NO concentration shifts towards leaner conditions with increasing pressure. In addition, the NO concentration increases gradually with increasing equivalence ratio, and then rapidly drops after reaching the peak NO concentration. In fact, the relative behavior of the [NO] vs. equivalence ratio curves as a function of pressure is more accurate for the MB model than for the GMK-DB model for lean flames. However, the MB mechanism greatly underpredicts the NO concentrations measured in these flames. (Note that the NO concentration axis in Fig. 4.6 is scaled at 1/5 the size of that in Figs. 4.4 and 4.5.) Similar discrepancies were noted by Garo *et al.* [1992] in their comparisons between measurements and MB modeling of low-pressure $CH_4/O_2/NH_3$ flames. Unlike the relatively minor quantitative discrepancies found for the GMK-DB mechanism, these results indicate that modifications are necessary in the MB reaction mechanism; the reasons behind the underprediction of [NO] will be discussed later.

Figure 4.8 can be used to compare the qualitative behavior and accuracy of the two mechanisms with respect to variations in pressure. As can be seen, both mechanisms predict with good accuracy the equivalence ratio corresponding to the peak NO concentration, although the GMK-DB mechanism does this slightly better. The GMK-DB mechanism is also better at predicting the location of the half peak NO concentration on the rich side; however, the MB mechanism is more accurate on the lean side. This indicates that some of the qualitative disagreement found for lean flames when using the GMK-DB mechanism might be removed with judicious application of the elementary reactions in the MB mechanism. Finally, it appears that both mechanisms give roughly the same sized band of equivalence ratios for those flames having an NO concentration equal to at least half the peak NO concentration.
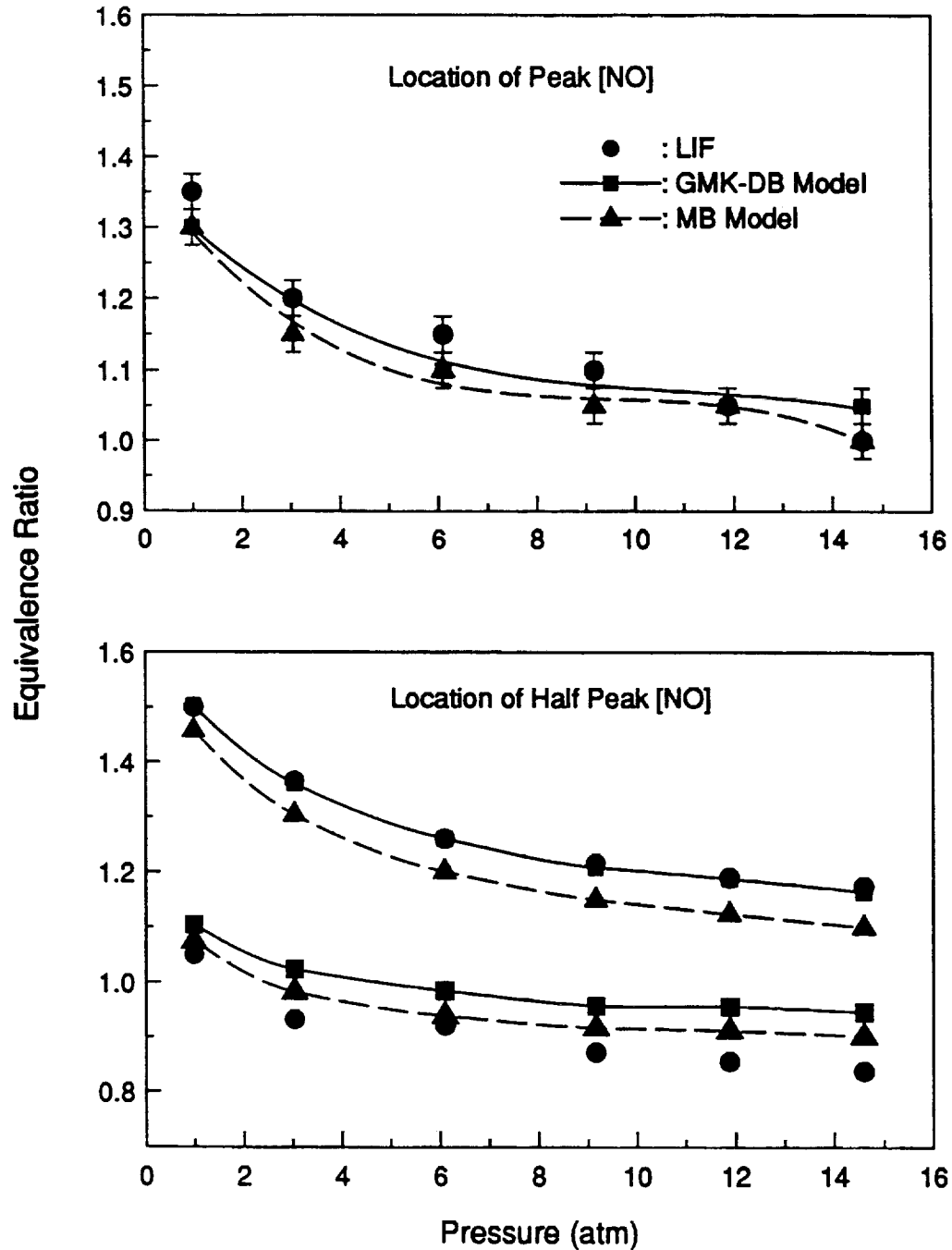
Figure 4.8: Comparisons of experimental and predicted locations on the [NO] vs. ϕ
curves. Both the predictions from the GMK-DB and the MB model are
shown. The top plot represents the equivalence ratio at peak [NO] for each
pressure. The bottom plot represents the locations corresponding to the
half-maximum [NO] on the rich and lean sides of the [NO] vs ϕ curves. The
data at 1 atm are taken from Reisel *et al.* [1993].

At this point it should be noted that the above comparisons and observations may only apply for $C_2H_6/O_2/N_2$ flames. The results of the chemical kinetics modeling could be greatly affected by fuel type. Nitric oxide is produced mostly through the prompt-NO reaction path at the lower temperatures of these flames, and this path depends strongly on the type of fuel. The GMK-DB and MB mechanisms were developed primarily for CH_4, whose structure is similar to C_2H_6. However, the same level of agreement may not hold for non-paraffinic fuels.

In an attempt to determine the reasons for the severe underprediction of NO concentration encountered when using the MB mechanism, several variations on both the reaction mechanism and the associated temperature profile have been considered. The results produced by these variations at 9.15 atm are shown in Fig. 4.9 as a representative sample of this work. The factors which were of most concern were the lower predicted temperature for the MB mechanism compared to that found with the GMK-DB mechanism and the different rate coefficient used for the primary prompt-NO reaction, i.e., $CH + N_2 \leftrightarrow HCN + N$ (F1). In addition, the MB mechanism includes the reaction

$$CH + H_2O \leftrightarrow CH_2O + H ,$$ (MB32)

which depletes a large amount of the CH in the flame. Figure 4.9 contains plots of the results of the energy solution for the GMK-DB mechanism, and four variations on the MB mechanism: (1) the previously shown energy solution; (2) use of the temperature profile from the energy solution and the Dean *et al.* (1988) rate coefficient for reaction (F1); (3) case (2) with the removal of reaction (MB32); and (4) case (3) with the temperature profile found via the GMK-DB mechanism. The results, at all the pressures, indicate that the changes associated with case (4) (MB-4 in Fig. 4.9) provide a solution on par with the GMK-DB mechanism in terms of quantitative agreement with the LIF measurements.
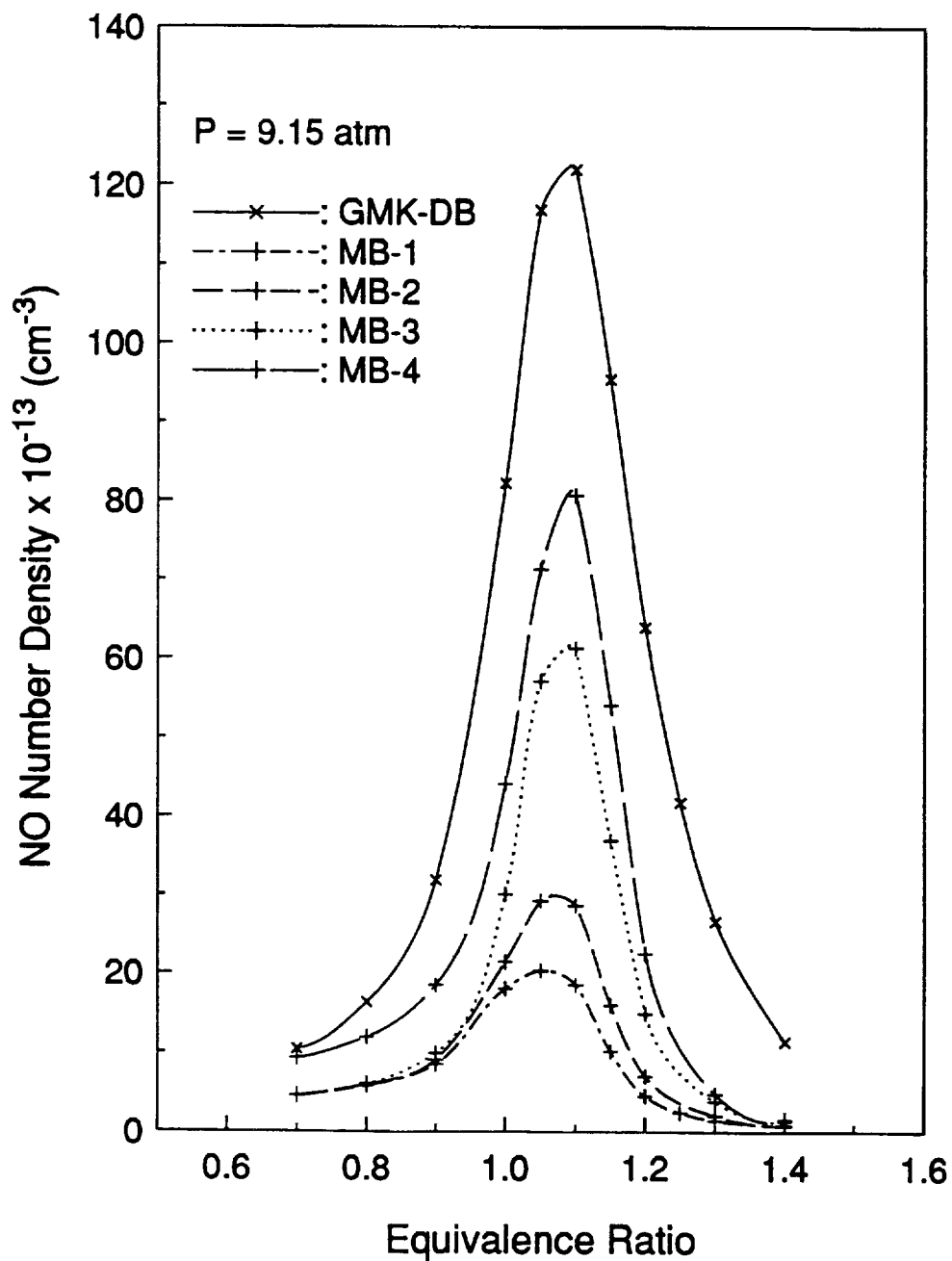
Figure 4.9: Calculated NO concentrations at 9.15 atm for a series of reaction mechanisms and temperature profiles. Shown are the results of the energy solution for the GMK-DB mechanism, and four variations on the MB model: MB-1, the energy solution; MB-2, temperature from MB-1 with Dean *et al.* [1988] rate coefficient; MB-3, temperature from MB-1 with Dean *et al.* rate coefficient and with reaction (MB32) removed; MB-4, MB-3 with temperature from GMK-DB energy solution.
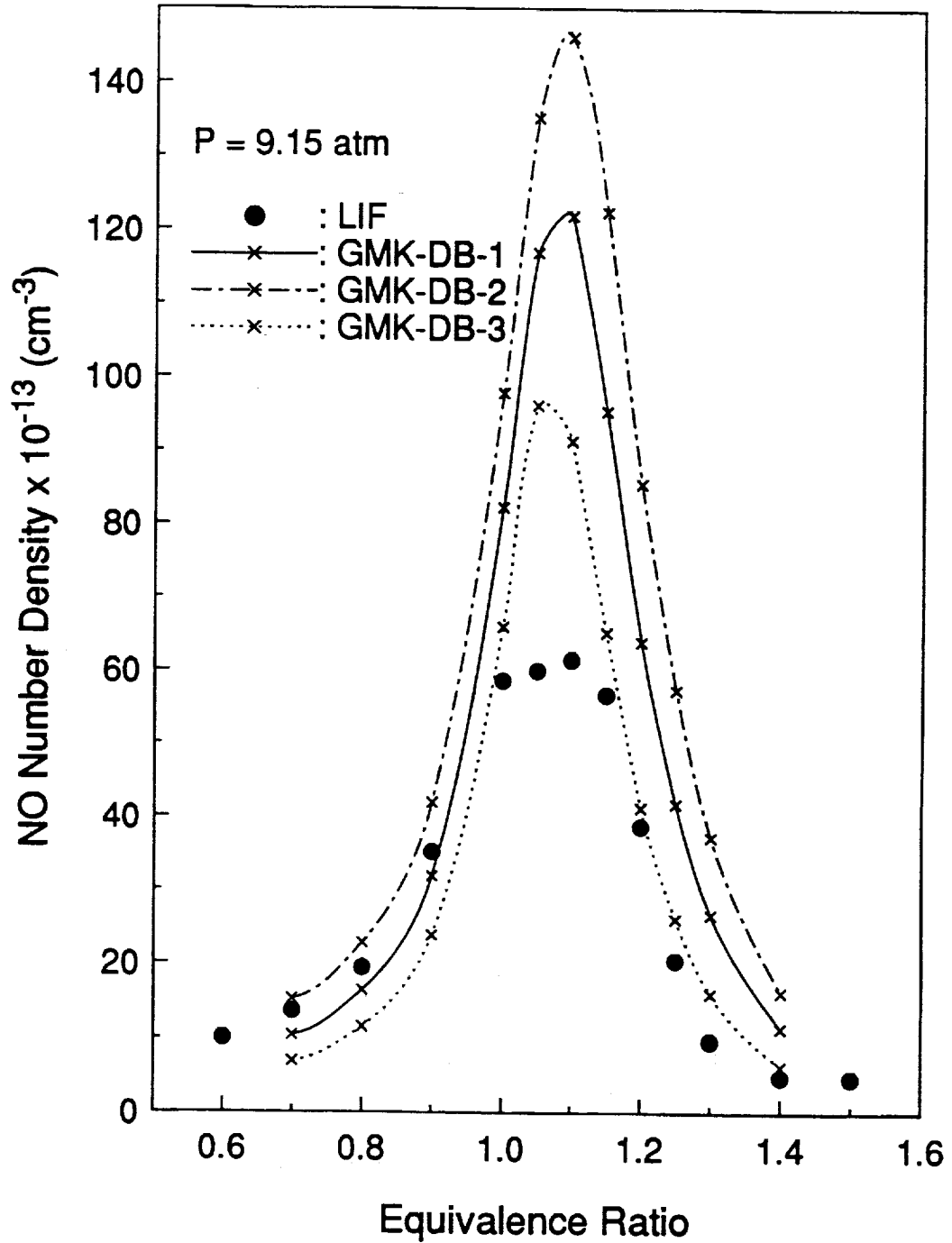
Figure 4.10: Calculated NO concentration at 9.15 atm using the GMK-DB mechanism. GMK-DB-1 represents the energy solution, GMK-DB-2 employs a temperature profile equal to that of the energy solution +50K, and GMK-DB-3 uses a temperature profile equal to that of the energy solution -50K.

The large change in [NO] obtained upon the removal of reaction (MB32) indicates that the inclusion of this reaction requires refinement of the remainder of the kinetics model to account for the underprediction of NO concentrations at high pressure.

Another factor requiring investigation is the effect of small temperature variations on the modeling results. Typical solutions are shown in Fig. 4.10 for the 9.15 atm flames. Here, 50 K has been added and subtracted from the temperature profile found by the energy solution for the GMK-DB mechanism. As can be seen, these small temperature fluctuations strongly affect the quantitative agreement with LIF measurements, but not the qualitative behavior of the model results. Therefore, the choice of the energy solution is an acceptable modeling technique for the purpose of assessing the influence of pressure on NO behavior. However, discrepancies in quantitative agreement by as much as a factor of two can occur for a temperature disparity of only ~100 K. Thus, precise quantitative comparisons require that the flames be modeled using an accurately measured flame temperature profile; unfortunately, these are very difficult to obtain experimentally in high-pressure flames.

It is also of interest to determine the relative contributions of each NO-production path to the total NO contribution. To do this, the GMK-DB model has been run for three cases: (1) with the N_2O-intermediate and thermal-NO reactions removed, (2) with the thermal-NO reactions removed, and (3) with the complete mechanism. For each scheme, the temperature profile used was that found from the energy solution of the GMK-DB model. This procedure allows determination of the contributions from each mechanism. Representative results are shown in Fig. 4.11 for the flames at 9.15 atm. As can be seen, NO production in the rich flames is dominated by the prompt-NO reactions, while all three paths are important in the lean flames. This finding confirms previous results [Drake et al, 1991], and also indicates that it may be sufficient to model many rich flames without the thermal and N_2O-intermediate paths.
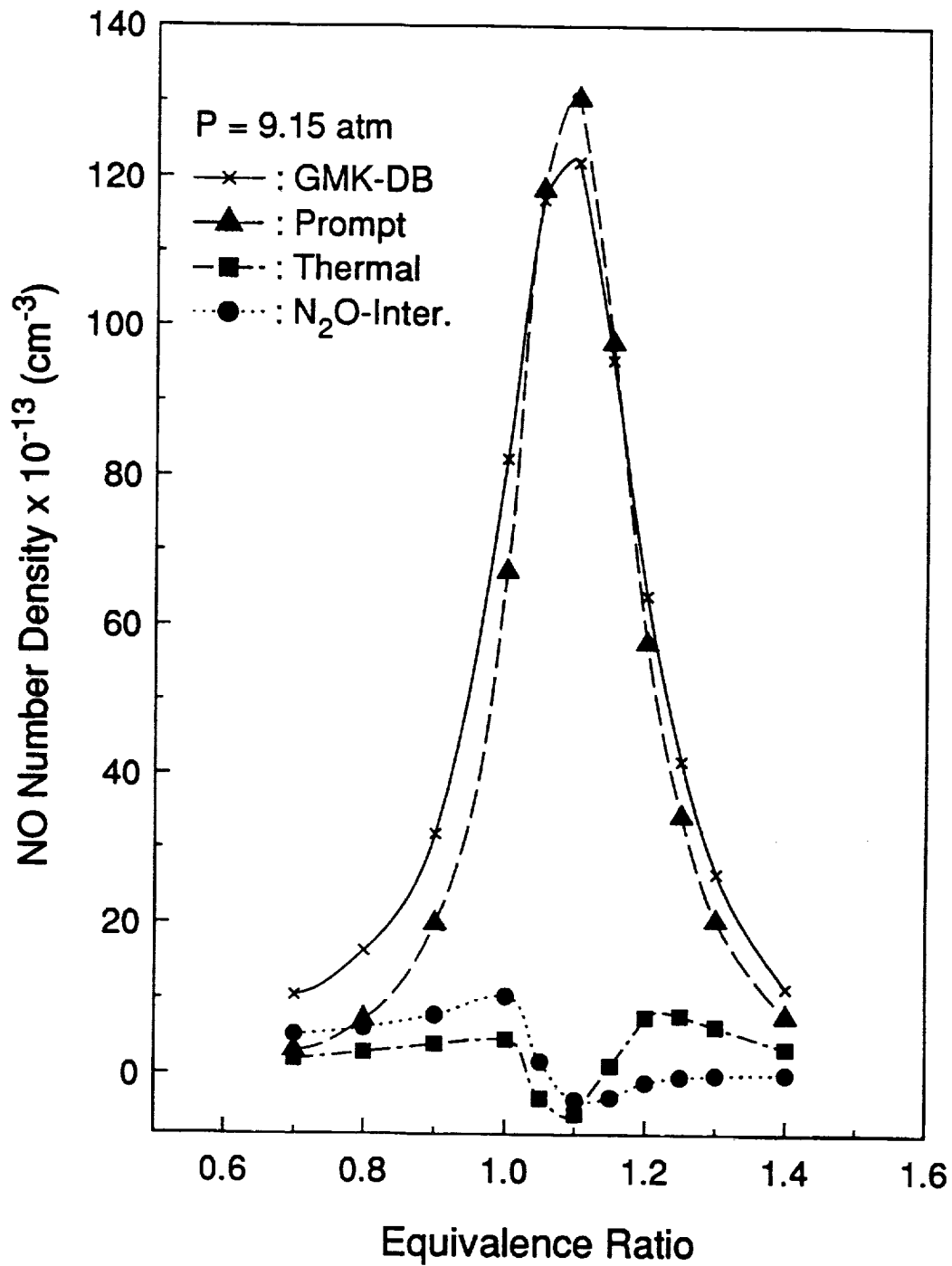
Figure 4.11:   Relative contributions of each NO production path to the total calculated NO concentration for the energy solution of the GMK-DB mechanism at 9.15 atm.

It is important to determine the reasons for the shift in peak NO concentration towards leaner conditions with increasing pressure. One possibility is that this behavior is related to the location of the flame front, which moves closer to the burner surface with increasing pressure. The distance of the flame from the burner is an important factor in the resulting flame temperature [Ferguson and Keck, 1979]. However, this possibility is discounted for two reasons. First, plots of flame front location vs. equivalence ratio (as determined by the location of maximum [CH] from the GMK-DB mechanism) are similar in shape at each pressure; the flame is closest to the burner in stoichiometric and slightly rich flames, and then moves further away from the burner for richer or leaner flames. Second, data taken at 3 atm for two sets of flames with different total flow rates (which alters the location of the flame front for a given stoichiometry) indicates that the shape of the [NO] vs. equivalence ratio curve does not change substantially with total flow rate, and that the peak [NO] occurs at the same equivalence ratio.

Kinetic modeling indicates that the few pressure-dependent reactions in the reaction mechanisms are also not responsible for the shift in peak NO concentration with pressure, as changes in specific reaction rates at different pressures did not significantly affect the results. Instead, it appears that this shift is primarily caused by the increasing importance at higher pressures of CH production from CH_2 and OH in near-stoichiometric flames; i.e.,

$$CH_2 + OH \leftrightarrow CH + H_2O \quad . \tag{GMK-DB52}$$

In the following discussion, "maximum concentration" refers to the highest concentration as a function of distance above the burner in a given flame at a given pressure, while "peak concentration" refers to the highest concentration when the maximum concentration is plotted as a function of equivalence ratio at a given pressure.

The shift in peak NO concentration with pressure is directly caused by a shift in the equivalence ratio corresponding to the peak CH concentration; this is to be expected as the majority of NO in rich flames is formed through the prompt-NO path, which is dominated
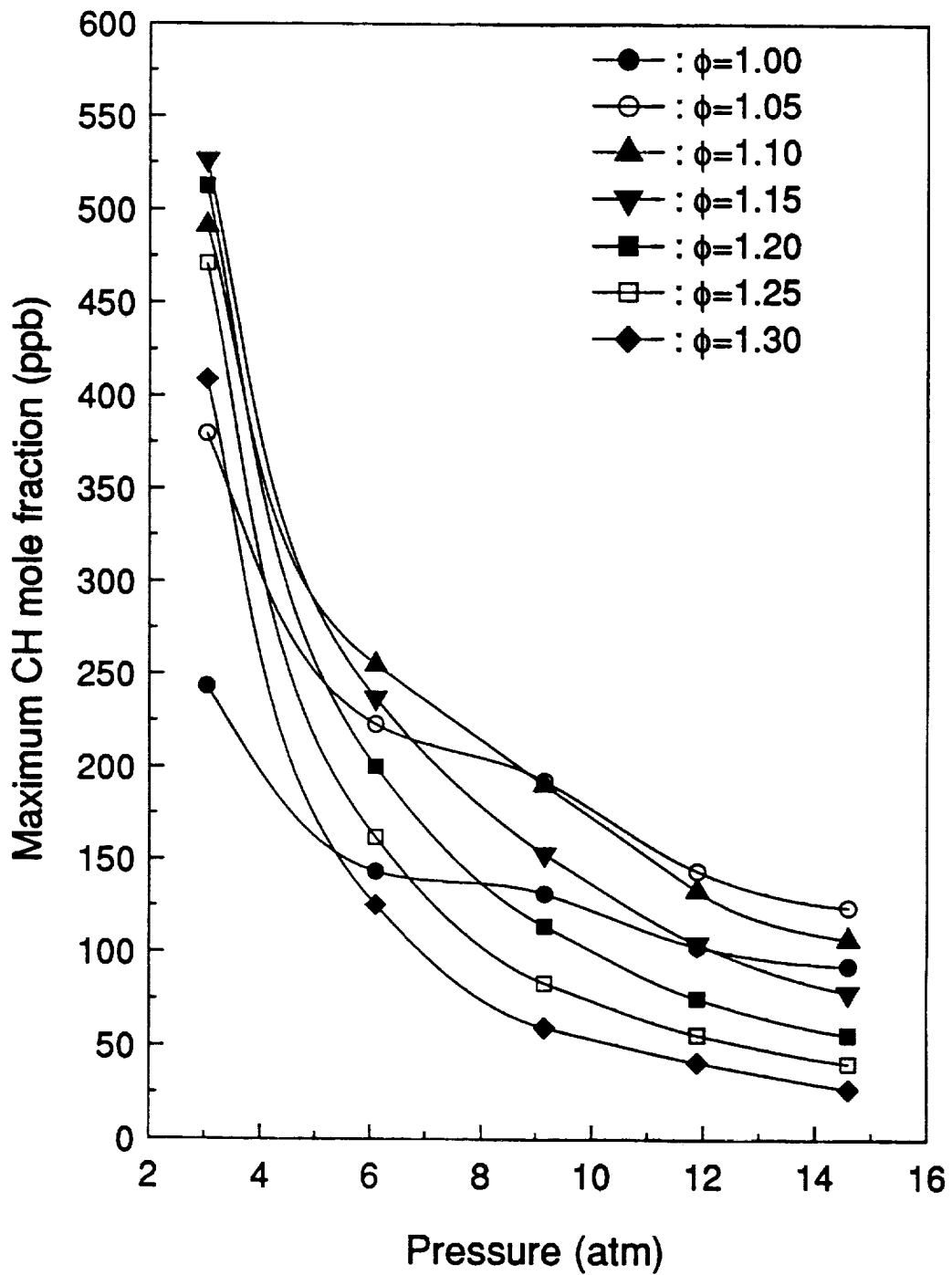
Figure 4.12: Calculated maximum CH concentrations using the GMK-DB mechanism as a function of pressure and equivalence ratio. Note that the shift in peak [NO] with increasing pressure is mimicked by that for [CH].

by reaction (F1). This shift is apparent in Fig. 4.12, which shows the maximum CH concentration vs. pressure for flames of varying equivalence ratio. The maximum [CH] drops for each equivalence ratio with increasing pressure, but drops more rapidly for richer flames. The result is that the equivalence ratio corresponding to the peak [CH] decreases with increasing pressure in a manner similar to that for peak [NO] vs. pressure (see Fig. 4.8). However, the question remains as to why the equivalence ratio corresponding to the peak [CH] shifts towards leaner conditions with rising pressure.

CH is formed from both CH_2 and C_2H through reaction GMK-DB52 above, plus the following reactions:

$$CH_2 + H \leftrightarrow CH + H_2 \quad , \qquad \text{(GMK-DB47)}$$

$$CH_2 + O \leftrightarrow CH + OH \quad , \qquad \text{(GMK-DB50)}$$

and

$$C_2H + O \leftrightarrow CH + CO \quad . \qquad \text{(GMK-DB120)}$$

While a plot of the maximum C_2H concentration as a function of pressure and equivalence ratio indicates considerable shifting in the equivalence ratio corresponding to peak [C_2H], the rate of reaction GMK-DB120 is too small in comparison to the sum of the rates of GMK-DB47, 50, and 52 (< 0.3%) to induce a significant shift in the peak [CH].

A plot of the variation in the maximum CH_2 concentration as a function of pressure and equivalence ratio is shown in Fig. 4.13. As can be seen, many similarities exist between the curves in Figs. 4.12 and 4.13; however, the equivalence ratio curves in Fig. 4.13 are not in the same order as in Fig. 4.12. Table 4.3 presents the forward reaction rates for reactions GMK-DB47, 50 and 52 at $\phi=1.0$, 1.1, and 1.25, for five different pressures. These rates were calculated at the location corresponding to the highest rate of [CH] production. Similar results were found at the location of maximum [CH] in the flames. The modest effect of pressure on these reaction rates stems from the strong reduction in the concentrations of CH_2, OH, O, and H with increasing pressure.
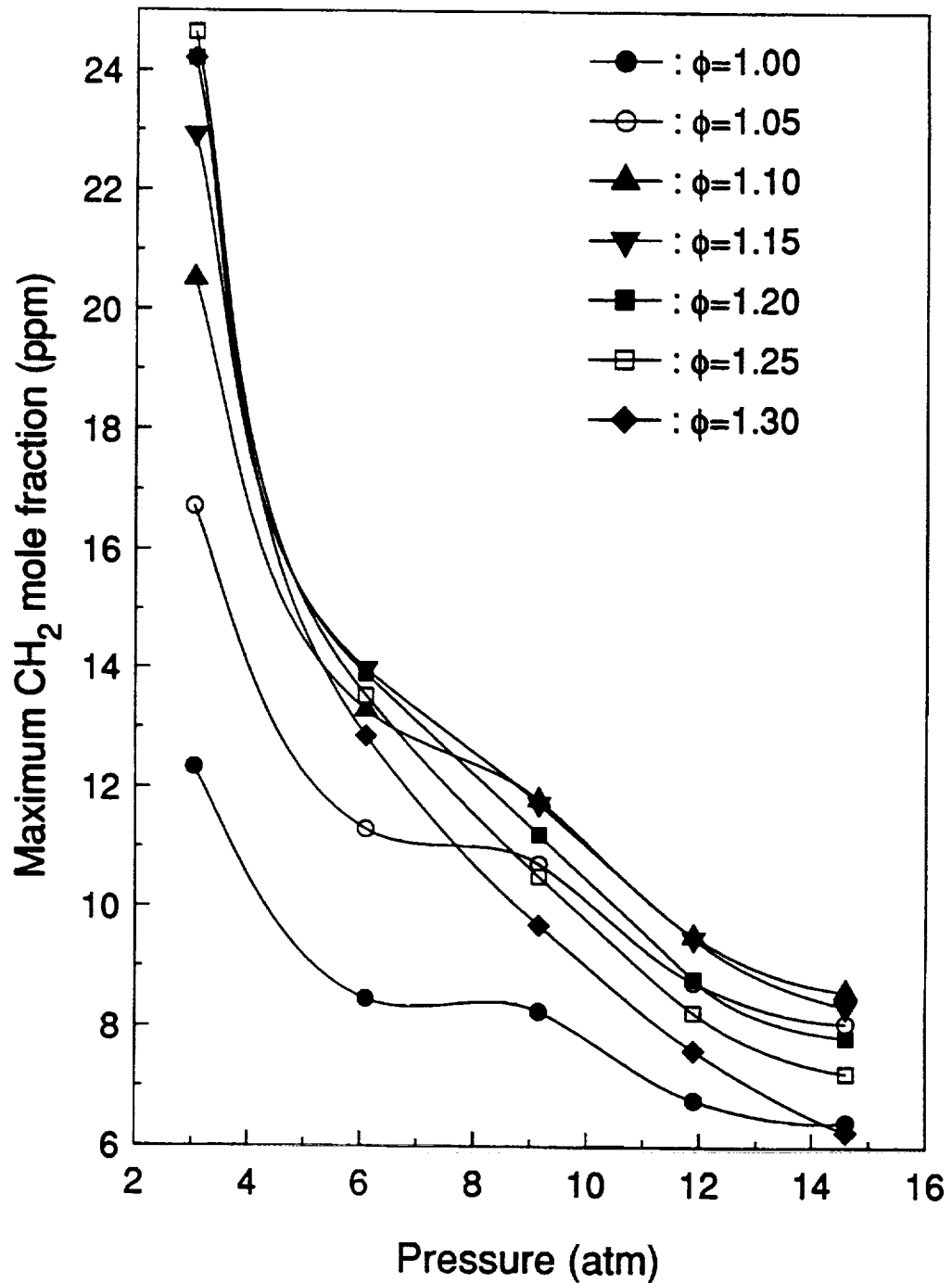
Figure 4.13: Calculated maximum CH_2 concentrations using the GMK-DB mechanism as a function of pressure and equivalence ratio. Note that the order of the flames at a given pressure differs from that of CH in Fig. 4.12. Changes in the rate of CH formation with equivalence ratio and pressure cause the different order for CH compared to CH_2.

Table 4.3: Forward reaction rates of CH forming reactions at location of maximum rate of [CH] production. Listed are the rates of the $CH_2+(H,O,OH)$ reactions (GMK-DB47, GMK-DB50, GMK-DB52), and the sum of the three rates.

	Pressure (atm)	GMK-DB47 Rate $(mole \cdot cm^{-3} \cdot s^{-1})$	GMK-DB50 Rate $(mole \cdot cm^{-3} \cdot s^{-1})$	GMK-DB52 Rate $(mole \cdot cm^{-3} \cdot s^{-1})$	Sum
$\phi=1.00$	3.04	5.07E-5	9.52E-7	7.91E-5	1.31E-4
	6.10	7.40E-5	1.57E-6	1.71E-4	2.46E-4
	9.15	8.58E-5	2.09E-6	2.83E-4	3.71E-4
	11.9	7.87E-5	1.98E-6	2.92E-4	3.72E-4
	14.6	1.12E-4	3.65E-6	5.94E-4	7.09E-4
$\phi=1.10$	3.04	1.02E-4	9.76E-7	8.68E-5	1.90E-4
	6.10	1.84E-4	1.89E-6	2.23E-4	4.09E-4
	9.15	2.08E-4	2.19E-6	3.21E-4	5.31E-4
	11.9	1.72E-4	1.74E-6	2.62E-4	4.36E-4
	14.6	1.96E-4	2.08E-6	3.50E-4	5.49E-4
$\phi=1.25$	3.04	1.16E-4	6.53E-7	5.20E-5	1.69E-4
	6.10	1.44E-4	7.59E-7	7.57E-5	2.20E-4
	9.15	1.61E-4	8.68E-7	1.10E-4	2.72E-4
	11.9	1.89E-4	9.24E-7	1.31E-4	3.21E-4
	14.6	1.21E-4	6.65E-7	8.70E-5	2.08E-4

C-2.

One can see from the sum of the reaction rates listed in Table 4.3 that, as the pressure increases, the near-stoichiometric flames become more "efficient", relative to the rich flames, at producing CH from CH_2. Table 4.3 also indicates that the rates of reactions GMK-DB47 and GMK-DB50 remain relatively constant with pressure. However, the rate of reaction GMK-DB52 varies significantly with pressure for the $\phi=1.00$ flame, and to a lesser degree for the $\phi=1.10$ flame. This indicates that reaction GMK-DB52 gains importance in the CH formation process as the pressure increases for near-stoichiometric flames. This effect of pressure, in turn, explains why the order of the maximum [CH] differs from that of the maximum [CH_2] at a given pressure, leading to the shifting behavior in the peak [CH]. In summary, the shift in equivalence ratio corresponding to the peak [NO] toward leaner conditions with pressure is caused by a similar shift in the peak [CH], which is caused by the variation with pressure and equivalence ratio of the rate of CH production from CH_2 and OH.

The above reasoning is clearly based on the currently accepted kinetics models for NO formation. Future changes in the chemical kinetics might result in a new explanation for the pressure-dependent shifting behavior [Bozzelli *et al.*, 1993]. However, owing to the good qualitative agreement between the chemical kinetics models and the LIF data, major modifications to the existing kinetics models are not anticipated. While fine tuning of the models appears necessary, this should not change the explanation for the shifting behavior.

Similarly, the comparison of the GMK-DB and MB results to the LIF data should not be construed as favoring one model over the other. The sensitivity of the predicted NO concentrations to small variations in flame temperature strongly suggests caution when making quantitative comparisons to model predictions. Considering the importance of reaction (MB32), the good agreement between the LIF data and the GMK-DB results could easily be fortuitous. On the other hand, the poor agreement with the MB model

indicates that further work is surely necessary.

4.5 Summary

The feasibility of LIF measurements of NO down to ~1 ppm in low-temperature, premixed laminar flames at pressures up to 14.6 atm has been demonstrated. For C_2H_6/O_2 $/N_2$ flames, the equivalence ratio corresponding to the peak NO concentration shifts towards lower equivalence ratios with increasing pressure. Comparisons between the measurements and two chemical kinetics models indicate that the GMK-DB model accurately predicts the pressure trends found in the measurements, and also provides generally good agreement with the measured NO concentrations. However, the MB model, while correctly predicting the pressure trends, significantly underpredicts the NO concentrations in these flames; this indicates that modification of the MB model may be necessary for high-pressure flames. In addition, most of the NO produced in these flames arises from the prompt-NO reaction path. Finally, the shift in peak NO concentration towards lower equivalence ratios with increasing pressure appears to be primarily due to the increase in importance, in near-stoichiometric flames, of the reaction forming CH from CH_2 and OH.

CHAPTER 5

QUANTITATIVE LIF MEASUREMENTS AND MODELING OF NO

IN HIGH-PRESSURE $C_2H_4/O_2/N_2$ FLAMES

5.1 Introduction

High-pressure combustion applications, such as gas-turbine engines, are a major source of nitric oxide (NO) emissions. As the environmental problems caused by high NO emissions grow, it has become imperative to reduce NO emissions from combustion processes. The achievement of this goal by combustion designers requires, among other things, a thorough understanding of the chemical kinetics involved in the production of NO at high-pressure. Such understanding, in turn, mandates accurate *in situ* measurements of NO concentration.

Quantitative measurements of NO concentration can be obtained using both physical techniques, such as probe-sampling [Heberling, 1977; Leonard and Correa, 1990; Drake *et al.*, 1991], and optical techniques, such as laser-induced fluorescence (LIF) [Morley, 1981, 1982; Chou *et al.*, 1983; Cattolica *et al.*, 1989; Heard *et al.*, 1992; Reisel *et al.*, 1993]. Probe-sampling combined with chemiluminescent detection is advantageous since it possesses a lower detection limit, is easier to use, and is less expensive than laser-based methods. However, a physical probe can disrupt the flow field, potentially altering the concentrations of radical species; moreover, such probes may not be able to withstand the harsh conditions of practical combustion environments [Miller and Fisk, 1987]. These disadvantages can be overcome by employing optical techniques. Optical procedures allow for remote sensing of numerous species in a variety of environments. Unlike sam-

pling probes, optical methods generally do not alter the combustion process; in addition, many combustors are more readily adaptable to optical access than to physical sampling probes. Finally, precise spatial resolution is achievable through the use of optical methods.

The feasibility of making quantitative LIF measurements of NO in $C_2H_6/O_2/N_2$ flames up to 14.6 atm has been demonstrated in Chapter 4. These results showed that the equivalence ratio corresponding to the peak [NO] at a given pressure shifts towards leaner conditions with increasing pressure. In addition, the measured pressure shift was successfully modeled using two chemical kinetics schemes [Miller and Bowman, 1989; Drake and Blint, 1991]; the model from Drake and Blint [1991] also provided good quantitative agreement with the measured NO concentrations.

In this chapter, this work is extended by presenting LIF measurements of NO in flat, laminar, $C_2H_4/O_2/N_2$ flames at pressures up to 11.9 atm. By comparing NO measurements obtained from two different excitation lines, the internal consistency of the LIF procedure is verified. These measurements also allow for investigation into whether the shifting behavior is limited to paraffinic fuels (like ethane), or if, as anticipated, it is a more universal phenomenon. In addition, by modeling the flames using two different reaction mechanisms, the ability of current chemical kinetics schemes to predict [NO] in high-pressure $C_2H_4/O_2/N_2$ flames is evaluated. One of these is the Glarborg-Miller-Kee model as modified by Drake and Blint (GMK-DB) [Glarborg et al., 1986; Drake and Blint, 1991]; the other is the hydrocarbon scheme of Miller and Melius [1992] combined with the nitrogen kinetics of the GMK-DB model (MME-DB). Comparisons between the predicted results and the LIF measurements provide a test of the ability of these mechanisms to predict the effects of high pressure on NO emissions from premixed ethylene flames.

5.2 Laser-Induced Fluorescence Methodology

The laser system and optical layout used in performing the LIF measurements of NO are described in Chapter 3. The burner used for the measurements was a 2.5-cm diameter, water-cooled, sintered-bronze McKenna flat-flame burner. The burner was located inside the high-pressure combustion facility described by Carter *et al.* [1989].

When performing a linear LIF measurement, one must be concerned with the effects of both laser power fluctuations and quenching variations on the fluorescence signal. One way to avoid such effects is to employ laser-saturated fluorescence (LSF), which has been previously applied with broadband detection to NO at atmospheric pressure [Reisel *et al.*, 1993]. However, as discussed in Chapter 4, saturated conditions are difficult to maintain for NO measurements above 3 atm. For linear fluorescence measurements, corrections for laser power fluctuations can be made by normalizing the fluorescence signal using the measured laser power. Quenching variations could be handled in a similar manner; however, the measurement of quenching rate coefficients is not a trivial task. By comparing measurements obtained using both linear and saturated LIF, it has been previously found that quenching variations at a given pressure are not significant for the previous range of flame conditions [Reisel *et al.*, 1993]. To confirm that this result is also true for the $C_2H_4/O_2/N_2$ flames of this study, the quenching rate coefficients have been calculated in the post-flame zone using equilibrium concentrations and the quenching cross-sections from Drake and Ratcliffe [1993]. The quenching rate coefficient per unit pressure, Q/P, can be calculated from

$$\frac{Q}{P} = \frac{1}{kT}\left(\frac{8kT}{\pi}\right)^{0.5} \sum_i \frac{X_i\sigma_i}{\sqrt{\mu_i}} \quad , \tag{5.1}$$

where k is Boltzmann's constant, T is the temperature, X_i is the mole fraction of quenching species i, σ_i is the quenching cross-section of NO with species i, and μ_i is the reduced mass

between species i and NO. Only the species studied by Drake and Ratcliffe [1993] were considered for the calculations (N_2, O_2, H_2O, CO_2, CO, C_2H_6, H_2, NO, H, OH, and O); these include the dominant quenching species in the post-flame zone.

The quenching variation proves to be relatively small ($\leq 15\%$) over most of the flame conditions for which linear fluorescence is required ($P \geq 6.1$ atm) in the $C_2H_4/O_2/N_2$ flames. A few of the flames with $\phi \geq 1.4$ have quenching rate coefficients which vary from the calibration flame by ~20%; however, even this difference is less than the uncertainty in the measurements. Greater differences would arise if the linear fluorescence measurements were extended to flames having larger equivalence ratios ($\phi \approx 1.8$); however, measurements at these equivalence ratios were only performed at lower pressures, for which LSF was employed.

5.3 Chemical Kinetics Modeling Calculations

NO is produced through three main reaction mechanisms [Drake and Blint, 1991]: (1) the Zeldovich, or thermal-NO, mechanism [Zeldovich, 1946], (2) the N_2O-intermediate mechanism [Wolfrum, 1972; Malte and Pratt, 1974], and (3) the prompt-NO mechanism [Fenimore, 1971]. The amount of NO formed through each of these mechanisms depends on the temperature, pressure, and equivalence ratio of the flame. The details of these paths can be found in Chapter 2.

Most of the experimental flames in this study, as well as a number of variations on these flames, were investigated through computer modeling. The modeling of the chemical kinetics was performed using the Sandia steady, laminar, one-dimensional, premixed flame code [Kee *et al.* , 1985]. The details of the modeling can be found in Chapter 3.

Previously, Reisel *et al.* [1993] found that most of the NO produced in atmospheric-pressure versions of similar low-temperature $C_2H_6/O_2/N_2$ flames is produced in the flamefront rather than in the post-flame region. Owing to the similar temperatures of the $C_2H_4/O_2/N_2$ flames of this study, it is expected that there will again be little post-

flame thermal-NO production. As discussed in Chapter 3, modeling the flamefront NO in such flames generally requires consideration of all three reaction mechanisms. In particular, while the prompt-NO mechanism does not contribute to NO production in the post-flame zone (where the measurements are taken), its inclusion remains necessary since most of the NO produced in the flamefront is related to the prompt-NO pathway.

The primary goal of the kinetics modeling effort is to assess the ability of the kinetics models to predict the effects of pressure on NO concentration. To do this, the solution of the coupled species-energy equations is employed to determine the temperature profile in these flames. A burner surface temperature of 300 K is used as a boundary condition to mimic heat loss to the burner. While the calculated temperature profile will not agree precisely with the actual temperature profile (leading to potential errors in quantitative agreement), the calculated temperatures agree sufficiently with the measured temperatures to allow for accurate assessment of the pressure trends.

Two different mechanisms have been used as the chemical kinetics scheme for the computer model. Both are based on the comprehensive mechanism assembled by Glarborg et al. [1986]. The first mechanism (GMK-DB) is taken from the set of elementary reactions listed by Drake and Blint [1991]. This reaction mechanism considers 49 species and over 200 reactions. Drake and Blint [1991] adopted most of the reaction mechanism from Glarborg et al. [1986]; however, they made a few modifications. These include the introduction of pressure dependency into four unimolecular reactions, the addition of a C_3H_8 reaction mechanism, and the introduction of rate parameters for the reaction

$$CH + N_2 \leftrightarrow HCN + N \quad \text{(R1)}$$

based on measurements in a high temperature shock tube [Dean et al., 1988]. The unimolecular rate parameters at pressures of 1.0, 3.05, 6.1, 9.15, and 11.9 atm are listed in Table 3.1.

The second mechanism (MIME-DB) is a combination of the hydrocarbon mechanism assembled by Miller and Melius [1992] and the nitrogen kinetics of the GMK-DB model. The Miller-Melius mechanism was designed to model rich combustion of aliphatic fuels such as ethylene and acetylene. The mechanism contains most of the Miller-Bowman [1989] mechanism for modeling small hydrocarbon species, and adds many larger hydrocarbon compounds. Due to the size of this mechanism, the coupled species-energy equations were not solved for the complete mechanism. Rather, only the hydrocarbon kinetics were solved using the coupled species-energy solution; the entire mechanism was then solved using the temperature profile from this partial solution. A sample case was run with the full mechanism using the energy solution, and the temperature profile from the reduced and full mechanisms were found to be nearly identical.

5.4 Results and Discussion

Quantitative LIF measurements of NO were performed in flat, laminar, high-pressure $C_2H_4/O_2/N_2$ flames. Data were obtained at five pressures over a range of 1.0-11.9 atm. The purity of the C_2H_4 was greater than 99.9%. The temperatures of these flames, as measured with radiation-corrected Pt-Pt/10%Rh thermocouples in the post-flame region, ranged from 1600 to 1850 K (precision ±30 K, accuracy ±75 K). A few of the temperature measurements are listed in Table 5.1. All of the flames had a dilution ratio $(\dot{V}_{N_2}/\dot{V}_{O_2})$ of 3.1. The total flow rates were held constant at each pressure, and were as follows: 3.5 slpm (1.0 atm), 6.18 slpm (3.05 atm), 9.10 slpm (6.10 atm), 10.95 slpm (9.15 atm), and 12.75 slpm (11.9 atm).

To avoid possible errors due to changes in the quenching environment, it would be desirable to apply laser-saturated fluorescence (LSF) to the NO measurements [Reisel et al., 1993]. However, as discussed in Chapter 4, the broadband LIF signal resulting from

Table 5.1: Radiation-corrected thermocouple measurements (K) of selected $C_2H_4/O_2/N_2$ flames. The temperatures listed at $\phi=1.4$ for flames at 6.1 and 9.15 atm were actually measured at $\phi=1.35$. The precision is ±30 K and the accuracy is ±75 K.

ϕ	Pressure (atm)				
	1.00	3.05	6.10	9.15	11.9
0.90	1625	1650	1640	1635	1645
1.20	1810	1785	1740	1710	1690
1.40	1840	1750	1740	1725	1695

excitation of the $Q_2(26.5)$ transition of NO does not remain saturated above 3 atm; in fact, the LIF measurements display a linear variation of fluorescence signal with laser power at pressures greater than 6 atm. However, as discussed above, the quenching variation with equivalence ratio at a given pressure is small, thus allowing for quantitative measurements of NO despite neglecting the variation in quenching rate coefficient. The measurements discussed below were obtained with a laser energy of ~1 mJ/pulse; these represent well-saturated LIF measurements at 1 atm, partially-saturated measurements at 3.05 atm, and linear LIF measurements at 6.1, 9.15, and 11.9 atm. Linear corrections were made for laser power fluctuations at pressures above 6.1 atm, non-linear corrections were made at 3.05 atm, and no corrections were made at 1 atm.

The measurements were calibrated using the following procedure, applied at each pressure. Measurements of the fluorescence voltage from the burnt-gas region of the $\phi=0.90$ flame were obtained for several different levels of doped NO. It is assumed that

the doped NO does not react through the flame, and that the amount of NO found in this flame is small compared to the amount of doped NO. The former assumption is supported by computer modeling, which indicates that the burnt-gas NO concentration is equal to the doped NO concentration to within 5% for these lean flames.

The data from several doping conditions, when plotted as fluorescence signal vs. doped [NO], form a straight line. The slope of this line was used to obtain a fluorescence voltage calibration, which was then applied to the fluorescence signal measured in the undoped ϕ=0.90 flame. The observed linear relationship further indicates that the NO undergoes little reaction in this flame. NO concentrations in the other flames at the same pressure were determined from the measured fluorescence signal using the NO concentration vs. signal voltage calibration determined in the ϕ=0.90 flame. Since only small changes occur in the quenching environment at a given pressure, corrections for any variation in quenching between flames was deemed unnecessary. Quenching corrections approaching ±20% would only occur for those LIF measurements at P≥6.1 atm and ϕ>1.4. Thus, by calibrating at each pressure, it is not necessary to make corrections for changes in the quenching environment due to pressure, or for changes in the optical alignment which result from maximizing the NO fluorescence signal at each pressure. This calibration procedure also allows us to neglect changes in the spectral linewidth due to pressure broadening, variations in the spectral line overlap with pressure, and changes in rotational energy transfer with pressure.

The results of the LIF measurements are shown in Fig. 5.1, and are tabulated in Table 5.2. The measurements were taken in the post-flame zone, 3 mm above the burner surface at each pressure except at 1 atm, for which the measurements were taken at 5 mm above the burner surface. The trends in the data are very similar to those found for previous LIF measurements in $C_2H_6/O_2/N_2$ flames (Chapter 4). As the equivalence ratio increases, the [NO] rises steadily through a rich peak and then rapidly decreases. In addition, the peak

[NO] at a given pressure shifts towards leaner conditions with increasing pressure. The latter feature was anticipated, based upon the analysis in Chapter 4 for ethane flames, which suggested that the shift was primarily due to the reaction

$$CH_2 + OH \leftrightarrow CH + H_2O \quad , \tag{R2}$$

which promotes CH production at leaner conditions with increasing pressure. In the region of maximum CH production, the forward reaction rate dominates (~40 times greater). In general, CH is produced from CH_2 through reactions with OH, O, and H. As the pressure increases, the near-stoichiometric flames become more "efficient", relative to the rich flames, at producing CH from CH_2. This improved efficiency is due primarily to the increasing importance of reaction (R2). The [O] and [H] decrease steadily with increasing pressure, as does the [OH] in moderately rich flames. However, the [OH] does not decrease as rapidly with pressure in slightly rich flames. Consequently, the peak [NO] shifts towards stoichiometric conditions with increasing pressure. The similar behavior of ethane and ethylene flames suggests that reaction (R2) is the basis for a universal NO phenomenon during high-pressure hydrocarbon combustion.

To verify the consistency of the LIF method, a comparison is made of measurements of [NO] using two different excitation lines. Sample results for this study are presented in Fig. 5.2. Here, the LIF measurements are performed using both the $Q_2(26.5)$ line and the $R_1(18.5)$ line. Based on Boltzmann fraction calculations, the fluorescence from the $R_1(18.5)$ line should depend more strongly on temperature than that from the $Q_2(26.5)$ line; therefore, the $R_1(18.5)$ line is a less desirable line to use for an LIF measurement. Figure 5.2 presents the results of the measurements from 3.05 to 9.15 atm; the results were similar at 1 atm and at 11.9 atm. As can be seen from the comparative measurements, there appears to be little if any difference attributable to the excitation transition. The
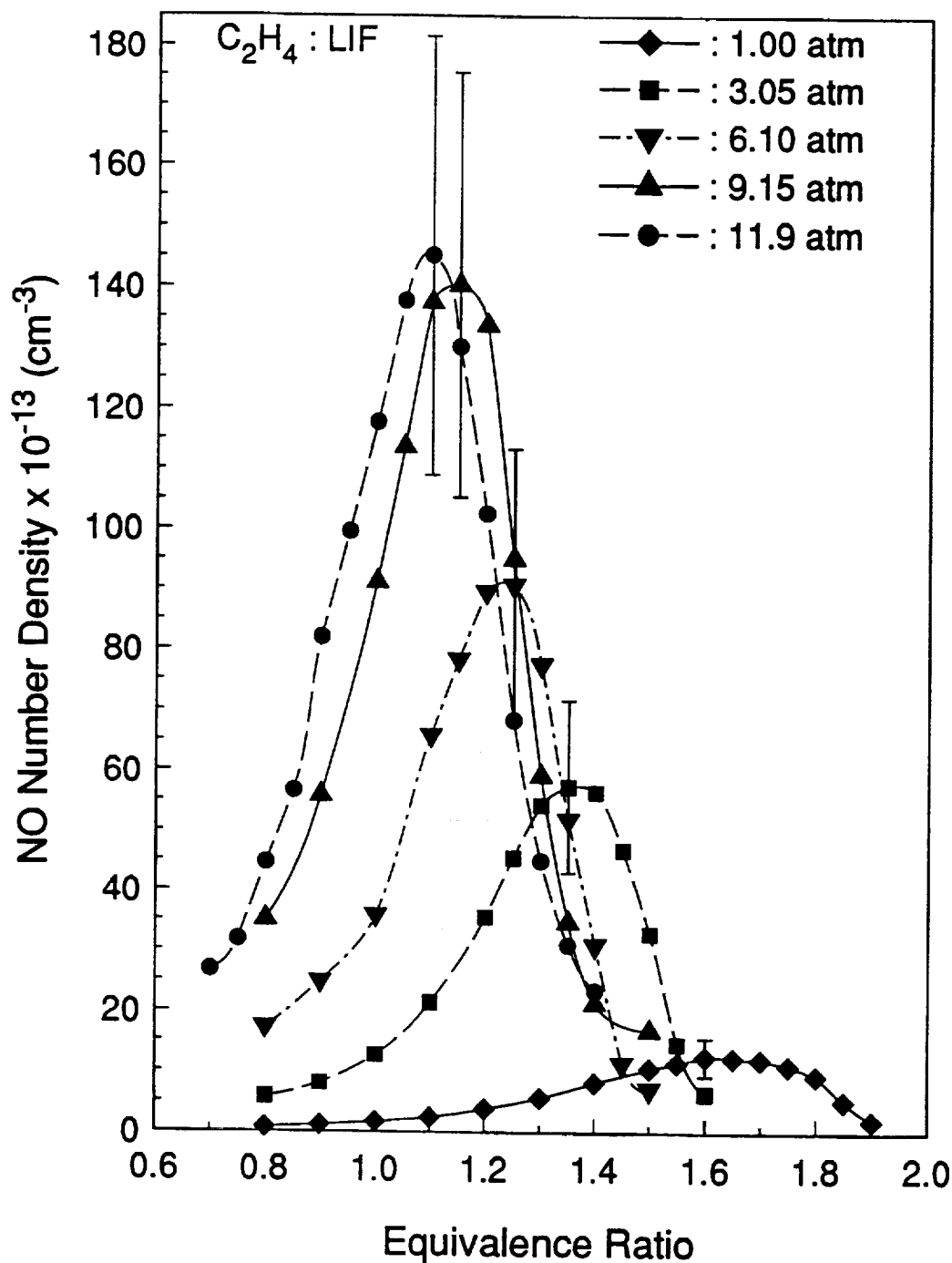
Figure 5.1: LIF measured NO concentrations in high-pressure $C_2H_4/O_2/N_2$ flames. The measurements were taken 5 mm above the burner for the 1.0 atm flames, and 3 mm above the burner for the high-pressure flames. The dilution ratio was 3.1 for all flames, and the total flow rates were 3.50 slpm (1.0 atm), 6.18 slpm (3.05 atm), 9.1 slpm (6.10 atm), 10.95 slpm (9.15 atm), and 12.75 slpm (11.9 atm). The uncertainty shown is the estimated accuracy of ± 25%. The precision of the measurements is <7.5%.

Table 5.2: Measured NO number densities ($\times 10^{-13}$ cm^{-3}) in the $C_2H_4/O_2/N_2$ flames of this study. The precision is ±7.5%, and the estimated accuracy is ±25%. (-- indicates no measurement at this condition.)

ϕ	Pressure (atm)				
	1.00	3.05	6.10	9.15	11.9
0.70	--	--	--	--	26.7
0.75	--	--	--	--	31.7
0.80	0.71	5.8	17.3	35.0	44.7
0.85	--	--	--	--	56.7
0.90	1.1	8.0	24.8	55.8	82.0
0.95	--	--	--	--	99.6
1.00	1.6	12.6	35.8	91.2	117.8
1.05	--	--	--	113.7	137.8
1.10	2.4	21.4	65.8	137.5	145.3
1.15	--	--	78.3	140.4	130.3
1.20	3.9	35.5	89.6	133.8	102.6
1.25	--	45.5	90.7	95.0	68.4
1.30	5.6	54.3	77.5	59.2	45.0
1.35	--	57.3	51.9	34.7	30.9
1.40	8.1	56.4	30.8	21.3	23.4
1.45	--	46.8	11.3	--	--
1.50	10.5	32.8	7.1	16.8	--
1.55	11.5	14.6	--	--	--
1.60	12.4	6.4	--	--	--
1.65	12.3	--	--	--	--
1.70	12.0	--	--	--	--
1.75	11.0	--	--	--	--
1.80	9.3	--	--	--	--
1.85	5.2	--	--	--	--
1.90	2.0	--	--	--	--
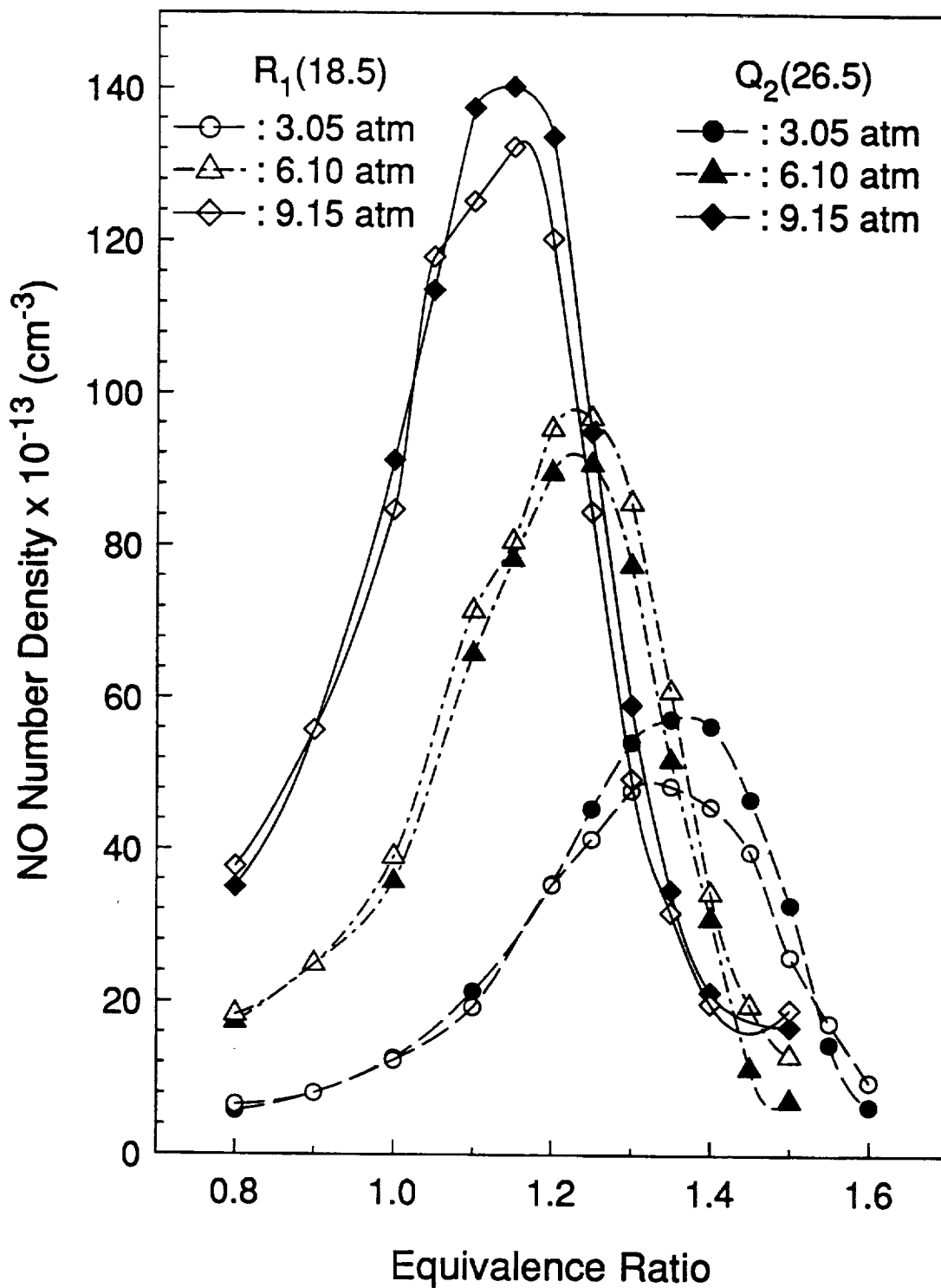
Figure 5.2: Comparisons between LIF measurements of NO concentration obtained using two different spectral lines for excitation at three pressures. The results found using the $Q_2(26.5)$ agree very well with those found using the $R_1(18.5)$ line.

measurements using one line fall within the uncertainty of the other. The worst agreement appears in the 3.05-atm flames. This difference may be attributable to the partially saturated fluorescence behavior that exists at this pressure; i.e., different degrees of saturation may exist for the two lines. Even with this possible discrepancy, the two measurements are still within acceptable accuracy, indicating that the LIF measurements are essentially independent of the chosen excitation line.

The results from the computer modeling are shown in Figs. 5.3 and 5.4. Figure 5.3 presents the results for [NO] using the GMK-DB model; Fig. 5.4 contains the results using the MIME-DB model. Note that the scales of the NO number density axis are different for both Figs. 5.3 and 5.4 than that used in Fig. 5.1. Both models follow trends similar to the measurements; however, they tend to underpredict both the peak [NO] and its corresponding equivalence ratio. One noticeable difference in the qualitative behavior of the two models is that for the GMK-DB scheme, the regions of decreasing [NO] on the rich side fall on approximately the same curve at all pressures. However, for the MIME-DB model, the regions fall on different curves at different pressures, which is similar to the behavior observed in the measurements. This similarity may be important for future chemical kinetics modifications.

In general, the predicted temperatures were in good agreement (± 50 K) with the measured temperatures. The MIME-DB temperatures tended to be ~10-50 K lower than the GMK-DB temperatures. The only significant deviations between the measured and modeled temperatures occurred in the lean flames (for which the measured temperatures are ~100-150 K lower than the GMK-DB predicted temperatures), and in the rich flames at atmospheric pressure (for which the measured temperatures are ~150 K higher than the
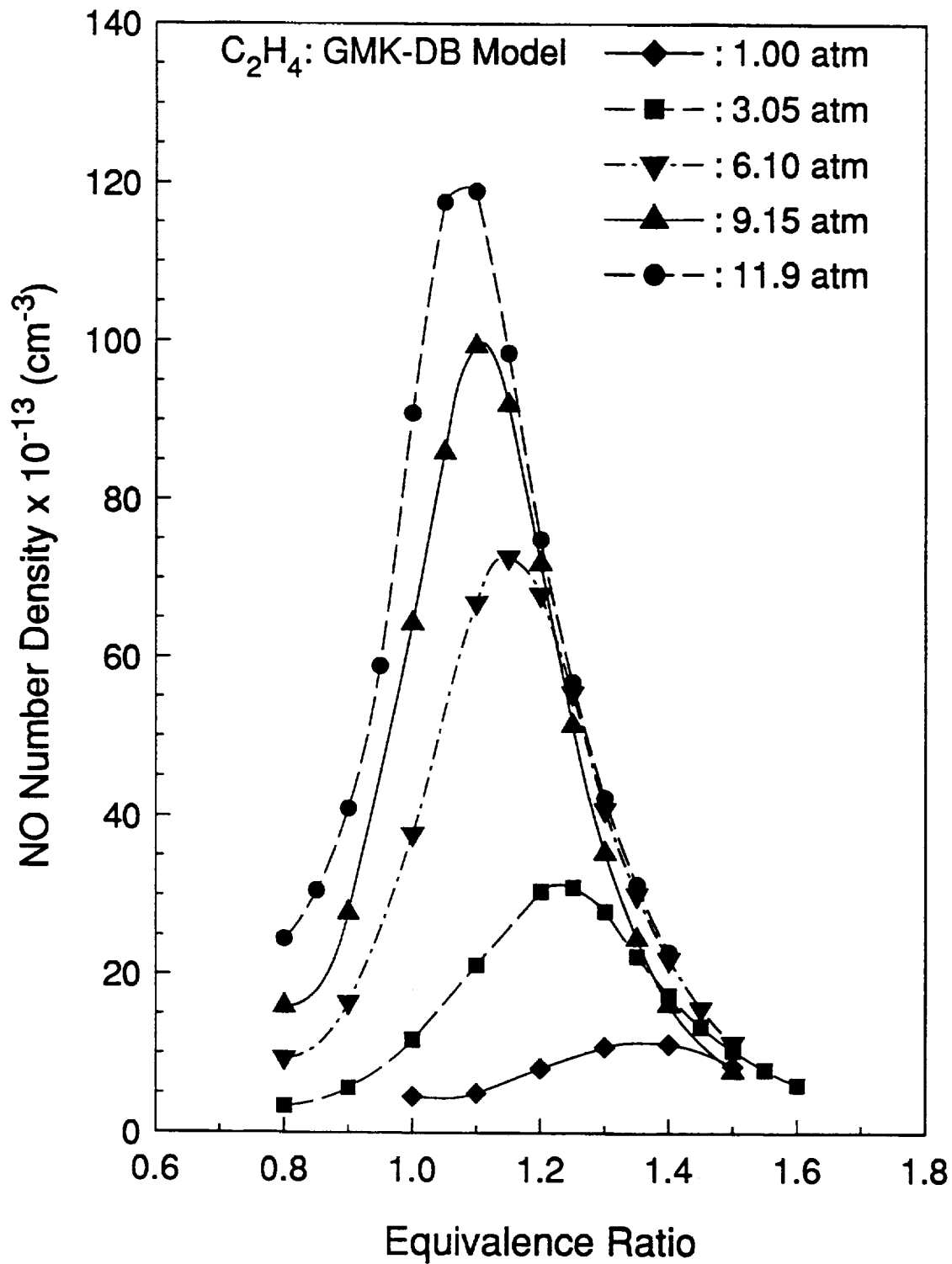
Figure 5.3: NO concentrations found for the experimental flames by solving the coupled species-energy equations using the GMK-DB reaction mechanism. The concentrations are at the same heights as the measurements shown in Fig. 5.1.
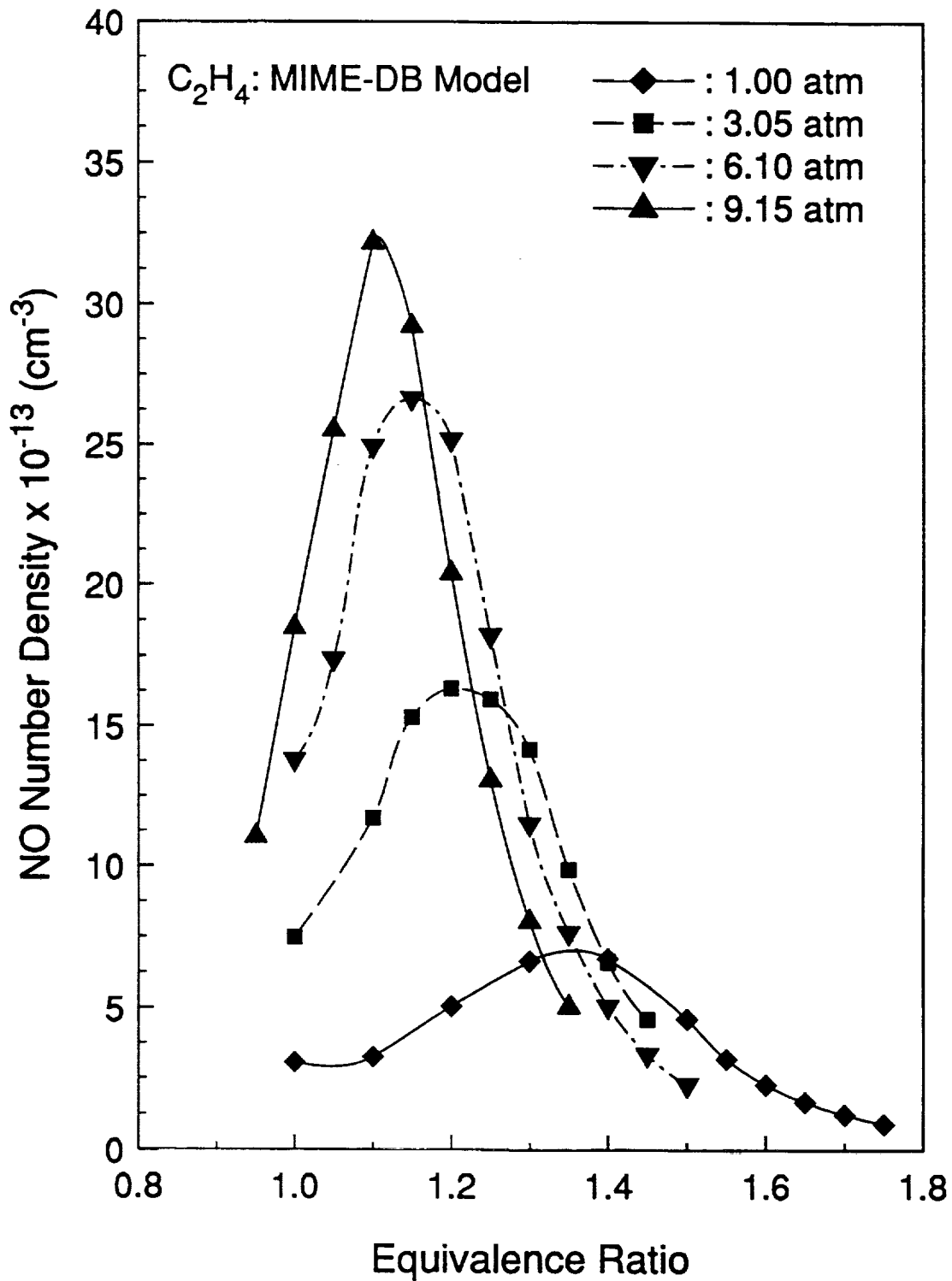
Figure 5.4:   NO concentrations found for the experimental flames by solving the coupled species-energy equations using the MIME-DB reaction mechanism. The concentrations are at the same heights as the measurements shown in Fig. 5.1.

GMK-DB predicted temperatures). The measured temperatures of the rich flames at atmospheric pressure were high in comparison to the same flames at greater pressures; it is expected that these temperatures would be approximately equal. The higher temperatures at atmospheric pressure could be due to catalytic effects on the uncoated thermocouple; these effects may be more significant at atmospheric pressure since the flame front is located higher above the burner. Nevertheless, these deviations are not significant enough to affect the comparative trends between the measurements and the predictions.

Figure 5.5 compares plots of the equivalence ratio corresponding to the peak [NO], and the equivalence ratios corresponding to the half-peak [NO], at each pressure, as found by both modeling and measurements. The two models follow very similar qualitative trends, which show a shift in the curves towards leaner conditions with increasing pressure. While these trends are similar to the measured trends, the measurements give consistently higher equivalence ratios than the predictions for both the peak and half-peak [NO] values. The agreement is especially poor at lower pressures, with improved agreement at higher pressures. Figures 5.6 and 5.7 offer direct comparisons of the measured and modeled NO concentrations at 3.05 and 9.15 atm. In general, poor qualitative agreement is obtained for flames richer than $\phi=1.2$ at lower pressures ($P\leq6.1$ atm). Better qualitative agreement is obtained at higher pressures ($P\geq9.15$ atm).

Figures 5.6 and 5.7 also show that both models underpredict the measured NO concentrations, particularly in the moderately rich flames. For the GMK-DB model at lower pressures, this difference is directly due to a significant underprediction of the equivalence ratio corresponding to the peak [NO] (see Fig. 5.5). For flames at $P\leq6.1$ atm, the GMK-DB model adequately predicts the [NO] up to an equivalence ratio of ~1.2, but then underpredicts the [NO] at higher equivalence ratios (see Fig. 5.6). Because the calculated [NO] peaks at a lower equivalence ratio, the quantitative agreement becomes progressively poorer in richer flames. At higher pressures (see Fig. 5.7), the GMK-DB
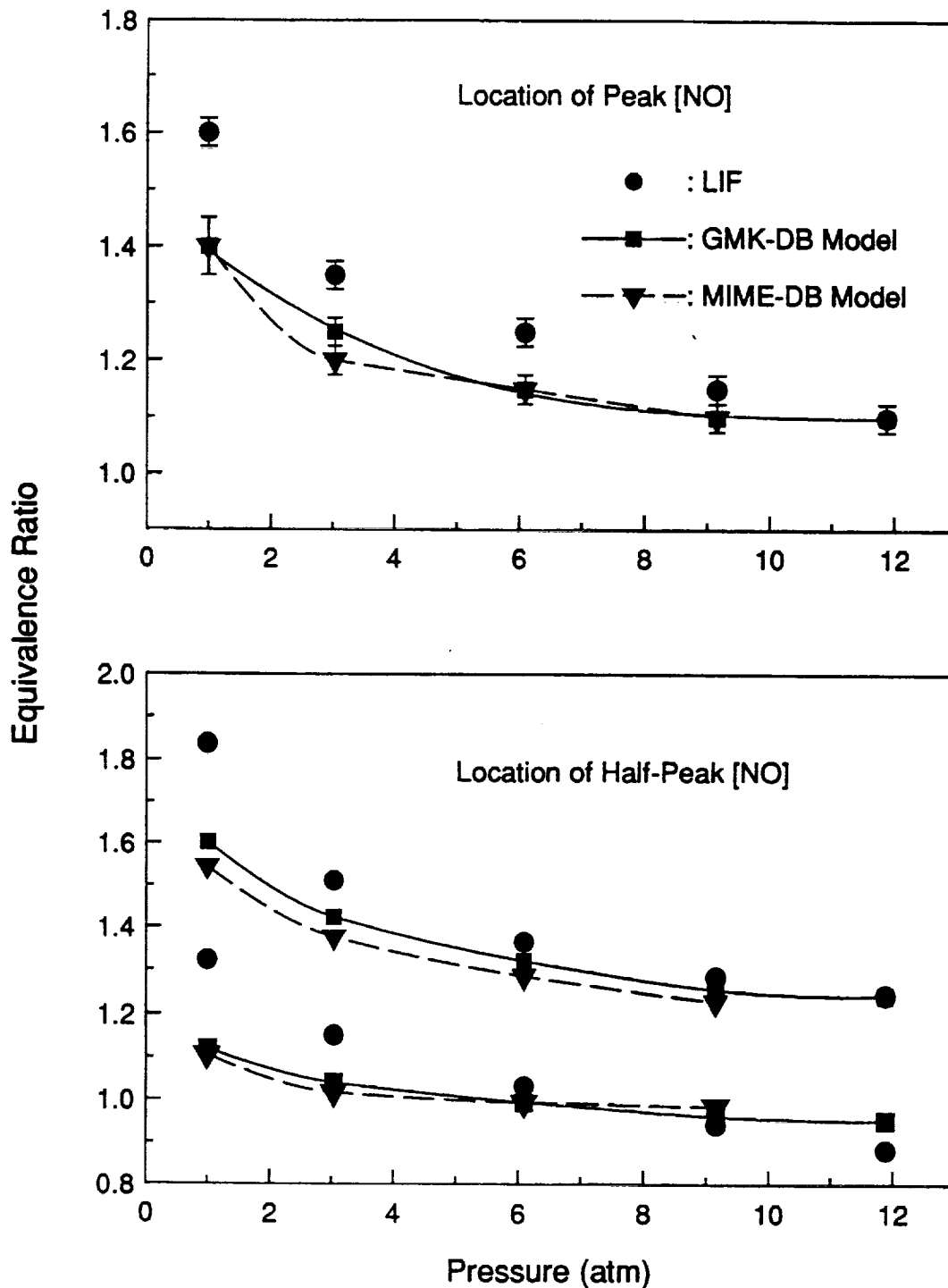
Figure 5.5: Comparisons of experimental and predicted locations on the [NO] vs. φ curves. Both the predictions from the GMK-DB and the MIME-DB model are shown. The top plot represents the equivalence ratio at peak [NO] for each pressure. The bottom plot represents the locations corresponding to the half-maximum [NO] on the rich and lean sides of the [NO] vs φ curves.
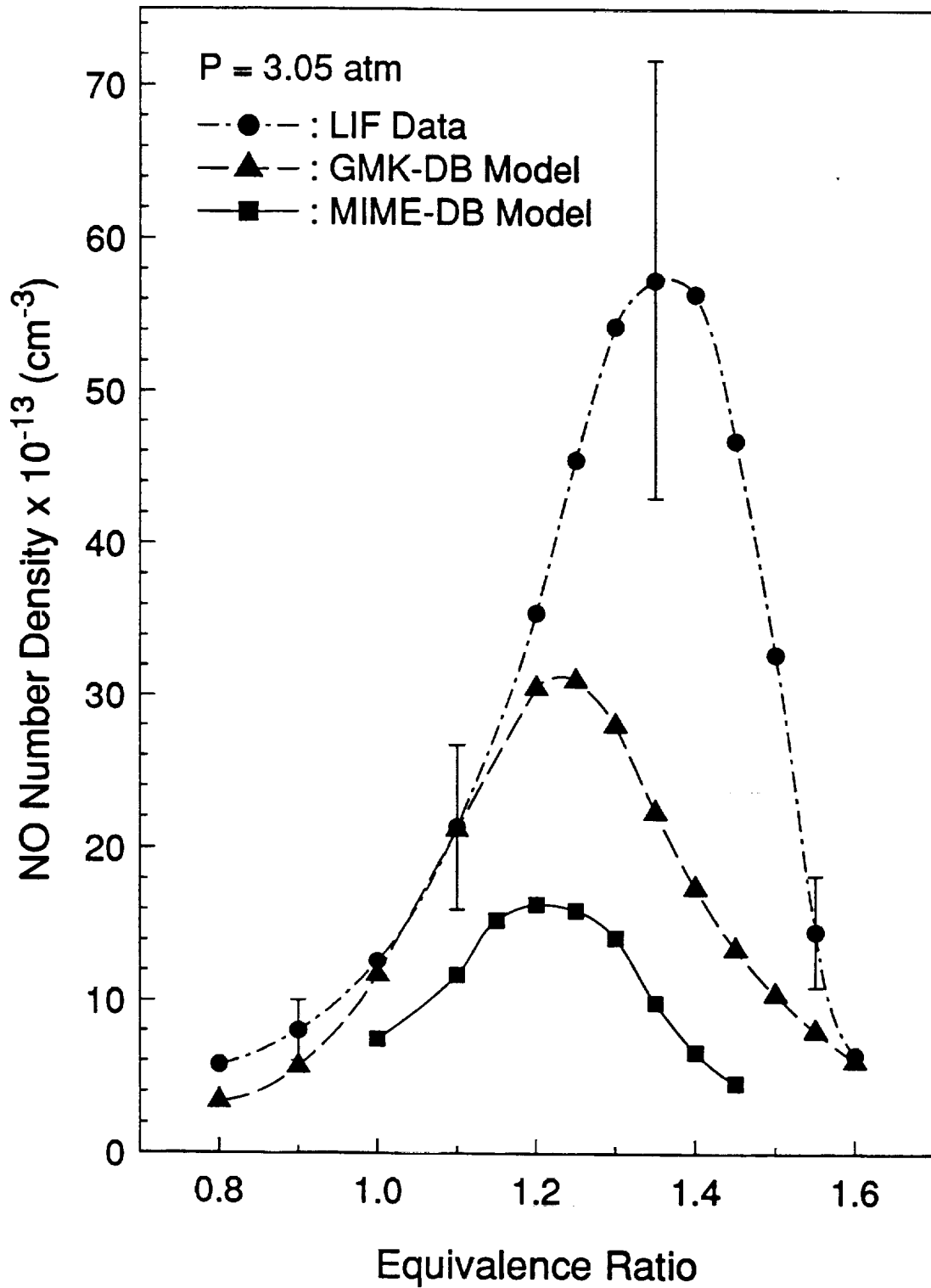
Figure 5.6: Comparison of the measured and predicted NO concentrations for the flames at 3.05 atm. The results from both the GMK-DB and MIME-DB models are shown.
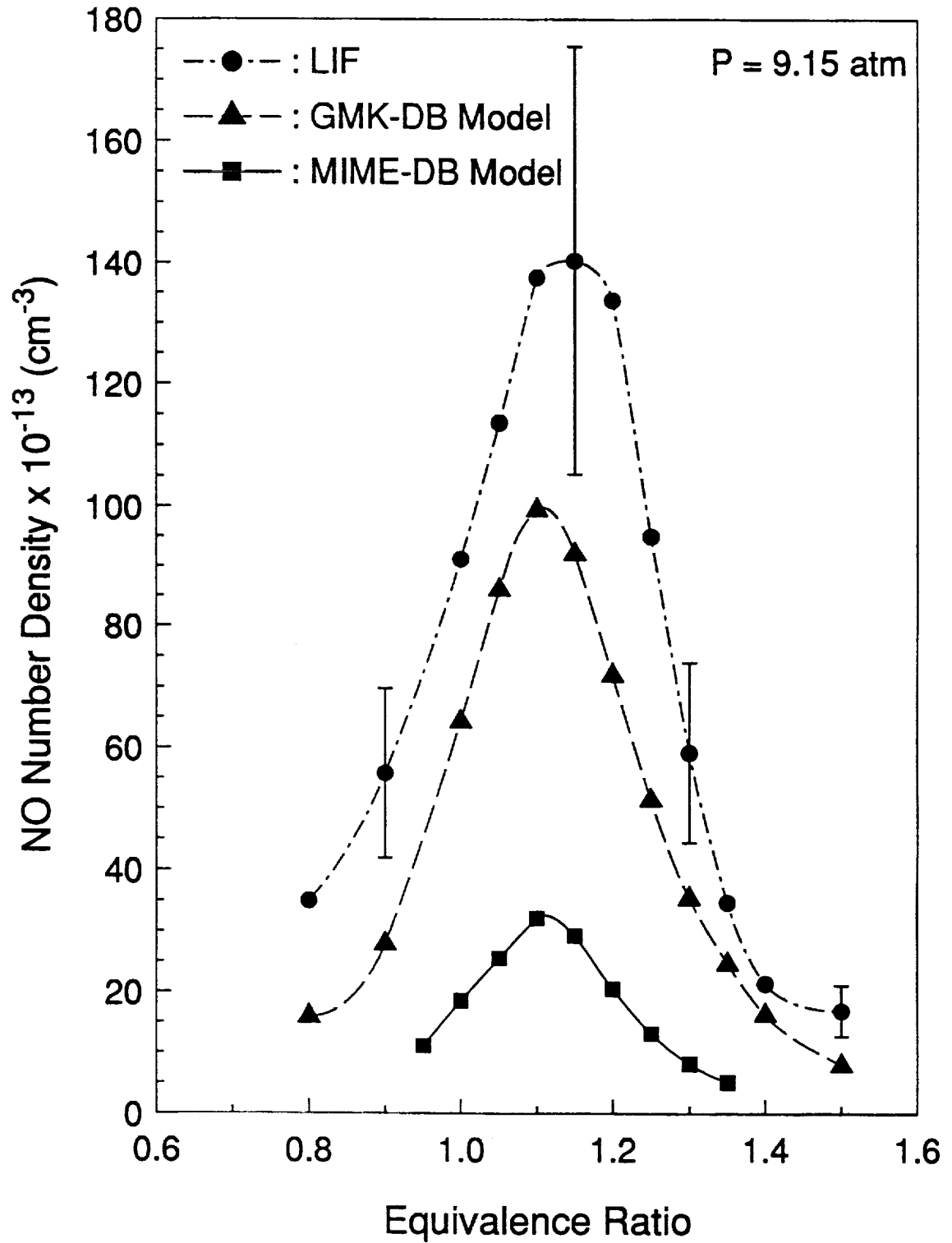
Figure 5.7: Comparison of the measured and predicted NO concentrations for the flames at 9.15 atm. The results from both the GMK-DB and MIME-DB models are shown.

model demonstrates good qualitative agreement with the measurements, but continues to demonstrate a quantitative underprediction of [NO]. The GMK-DB model also provides good predictions of the [NO] in highly rich flames, i.e., well above the equivalence ratio corresponding to the peak [NO]. In general, then, the GMK-DB model appears to be useful for predicting [NO] for $\phi \le 1.2$ at all pressures, and for all equivalence ratios at $P \ge 9.15$ atm. The improved agreement at higher pressures results from the shift in the equivalence ratio corresponding to the peak [NO] towards stoichiometric conditions for both the measurements and predictions.

The MIME-DB model provides a qualitative behavior similar to that of the GMK-DB model, but predicts a much lower [NO] (see Figs. 5.6 and 5.7). The MIME-DB model includes most of the same kinetics for smaller hydrocarbons as the mechanism of Miller and Bowman [1989]. Because larger hydrocarbons are not formed in high concentrations for most of these flames (since the equivalence ratio is below sooting conditions), results from the previous analysis of ethane flames for prompt-NO formation from the Miller-Bowman scheme (Chapter 4) may be applied to this investigation. In particular, it was found that the inclusion of

$$CH + H_2O \leftrightarrow CH_2O + H \tag{R3}$$

in the Miller-Bowman model depletes a large amount of CH from the flame; the removed CH is then unable to form NO via reaction (R1). A test was performed in which six rich flames at different pressures were modeled using the MIME-DB mechanism, both with and without reaction (R3). The [NO] increased 45-90% with this reaction removed; while the resulting [NO] is still smaller than that from the GMK-DB model, the two predictions are in better agreement. However, reaction (R3) probably belongs in the mechanism; therefore, its inclusion requires additional kinetic modifications to compensate for the resulting reduction in NO formation.

The effect of fuel type on the variation of [NO] with equivalence ratio can be seen in Fig. 5.8. Figure 5.8 is a comparison of the equivalence ratios corresponding to the peak [NO] and half-peak [NO] as found for the C_2H_4 flames of this study and the C_2H_6 flames of Chapter 4. As noted previously, fuel type can affect the amount of prompt-NO formed for a given equivalence ratio. From Fig. 5.8, it is clear that high NO levels occur in leaner flames for C_2H_6 as compared to C_2H_4. The difference between the two fuels is more pronounced at lower pressures. All of the characteristic equivalence ratios show improved agreement with increasing pressure, as the equivalence ratios corresponding to the peak [NO] approach unity for both fuels at higher pressures. Bachmaier *et al.* [1973] similarly found that prompt-NO formation peaks at a higher equivalence ratio for C_2H_4 compared to C_2H_6 flames at atmospheric pressure. The present work demonstrates that this difference resulting from fuel type is considerably reduced at higher pressures.

An important question is why both models are predicting the peak NO concentration to be in a leaner flame than that found from the measurements at lower pressures (see Fig. 5.5). Recall that the [NO] is underpredicted in moderately rich flames at lower pressures, but that the quantitative agreement is much better for $\phi < 1.2$. In the following, a possible explanation for this behavior is presented; however, additional experimental data will be needed to confirm this hypothesis. Recall that much of the difference between the GMK-DB and MIME-DB models is due to the inclusion of reaction (R3) in the MIME-DB model. Other than that, the two models behave in roughly the same manner (much like the GMK-DB model and the Miller-Bowman [1989] model for ethane flames of Chapter 4); thus, conclusions which are valid for one model will be deemed to be valid for the other. Due to the large percentage of prompt-NO formed in the rich flames, the predicted inaccuracy in [NO] should be caused by the hydrocarbon kinetics. To determine a model's accuracy at predicting species profiles, one must usually rely on low-pressure
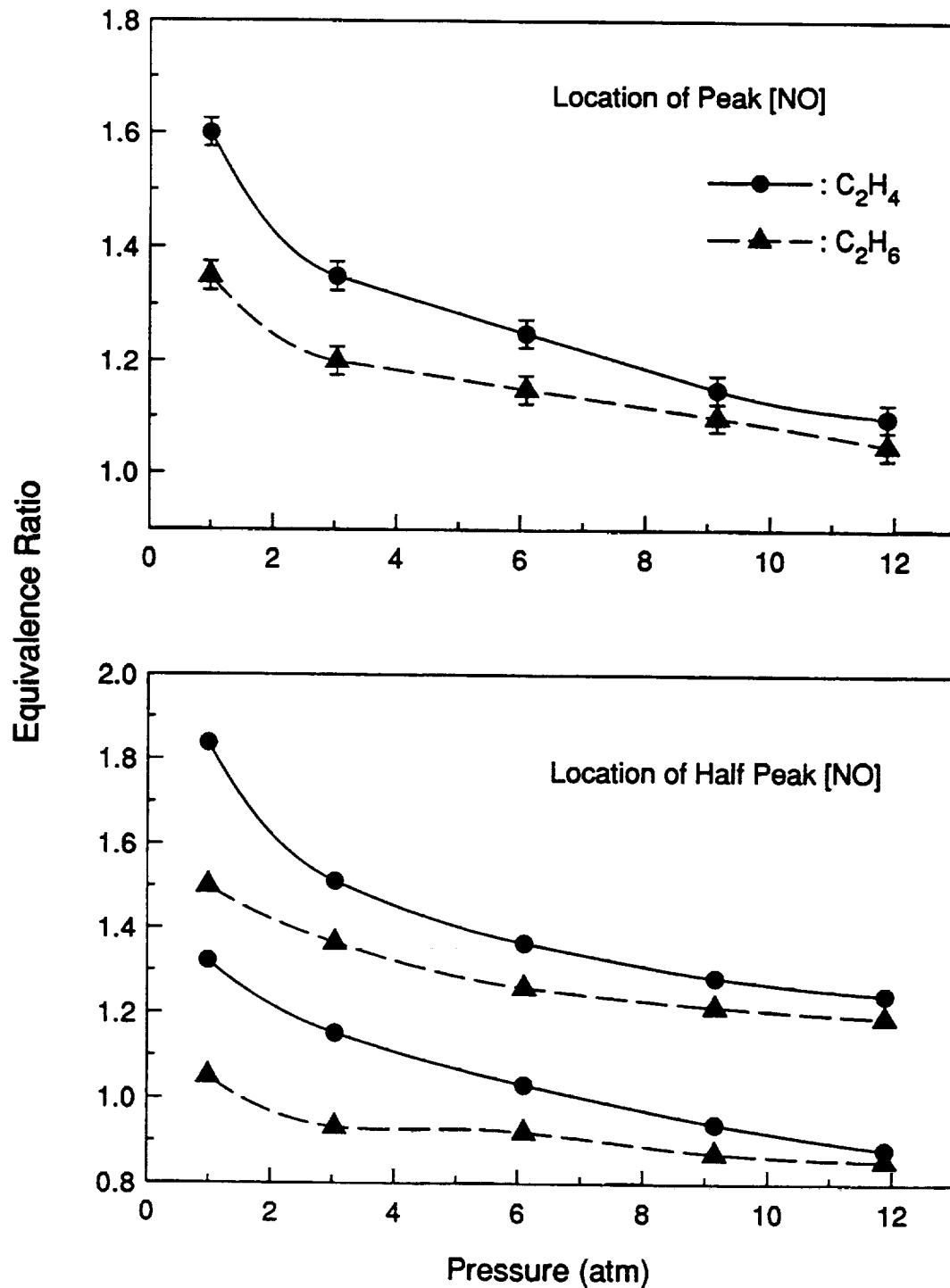
Figure 5.8: Comparison of the measured equivalence ratios corresponding to peak and half peak [NO] for the $C_2H_4/O_2/N_2$ flames of this study, and the $C_2H_6/O_2/N_2$ flames of Chapter 4. Both sets of flames have a dilution ratio of 3.1 and the same volumetric flow rates.

data (as flames at high pressure are located too near the burner surface to adequately resolve the spatial profiles of many radicals). Applying results from low-pressure flames to high-pressure flames may not be very accurate; however, it is assumed that such an extrapolation should lead to approximately correct results.

Bernstein *et al.* [1993] found that the Miller-Bowman mechanism [1989] accurately predicts the location of the peak CH concentration in stoichiometric, low-pressure C_2H_4 /O_2/Ar flames. Owing to the similarities between the Miller-Bowman mechanism and the MIME-DB mechanism, one would expect similar behavior from the MIME-DB mechanism. Miller *et al.* [1991] compared measured [CH] profiles with predictions from the Miller-Melius [1992] mechanism in low-pressure C_2H_2 /O_2 /Ar flames at several stoichiometries. They again found that the measured and modeled [CH] profiles agreed well in a near stoichiometric flame, much like the results of Bernstein *et al.* [1993] for the C_2H_4 flame. However, the calculated [CH] profile peaked closer to the burner than that for the measured profile in richer flames ($\phi \geq 1.6$); the discrepancy increased with increasing equivalence ratio. If this behavior applies to C_2H_4 flames as well, one would expect that in very rich flames, the predicted [CH] profile would peak substantially nearer the burner surface than the actual [CH] profile. Such behavior may lead to an underprediction of the amount of prompt-NO in richer flames, for the residence time of CH at high temperatures would be smaller for the model than for the experiment. Hence, the calculated equivalence ratio corresponding to the peak [NO] would be at a lower equivalence ratio than that indicated by the measurements. On the other hand, the near-stoichiometric flames would have similar predicted and experimental [CH] profiles, which explains the good predictions for [NO] at $\phi < 1.2$. For flames at higher pressure, the overall qualitative agreement is better because the measured equivalence ratio corresponding to the peak [NO] has shifted far enough towards stoichiometric conditions to satisfy $\phi < 1.2$.

5.5 Summary

In summary, LIF measurements of NO concentration have been obtained in laminar, premixed, flat $C_2H_4/O_2/N_2$ flames at pressures ranging from 1.0 to 11.9 atm. The temperatures of these flames were between 1600 and 1850 K. NO measurements obtained from the excitation of two different spectral lines were found to give very similar results. As expected from previous work, the equivalence ratio corresponding to the peak [NO] at a given pressure shifts towards stoichiometric conditions with increasing pressure. The LIF measurements demonstrate that the equivalence ratio corresponding to the peak [NO] at a given pressure occurs in a richer flame for the ethylene flames than for the ethane flames of Chapter 4; the stoichiometry of this point becomes more similar at higher pressures. Both the GMK-DB and MIME-DB mechanisms tend to underpredict the [NO] in these flames, although the GMK-DB model offers more quantitative accuracy than the MIME-DB model. Qualitatively, both models exhibit similar behavior; the predictions are fairly poor at lower pressures, and better at higher pressures. This behavior is mostly caused by the underprediction of [NO] in moderately rich flames at lower pressures, which causes inaccurate prediction of the equivalence ratio corresponding to the peak [NO] at a given pressure. The agreement is better at higher pressures because the equivalence ratio at the peak [NO] approaches stoichiometric conditions for both the measurements and predictions. The same rationale also explains the reduced influence of fuel type at higher pressures.

CHAPTER 6

TRANSPORTABILITY OF A LASER-INDUCED FLUORESCENCE

CALIBRATION OF NITRIC OXIDE

6.1 Introduction

As environmental regulations become more stringent, reduction of nitric oxide emissions from combustion applications such as gas-turbine engines is becoming an increasingly important goal. To achieve this goal, an understanding of the formation mechanisms of NO is required. This in turn requires the ability to perform accurate quantitative *in situ* measurements of the concentrations of various flame species, including NO. Such measurements will allow for the refinement of chemical kinetics models, which can then be used with more certainty in the design of future combustion schemes and equipment.

One way to achieve accurate measurements of [NO] at ppm levels is to use laser-induced fluorescence (LIF) [Morley, 1981, 1982; Chou *et al.*, 1983; Cattolica *et al.*, 1989; Heard *et al.*, 1992; Reisel *et al.*, 1993]. Accurate quantitative LIF measurements require reliable calibrations of the LIF signal originating from the NO. Techniques used to calibrate the LIF measurement range from spectral absorption [Chou *et al.*, 1983] to direct evaluation of the fluorescence signal from known concentrations of NO [Morley, 1981, 1982, Reisel *et al.*, 1993]. Whatever calibration technique is used, one must be concerned with the transportability of the calibration factor from the calibration conditions to the measurement conditions. This issue could be avoided by calibrating the fluorescence measurement in every flame studied; however, such a procedure would be impractical for

studies involving large numbers of flames.

In this chapter, the theoretical transportability of the calibration factor is investigated for linear LIF measurements of [NO]. In particular, comparisons are made between predicted fluorescence signals for a fixed NO mole fraction at the calibration and measurement conditions for several calibration schemes. The flames considered are laminar, premixed, high-pressure $C_2H_6/O_2/N_2$ flames. Many of the same concepts would apply to other types of flames as well. Finally, a discussion is given of some practical problems that would arise when attempting to use the same calibration factor at considerably different operating conditions.

6.2 Theoretical Considerations

The primary concern with using a calibration factor determined at one set of conditions at another set of conditions is the change in the fluorescence signal between these two conditions for the same NO mole fraction. Assuming a two-level model of the molecule, the fluorescence signal monitored by a photomultiplier tube, V_f (V), is given by [Laurendeau and Goldsmith, 1989]

$$V_f = \beta h c \nu_f G V_c \left(\frac{\Omega_c}{4\pi}\right)\left(\frac{A_{ul}}{A_{ul}+Q_{ul}}\right)N_l^0 W_{lu} \quad , \qquad (6.1)$$

where β is a parameter accounting for the detection efficiency of the optics and nonuniform irradiation, h is Planck's constant, c is the speed of light, ν_f is the fluorescence frequency (cm^{-1}), G is the photomultiplier gain (V/W), V_c is the fluorescence collection volume (cm^3), Ω_c is the solid angle of the collection optics (sr), A_{ul} is the rate coefficient for spontaneous emission (s^{-1}), Q_{ul} is the rate coefficient for electronic quenching (s^{-1}), W_{lu} is the rate coefficient for absorption (s^{-1}), and N_l^0 is the initial number density of the two-level system. The assumptions accompanying Eq. (6.1) are discussed by Laurendeau and Goldsmith [1989] and also in Chapter 2. As indicated by Reisel et al. [1993], additional

factors, such as rotational energy transfer, are encountered when considering broadband fluorescence from other excited levels. However, these additional factors will be neglected here, for they have little influence on the trends and conclusions.

The quenching rate coefficient per unit pressure, Q_{ul}/P ($s^{-1} \cdot atm^{-1}$), is given by

$$\frac{Q_{ul}}{P} = \frac{1}{kT} \left(\frac{8kT}{\pi} \right)^{0.5} \sum_i \frac{X_i \sigma_i}{\sqrt{\mu_i}} \quad , \tag{6.2}$$

where k is Boltzmann's constant, T is the temperature (K), X_i is the mole fraction of quenching species i, σ_i is the quenching cross-section of NO with species i (cm^2), and μ_i is the reduced mass between species i and NO. Assuming ideal gas behavior, N_l^0 is given by

$$N_l^0 = \frac{X_{NO} P}{kT} f_B \quad , \tag{6.3}$$

where f_B is the Boltzmann fraction relating N_l^0 to the total number density. For NO, Q_{ul} is much larger than A_{ul} at $P \geq 1$ atm [Reisel et al., 1992, Chapter 4], so Eq. (6.1) can be rewritten as

$$V_f = \zeta \frac{X_{NO}}{kT} \frac{A_{ul} W_{lu}}{Q_{ul}/P} f_B \quad , \tag{6.4}$$

where

$$\zeta = \beta h c v_f G V_c \left(\frac{\Omega_c}{4\pi} \right) \quad . \tag{6.5}$$

Typically, the excitation line is chosen such that the Boltzmann fraction is insensitive to temperature variations over the range of measurement conditions. From Eq. (6.4), it can be seen that the fluorescence signal is directly proportional to the rate coefficient for absorption and inversely proportional to that for electronic quenching.

To determine the relationship between the fluorescence signal for a calibration condition, V_{cal}, and for a measurement condition, V_{flame}, at a given NO mole fraction, X_{NO},

one may take a ratio of Eq. (6.4) for the two cases. If we assume that ζ is a constant and that the laser frequency is situated on the identical portion of the NO spectrum for the two conditions, the ratio for the two fluorescence signals is given by

$$\frac{V_{flame}}{V_{cal}} = \frac{T_{cal}}{T_{flame}} \cdot \frac{W_{lu,flame}}{W_{lu,cal}} \cdot \frac{f_{B,flame}}{f_{B,cal}} \cdot \frac{(Q_{ul}/P)_{cal}}{(Q_{ul}/P)_{flame}} \quad , \tag{6.6}$$

where the subscript "*flame*" refers to the measurement condition, and "*cal*" refer to a calibration condition. The rate coefficient for stimulated absorption is given by [Partridge, 1994]

$$W_{lu} = \Gamma_{lu} B_{lu} I_{v}^{0} T_{L} \quad , \tag{6.7}$$

where I_{v}^{0} is the peak spectral laser irradiance (W/cm^2•cm^{-1}), B_{lu} is the Einstein coefficient for absorption (cm^2•cm^{-1}/J), and T_{L} is a nondimensional temporal distribution function normalized at the peak of the laser pulse. In Eq. (6.7), Γ_{lu} is the fractional overlap integral between the absorption line and the laser line, i.e.,

$$\Gamma_{lu} = \int_{-\infty}^{+\infty} Y(v) G(v) dv \quad , \tag{6.8}$$

where $Y(v)$ is the absorption spectral lineshape function (cm) and $G(v)$ is a nondimensional laser spectral lineshape function. Since $G(v) \leq 1$, Γ_{lu} approaches unity only for a broadband light source. While Eq. (6.6) was developed for a two-level model, it can nevertheless be employed for a multilevel system. Due to the small rotational constant for NO [Freedman and Nicholls, 1980], there is rapid rotational redistribution of the population in the directly excited level. As a result, the directly excited population quickly spreads over the entire manifold of rovibronic levels in the upper electronic state. Broadband fluorescence then encompasses the emission from all of the excited rovibronic levels in the upper electronic state to all the accessible rovibronic levels in the ground electronic state. Thus, the fluorescence from the excited electronic state can be thought of

as being from a single level, and the absorption, while actually calculated from the contribution of many rovibronic levels in the ground electronic state, can also be thought of as if it were from a single level.

Since Q_{ul}/P is independent of pressure (see Eq. (6.2)), Eq. (6.6) contains no explicit pressure dependence. However, a change in pressure indirectly affects the fluorescence ratio, through the influence of pressure broadening on the overlap integral, Γ_{lu}. For NO broadened by N_2, Chang et al. [1992] found that the spectral linewidth due to collisional broadening, Δv_C (cm^{-1}), is given by

$$\Delta v_C = 0.585 \left(\frac{295K}{T} \right)^{0.75} P \quad .$$

(6.9)

Recently, DiRosa and Hanson [1994] measured similar collisional parameters for NO broadened by H_2O, O_2, and NO near room temperature. However, these new parameters are not considered in this analysis as N_2 is the dominant species in most flames, and the changes produced by considering these separate species would be small. Moreover, the broadening parameters for other species such as CO_2 and the influence of temperature are still unknown. On the other hand, Eq. (6.9), however, does not consider the effects of Doppler broadening on the fluorescence signal. The relative widths of collisional and Doppler broadened spectral lines can be determined through the Voigt "a" coefficient [Lucht et al., 1978],

$$a = \sqrt{\ln 2} \frac{\Delta v_C}{\Delta v_D} \quad ,$$

(6.10)

where Δv_D is the Doppler linewidth (cm^{-1}), i.e.,

$$\Delta v_D = 2 \left(\frac{2kT \ln 2}{mc^2} \right)^{0.5} v_0 \quad ,$$

(6.11)

where m is the mass of the absorber and v_0 is the centerline transition frequency (cm^{-1}). The Voigt a parameters have been calculated for the $Q_2(26.5)$ transition of the $\gamma(0,0)$ band

of NO over a range of temperatures and pressures. As can be seen from the tabulated values in Table 6.1, the effects of Doppler broadening can be substantial at lower pressures, while the spectral lines at higher pressures are primarily collisionally broadened. The important conclusion is that a spectral line broadens and decreases in peak intensity with increasing pressure, thus reducing the amount of absorption that occurs when using a well-tuned laser with a narrow spectral linewidth.

In addition to the effects of pressure, temperature changes can also produce variations in the fluorescence ratio of Eq. (6.6). First, there is the direct effect of temperature through the number density. The quenching rate coefficient is also affected by the temperature. Furthermore, as indicated by Eqs. (6.9) and (6.11), both the Doppler and collisional linewidths are functions of temperature. Finally, the Boltzmann fraction of the directly excited rovibronic levels also depends on the temperature. While corrections for changes in the number density with temperature can easily be made, it is more difficult to correct for changes in the spectral linewidth and the Boltzmann fraction with temperature. Such corrections are particularly difficult when portions of several spectral lines are excited simultaneously.

The Boltzmann fraction, $f_B(T)$, for a particular rovibronic level in the ground electronic state of NO is given by

$$f_B = \frac{2J''+1}{Z_r Z_v Z_e} \exp\left\{\frac{-E}{T}\left[\frac{k}{hc}\right]\right\} \quad , \tag{6.12}$$

where E is the total molecular energy [Reisel et al., 1992], J'' is the ground state rotational quantum number, and Z_r, Z_v, and Z_e are the rotational, vibrational and electronic partition functions, respectively [Lucht et al., 1978]. As described by Reisel [1991], the population becomes more evenly distributed over a wider range of rotational levels at flame temperatures (1700 K) as opposed to room temperature. To minimize the effects of a variable

Table 6.1: Calculated Voigt a parameter for the Q_2(26.5) line of the γ(0,0) band of NO for flames at different temperatures and pressures. The calculation considers the collisional broadening to be solely due to N_2.

Pressure (atm)	Temperature (K)				
	1500	1750	2000	2250	2500
1	0.641	0.528	0.447	0.386	0.338
3	1.922	1.585	1.341	1.157	1.015
6	3.844	3.170	2.683	2.316	2.030
9	5.766	4.755	4.024	3.473	3.045
12	7.688	6.341	5.366	4.631	4.060
15	9.610	7.926	6.707	5.789	5.075

Boltzmann fraction on Eq. (6.6), a spectral line can be chosen which has a relatively constant Boltzmann fraction over the range of temperatures being investigated. Due to the compactness of the NO spectrum, it is also desirable to choose a spectral line whose neighboring lines are similarly insensitive to thermal changes in the Boltzmann fraction.

6.3 Modeling Calculations

Calibration effects were assessed for a variety of premixed, laminar, flat, C_2H_6/O_2 /N_2 flames, with pressures ranging from 1 to 15 atm and temperatures ranging from 1500 to 2500 K. Two different dilution ratios ($\dot{V}_{N_2}/\dot{V}_{O_2}$), ψ=3.1 and ψ=3.76, were considered, and the equivalence ratios ranged from ϕ=0.6 to ϕ=1.6. The required fluorescence quenching rate coefficients were calculated in the post-flame region using the assumption of chemical equilibrium.

The calculations employed the following procedure. First, a computer simulation of the spectrum of NO was generated using two computer programs written by Seitzman [1991]. The first of these programs calculates the transition frequencies and line strengths for the NO spectral lines in the $\gamma(0,0)$ band. Using this information, the second program assigns a Voigt spectral profile to each line, and sums the contribution of each spectral line over a given range of frequencies to generate the NO spectrum. As input for the program, a collisional spectral linewidth was calculated at each pressure and temperature using Eq. (6.9). The program evaluates the associated Doppler linewidth, and then calculates the appropriate Voigt profile from the two linewidths [Humlícek, 1979]. Spectra were generated for the region of the $\gamma(0,0)$ band of NO surrounding the $Q_2(26.5)$ line ($v \approx 44330$ cm^{-1}). Figure 6.1 presents a comparison between the experimentally measured spectrum near the $Q_2(26.5)$ line and the theoretically generated spectrum, which considered the convolution of the laser with the NO spectrum. The laser FWHM was chosen as 0.7 cm^{-1} for the convolution. As can be seen in Fig. 6.1, good agreement exists between the two spectra, indicating that the spectral linewidths used in the modeling are reasonably accurate. The lines in the calculated spectrum are actually slightly narrower than those in the experimental spectrum, a result consistent with a small degree of saturation broadening at 3.05 atm. The accuracy of the laser spectral linewidth also requires further verification.

The output of the program is the absorption coefficient per unit pressure as a function of spectral location. The spectral absorption coefficient, $\alpha(v)$, for a single spectral line (cm^{-1}) is given by [Measures, 1984]

$$\alpha(v) = hcvB_{lu}N_i^0Y(v) \quad , \tag{6.13}$$

where the Einstein B coefficient for absorption is [Lucht et al., 1978]

$$B_{lu} = \frac{\pi e^2}{m_e hc^3v}f_{v''v'}\frac{S_{J''J'}}{2J''+1} \quad , \tag{6.14}$$
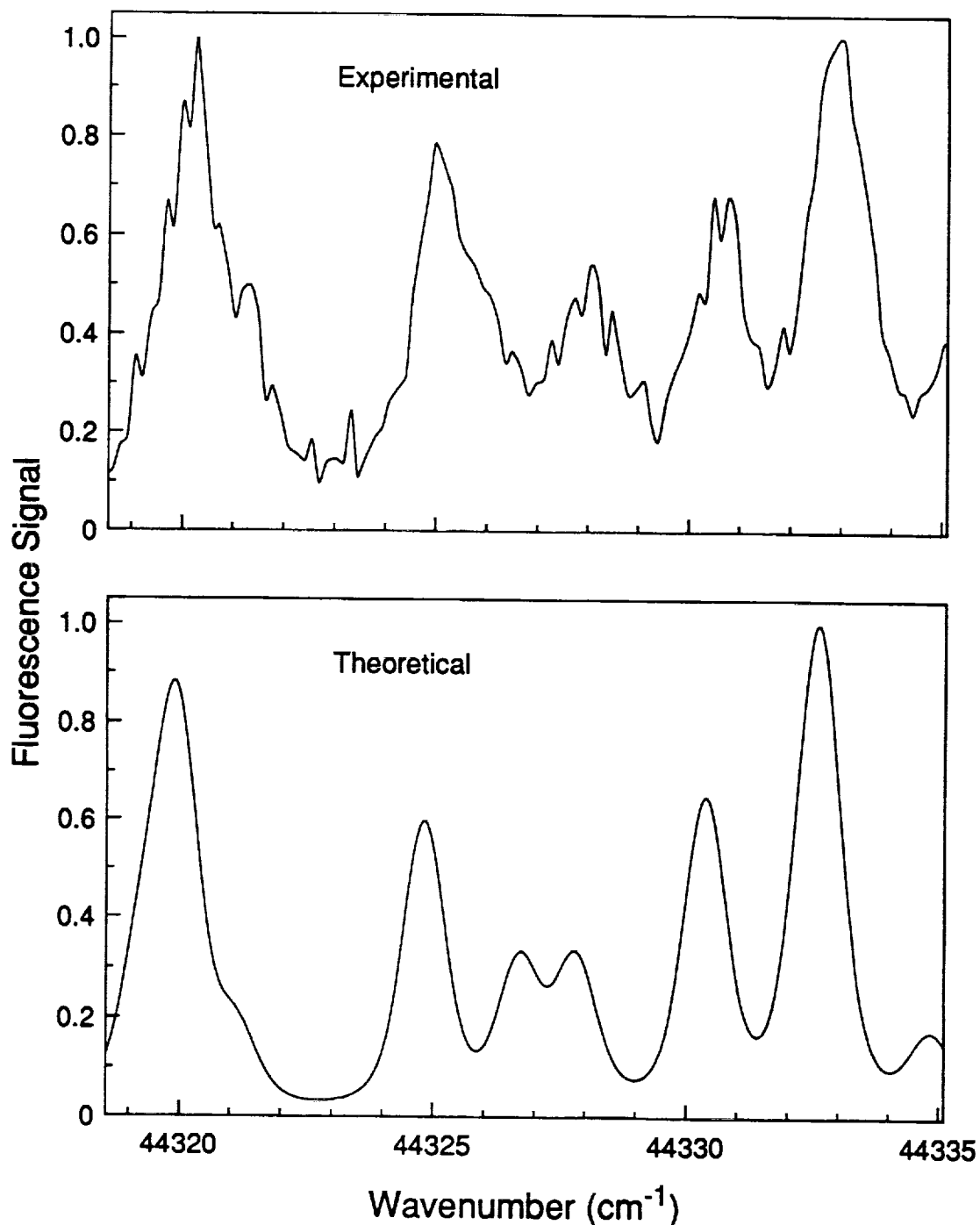
Figure 6.1: Comparison of two NO spectra for P = 3 atm near the $Q_2(26.5)$ line ($v\approx44330$ cm^{-1}). The top plot represents an experimentally measured spectrum, while the bottom plot represents a theoretical spectrum generated using the programs of Seitzman [1991] for convolution with a laser having a FWHM of 0.7 cm^{-1}.

where e is the electronic charge, m_e is the electron mass, $S_{J''J'}$ is the Hönl-London factor, and $f_{v''v'}$ is the band oscillator strength. The spectral lineshape function, $Y(v)$, is given by the Voigt profile:

$$Y(v) = \frac{2\sqrt{\ln 2}}{\sqrt{\pi}\Delta v_D} V(\xi, a) \quad , \tag{6.15}$$

where $V(\xi, a)$ is the Voigt function [Lucht et al.,1978], and

$$\xi = 2\sqrt{\ln 2}\left(\frac{v - v_0}{\Delta v_D}\right) \quad . \tag{6.16}$$

Substituting Eqs. (6.3), (6.14), and (6.15) into Eq. (6.13), the absorption coefficient per unit pressure for a single spectral line is given by

$$\frac{\alpha(v)}{P} = \left(\frac{\pi e^2}{m_e c^2}\right) f_{v''v'} \frac{S_{J''J'}}{2J''+1} f_B \frac{X_{NO}}{kT} \frac{2\sqrt{\ln 2}}{\sqrt{\pi}\Delta v_D} V(\xi, a) \quad . \tag{6.17}$$

The effects of neighboring lines must be considered to properly model NO absorption at high pressures. The overlap between the spectral profile and the laser lineshape must also be considered. The laser spectral lineshape, $G(v)$, can be modeled using a nondimensionalized Lorentzian function [Koechner, 1992]:

$$G(v) = \left\{4\left(\frac{v - v_0}{\Delta v_L}\right)^2 + 1\right\}^{-1} \quad . \tag{6.18}$$

where Δv_L is the laser spectral FWHM (cm^{-1}), v is the frequency, and v_0 is the center frequency of the laser pulse. Therefore, the integrated absorption per unit pressure for a given laser spectral lineshape is

$$\int_v \frac{\alpha(v)}{P}\frac{G(v)}{v}dv = \upsilon \int_v \sum_i f_{B,i}\left(\frac{S_{J''J'}}{2J''+1}\right)_i \frac{1}{\Delta v_{D,i}} V(\xi_i, a)\frac{G(v)}{v}dv \quad , \tag{6.19}$$

where

$$\upsilon = \left(\frac{\pi e^2}{m_e c^2}\right) f_{v''v'} \frac{X_{NO}}{kT} \frac{2\sqrt{\ln 2}}{\sqrt{\pi}} \quad , \tag{6.20}$$

and

$$\xi_i = 2\sqrt{\ln 2}\left(\frac{\nu - \nu_{0,i}}{\Delta\nu_{D,i}}\right) \quad . \tag{6.21}$$

Equation (6.19) can then be used in Eq. (6.6) by realizing that

$$\frac{T_{cal}}{T_{flame}} \cdot \frac{W_{lu,flame}}{W_{lu,cal}} \cdot \frac{f_{B,flame}}{f_{B,cal}} = \frac{T_{cal}}{T_{flame}} \cdot \frac{B_{lu,flame}}{B_{lu,cal}} \cdot \frac{f_{B,flame}}{f_{B,cal}} \cdot \frac{\Gamma_{lu,flame}}{\Gamma_{lu,cal}} \tag{6.22}$$

for the same temporal laser irradiance. On this basis, it can be shown that

$$\frac{B_{lu}f_B\Gamma_{lu}}{T} = \frac{k}{hc}\frac{1}{X_{NO}}\int_\nu \frac{\alpha(\nu)}{P}\frac{G(\nu)}{\nu}d\nu \quad , \tag{6.23}$$

so that

$$\frac{V_{flame}}{V_{cal}} = \frac{\left\{\int(\alpha(\nu)/P)\cdot(G(\nu)/\nu)d\nu\right\}_{flame}(Q_{ul}/P)_{cal}}{\left\{\int(\alpha(\nu)/P)\cdot(G(\nu)/\nu)d\nu\right\}_{cal}(Q_{ul}/P)_{flame}} \quad . \tag{6.24}$$

The integration of Eq. (6.19) was performed numerically using Simpson's 1/3 rule [Hoffman, 1992]. Equation (6.24) was evaluated by utilizing Eqs. (6.2) and (6.19).

Two laser spectral linewidths were used in the calculations of V_{flame}/V_{cal}: (1) $\Delta\nu_L = 0.2$ cm^{-1}, and (2) $\Delta\nu_L = 0.7$ cm^{-1}. These values were chosen as representative of a narrow and a wide bandwidth laser, respectively, and present a reasonable range for possible laser linewidths. The center frequency considered for excitation was the peak of the $Q_2(26.5)$ line ($\nu \approx 44330$ cm^{-1}). Two different dilution ratios were used for the flames: $\psi=3.1$ and $\psi=3.76$. Quenching rate coefficients were calculated in the post-flame zone using equilibrium concentrations and the quenching cross-sections from Drake and Ratcliffe [1993]. In these calculations, only the species studied by Drake and Ratcliffe were considered (N_2, O_2, H_2O, CO_2, CO, C_2H_6, H_2, NO, H, OH, and O); these include the dominant quenching species in the post-flame zone.

In the following discussion, two different cases will be discussed. Case A represents a laser spectral linewidth of 0.2 cm^{-1} and a dilution ratio of 3.1. Case B represents a laser spectral linewidth of 0.7 cm^{-1} and the same dilution ratio. The results for the calculations at a dilution ratio of 3.76 differ only slightly from these cases; in addition, the trends are the same for the two dilution ratios. For these different cases, Eq. (6.6) was solved considering three possible calibration schemes. The first scheme, termed "CS1" considers the possibility of calibrating at a given pressure, temperature, and equivalence ratio, and applying the calibration at different pressures in flames with the same temperature and equivalence ratio. For CS1, the fluorescence signal will change only because of the effects of pressure broadening on the NO spectrum. Scheme "CS2" considers the possibility of calibrating at the same pressure as the measurements, but at a different temperature and equivalence ratio. Thus, CS2 considers changes in the fluorescence signal resulting from the different quenching environments of the flames and from thermal effects on the number density, spectral line broadening, and the Boltzmann fraction. However, CS2 contains no change due to pressure broadening. Finally, "CS3" considers the possibility of calibrating at a different pressure, temperature and equivalence ratio compared to the measurement conditions. This case has changes in the fluorescence signal due to variations in quenching environment, Boltzmann fraction, number density, and both pressure and temperature broadening of the spectral lines. In all cases, it is assumed that calibration occurs in a the post-flame zone of a premixed, laminar flame, or in a similar environment. This assumption is made so that the calibration conditions are kept reasonably close to the measurement conditions. One could calibrate a LIF measurement in a flame by using the fluorescence signal for a room temperature flow of NO; however, the vastly different population distributions among the ground-state energy levels at room and flame temperatures may lead to considerably different rotational energy transfer environments, which, in turn, could lead to possible difficulties in calibration transportability.

6.4 Results and Discussion

The optimal calibration scheme would be to calibrate in each flame for which measurements occur. If this cannot be achieved, one should closely match the temperature and pressure of the calibration flame with the measured flames. This will result in a minimal difference between the calibration and measurement fluorescence signals. However, it is not always possible to perform such a calibration; for instance, one may have separate test and calibration facilities, with only the test facility having high-pressure capabilities. To study the transportability of a calibration found under different conditions, three possible calibration schemes have been investigated (CS1, CS2, and CS3).

Example results for CS1, the scheme in which the calibration flame is at the same temperature and equivalence ratio but at a different pressure compared to the measurements, are shown in Figs. 6.2 and 6.3. Recall that for CS1 the fluorescence signal is only changed by pressure broadening of the spectral lines. The results in Figs. 6.2 and 6.3 were obtained from Eq. (6.6) for five different temperatures, with calibration occurring at two different pressures, 1 and 6 atm. Figure 6.2 is for Case A, in which the laser excitation of NO is centered on the $Q_2(26.5)$ line and the laser spectral FWHM is 0.2 cm^{-1}. Figure 6.3 corresponds to Case B, for which laser excitation occurs at the same location but the laser FWHM is 0.7 cm^{-1}. Each figure presents the ratio V_{flame}/V_{cal} plotted versus pressure. Because the flame reactants are not important in CS1 (due to the constancy of the temperature and equivalence ratio between the measurement and calibration flames), Figs. 6.2 and 6.3 also apply for a flame with a dilution ratio of 3.76. These plots present the ratio of the fluorescence signals from the measurement and calibration conditions for the same NO mole fraction. In other words, for the results calibrated at 1 atm in Fig. 6.2, the fluorescence signal from 10 ppm of NO at 6 atm would be approximately 45% of the fluorescence signal from 10 ppm of NO at 1 atm. Therefore, if one were to employ a calibration obtained at atmospheric pressure to measurements taken at 6 atm, one would
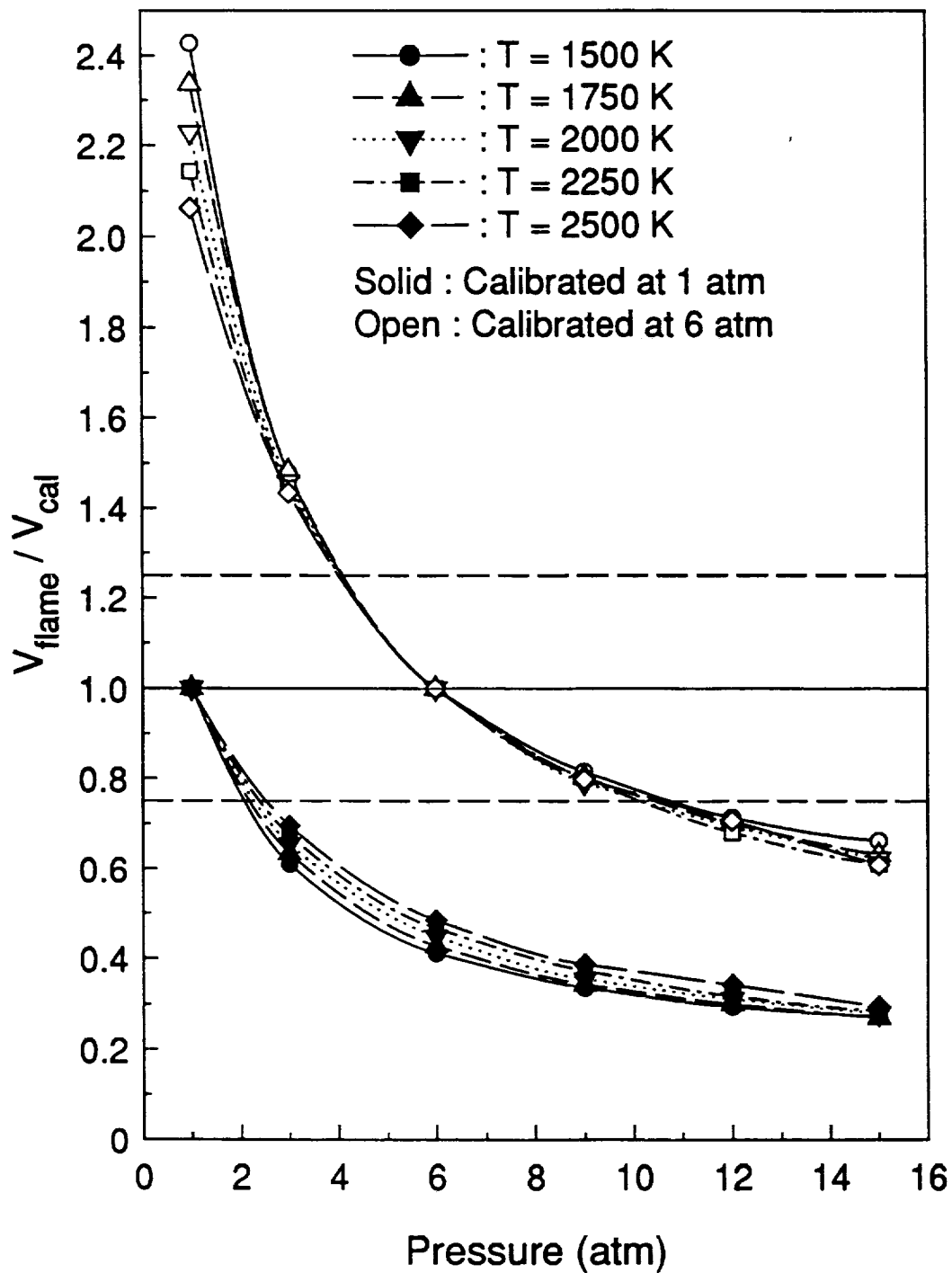
Figure 6.2: V_{flame}/V_{cal} vs. pressure for a calibration performed at a specified temperature and equivalence ratio, and applied at the same conditions at other pressures. A laser FWHM of 0.2 cm^{-1} is used, and the laser frequency is centered on the Q$_2$(26.5) line. The solid symbols represent calibration at 1 atm, and the open symbols represent calibration at 6 atm. The results apply for ψ=3.1 and ψ=3.76. (CS1, Case A)

Figure 6.3: V_{flame}/V_{cal} vs. pressure for a calibration performed at a specified temperature and equivalence ratio, and applied at the same conditions at other pressures. A laser FWHM of 0.7 cm^{-1} is used, and the laser frequency is centered on the $Q_2(26.5)$ line. The solid symbols represent calibration at 1 atm, and the open symbols represent calibration at 6 atm. The results apply for $\psi=3.1$ and $\psi=3.76$. (CS1, Case B)

conclude that an actual concentration of 10 ppm at 6 atm would only be 4.5 ppm.

On the plots, dashed lines are displayed corresponding to a range of $\pm 25\%$ from the condition corresponding to identical measurement and calibration conditions ($V_{flame} = V_{cal}$); in this study, this is the maximum acceptable variation between the calibration and the measurement. If the ratio falls within this region, the calibration is considered usable at the measurement condition. The size of this range depends on the degree of accuracy required by an individual application. In the previous case, for example, an acceptable calibration is one which would give anywhere between 12.5 and 7.5 ppm for an actual measurement of 10 ppm. This range was chosen to correspond to the calibration uncertainty in the quantitative LIF measurements of NO at high pressure in Chapters 4 and 5.

From the analysis of CS1, it appears that this calibration technique is limited in scope. Calibrating at 1 atm and applying the calibration at a higher pressure only meets the acceptability criterion of $\pm 25\%$ up to ~2.5 atm for case A. Calibrating at a high-pressure condition, such as at 6 atm, and applying the calibration factor at other pressures is more useful, although still limited. In this case, the acceptability criterion is met for a pressure range of ~4 atm to ~10.5 atm. Therefore, CS1 is useful over a wider range of pressures if calibration is performed at a higher pressure. This result is mostly due to the effects of pressure broadening on the spectrum. If the lines were dominated by pressure broadening, a doubling of the width of the spectral lines due to pressure broadening would be achieved by going from 1 to 2 atm, and also from 6 to 12 atm. Therefore, a small change in pressure at high pressure has less effect on the pressure broadening of a line than a similar change at low pressure. A second feature of CS1 is that the variation in signal is fairly independent of temperature, particularly at high pressure. This is a result of the increasing dominance of pressure broadening over Doppler broadening at high pressures. A third feature of CS1, as seen in the comparison between Figs. 6.2 and 6.3, is that the use of a larger spectral FWHM yields considerably less variation in V_{flame}/V_{cal}; with the laser

covering a larger spectral region, there is a reduced sensitivity to the decrease in centerline irradiance accompanying the broadening of a spectral line. Thus, for calibration at 6 atm, the acceptability criterion is now met for pressures between ~2.8 atm and ~16 atm.

The second calibration scheme to be investigated, CS2, involves calibrating at the same pressure as the measurements, but at a different temperature and equivalence ratio. CS2 eliminates the changes in absorption due to variations in pressure broadening, but includes changes due to the variations in number density, thermal linewidth, Boltzmann fraction, and quenching environment at a given pressure. Figure 6.4 contains plots of V_{flame} /V_{cal} vs. ϕ for two different pressures (3 and 15 atm) for Case A (spectral linewidth of Δv=0.2 cm^{-1}), with calibration performed at ϕ=0.80 and T=1500 K. Figure 6.5 contains similar plots at the same calibration conditions, but for Case B (spectral linewidth of Δv=0.7 cm^{-1}). Similar results were found when using the different dilution ratio of ψ=3.76. Calculations were also performed for calibration in the ϕ=0.80 flame at temperatures of 2000 and 2500 K, and for calibration at ϕ=0.60 and T=2000 K. All the results follow the same general trends; Figs. 6.4 and 6.5 are presented as typical plots.

A comparison of Figs. 6.4 and 6.5 shows that the effects of laser linewidth are not significant for excitation of the Q_2(26.5) rovibronic line for CS2. The calibration tends to be more transportable at lower pressures and for smaller temperature differences between the measured and calibration flames. It is usually unacceptable to directly apply the calibration found at one temperature to a measurement taken at a substantially different temperature (for example, calibrating at 1500 K and measuring at 2500 K). Even though the change due to quenching environment is relatively small, it is still best to calibrate at an equivalence ratio for which the quenching rate coefficient falls close to the average quenching rate coefficient for all the flames at a given pressure.
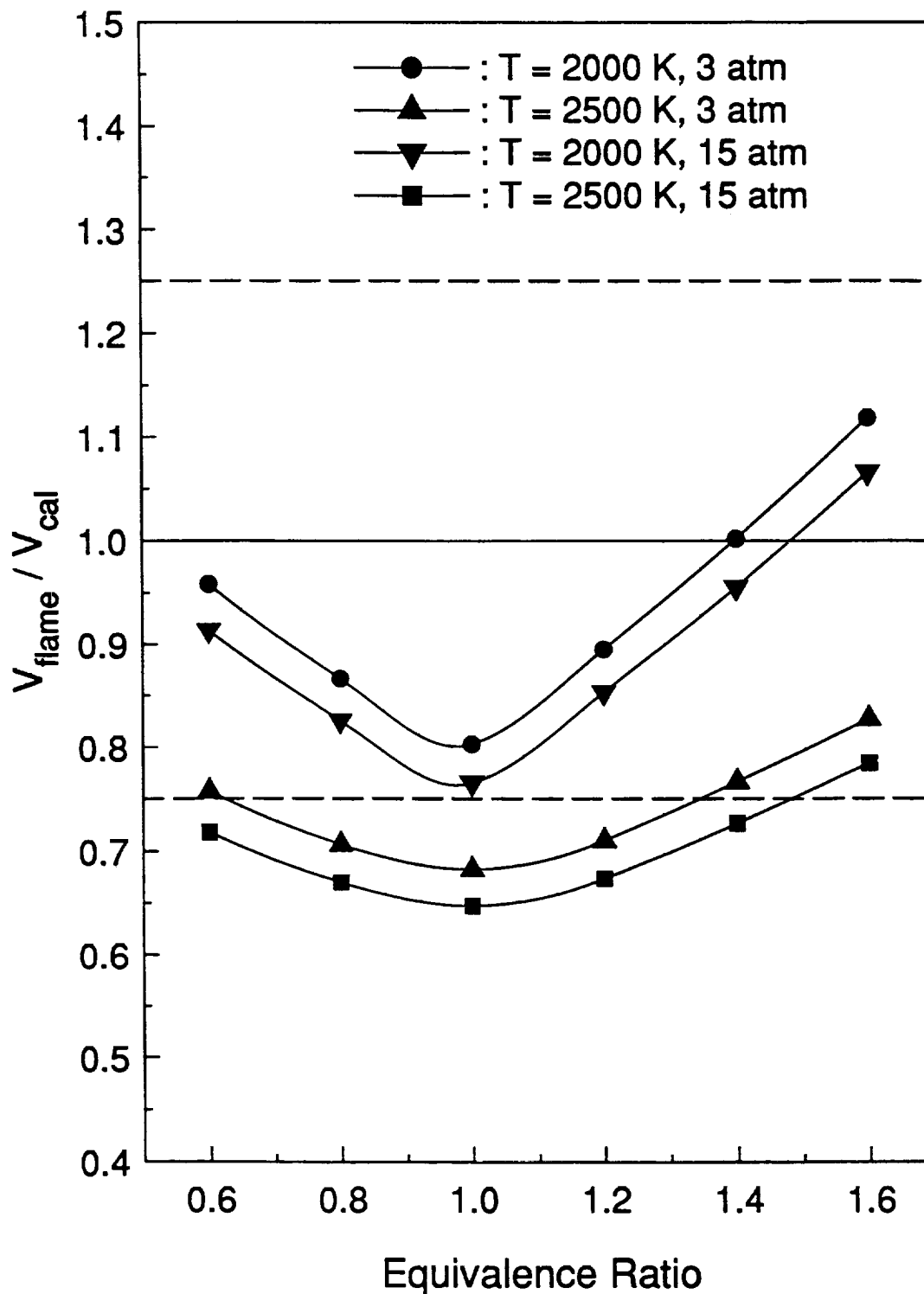
Figure 6.4: V_{flame}/V_{cal} vs. ϕ for calibration in a T=1500 K, ϕ=0.80, ψ=3.1 flame at the same pressure as the measured flames. The measured flames have different temperatures and equivalence ratios. A laser FWHM of 0.2 cm^{-1} is used, and the laser frequency is centered on the Q_2(26.5) line. (CS2, Case A)
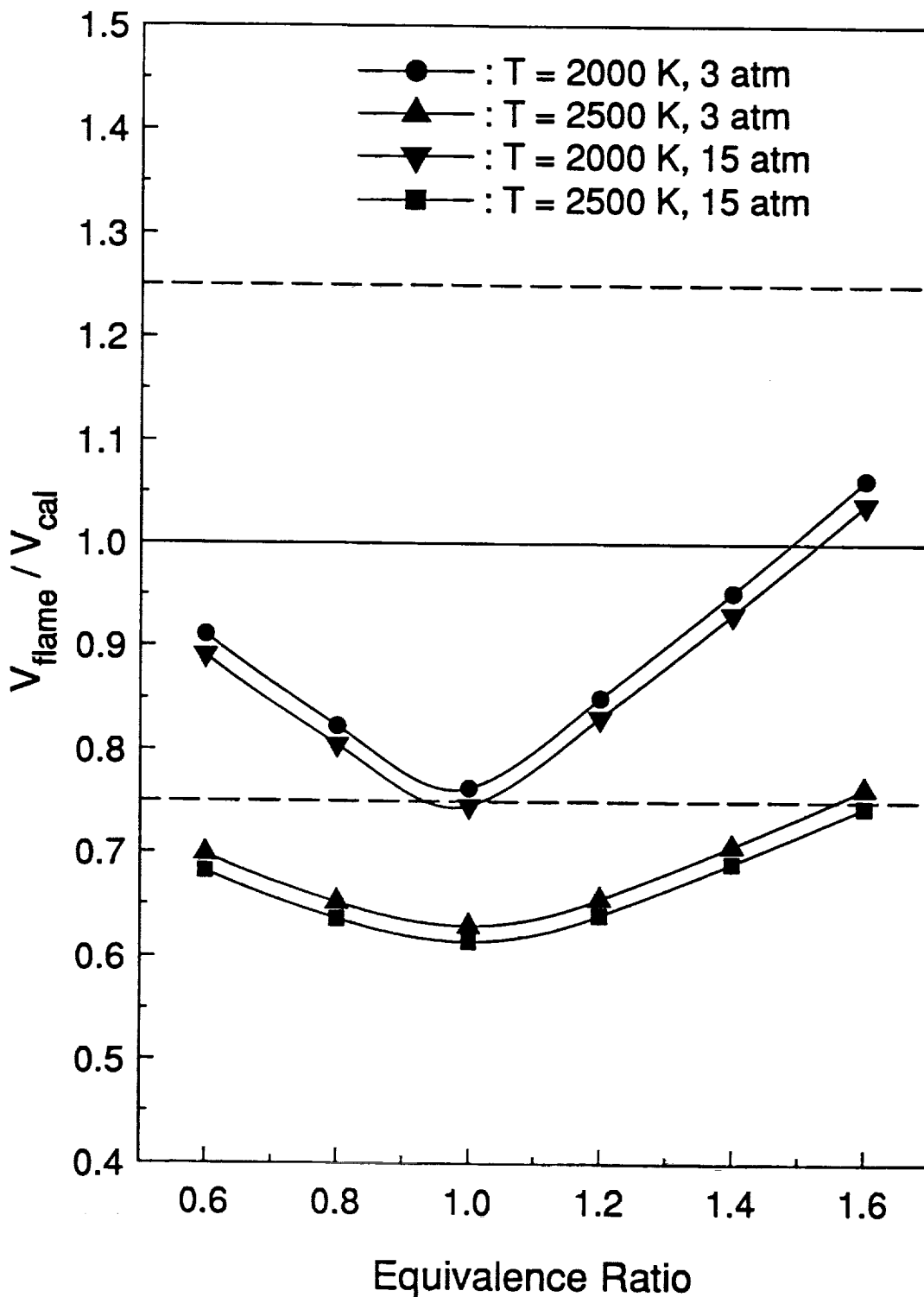
Figure 6.5: V_{flame}/V_{cal} vs. ϕ for calibration in a T=1500 K, ϕ=0.80, ψ=3.1 flame at the same pressure as the measured flames. The measured flames have different temperatures and equivalence ratios. A laser FWHM of 0.7 cm^{-1} is used, and the laser frequency is centered on the $Q_2(26.5)$ line. (CS2, Case B)

CS3 uses a calibration found at one temperature, pressure, and equivalence ratio, and applies the calibration factor to measurements taken with different sets of these parameters. For CS3, the change in fluorescence signal will result from both pressure and thermal broadening, changes in number density and Boltzmann fraction, and variations in the quenching environment. For this case, four example plots are presented: Fig. 6.6 is a plot of V_{flame}/V_{cal} vs. ϕ for Case A with calibration occurring at T=1750 K, P=1 atm, and ϕ=0.80; Fig. 6.7 is a plot of V_{flame}/V_{cal} vs. ϕ for Case B with the same calibration conditions as in Fig. 6.6; Fig. 6.8 is a plot of V_{flame}/V_{cal} vs. ϕ for Case A with calibration at T=1750 K, P=9 atm, and ϕ=0.80; Fig. 6.9 is a plot of V_{flame}/V_{cal} vs. ϕ for Case B with the same calibration conditions as in Fig. 6.8. In general, CS3 is not an acceptable calibration option. This is primarily due to the same problem as encountered with CS1; i.e., the effects of pressure broadening on absorption. The results do show some trends that could be used as possible guidelines for attempting to employ this scheme. Figs. 6.6 and 6.7 show that a calibration performed at 1 atm is usually not acceptable at higher pressures. On the other hand, Figs. 6.8 and 6.9 demonstrate that a calibration performed at high pressure is more likely to be acceptable, particularly at the larger laser linewidth. For calibration at 1 atm, typical correction factors of 0.2 to 0.8 are predicted for Case A and 0.4 to 1.0 for Case B for measurements at 3 to 15 atm. For calibration at 9 atm, typical correction factors for Case A range from 1.5 to 3.0 for measurements at 3 atm and from 0.6 to 1.3 for measurements at 15 atm. For Case B, typical correction factors range from 1.0 to 2.0 for measurements at 3 atm and from 0.6 to 1.2 for measurements at 15 atm. Thus, the closer the calibration pressure is to the measurement pressure, the more transportable the calibration. Similarly, calibration is preferable at a temperature as close as possible to the measured temperature. In addition, a larger spectral linewidth is often favorable.

At this point, it must be stressed that the above results are only theoretical calculations. If a calibration found at one condition were to be applied at a significantly different condition, one must take more than this analysis into consideration. The theoretical study makes several assumptions which may be difficult to maintain in an actual experiment, and therefore the transport of a calibration may be even more difficult. First, application of Eq. (6.6) assumes that the collection geometry and the detection efficiency are invariant. These conditions should be met when the calibration factor is determined using the same experimental apparatus as for the measurements. However, this criterion may not be met if, for example, one makes LIF measurements of NO in an IC engine, but uses a separate flat-flame burner facility for the calibration. Second, the above analysis assumes linear fluorescence behavior. It is quite easy to saturate NO at atmospheric pressure [Reisel *et al.* 1993], and some partial saturation may exist for the main absorption transitions at $P \leq 6$ atm. Laser-saturated fluorescence will lead to saturation broadening of the spectrum. This can substantially distort the spectrum, which will lead to additional excitation of neighboring lines [Carter and Laurendeau, 1994]. Therefore, the above ratios would not be applicable for saturated or partially saturated fluorescence measurements. Thirdly, the above analysis assumes that the laser is centered at the same spectral location for different conditions. In practice, this is very difficult to achieve at different pressures due to the pressure shifting of spectral lines [Chang *et al.*, 1992]; this shift requires adjustment of the laser wavelength as the pressure is varied. This adjustment makes it unlikely that the laser will be centered at precisely the same location in the spectrum at different pressures. Therefore, in summary, while the above analysis may not yield numbers that are directly applicable to an actual experiment, it does present approximate results and demonstrates pertinent trends. Furthermore, the analysis provides some guidelines as to acceptable conditions for using a particular calibration factor

Figure 6.6: V_{flame}/V_{cal} vs. ϕ for a calibration performed at a different pressure, temperature, and equivalence ratio than the measured flames. The calibration is performed at P=1 atm, T=1750 K, ϕ=0.80, and ψ=3.1. The calibration is applied at six equivalence ratios, three pressures and three temperatures. A laser FWHM of 0.2 cm^{-1} is used, and the laser frequency is centered on the $Q_2(26.5)$ line. (CS3, Case A)

● : P = 3 atm   Solid: T = 1500 K
▲ : P = 9 atm   Open: T = 2000 K
◆ : P = 15 atm   Dotted: T = 2500 K

V_{flame}/V_{cal}

1.4
1.2
1.0
0.8
0.6
0.4

0.6 0.8 1.0 1.2 1.4 1.6
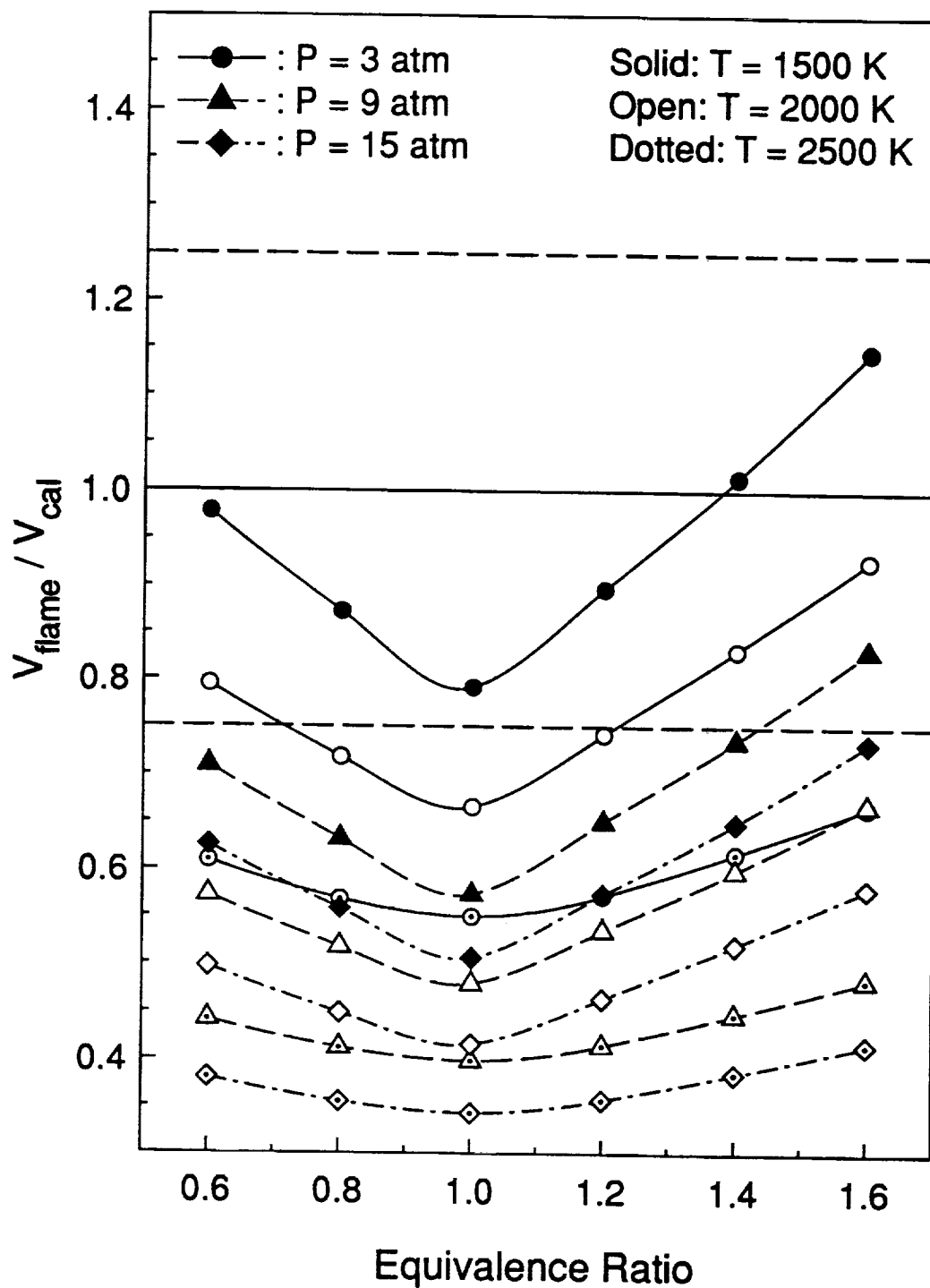
Equivalence Ratio

Figure 6.7: V_{flame}/V_{cal} vs. ϕ for a calibration performed at a different pressure, temperature, and equivalence ratio than the measured flames. The calibration is performed at P=1 atm, T=1750 K, ϕ=0.80, and ψ=3.1. The calibration is applied at six equivalence ratios, three pressures and three temperatures. A laser FWHM of 0.7 cm^{-1} is used, and the laser frequency is centered on the $Q_2(26.5)$ line. (CS3, Case B)

Figure 6.8: V_{flame}/V_{cal} vs. ϕ for a calibration performed at a different pressure, temperature, and equivalence ratio than the measured flames. The calibration is performed at P=9 atm, T=1750 K, ϕ=0.80, and ψ=3.1. The calibration is applied at six equivalence ratios, two pressures and three temperatures. A laser FWHM of 0.2 cm^{-1} is used, and the laser frequency is centered on the $Q_2(26.5)$ line. (CS3, Case A)
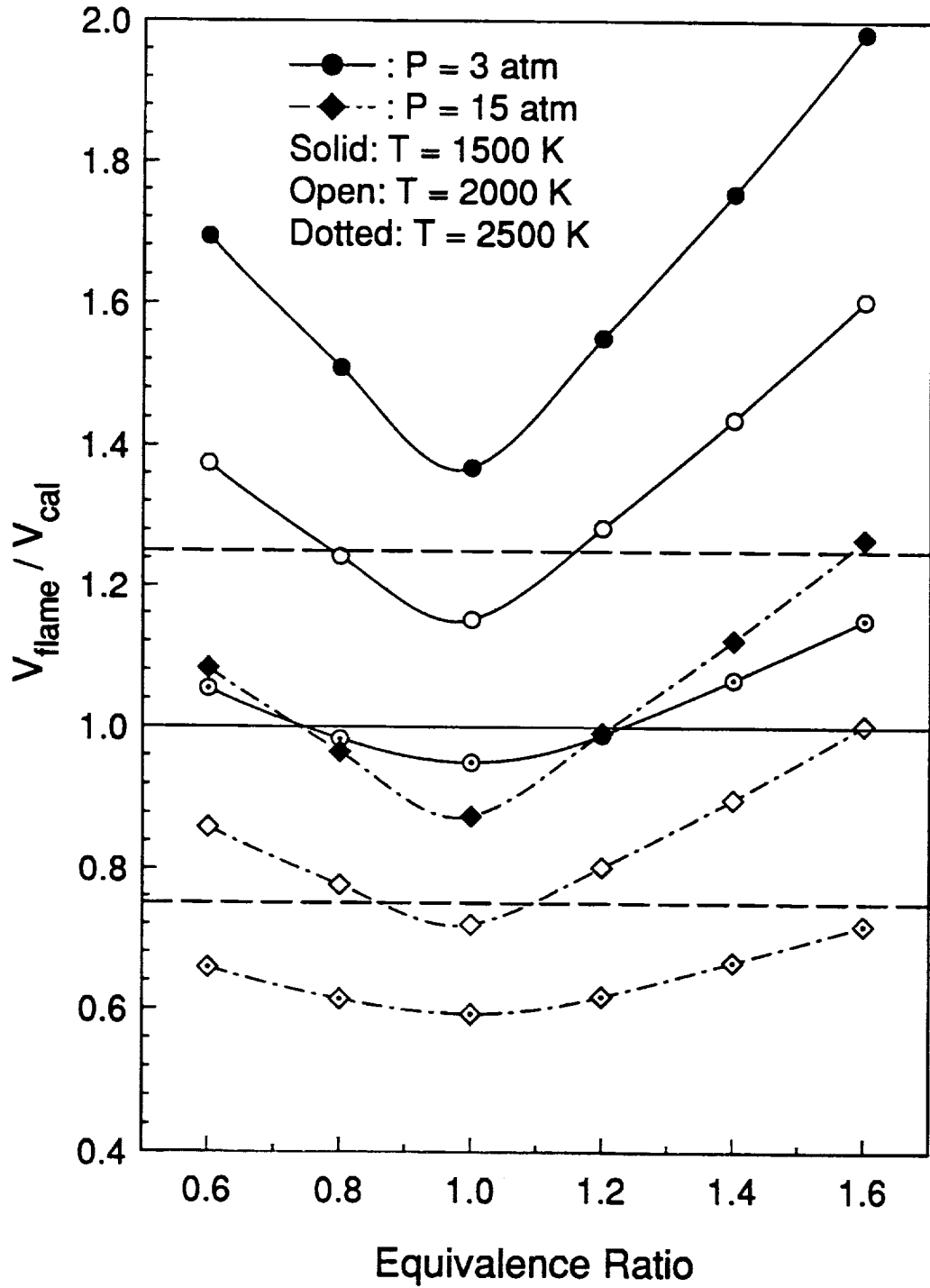
Figure 6.9: V_{flame}/V_{cal} vs. ϕ for a calibration performed at a different pressure, temperature, and equivalence ratio than the measured flames. The calibration is performed at P=9 atm, T=1750 K, ϕ=0.80, and ψ=3.1. The calibration is applied at six equivalence ratios, two pressures and three temperatures. A laser FWHM of 0.7 cm^{-1} is used, and the laser frequency is centered on the $Q_2(26.5)$ line. (CS3, Case B)

without correcting for spectral variations or changes in the quenching environment. The above analysis also provides guidelines as to what type of calibration scheme may have acceptable transportability if calibration at the measurement conditions is not possible.

Battles *et al.* [1994] employed an analysis similar to that shown above in an attempt to apply an atmospheric-pressure calibration to high-pressure flames. Their study involved only lean flames, and fewer quenching species were considered. In addition, the concentrations of the quenching species were calculated assuming complete combustion in the post-flame zone. Such assumptions can lead to some inaccuracies in the quenching rate coefficient. Battles *et al.* [1994] calculated NO spectra for different measurement conditions considering changes due to pressure and temperature effects, and used the resulting spectra to calculate appropriate changes in the overlap integral. Using the calculated overlap integral and the quenching rate coefficient, they determined how much the linear fluorescence signal should vary between the measurement conditions and the calibration condition (atmospheric-pressure flames). Inclusion of these corrections does improve the accuracy of the calibration over the scenario of making no corrections; checks of the quantitative LIF-based concentrations with a chemiluminescent analyzer measurement showed some discrepancies of 15-20%. This range of uncertainty is within the acceptability limits considered in this chapter. Therefore, Battles *et al.* [1994] have demonstrated that the transport of a calibration is possible if the appropriate corrections are properly taken into consideration. However, these corrections remain difficult to accurately compute, and the experimental difficulties associated with the application of the corrections discussed above must still be overcome.

6.5 Summary

In this chapter, the theoretical transportability of a calibration factor for a LIF signal has been investigated. NO in premixed, laminar, high-pressure $C_2H_6/O_2/N_2$ flames, with laser excitation occurring in the $\gamma(0,0)$ band, has been the focus of the investigation. An

analysis has been made of the effects of changes in temperature, pressure, and quenching environment on the fluorescence signal from possible measurement flames as compared to the fluorescence signal from an identical NO mole fraction in possible calibration flames. Three calibration schemes, considering two laser spectral linewidths and two dilution ratios, have been considered. The spectral region of NO used was that near the $Q_2(26.5)$ line of the $\gamma(0,0)$ band. Applying a calibration factor obtained at one pressure to measurements taken at another is difficult; a calibration is more transportable if one minimizes the pressure difference or calibrates at higher pressures. Calibration at both a different temperature and pressure compared to the measurements is more problematic, due primarily to the effects of pressure on the NO spectrum; again, a better chance of success occurs if one calibrates at high pressure. The use of a larger laser spectral line-width can provide significant improvement in the transportability of a calibration. Finally, there appears to be little effect of dilution ratio on the calibration transportability, provided that N_2 remains the dominant flame species.

CHAPTER 7

DETERMINATION OF TEMPERATURE BY RAYLEIGH SCATTERING

IN PREMIXED FLAT FLAMES AT ATMOSPHERIC PRESSURE

7.1 Introduction

Accurate measurement of flame temperatures is necessary for evaluating the chemical kinetics models used to predict species concentrations. Fine-wire thermocouples are generally used for flame temperature measurements; however, thermocouple measurements must be corrected for radiation losses, may suffer from catalytic effects, and may disturb the combustion process. These flaws can often lead to inaccurate temperature measurements. In addition, fine-wire thermocouples may not be able to withstand the high-temperature and high-pressure conditions present in practical combustors. Finally, thermocouples typically have an uncertainty of ±5% [Norton et al., 1993] which is larger than desired for accurate quantitative chemical kinetics comparisons.

To eliminate some of the problems associated with thermocouple measurements, it is desired to employ an optical thermometric technique. One non-intrusive technique which can be employed for temperature measurements utilizes Rayleigh scattering from gas molecules [Laurendeau, 1988]. Implementation of this method requires knowledge of the local gas composition; however, experimental determination of the gas composition (and hence the effective scattering cross-section) is often difficult in flames.

One way to avoid the effects of variable gas composition on the Rayleigh scattering signal would be to choose a flame which has a constant effective Rayleigh scattering cross-section. Dibble and Hollenbach [1981] found that premixed fuel/air flames display

only a small variation in effective scattering cross-section due to the constancy of the N_2 throughout the flame. However, this small variation must still be accounted for to obtain an accurate temperature measurement. Dibble and Hollenbach [1981] also identified a nonpremixed flame which has a constant scattering cross-section. This flame employs a fuel mixture of 38% methane and 62% hydrogen. Most nonpremixed flames do not have this fuel mixture; therefore, one must still be concerned with the effects of variable gas composition on the Rayleigh scattering signal in nonpremixed flames as well.

Rajan *et al.* [1984] used a detailed chemical kinetics model to estimate the species composition, and thus the mean scattering cross-section, as a function of the progress of the reaction in an atmospheric-pressure turbulent premixed flame. They used this information to investigate flame-turbulence interactions, as opposed to applying Rayleigh scattering to measure temperature. The temperature profile which they used for their computations was found by linearly interpolating between the known reactant and product temperatures; such a temperature profile may be very inaccurate. Stepowski and Cabot [1992] used an iterative Rayleigh scattering technique to determine temperature and mixture fraction in an atmospheric-pressure turbulent nonpremixed flame. Their iterative procedure evaluated the effective Rayleigh scattering cross-section based on a strained flame library coupled to relevant mixture fractions and temperatures.

Namer and Schefer [1985] used a simplified reaction mechanism to predict the major species concentrations in an atmospheric-pressure premixed flame. Namer and Schefer assumed that the hydrocarbon fuel was instantly oxidized to CO and H_2. Their kinetic mechanism contained 14 reactions which described the subsequent oxidation of CO and H_2; using this mechanism, the major species concentrations were calculated across the flame front. These concentrations were then used to determine effective Rayleigh scattering cross-sections from which the Rayleigh scattering signal could be corrected so as to account for variations in the gas composition. In this chapter, a similar approach is taken;

however, instead of assuming that the minor species are insignificant, the GMK-DB mechanism is used to provide a more accurate description of the flame chemistry. This should provide a more accurate representation of the flame composition, particularly through the flame front. Having calculated the gas composition, effective Rayleigh scattering cross-sections can be determined at each point in the flame. The Rayleigh scattering signal can then be corrected to give an accurate temperature measurement.

7.2 Experimental Method

The laser system and optical layout used to perform the Rayleigh scattering measurements have been described in Chapter 3; this setup was nearly identical to that which was used for the LIF measurements of NO. The primary modification from the LIF measurements is that the laser radiation was produced at a frequency of $v \approx 44355$ cm^{-1} ($\lambda \approx 225.4$ nm). This frequency was chosen to avoid nearby NO and O_2 spectral lines [Wysong *et al.*, 1989]. Other modifications include the placement of the power-monitoring photodiode, and the accompanying beam-splitter, before the burner facility. In this arrangement, the beam splitter was situated between the focussing lens and the turning mirror assembly. The pressure vessel was also removed for the atmospheric measurements presented in this chapter.

A significant source of interference for the Rayleigh scattering signal comes from background scattering off nearby surfaces such as the burner. To determine this background, the scattering signal was measured from two different gases as a function of height above the burner. The scattering was measured from helium, which has a very small differential Rayleigh scattering cross-section ($d\sigma_{He}/d\Omega = 2.8 \times 10^{-28}$ cm$^2 \cdot$sr^{-1} at $\lambda = 225.4$ nm), and then from N_2, which has a scattering cross-section ~80 times larger than that of helium ($d\sigma_{N_2}/d\Omega = 2.3 \times 10^{-26}$ cm$^2 \cdot$sr^{-1}). Using these two measurements, the scattering signal was extrapolated to zero cross-section as a function of height above the burner. The

resulting signal was deemed to be background scattering and was subtracted from the subsequent Rayleigh scattering measurements. A sample of this signal as a function of height above the burner is shown in Fig. 7.1.

As can be seen from Fig 7.1, the background signal decreases as a function of height above the burner. This result occurs because of the reduction in scattering from the burner surface with increasing distance between the collection volume and the burner. To give an idea of the relative signal sizes, the signal level in a typical post-flame measurement was 0.55-0.60 V, that for a typical room-temperature N_2 signal was ~3.2 V, and that for a typical room-temperature He signal was ~0.05 V. Therefore, in the post-flame zone, the flame measurement tended to be a factor of ~25 larger than the background measurement; however, near the burner surface, this factor was reduced to ~6.

As indicated previously, temperatures can be determined from Rayleigh scattering after correction for the local gas composition. To determine relevant species profiles, a comprehensive chemical kinetics mechanism, the GMK-DB mechanism [Drake and Blint, 1991], was employed along with the Sandia premixed one-dimensional flame code [Kee et al., 1985] and the measured temperature profile. After calculation of the species concentrations, an effective differential scattering cross-section was determined as a function of height above the burner. First, the differential scattering cross-section for each species was calculated using [Rudder and Bach, 1968]

$$\frac{d\sigma_i}{d\Omega} = \frac{4\pi^2(n_i - 1)^2}{\lambda^4 N_0^2} \cdot \frac{3}{3 - 4\rho_{v,i}} \quad .$$ (7.1)

Here, λ is the wavelength (cm), n_i is the index of refraction of the gas (determined from the correlations provided by Gardiner et al. [1981]) , N_0 is the number density (cm^{-3}) at standard temperature and pressure (0°C, 760 torr), and $\rho_{v,i}$ is the depolarization ratio which we assume in our calculations to be negligible. The effective differential cross-section of the gas can then be calculated from
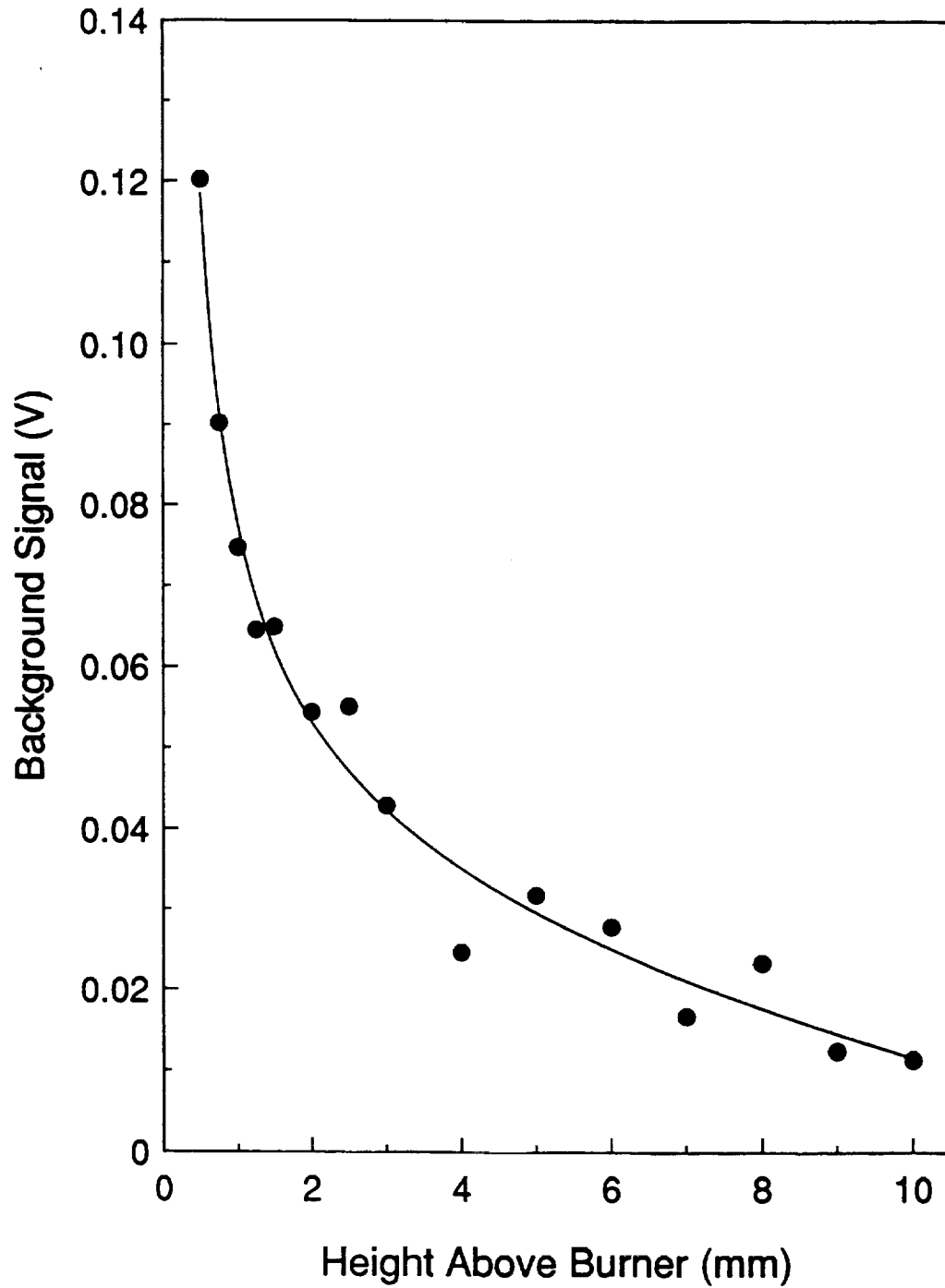
Figure 7.1:   Typical background scattering signal for the Rayleigh scattering measurements at atmospheric pressure.

$$\frac{d\sigma_{eff}}{d\Omega} = \sum_i X_i \frac{d\sigma_i}{d\Omega} \quad , \tag{7.2}$$

where X_i is the mole fraction of species i. For the ideal situation of polarization and scattering angles of 90°, the Rayleigh scattering signal is given by [Laurendeau, 1988]

$$S = \beta\Omega_c V_c \frac{P}{kT} I_L \frac{d\sigma_{eff}}{d\Omega} \quad , \tag{7.3}$$

where S is the measured Rayleigh scattering signal (W), β is the detection efficiency, Ω_c is the solid angle of the collection optics (sr), V_c is the collection volume (cm^3), P is the pressure, k is the Boltzmann constant, and I is the laser irradiance (W/cm^2). Based on Eq. (7.3), the temperature at a given pressure was determined using the effective differential cross-section from Eq. (7.2) and a ratio of the Rayleigh scattering signal from the flame and a calibration signal [Laurendeau, 1988]:

$$T_f = T_{cal} \frac{S_{cal} I_f (d\sigma_{eff}/d\Omega)}{S_f I_{cal} (d\sigma_{cal}/d\Omega)} \quad , \tag{7.4}$$

where T_f is the flame temperature and T_{cal} is the calibration temperature. The calibration gas was room-temperature N_2 at 1 atm. The corrected temperature profile from Eq. (7.4) was then used as a new input temperature for the flame code, and the kinetics were re-solved for new species concentrations. This process was continued until a converged solution was obtained.

Two different schemes can be used for obtaining the first solution from the kinetics model. In this chapter, the first correction for gas composition was made by employing the solution of the coupled species-energy equations. Alternatively, in situations for which the energy equation does not give a particularly accurate temperature profile, the initial temperature profile used in the solution procedure can be that obtained from the Rayleigh scattering measurements, but uncorrected for species composition. However,

the latter will tend to increase the number of iterations needed for convergence, as the first guess for the gas composition will be calculated at a significantly different temperature profile than that for the final temperature.

Typical variations of the effective differential scattering cross-section through a flame are presented in Fig. 7.2. Figure 7.2 contains the calculated differential scattering cross-section for three atmospheric-pressure flames; the species concentrations were found using the solution of the coupled species-energy equations. As can be seen, there can be a significant variation in scattering cross-section for a premixed flame, particularly through the flame front; in the post-flame zone, the scattering cross-section is nearly constant. Therefore, corrections accounting for variable gas composition may not be necessary at each point in the post-flame zone if a calibration gas with a similar scattering cross-section is used; however, the effective scattering cross-section varies enough in the flame front to warrant this consideration.

7.3 Results and Discussion

The results of the Rayleigh scattering measurements for three flat, laminar, atmospheric-pressure, $C_2H_6/O_2/N_2$ flames (total flow rate=3.5 slpm, $\dot{V}_{N_2}/\dot{V}_{O_2}$=3.1) are presented in Figs. 7.3 - 7.5. The equivalence ratios of these flames were ϕ=0.8 (Fig. 7.3), ϕ=1.0 (Fig. 7.4), and ϕ=1.3 (Fig. 7.5). In addition, radiation-corrected, uncoated Pt-Pt /10%Rh thermocouple measurements are provided for comparative purposes. The radiation corrections for the thermocouple measurements were performed using the corrections of Bradley and Matthews [1968]. The Rayleigh scattering data represent the average of two separate measurements at each spatial location. This averaging procedure was employed to obtain a better curve fit; the resulting smooth temperature profile was used as the input into the flame code. In each case, the data are fit to a function of the form

$$T(y) = P_{-1}y^{-1} + P_0 + P_1 y + P_2 y^2 + P_3 y^3 \quad . \tag{7.5}$$
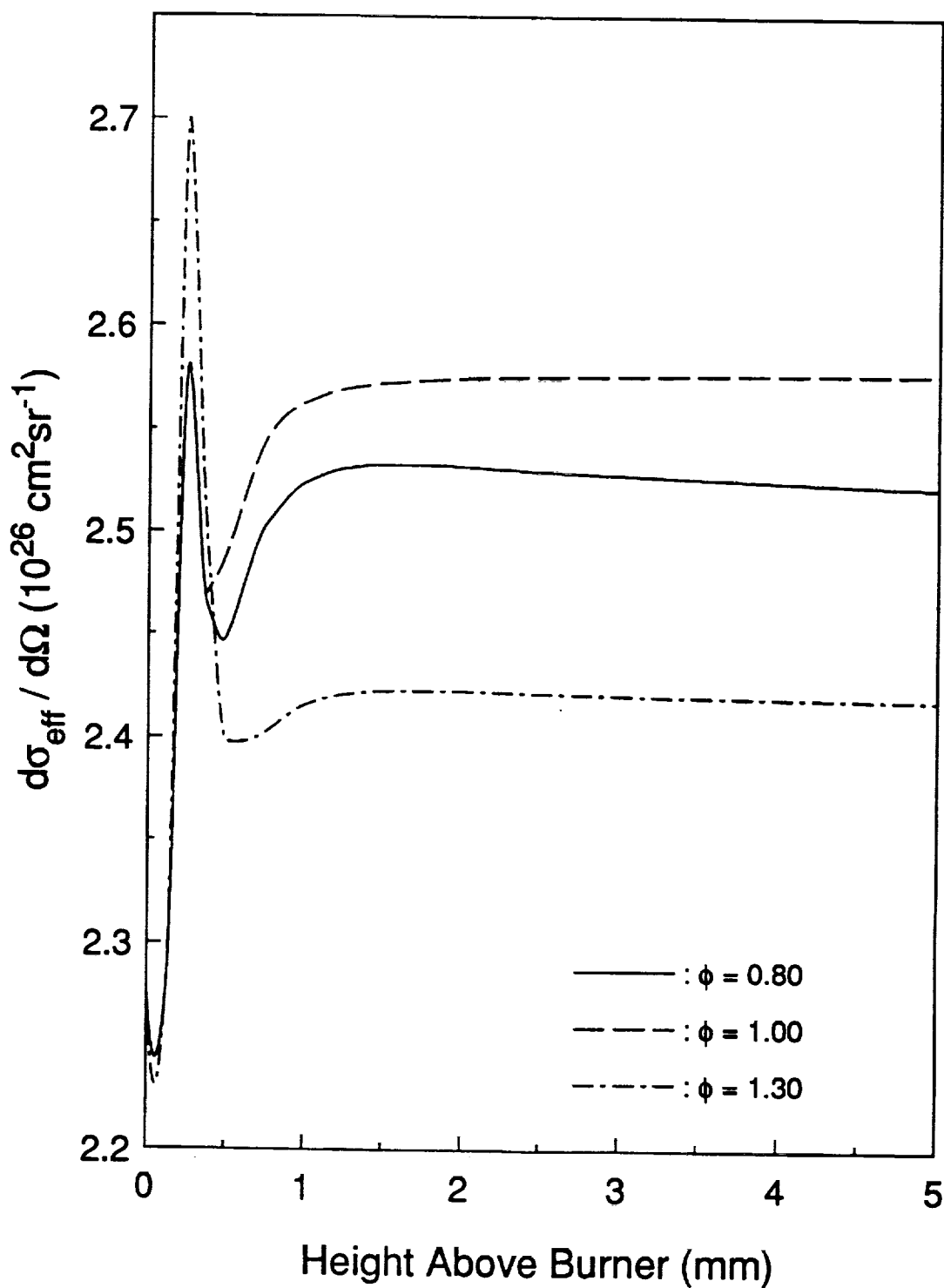
Figure 7.2:   The calculated effective differential Rayleigh scattering cross-section for three flames at atmospheric pressure. The gas composition was determined by the solution of the coupled species-energy equations.
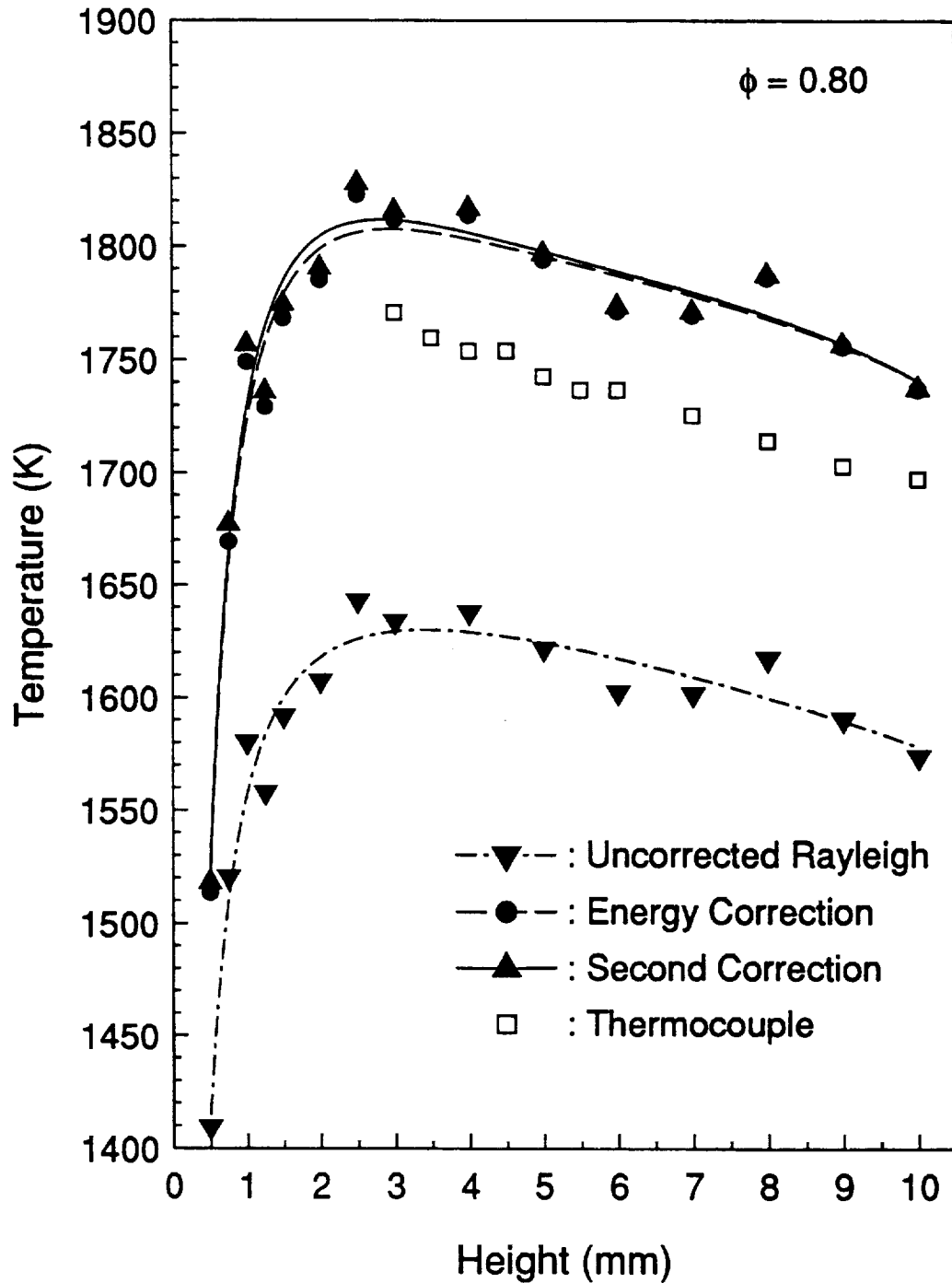
Figure 7.3:   Progression of Rayleigh scattering temperature-measurement solutions showing successive iterations in an atmospheric-pressure C_2H_6 /O_2 /N_2 flame at ϕ=0.80. The polynomial curve fits are also shown. Thermocouple measurements are presented for comparison. The uncertainty in both measurements is ±5%.
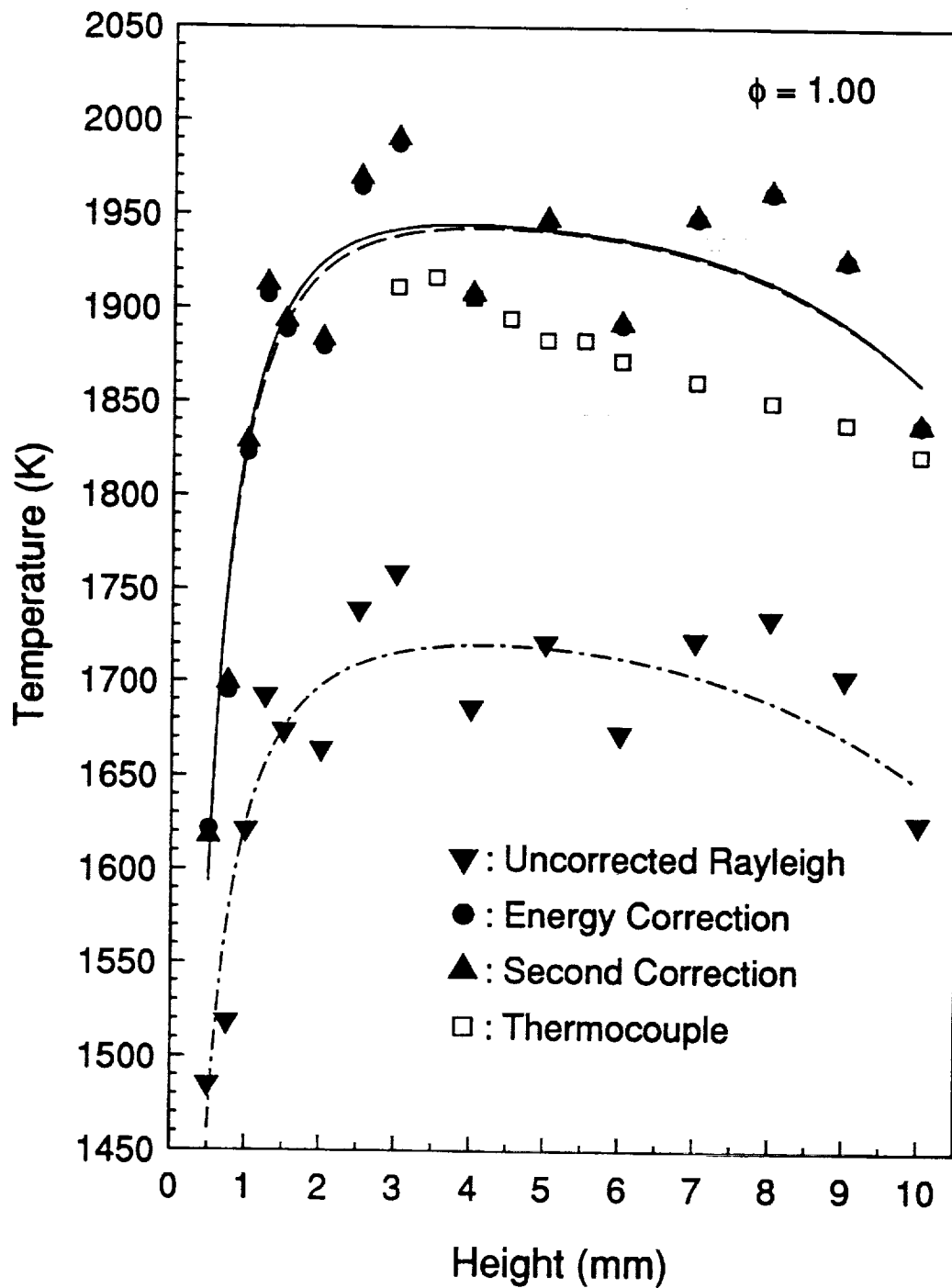
Figure 7.4: Progression of Rayleigh scattering temperature-measurement solutions showing successive iterations in an atmospheric-pressure C_2H_6 /O_2 /N_2 flame at ϕ=1.0. The polynomial curve fits are also shown. Thermocouple measurements are presented for comparison. The uncertainty in both measurements is $\pm5\%$.
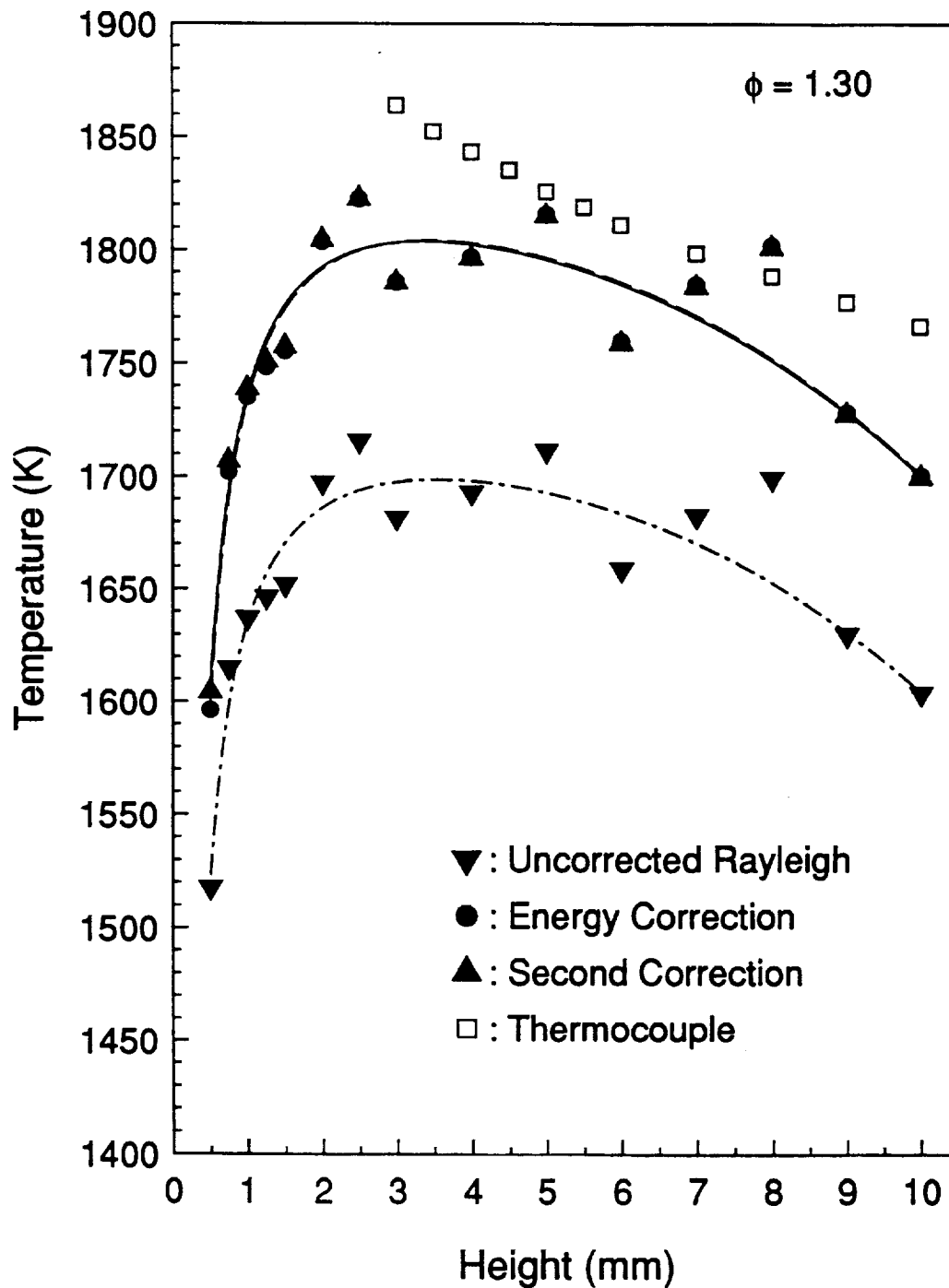
Figure 7.5: Progression of Rayleigh scattering temperature-measurement solutions showing successive iterations in an atmospheric-pressure C_2H_6 /O_2 /N_2 flame at ϕ=1.30. The polynomial curve fits are also shown. Thermocouple measurements are presented for comparison. The uncertainty in both measurements is ±5%.

Figures 7.3 - 7.5 show the Rayleigh scattering data uncorrected for gas composition ($\sigma_{eff} = \sigma_{cal}$), as well as the data corrected with the effective cross-sections found from the coupled species-energy solution. This first corrected temperature profile was then input into the flame code, and the species concentrations were recalculated using a fixed temperature solution. The second correction is obtained using the effective cross-sections found from this solution. In each case, the solution has reached approximate convergence, and further iterations are not necessary.

The results for the ϕ=0.80 and ϕ=1.00 flames show that the temperature measured with Rayleigh scattering is higher than that measured with the thermocouple, while the opposite is true for the ϕ=1.30 flame. The number of flames considered makes it difficult to determine if rich flames would always display a lower temperature from the Rayleigh scattering technique than from the thermocouple measurements. However, even if this is a trend, it does not appear to be significant over this range of equivalence ratios, owing to the good agreement between the two techniques.

A propagation of errors analysis produced an uncertainty (95% confidence level) in the Rayleigh scattering measurements of ±5% (Appendix C). The uncertainty in the thermocouple measurements is also estimated at ±5%. The two measurement techniques typically differ by approximately 50 K, which is within the range of uncertainty. The curve fit used for the input flame code temperature also falls within the uncertainty of the individual Rayleigh scattering measurements. As mentioned previously, it would be desirable to have a temperature measurement with a lower uncertainty for high-temperature chemical kinetics studies.

While these measurements of flame temperature appear to be accurate and consistent, there are several potential changes to the experimental technique which could improve the results. First, calibration at a temperature higher than room temperature should lead to more accurate results. The density ratio between the flame gases (at ~1800

K) and the current room-temperature calibration is a factor of six. If a calibration gas temperature of 600 K were used, this factor would drop to three. The corresponding ratio in Rayleigh scattering signal would also decrease from six to three. Due to the large Rayleigh scattering that occurs in the ultraviolet, neutral density filters are required to reduce the Rayleigh scattering signal such that it remains within the linear range of the photomultiplier tube. It is highly desirable to maintain the same combination of filters for an entire set of measurements; this eliminates any uncertainty in the attenuation of different sets of neutral density filters. Unfortunately, if the calibration gas measurements and the flame gas measurements are performed with the same set of filters, the flame gas measurements become over-attenuated. The flame measurements are then more susceptible to errors in the background signal and to system noise. By calibrating at a higher temperature, a smaller amount of signal attenuation would be required for the calibration gas resulting in a substantial increase in the signal level for the flame measurements.

A second improvement would be to calibrate with a cold gas mixture corresponding to the flame reactants. Such a calibration should reduce the variation in scattering cross-section between the calibration gas and the flame gas. However, the benefits of this change in premixed flames, for which the reactants and products are mostly N_2, are somewhat limited. It may also be better to use experimentally measured Rayleigh scattering cross-sections instead of calculated values. This would account for any depolarization of the laser beam and would eliminate errors associated with the curve fit for calculated scattering coefficients. Finally, one must also be careful to avoid fluorescence signals in the ultraviolet. This could be a problem with NO and O_2 in lean flames, and could also be a problem with large hydrocarbons in very rich flames.

7.4 Summary

Temperature measurements using an iterative Rayleigh scattering temperature measurement technique have been presented. This technique is similar to that of Namer

and Schefer [1985] but makes use of a more comprehensive chemical kinetics model and an iteration procedure to calculate the species concentrations in flat, premixed flames. These calculated species concentrations are used to determine the effective Rayleigh scattering cross-section, which is then used to correct the Rayleigh scattering measurements. The technique is shown to work at atmospheric pressure, and should be especially useful for temperature measurements in high-pressure flames, as the Rayleigh scattering signal scales linearly with total number density [Laurendeau, 1988].

CHAPTER 8

QUANTITATIVE MEASUREMENTS OF NITRIC OXIDE IN

LAMINAR, HIGH-TEMPERATURE $C_2H_6/O_2/N_2$ FLAMES

8.1 Introduction

Current environmental concerns mandate the reduction of nitric oxide from combustion applications such as gas-turbine engines. To achieve this goal, an understanding is required of the formation mechanisms of NO. This, in turn, requires the ability to perform accurate quantitative *in situ* measurements of the concentrations of various flame species, including NO. Accurate concentration measurements will allow for the refinement of current chemical kinetics models, which can then be used to design future combustion schemes and equipment.

Quantitative measurements of NO concentration can be obtained using both physical techniques, such as probe-sampling [Heberling, 1977; Leonard and Correa, 1990; Drake *et al.*, 1991] and optical techniques, such as laser-induced fluorescence (LIF) [Morley, 1981, 1982; Chou *et al.*, 1983; Cattolica *et al.*, 1989; Heard *et al.*, 1992; Reisel *et al.*, 1993]. Probe-sampling combined with chemiluminescent detection is advantageous since it possesses a lower detection limit, is easier to use, and is less expensive than laser-based methods. However, a physical probe can disrupt the flow field, potentially altering the concentrations of radical species; moreover, such probes may not be able to withstand the harsh conditions of practical combustion environments [Miller and Fisk, 1987]. These disadvantages can be overcome by employing optical techniques. Optical procedures allow for remote sensing of numerous species in a variety of environments. Unlike sam-

pling probes, optical methods generally do not alter the combustion process; in addition, many combustors are more readily adaptable to optical access than to physical sampling probes. Finally, precise spatial resolution is achievable through the use of optical methods.

Previously, the feasibility of making quantitative LIF measurements of NO has been demonstrated in laminar, low-temperature ($1600 \leq T \leq 1850K$), $C_2H_6/O_2/N_2$ flames up to 14.6 atm (Chapter 4). In these flames, most of the NO is formed in the flame front, producing flat profiles of NO in the burnt-gas region. In this chapter, this work is extended by presenting LIF measurements of NO in lean, laminar, high-temperature ($2100 \leq T_{max} \leq 2300$ K), $C_2H_6/O_2/N_2$ flames at equivalence ratios of 0.7 to 0.95 and pressures of 1.0 and 3.05 atm. The flames studied exhibit a steady rise in NO concentration with increasing height above the burner, indicating that significant thermal-NO production occurs in the burnt-gas region. To evaluate the predictive capability of current chemical kinetics models with respect to the NO production in these flames, the flames are also modeled using the reaction mechanism of Glarborg et al. [1986], as modified by Drake and Blint [1991] (GMK-DB).

8.2 Experimental Techniques

The laser system and optical layout used to perform the LIF measurements of NO are described in Chapter 3. The burner used for the measurements was a 1.3x1.3 cm premixed Hencken burner, which consists of densely packed, 0.5-mm diameter, stainless steel tubes. The burner was located inside the high-pressure combustion facility described by Carter et al. [1989]. The $Q_2(26.5)$ line of NO was used for absorption, and the fluorescence was detected from the $\gamma(0,1)$ band. The image of the entrance slit over the burner was 80 μm $\times$ 6.7 mm. Each data point was averaged over 600 laser shots.

As discussed in Chapter 4, the effects of fluorescence quenching and fluctuating laser power can affect a LIF measurement. In this chapter, broadband laser-saturated fluorescence (LSF) [Reisel et al., 1993] is used to attempt to overcome these effects. However, while the measurements were well saturated at 1 atm [Reisel et al., 1993], only weak saturation existed at 3.05 atm (Chapter 4). For the measurements at 3.05 atm, non-linear corrections were made for laser power variations. In addition, we assumed that fluorescence quenching does not vary significantly over the range of our measurements, either within or among the flames, at a given pressure. This assumption was confirmed at atmospheric pressure by measuring profiles of [NO] using both saturated and linear fluorescence, and demonstrating good agreement between the two techniques. Figure 8.1 shows the normalized fluorescence data in two atmospheric-pressure flames taken with both LIF and LSF. The laser energy over the burner was ~30 μJ/pulse for the LIF measurements and ~2 mJ/pulse for the LSF measurements.

Post-flame temperatures were measured using a Rayleigh scattering technique similar to that of Namer and Schefer [1985] as described in Chapter 7. For this technique, measurements of the Rayleigh scattering at 225.4 nm were taken as a function of height above the burner. To correct for the change in effective Rayleigh scattering cross-section which results from variable gas composition, the Sandia flame code [Kee et al., 1985] was used to calculate the mole fractions of each species corresponding to each experimental location. The Rayleigh scattering cross-section for each gaseous component was calculated at 226 nm via the correlations of Gardiner et al. [1981]. Effective Rayleigh scattering cross-sections were next determined as a function of height above the burner. These were then used to evaluate flame temperatures by correcting for the differences in scattering cross-sections for the flames as compared to the calibration gas (pure N_2 at room temperature).
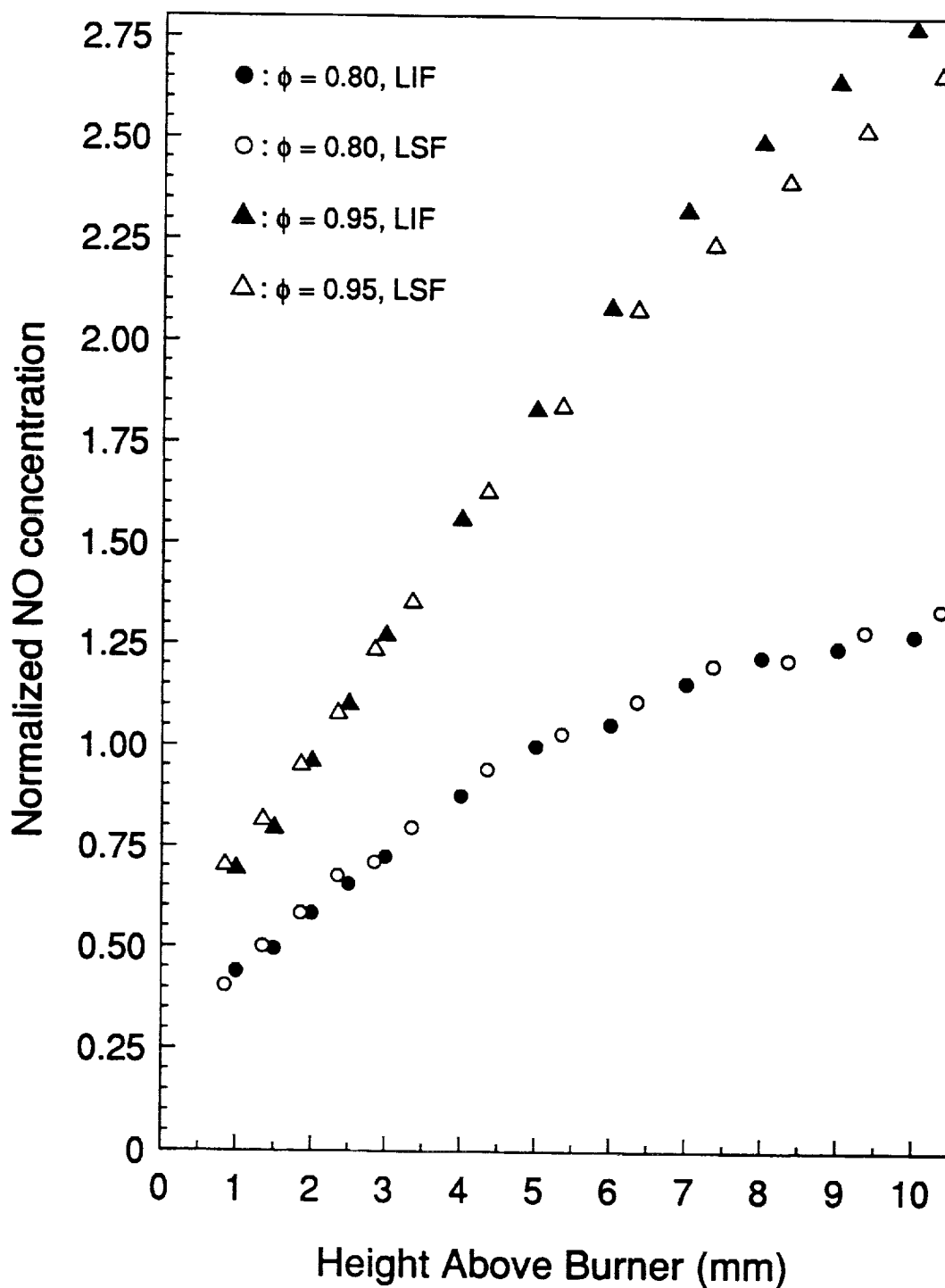
Figure 8.1: Relative measured [NO] in two atmospheric-pressure flames. The measurements were performed using both LIF and LSF, and the good agreement between the two suggests that there is little change in the quenching environment for these two flames.

The same experimental apparatus was used for the Rayleigh scattering measurements as for the LIF measurements, with the following modifications. The power monitoring photodiode was moved to a location before the pressure vessel. The image of the entrance slit was reduced to 67μm x 1.3 mm to reduce background scattering. The excitation frequency was changed to $v \approx 44355$ cm^{-1}; at this frequency no significant interference occurs owing to fluorescence originating from NO or O_2. The monochromator was tuned for maximum detection of the Rayleigh scattering signal at $\lambda \approx 225.4$ nm. Finally, the Rayleigh scattering signal was processed with a Stanford Research System SR250 boxcar averager and gated integrator, using a 6-ns temporal gate width.

8.3 Modeling

NO is produced through three main reaction mechanisms [Drake and Blint, 1991]: (1) the Zeldovich, or thermal-NO, mechanism [Zeldovich, 1946], (2) the N_2O-intermediate mechanism [Wolfrum, 1972; Malte and Pratt, 1974], and (3) the prompt-NO mechanism [Fenimore, 1971]. The details of these paths can be found in Chapter 2. The amount of NO formed through each of these mechanisms depends on the temperature, pressure, and equivalence ratio of the flame. However, the only path producing substantial amounts of post-flame NO is the Zeldovich mechanism. This path is highly temperature dependent, producing only small amounts of NO at temperatures less than 1900 K. In the post-flame zone, the rate of NO production depends directly on the temperature: the higher the temperature, the greater the rate of NO production.

The experimental flames in this study were investigated through computer modeling. The modeling of the chemical kinetics was performed using the Sandia steady, laminar, one-dimensional, premixed flame code [Kee et al., 1985]. The details of the modeling can be found in Chapter 3.

The reaction mechanism used as input to the computer model was assembled by Glarborg *et al.* [1986] and modified by Drake and Blint [1991]. This reaction mechanism consists of 49 species and over 200 reactions. Drake and Blint adopted most of the reaction mechanism from Glarborg *et al.*; however, they made a few modifications. These included the introduction of pressure dependency into four unimolecular reactions, the addition of a C_3H_8 reaction mechanism, and the introduction of rate parameters for the reaction $CH + N_2 \leftrightarrow HCN + N$ based on measurements in a high-temperature shock tube [Dean *et al.*, 1988]. The rate parameters for the unimolecular reactions at 3.05 atm are given by Drake *et al.* [1991] and in Chapter 3.

Obtaining a temperature profile by Rayleigh scattering near the burner surface was difficult because of the large background scattering. Therefore, the energy equation was solved to obtain a temperature profile for the kinetics modeling. A temperature profile was also derived which represented the energy solution adjusted by the difference between the energy solution temperature and the average of the temperature measurements in the post-flame zone. Hence, [NO] profiles were calculated using two temperature profiles for each flame: (1) that from the energy solution; and (2) that from the energy solution scaled to the average measured post-flame temperature (the "measured" profile). A burner surface temperature of 300 K was used as a boundary condition. Since the burner is uncooled, this surface temperature may be too low. Consequently, a sample test case was run for the ϕ=0.95 flame at 1 atm by employing a burner surface temperature of 1000 K. The results for these two boundary conditions were similar, suggesting that the choice of the initial temperature for the reactants does not significantly affect the chemical kinetics calculations for these flames. This result is shown in Fig. 8.2, which shows the calculated temperature and [NO] profiles for the ϕ=0.95 flame solved with inlet temperatures of 300 K and 1000 K.
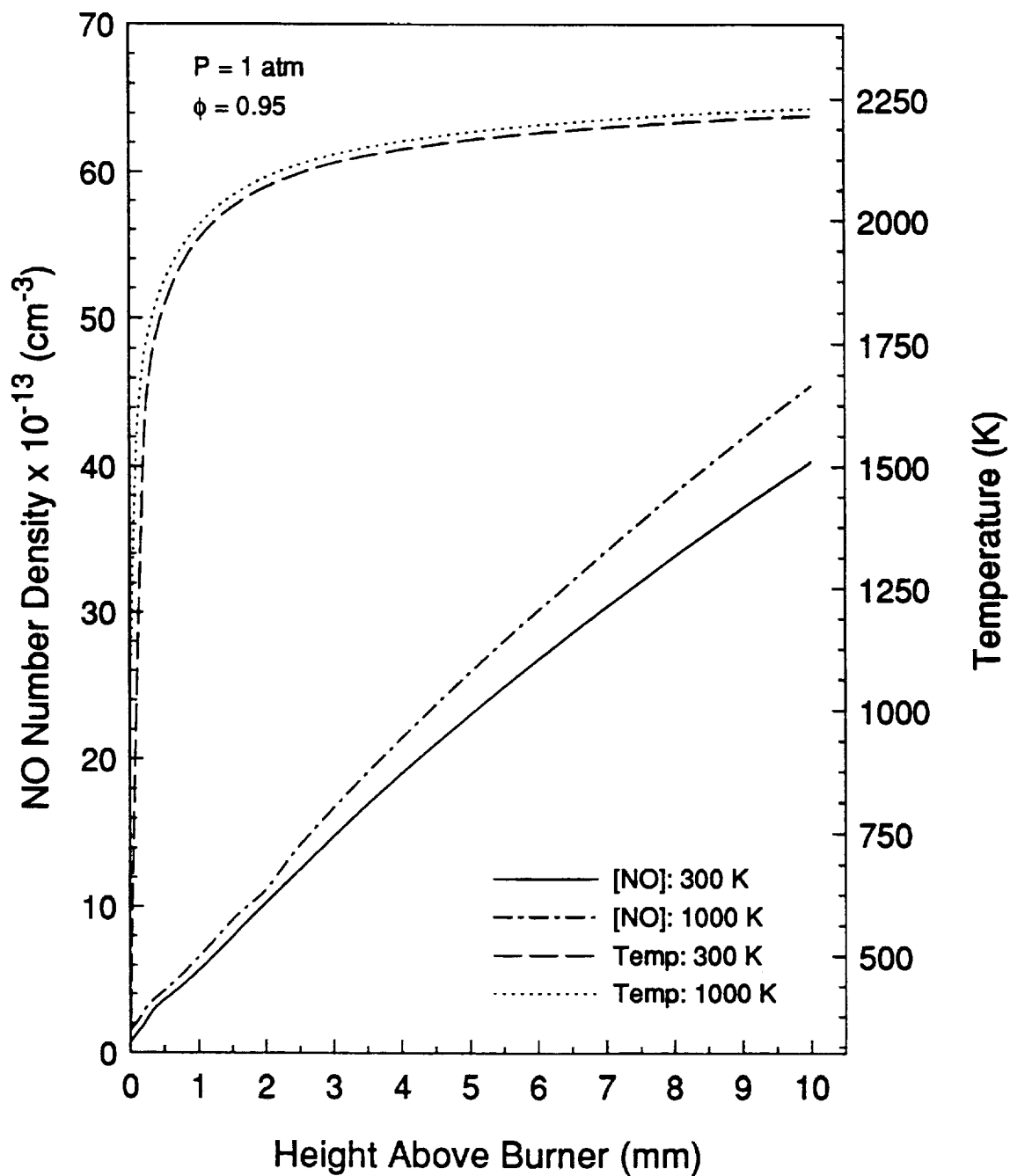
Figure 8.2:   Calculated temperature and [NO] profiles for the φ=0.95, P=1 atm flame. Two different boundary temperatures were used: 300 K and 1000 K.

8.4 Results and Discussion

Using the experimental apparatus described above, quantitative LIF measurements of NO were performed in lean, laminar, $C_2H_6/O_2/N_2$ flames at pressures of 1.0 and 3.05 atm. The post-flame temperatures of these flames, as measured using Rayleigh scattering, ranged from 2100 to 2300 K. The precision of the temperature measurements at the 95% confidence level, as determined by a propagation of errors analysis, was ~5% (Appendix C). All of the flames had a dilution ratio ($\dot{V}_{N_2}/\dot{V}_{O_2}$) of 2.8. The total flow rates were 3.5 slpm for the atmospheric-pressure flames and 9.0 slpm for the flames at 3.05 atm. The equivalence ratios and pressures of the five flames of this study are listed in Table 8.1.

As indicated above, comparisons between linear and saturated fluorescence at atmospheric pressure demonstrated good agreement between the two techniques. This indicates that the NO fluorescence quenching environment, both in a flame and between flames, is essentially constant for the range of experimental conditions at a given pressure. On this basis, the fluorescence signals at a given pressure were calibrated using the following procedure. Measurements of the fluorescence voltage from the burnt-gas region of a lean flame were obtained for three different levels of doped NO. It is assumed that the doped NO does not react through the flame, and that the amount of NO found in this flame is small compared to the amount of doped NO. The former assumption is supported by computer modeling, which indicates that the burnt-gas NO concentration is equal to the doped NO concentration to within 5% for these lean flames. Calibration was performed 5 mm above the burner surface in the ϕ=0.80 flame at 1 atm (flame A) and in the ϕ=0.75 flame at 3.05 atm (flame D). At a given pressure, the ratio of fluorescence signals for any two flames, or any two points in a flame, represents the ratio of NO number densities.

The data from the three doping conditions, when plotted as fluorescence signal vs. doped [NO], form a straight line. The slope of this line was used to obtain a fluorescence

Table 8.1:   Experimental conditions and temperatures for the flames of this study. The energy solution temperature at 7 mm above the burner, the average measured post-flame temperature, and the temperature calculated with Eq.(8.1) at 7 mm above the burner are tabulated.

Flame	ϕ	P (atm)	Energy (K)	Measured (K)	Calculated (K)
A	0.80	1.00	2115	2135	2140
B	0.95	1.00	2190	2270	2260
C	0.70	3.05	2085	2100	2080
D	0.75	3.05	2120	2185	2150
E	0.82	3.05	2175	2290	2220

voltage calibration, which was then applied to the fluorescence signal measured in the undoped calibration flame. The observed linear relationship further indicates that the NO undergoes little reaction in this flame. NO concentrations in the other flames at the same pressure were determined from the measured fluorescence signal using the NO concentration vs. signal voltage calibration determined in the calibration flame. With the nearly constant quenching environment, corrections for any variation in quenching between flames was deemed unnecessary.

By calibrating at each pressure, no corrections are required for both changes in the quenching environment (due to pressure changes) and changes in the optical alignment which results from maximizing the NO fluorescence signal at each pressure. This calibration procedure also does not require corrections originating from changes in the spectral linewidth due to pressure broadening, variations in spectral line overlap with pressure,

and changes in rotational energy transfer with pressure.

Figures 8.3 - 8.7 show profiles of the NO concentration as a function of height above the burner for five lean, premixed $C_2H_6 / O_2 / N_2$ flames. Each figure also contains the predicted [NO] profiles from the solution of the energy equation (solid line) and from the measured temperature profile (dot-dashed line). The temperature profile from the energy solution is also shown. The post-flame temperatures as determined by the energy solution and by the average post-flame measured temperatures are listed in Table 8.1. Note that the energy solution temperatures are within the uncertainty of the measured temperatures except for flame E, for which the difference is just larger than the uncertainty. As can be seen for these five lean flames, the [NO] increases steadily as a function of height above the burner. This behavior is consistent with the Zeldovich mechanism for NO production in high-temperature lean flames. The precision of the NO measurements (95% confidence interval) is better than ±7% (due to statistical uncertainty); the accuracy of the measurements is estimated at ±25%, due primarily to calibration considerations (Appendix C).

For the atmospheric-pressure flames (Figs. 8.3-8.4), the energy solution provides a fairly accurate prediction; the [NO] is underpredicted slightly, but the rates of NO production (as indicated by the slopes) for the predictions and measurements are quite close. The underprediction of [NO] arises mostly from the chemical kinetics in the flame front. When using the measured post-flame temperature, the predicted and measured NO profiles for flame A are in reasonable agreement both quantitatively and qualitatively, particularly within 7 mm of the burner surface. The results for flame B are not as good, with the predictions indicating a significantly higher rate of NO production; this disagreement suggests that the measured temperatures are too high. However, as mentioned previously, the uncertainty in the temperature measurements is large enough to include the energy solution temperatures for these flames. For both flames, the measured rates of NO pro-
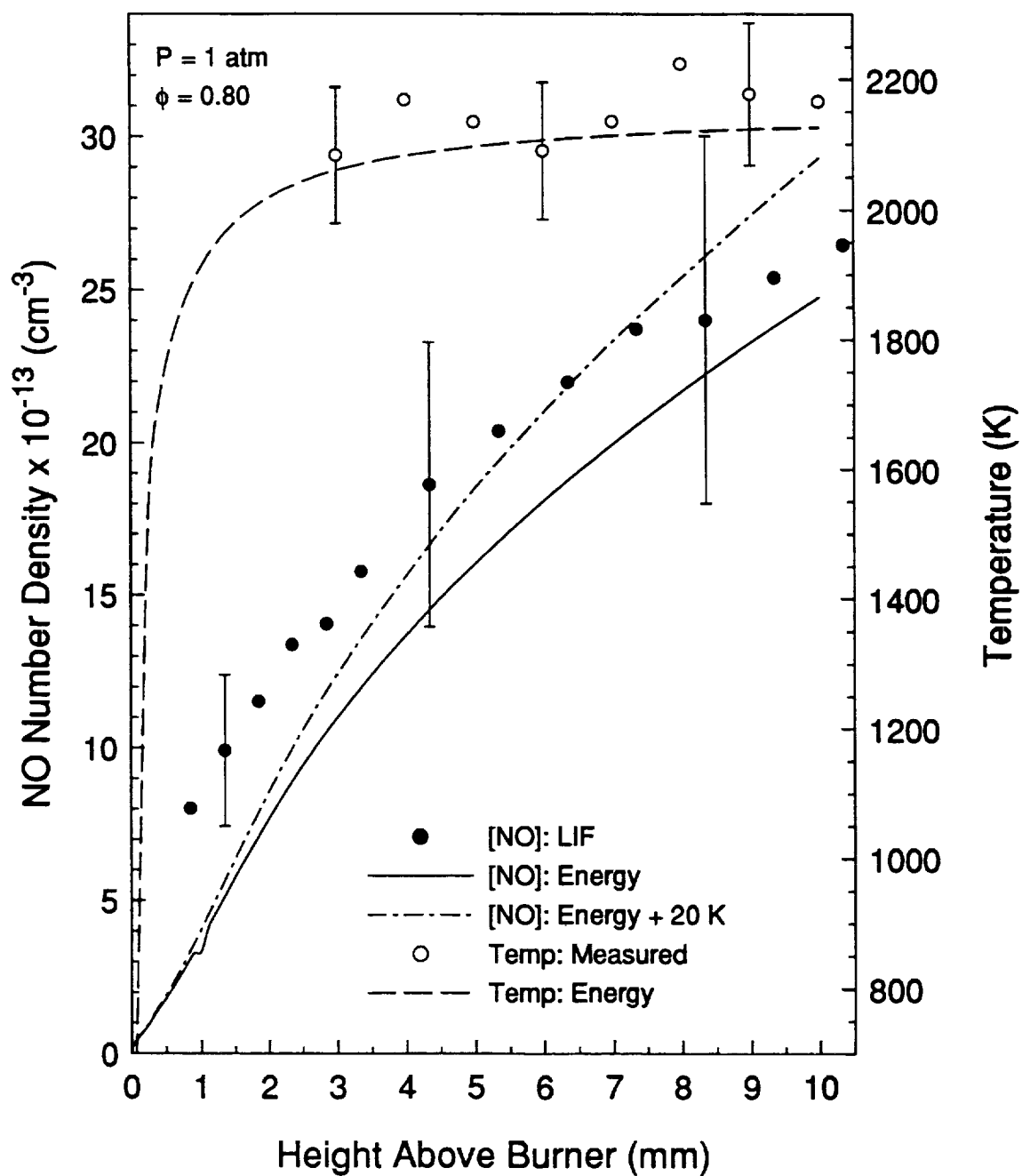
Figure 8.3: Measured and calculated [NO] in the P=1 atm, φ=0.80 flame (flame A). The temperature profile calculated from the energy solution, and the measured temperatures in the post-flame zone, are also shown. For this case, the average post-flame measured temperature was 20 K higher than the energy solution temperature.
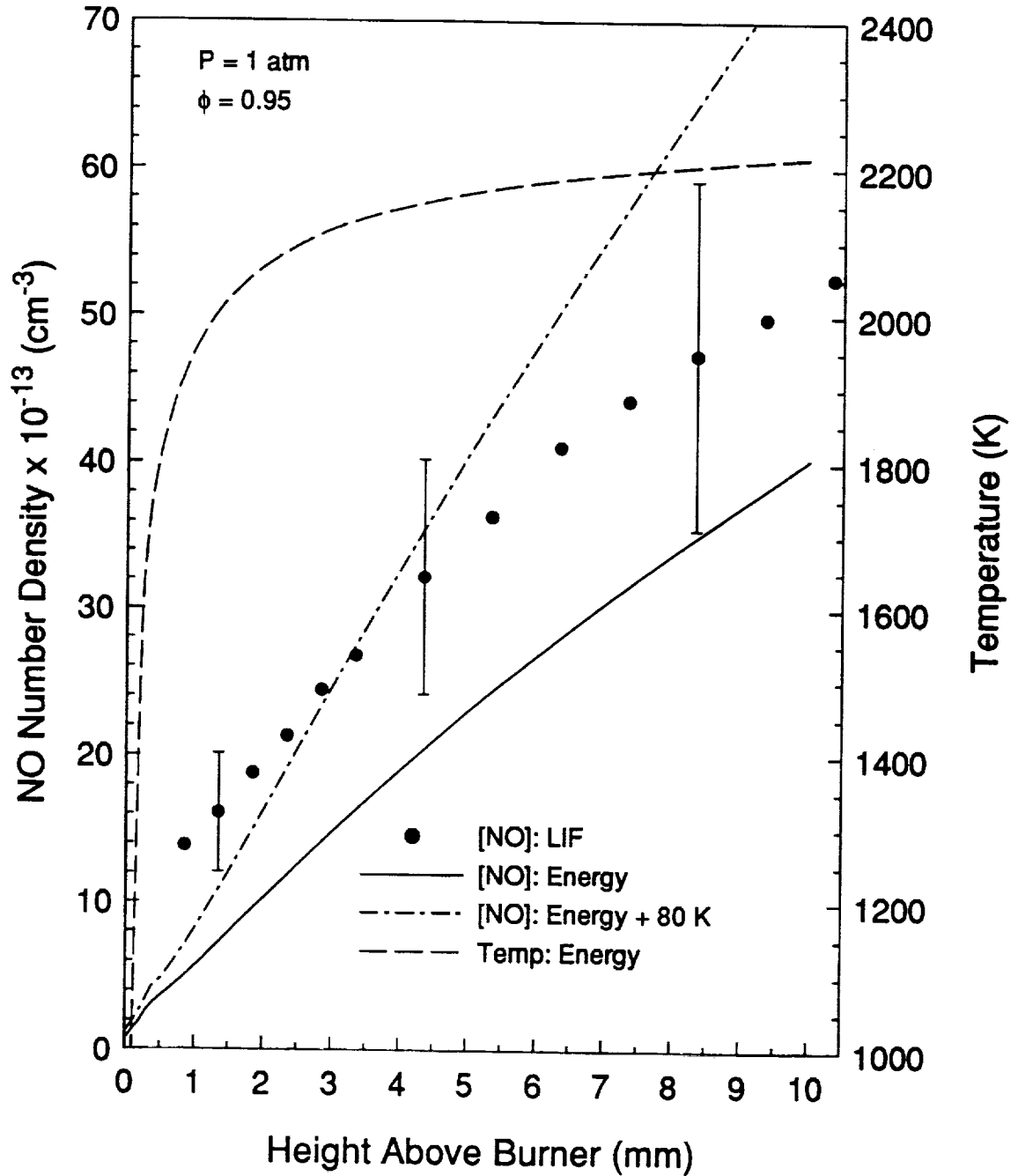
Figure 8.4: Measured and calculated [NO] in the P=1 atm, ϕ=0.95 flame (flame B). The temperature profile calculated from the energy solution is also shown. For this case, the average post-flame measured temperature was 80 K higher than the energy solution temperature.
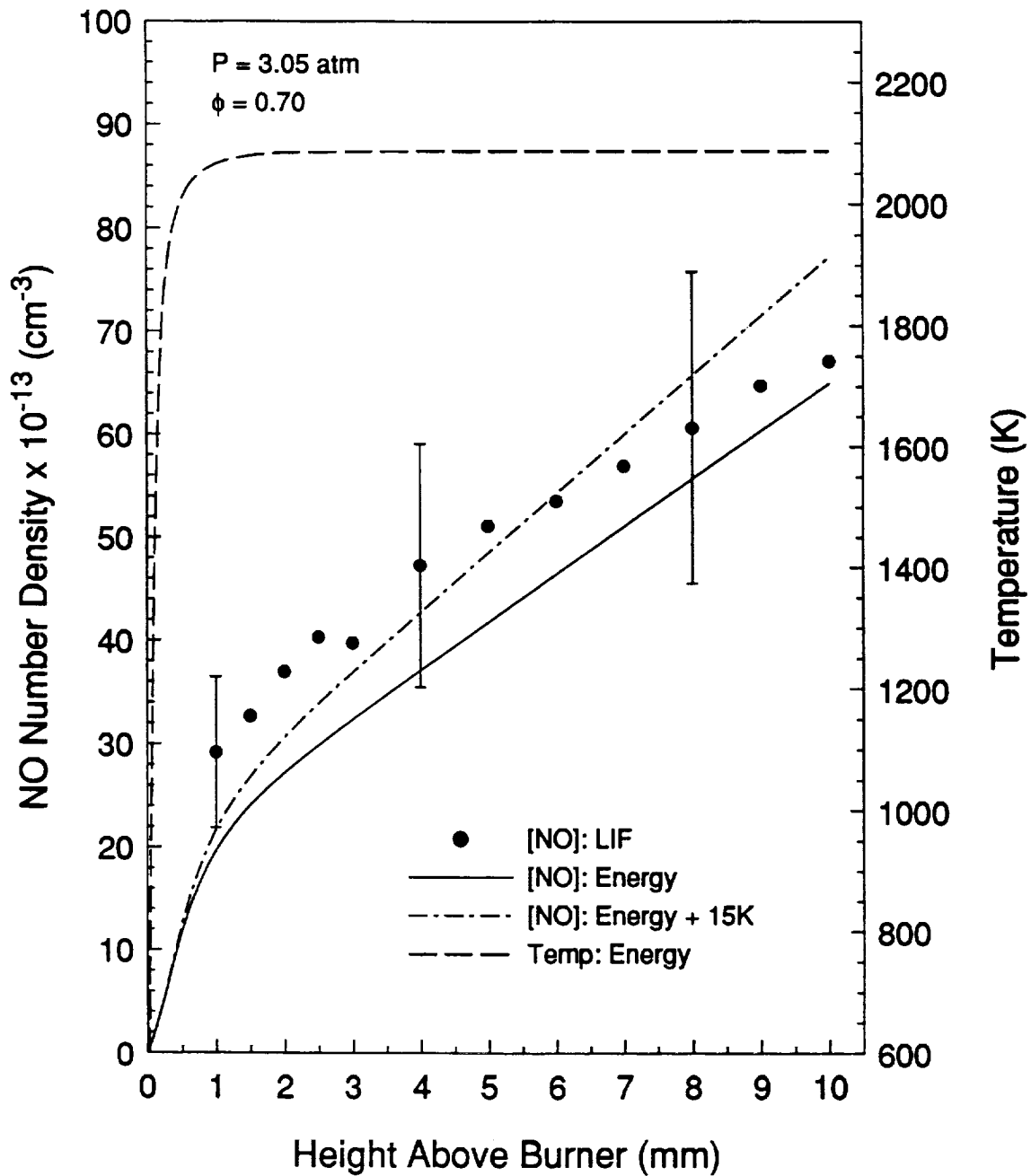
Figure 8.5: Measured and calculated [NO] in the P=3.05 atm, φ=0.70 flame (flame C). The temperature profile calculated from the energy solution is also shown. For this case, the average post-flame measured temperature was 15 K higher than the energy solution temperature.
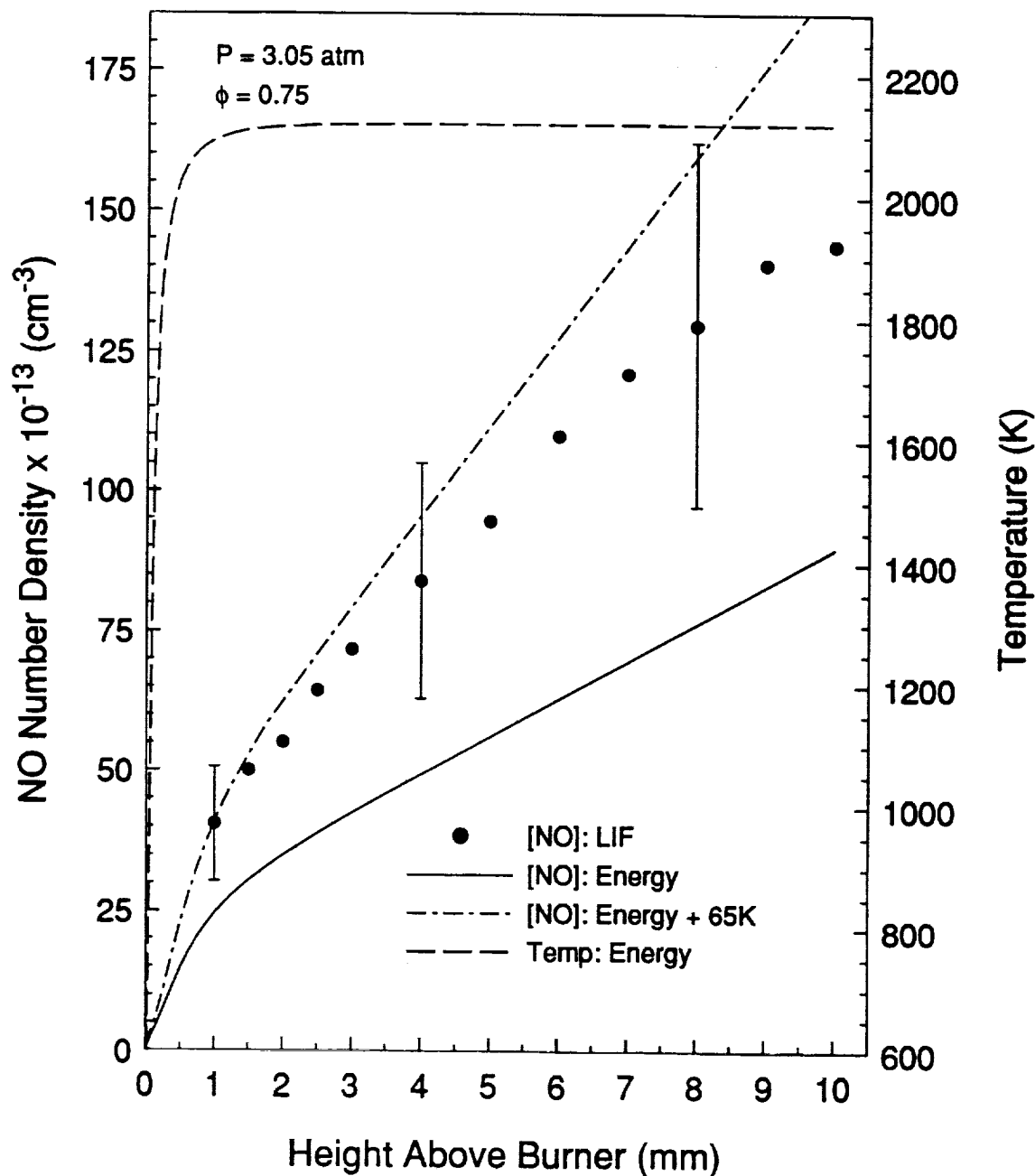
Figure 8.6: Measured and calculated [NO] in the P=3.05 atm, φ=0.75 flame (flame D). The temperature profile calculated from the energy solution is also shown. For this case, the average post-flame measured temperature was 65 K higher than the energy solution temperature.
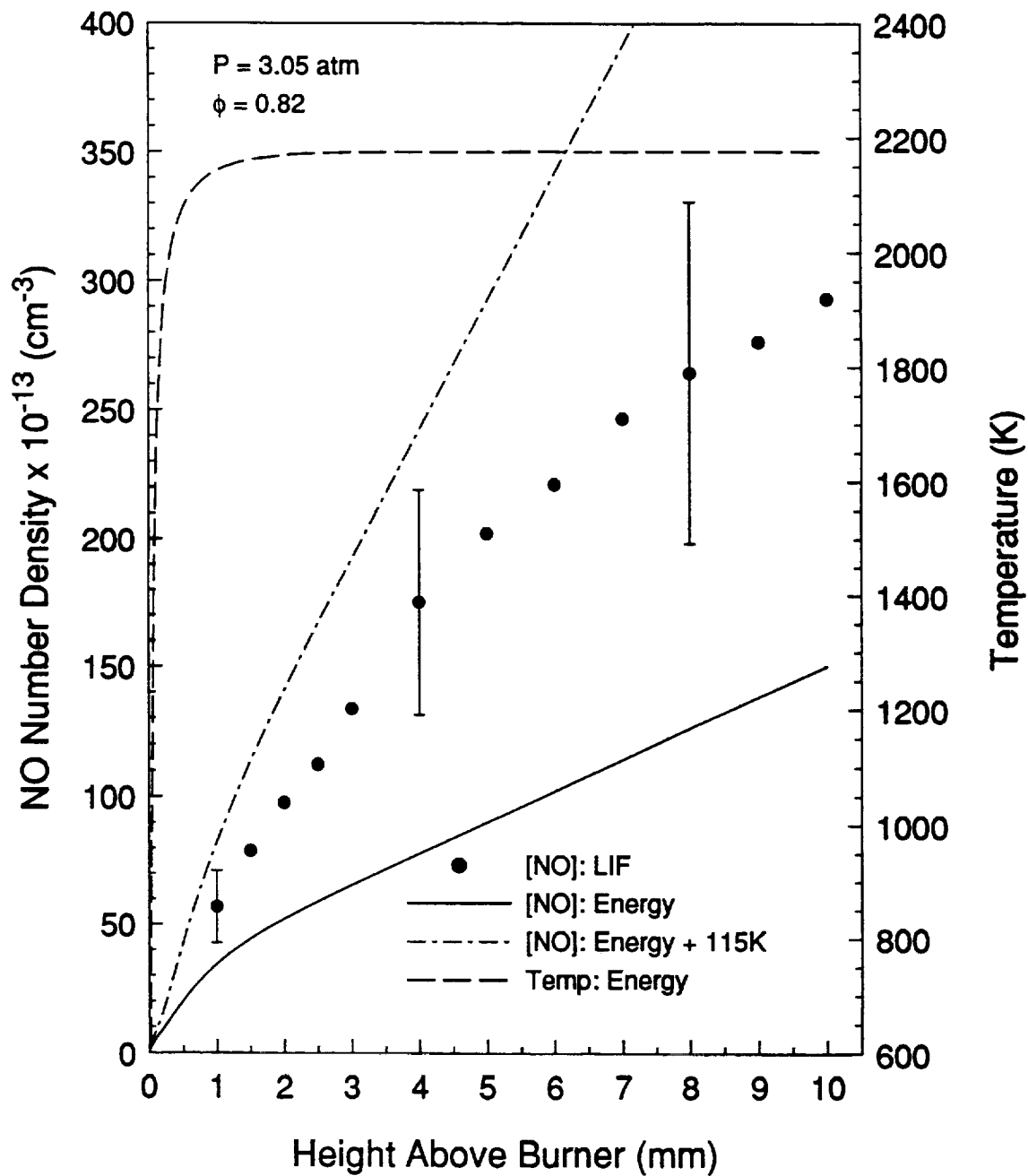
Figure 8.7: Measured and calculated [NO] in the P=3.05 atm, φ=0.82 flame (flame E). The temperature profile calculated from the energy solution is also shown. For this case, the average post-flame measured temperature was 115 K higher than the energy solution temperature.

duction tend to be less than the calculated rates at heights greater than 7 mm above the burner. This is probably due to the lack of radiative cooling in the modeled conditions as opposed to the experimental conditions.

Figure 8.3 also contains the temperature measurements found via Rayleigh scattering in the post-flame zone. These are presented as typical temperature measurements within the post-flame region of all the flames. As can be seen, there is a significant amount of scatter in the temperature measurements. Such scatter makes it very difficult to obtain a realistic temperature profile for these flames. However, the average post-flame temperature can be easily calculated from these measurements.

The results for the flames at 3.05 atm (Figs. 8.5-8.7) are similar to those at 1.0 atm. For flame C, the energy solution agrees well with the measured [NO] profile. The agreement with the energy solution is only fair for flames D and E (Figs. 8.6-8.7); a comparison of the slopes again indicates an underprediction of the experimental temperature. In addition, the [NO] is again consistently underpredicted, owing to flamefront effects. Comparisons between the measurements and predictions when using the measured post-flame temperatures show good agreement for flames C and D (particularly within 7 mm of the burner), but poorer agreement for flame E. The lack of radiative cooling in the modeling is again apparent in the results for flames C and D. The energy solution temperature is just below the range of temperature uncertainty for flame E. However, based upon the rates of NO production, the energy solution temperature appears to be too low, indicating that the actual temperature is within the uncertainty of the measurements.

While three of the measured temperatures in the five flames appear to yield rates of NO production which agree well with the model, two of the measurements appear to yield a temperature profile that produces too high a NO production rate when compared to the predictions. For flames B and E (Figs. 8.4 and 8.7), the energy solution appears to be as

useful as that obtained with the "measured" temperature profile. Therefore, use of the energy solution is probably acceptable for these flames. More importantly, these results demonstrate the necessity of having more precise temperature measurements for evaluation of the kinetics of high-temperature NO production. Changes in temperature of ~100 K (such as for flame E in Fig. 8.7) can cause the modeling to go from strongly underpredicting to strongly overpredicting the rate of NO production.

For comparative purposes, flame temperatures were also calculated using the following expression for the rate of thermal NO formation [Drake, 1993]:

$$\frac{d[NO]}{dt} = 1.45 10^{17} T^{-0.5} \exp\left(-\frac{69640}{T}\right) [O_2]_{eq}^{0.5} [N_2] \quad . \tag{8.1}$$

The temperature was calculated from the measured [NO] profile, the predicted [O$_2$] and [N$_2$], and the gas velocity from the flame code. The calculations were performed at a height of 7 mm above the burner. The results for these calculations are listed in Table 8.1. The calculated temperatures are in good agreement with the measurements for flames A and C, and fall between the measured and calculated temperatures for flames B, D, and E. It appears that both the measured and predicted flame temperatures are consistent with the temperatures required for post-flame NO formation.

The possible effect of O$_2$ interference is of considerable concern with respect to LIF measurements of [NO] in high-temperature flames. Reisel *et al.* [1993] found no significant interference when using the Q$_2$(26.5) line for low-temperature measurements (whereas, there would be significant interference for the R$_1$(17.5) line). However, Battles *et al.* [1994] raise the possibility of potential interference from high-order Schumann-Runge lines of O$_2$ when employing laser excitation in this region of the NO spectrum. To determine if a significant O$_2$ problem exists for these measurements, an excitation scan was taken around the region of the Q$_2$(26.5) line of NO in the post-flame zones of both flames A and B. Detection occurred in the γ(0,1) band of NO. The scans were similar for

both flames, and the result for flame A is shown in Fig. 8.8. The spectral features shown in Fig. 8.8 agree well with the known line positions of NO [Deézsi, 1958]. The scan also appears to be very similar to comparable scans in low-temperature flames [Reisel *et al.*, 1993]. Therefore, O_2 interference does not appear to be a significant problem in these measurements.

8.5 Summary

In this chapter, NO concentration profiles, found via LIF, in lean, high-temperature $C_2H_6/O_2/N_2$ flames at 1.0 and 3.05 atm have been presented and compared to appropriate chemical kinetics calculations. The input temperature profiles used for the predictions were the calculated profile from the energy solution, and this profile scaled to match the average post-flame temperature as measured by Rayleigh scattering. The agreement between the measured [NO] and the results from the energy solution appears to be consistently acceptable, while using the measured temperature profiles occasionally provides a rate of NO production that is too high compared to the measurements. Although the measured temperature may be too high, this assertion is difficult to defend owing to the uncertainty in the temperature measurements. Thus, more precise temperature measurements are needed for firm evaluation of the accuracy of chemical kinetics models for NO formation at high temperature. Finally, there appears to be little interference from O_2 in these LIF measurements.
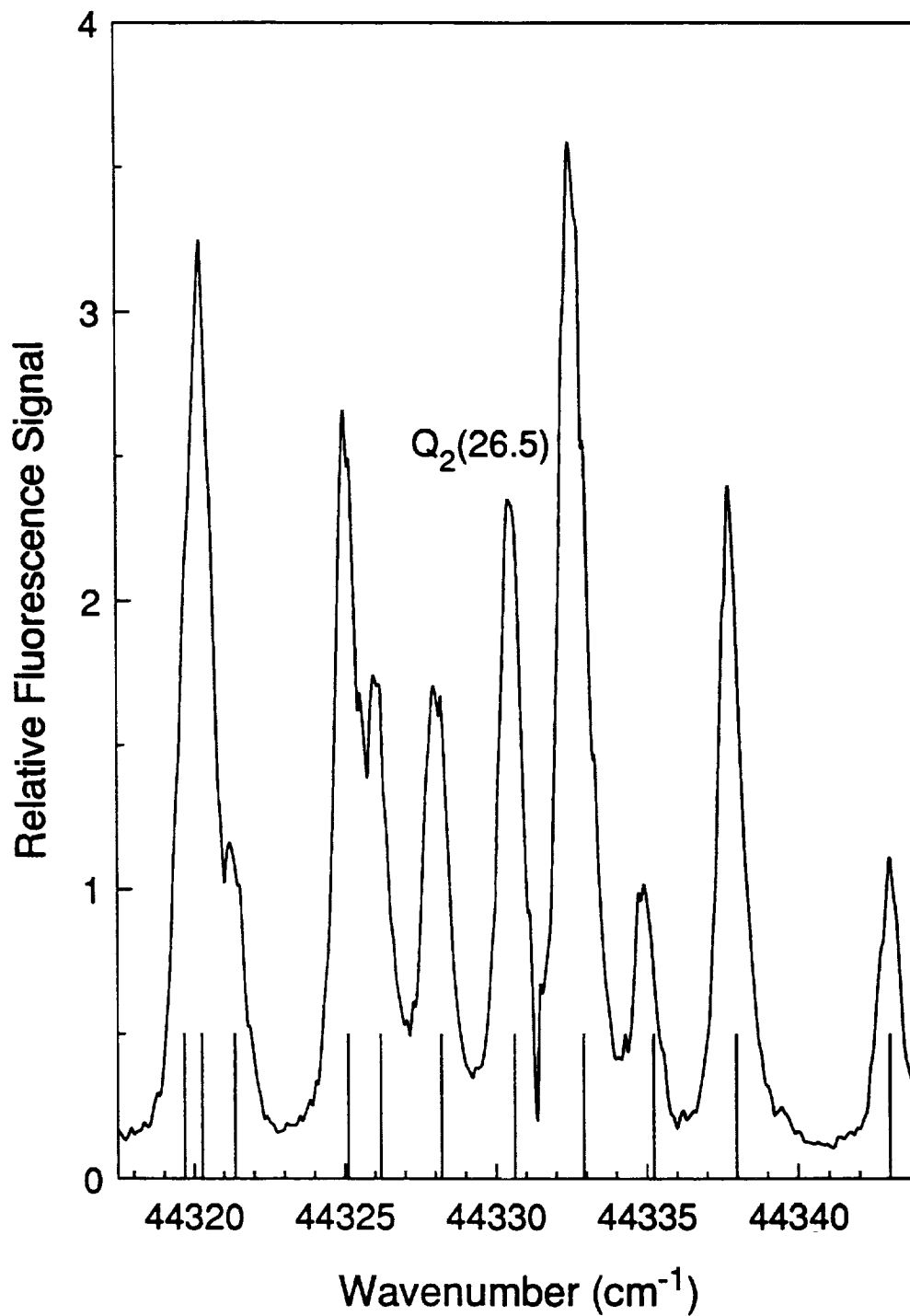
Figure 8.8:   Excitation scan over the region containing the $Q_2(26.5)$ line ($\nu \approx 44330$ cm^{-1}) of NO. Detection occurred in the $\gamma(0,1)$ band of NO. The scan was taken in the P=1 atm, ϕ=0.80 flame (flame A). Locations of known NO spectral lines [Deézsi, 1958] are also plotted.

CHAPTER 9

LASER-INDUCED FLUORESCENCE MEASUREMENTS

OF NITRIC OXIDE IN TURBULENT FLAMES

9.1 Introduction

High-pressure combustion applications, such as gas-turbine engines, are a major

source of nitric oxide (NO) emissions. As the environmental problems caused by high NO

emissions grow, it has become imperative to reduce NO emissions from combustion

processes. The achievement of this goal by combustion designers requires, among other

things, a thorough understanding of the chemical kinetics involved in the production of

NO at high-pressure. Such understanding, in turn, mandates accurate *in situ* measure-

ments of NO concentration.

Many practical combustion devices operate under turbulent conditions. To obtain

measurements in a turbulent flame, it is desirable to use an optical diagnostic technique as

opposed to using a physical sampling probe. Optical procedures allow for remote sensing

of numerous species in a variety of environments [Miller and Fisk, 1987]. Unlike sam-

pling probes, optical methods generally do not alter the combustion process; in addition,

many combustors are more readily adaptable to optical access than to physical sampling

probes. Precise spatial resolution is also achievable through the use of optical methods.

Finally, an optical diagnostic technique such as laser-induced fluorescence (LIF) allows

concentration measurements to be obtained over very short time-scales; this allows for

instantaneous concentration measurements as opposed to time-averaged quantities.

The feasibility of making quantitative LIF measurements of NO in laminar flames has been demonstrated in Chapters 4, 5 and 8. These measurements were made by averaging the fluorescence signal over 600 laser shots. In the laminar flame measurements, a fluorescence signal was detected on each laser shot; however, 600 laser shots were taken to reduce the uncertainty in the average concentration. Due to the fluctuations in the flow field for turbulent combustion, it is desirable to obtain single-shot measurements of the NO concentration. The single-shot measurements can then be grouped into a probability density function (pdf); such a representation provides a distribution of the NO concentration over time at a given location in the flame.

Laser-induced fluorescence has previously been used to measure NO concentrations in turbulent nonpremixed flames [Carter and Barlow, 1994]. However, it is desirable to determine the feasibility of measuring [NO] in turbulent flames with the current apparatus, as well as to evaluate the detection limit of the experimental apparatus for single-shot measurements. This chapter presents preliminary results which address these two issues. Because the measurements are performed at 1 atm, broadband laser-saturated fluorescence (LSF) [Reisel et al., 1993] is employed for the measurements. LSF has been used previously to measure [OH] in turbulent flames [Lucht et al., 1984; Drake and Pitz, 1985]. The LSF signal is nearly independent of the fluorescence quenching environment; therefore, the variable quenching environment of a turbulent flame should not affect the measurements.

9.2 Experimental Apparatus

The laser system and optical layout used for performing the LSF measurements of [NO] are described in Chapter 3. Both the 2.5-cm diameter, water-cooled, sintered-bronze McKenna flat-flame burner and the 1.3x1.3 cm premixed Hencken burner were used in portions of this preliminary investigation. To provide a more clearly turbulent combustion environment, a simple burner was also fashioned using a 1.6 mm (ID) tube through which

a fuel jet was directed into the atmosphere. The burner was located in the high-pressure combustion facility described by Carter *et al.* [1989]; however, the pressure vessel was removed for this study.

One concern of this work was the generation of turbulence in a flame. Two different schemes were used in an attempt to produce a turbulent flame. First, a nickel-chromium wire mesh (B&S gauge 24, 16 mesh) was placed in the laminar flow of the McKenna and Hencken burners in an attempt to trip the premixed flame from laminar flow into turbulent flow. However, the success of this approach was difficult to evaluate. Therefore, to be more certain of the turbulent nature of the flame, a nonpremixed flame was formed using a fuel jet emanating from the tube burner.

9.3 Results and Discussion

In this study, there are three issues of concern: (1) the ability to measure pdfs of [NO] with the current experimental apparatus; (2) the ability to generate turbulent flames with the apparatus; and (3) the single-shot detectability limit of the [NO] measurements in turbulent flames. The first issue can be addressed in laminar flames as well as in turbulent flames. It would be desirable to resolve the second issue by measuring significantly different pdfs in turbulent and laminar flames; if this cannot be done (i.e., if the pdfs are similar), the determination of turbulence must be assessed through qualitative observations and calculation of the Reynolds number of the flow. The third issue can be addressed through an analysis of the signal-to-noise ratio of the measurements.

It was anticipated that pdfs of [NO] could be constructed using the current experimental apparatus, for a measurable fluorescence signal was obtained for each of the 600 laser shots taken in the laminar flames of Chapters 4, 5, and 8. To perform single-shot [NO] measurements, LSF was used as the diagnostic technique. The laser energy above the burner was ~1 mJ/pulse. To demonstrate the feasibility of obtaining a pdf of [NO] in these flames, the results from a laminar, atmospheric-pressure, $C_2H_6/O_2/N_2$ flame on a

Hencken burner are presented as an example. This flame was a ϕ=0.95, ψ=2.94 flame with a volumetric flow rate of 4.8 slpm. Figure 9.1 contains the single-shot measurements of the fluorescence voltage from this flame, obtained over 5000 laser shots, and divided into 20 different bins, each with a width of 0.025 V. The measurements were obtained 12 mm above the burner. The average of the 5000 laser shots was 0.208 V, and the standard deviation was .055 V. This results in a relative standard deviation (the standard deviation divided by the average) of 0.26. The fluorescence signal could easily be converted into a NO concentration through the use of an appropriate calibration factor. As can be seen from Fig. 9.1, pdfs of [NO] can be easily generated in laminar flames with the current experimental apparatus. Similar pdfs have also been generated for laminar, premixed flames stabilized on the McKenna burner.

The second issue to be addressed was the feasibility of generating a simple turbulent flame. The first approach taken was to attempt to trip a laminar flame to produce a turbulent combustion environment. It was uncertain what effect this approach would have on the pdf of [NO]. If the flame were tripped in or before the flame front, a possibility existed that there would be a broader pdf of [NO]. However, if the flame was tripped after the NO had been formed, it was questionable as to whether there would be any change in the pdf, for the turbulent fluctuations would just be "fluctuations" of a constant [NO]. On this basis, two approaches were taken to obtain the tripping; first, a nickel-chromium screen was placed next to the McKenna burner surface, and second, the screen was placed ~5 mm above the surface of the Hencken burner, in the region of thermal-NO formation. The former approach was taken in an attempt to place the screen below or in the flame front. The latter approach was taken in an attempt to trip the thermal-NO production region into turbulence, which was thought more likely due to the higher velocities above the Hencken burner. The pdfs obtained with both of these methods were very similar to the pdfs obtained without the screen. A sample is shown in Fig. 9.2, which contains a pdf
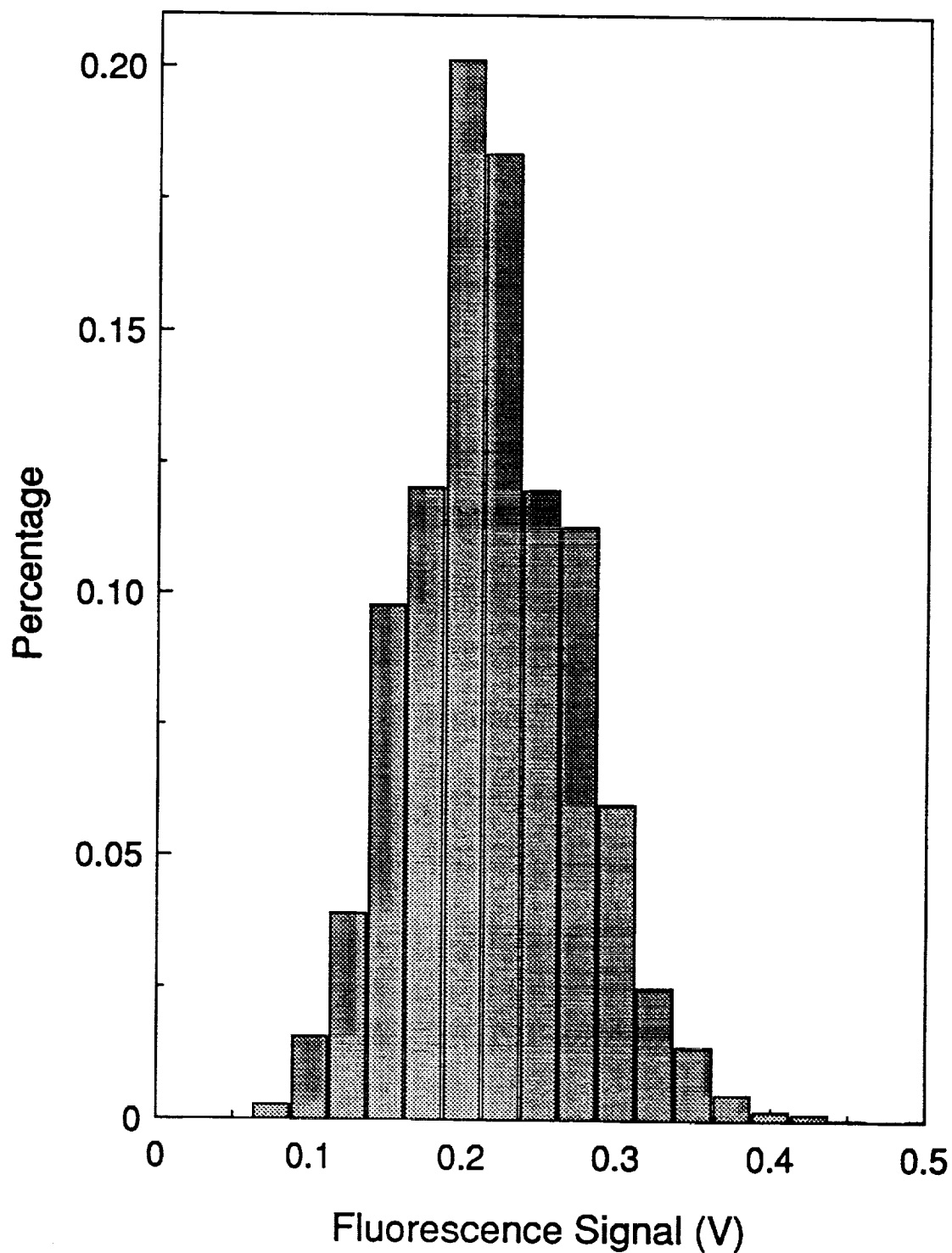
Figure 9.1: Probability density of the NO LSF signal for a laminar flame using a Hencken burner. The data were taken 12 mm above the burner for 5000 single-shot measurements. The equivalence ratio of the flame was φ=0.95.
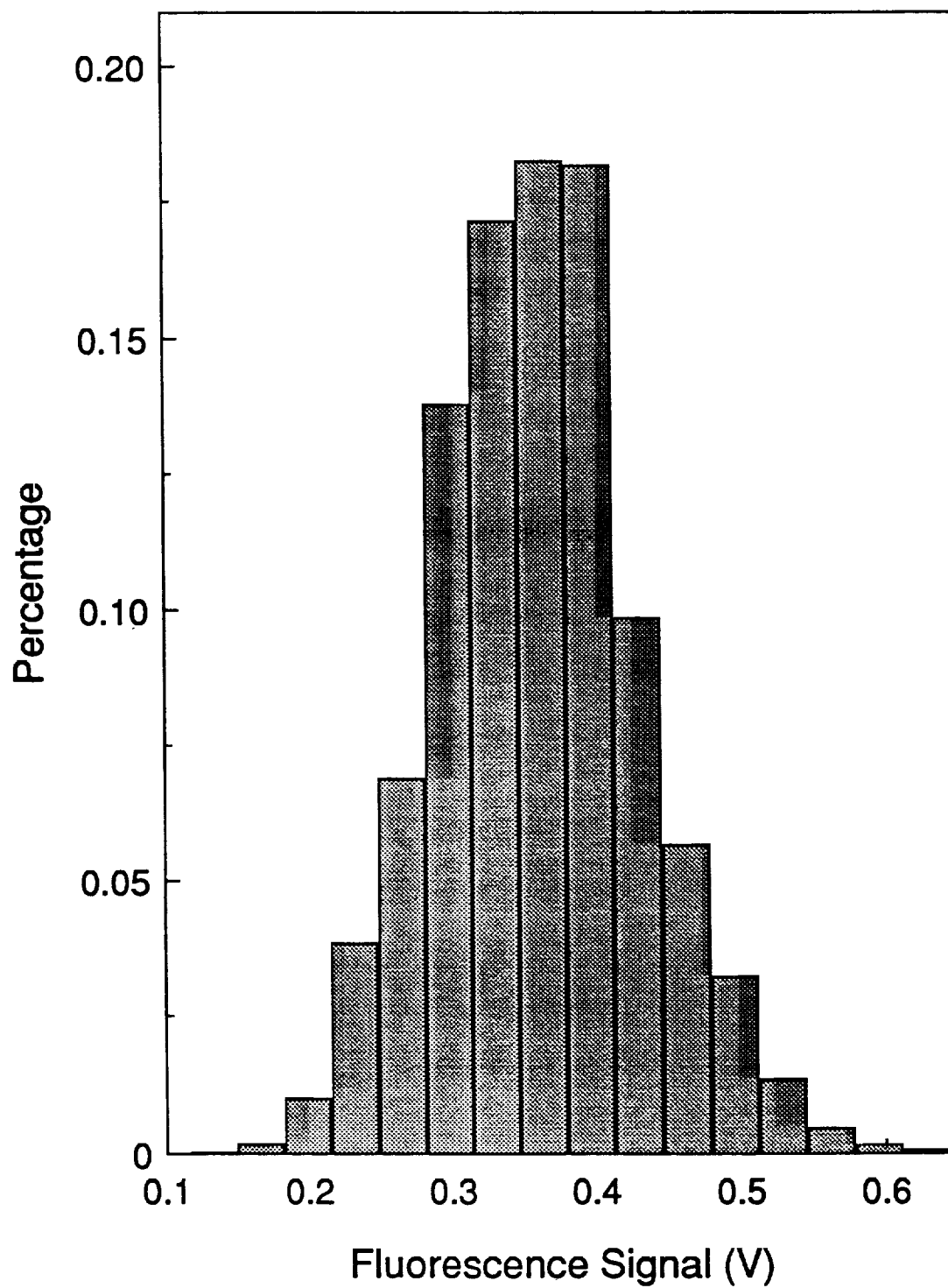
Figure 9.2: Probability density of the NO LSF signal for a flame using a Hencken burner with a screen placed ~5 mm above the burner. The data were taken 15 mm above the burner for 5000 single-shot measurements. The equivalence ratio of the flame was ϕ=0.95.

of the single-shot LSF measurements of the NO fluorescence signal in the same Hencken burner flame as in Fig. 9.1, but with the measurements taken 15 mm above the burner (~10 mm above the screen). In this case, the relative standard deviation of the measurements was 0.20. Since these measurements are not distributed over a wider region, no clear indication exists concerning turbulent behavior. This result does not mean that the flow field has not been tripped to turbulence. It is just an indication that the screen does not cause additional fluctuations in the [NO].

The second attempt to produce a turbulent flame was to flow a nonpremixed jet of fuel into the ambient environment. This was done by delivering a mixture of 1.87 slpm C_2H_6 and 0.55 slpm N_2 through a 1.6 mm (ID) tube into the atmosphere. The Reynolds number of the cold-gas flow was ~2200, which should indicate a flow in the transition region between laminar and fully turbulent behavior. The flow did visibly exhibit some turbulent behavior. The flame was lifted ~2 cm above the exit of the tube, and measurements were performed ~10.5 mm above the burner. A schematic representation of this flame is provided in Fig. 9.3. Pdfs were obtained at two locations in the flame; location "X" was in the center of the flame, and location "Y" was at the edge of the flame. It would be desirable to perform the measurements higher above the burner, so that the turbulent flow could be more developed. However, due to the current experimental configuration, this downstream location was the furthest above the burner that the measurements could be performed.

Figure 9.4 contains a pdf obtained near the center of the flame (location "X" in Fig. 9.3). The relative standard deviation of the pdf is 0.35; this value is slightly higher than that obtained for the laminar flames. However, the pdf still appears to be Gaussian, much like that obtained in a laminar flame. This result indicates that the small level of turbulence in this flame does not significantly alter the pdf of [NO] in the flame. The distribution is somewhat broader, but the pdf is still similar to the laminar flames.
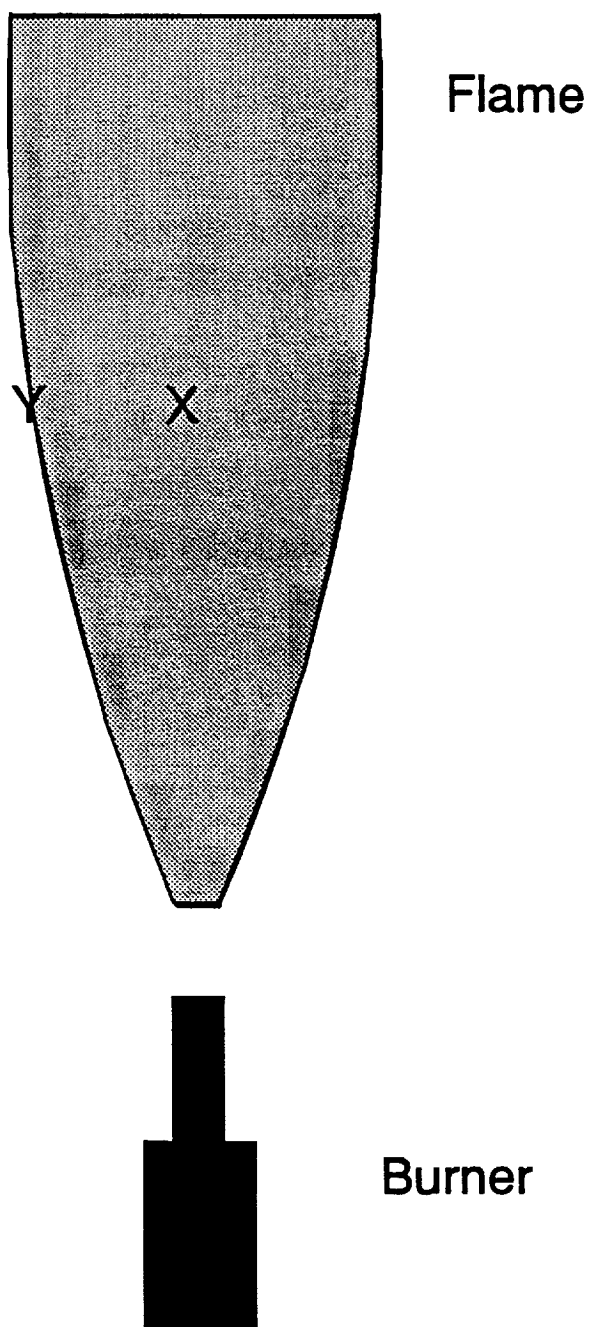
Figure 9.3: Schematic diagram of the nonpremixed jet flame. The tube burner had an ID of 1.6 mm and the flame was lifted ~2 cm above the burner. Measurements of the pdf of NO were taken at two locations (~10.5 mm above the burner); location "X" was in the center of the flame, and location "Y" was at the edge of the flame.
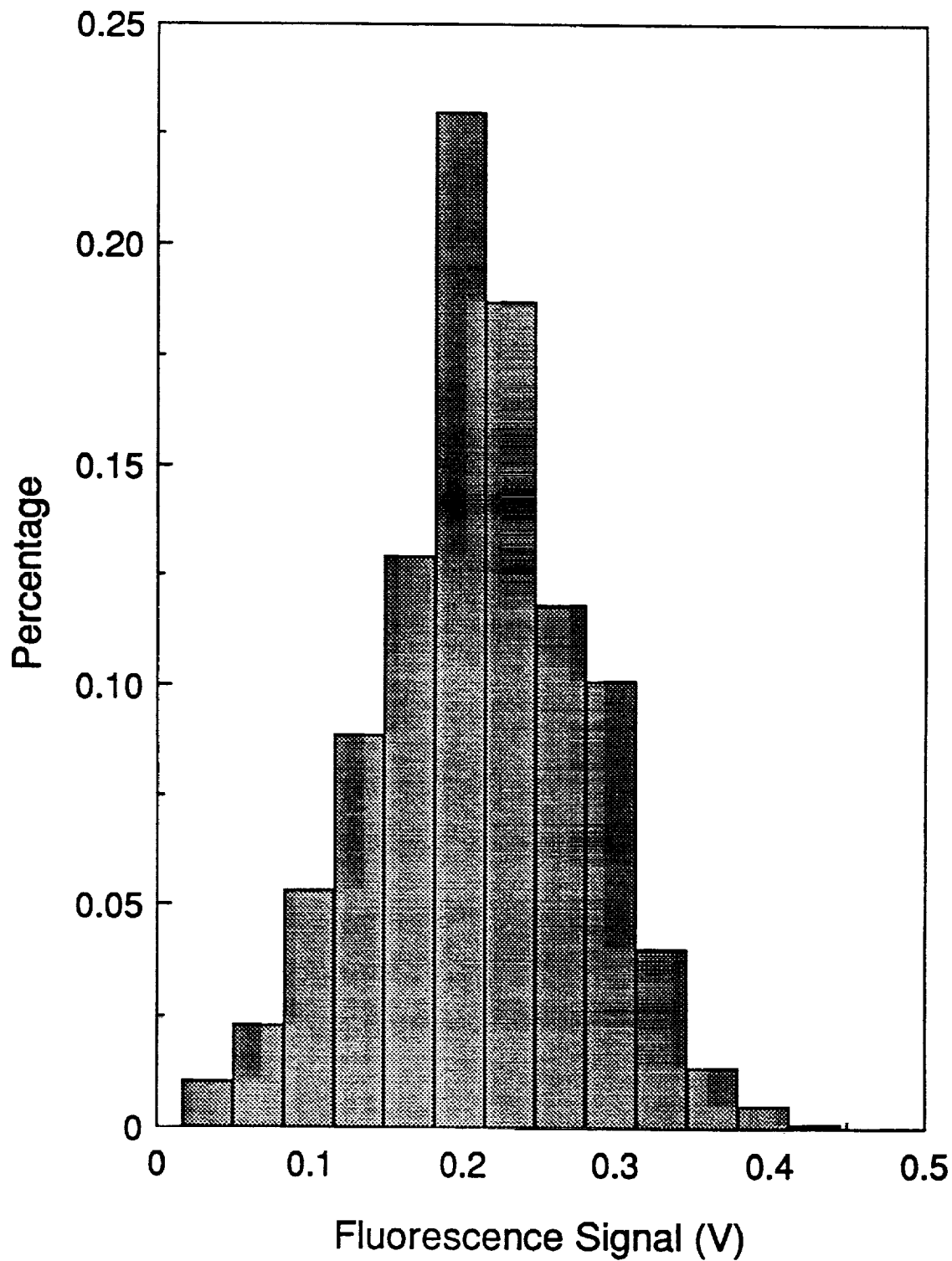
Figure 9.4: Probability density of the NO LSF signal for a nonpremixed turbulent jet flame (Re≈2200). The data were taken 10.5 mm above the burner in the center of the flame by employing 5000 single-shot measurements.

Figure 9.5 contains a pdf obtained near the edge of the jet flame (location "Y" in Fig. 9.3). This region represents the area over which the flame is rapidly fluctuating. There-fore, there should be a considerably different pdf of [NO]; this is indeed the case as seen in Fig. 9.5. In fact, the relative standard deviation of the single-shot measurements is 0.66. In Fig. 9.5, the distribution of [NO] is heavily weighted towards low levels of NO con-centration. However, there are also a substantial number of measurements with large NO concentrations. In short, Fig. 9.5 demonstrates that measurements of NO concentration with LSF are feasible with the current experimental apparatus in fluctuating environ-ments. However, Fig 9.4 does not provide a clear indication as to whether or not a pdf of [NO] in the center of a turbulent flame would be significantly different from that in a laminar flame.

The third issue that needs to be addressed is the single-shot detection limit. As a first step, it is desirable to determine if the measurements are governed by photon statistics. For this purpose, previous results obtained with the Hencken burner are considered; in fact, the flame conditions are identical to those of flame A in Chapter 8. A measurement was performed, over 600 laser shots, with no attenuation of the fluorescence signal, and the single-shot relative standard deviation was found to be 0.21. The fluorescence was then attenuated by a factor of 3.9, and the relative standard deviation increased to 0.40. For photon statistics (Poisson statistics), one would expect the relative standard deviation to increase by a factor of the square root of the attenuation [Larson, 1969]. In this case, one would then expect the relative standard deviation to become 0.41. Therefore, it appears that the measurements are indeed governed by photon statistics.

To analyze the single-shot detection limit, a flame (ϕ=0.80) used for the calibration of the atmospheric-pressure measurements in the McKenna burner can considered. This flame was chosen because its [NO] is already near the anticipated detection limit. For this flame, the signal-to-noise ratio (i.e., the inverse relative standard deviation) for a single
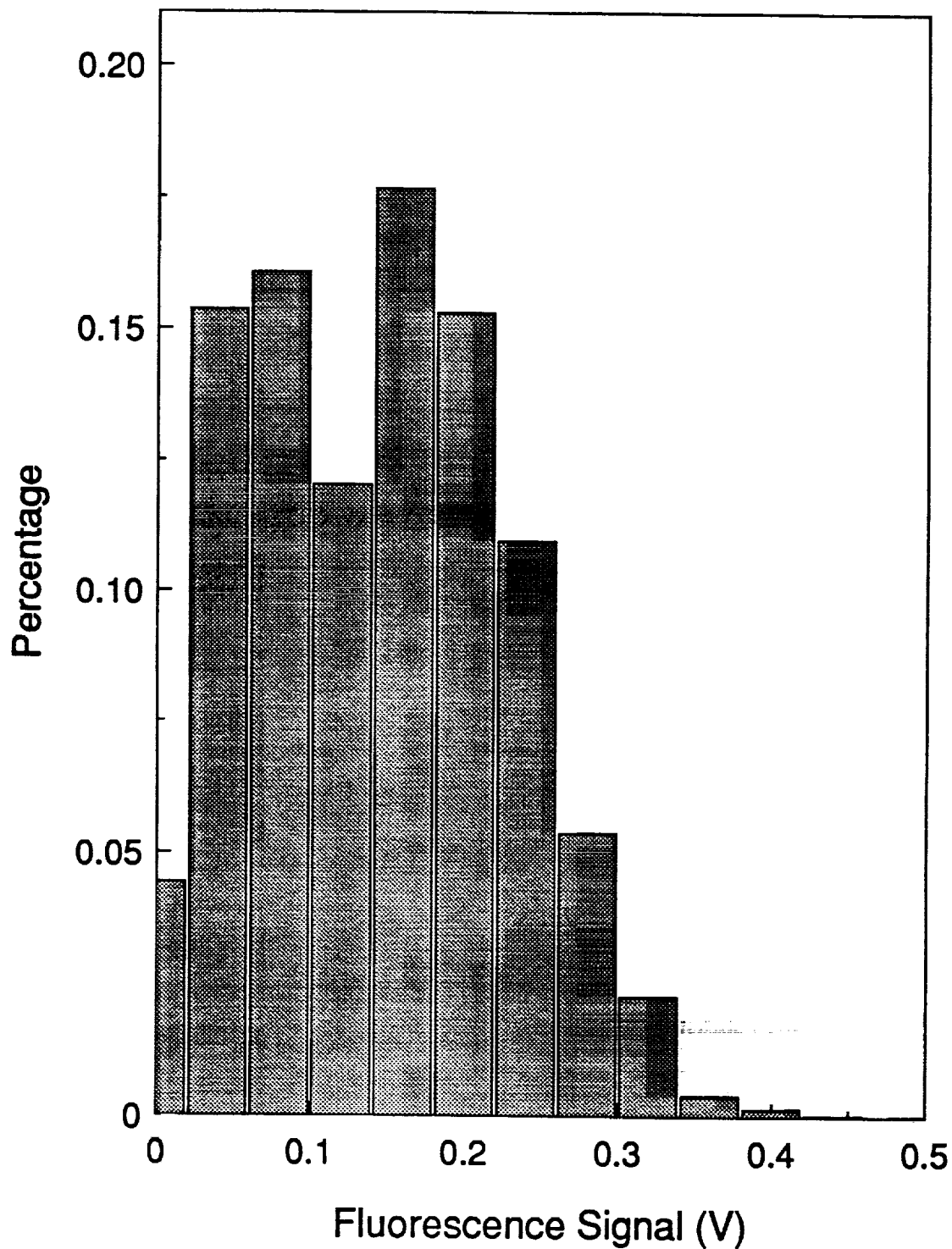
Figure 9.5: Probability density of the NO LSF signal for a nonpremixed turbulent jet flame (Re≈2200). The measurements were taken 10.5 mm above the burner at the edge of the flame by employing 5000 single-shot measurements.

C-3.

shot was 2.03, and the NO concentration was 9 ppm ([NO]$\approx 3.7\times 10^{13}$ cm^{-3}). The measurement was performed over 600 laser shots, so that the ratio of the mean to the standard deviation of the mean was ~50. This reference measurement will be designated with a subscript "0". Since the fluorescence voltage is directly related to the concentration, the concentration is directly related to the associated number of detected photons. For photon statistics [Larson, 1969],

$$\overline{V} = \frac{N}{N_0}\overline{V}_0 \quad ,$$

(9.1)

and

$$\sigma = \sqrt{\frac{N}{N_0}}\sigma_0 \quad ,$$

(9.2)

where $\overline{V}$ is the average voltage, N is the NO concentration (or, correspondingly, the number of photons), and σ is the standard deviation. An acceptable ratio of the average to the standard deviation must be selected so as to determine the detection limit. In this case, it will be set equal to 1.0; this value is normally considered to be the lowest acceptable ratio for a meaningful single-shot measurement [Dreier and Rakestraw, 1990]. Therefore, combining Eqs. (9.1) and (9.2)

$$\frac{\overline{V}}{\sigma} = \frac{\overline{V}_0}{\sigma_0}\sqrt{\frac{N}{N_0}} \quad .$$

(9.3)

Rearranging and setting Eq. (9.3) to unity,

$$N = \left(\frac{\sigma_0}{\overline{V}_0}\right)^2 N_0 \quad .$$

(9.4)

Solving Eq. (9.4) yields a single-shot detection limit of ~2 ppm in a ϕ=0.80 flame at atmospheric pressure ([NO]$\approx 7.6\times 10^{12}$cm^{-1}), for the LSF measurements. This value would, of course, change if a different choice were made for the minimum $\overline{V}/\sigma$. For comparative purposes, Carter and Barlow [1994] report a signal-to-noise ratio of 8 for [NO]=2$\times 10^{13}$

cm^{-3} at atmospheric pressure. Therefore, Carter and Barlow [1994] have a lower detection limit than that reported here at a signal-to-noise ratio of unity. Their lower detection limit can be attributed to a larger spatial probe volume, a larger temporal detection gate, and their detection of fluorescence over a larger spectral region.

9.4 Summary

In this chapter, the feasibility of performing single-shot LIF measurements of NO in a turbulent flame has been investigated. It has been found that the measurement of pdfs of [NO] is feasible using LSF with the current experimental apparatus. The generation of clearly turbulent flames was found to be somewhat more difficult. Attempts to produce turbulence through tripping the flow with a screen were inconclusive, and it is difficult to obtain a jet with a sufficiently high Reynolds number with the current equipment. Finally, a single-shot detection limit of ~2 ppm was obtained in an atmospheric-pressure, $\phi=0.80$ flame.

CHAPTER 10

CONCLUSIONS AND FUTURE WORK

10.1 Conclusions

In this study, the method of laser-induced fluorescence (LIF) has been applied to the measurement of nitric oxide concentration in a variety of hydrocarbon flame environments. These environments include the following: atmospheric- and high-pressure ($P <$ 15 atm), premixed, laminar, low-temperature ($1600 < T < 1850$ K) $C_2H_6/O_2/N_2$ and C_2H_4 $/O_2/N_2$ flames; premixed, laminar, high-temperature ($2100 < T < 2300$ K) $C_2H_6/O_2/N_2$ flames (up to 3.05 atm); and turbulent atmospheric-pressure nonpremixed ethane flames. The results from the laminar flame work have been compared to the predictions of three current comprehensive chemical kinetics models. A Rayleigh scattering temperature measurement technique was also developed and applied to several laminar flames. In addition, the theoretical transportability of a calibration obtained at one set of conditions was explored for application to another set of conditions.

Perhaps the most important conclusion obtained from this study is that it is feasible to perform quantitative LIF measurements of NO concentration in both laminar and turbulent premixed flames at high pressure. Such flames do not exhibit significant changes in the quenching environment, thereby allowing any changes in the quenching rate coefficient to be neglected at a given pressure. The measurement technique works for laminar flames up to at least 15 atm. Above 15 atm, the limiting factor in the applicability of LIF to NO measurements is not the increase in the quenching rate coefficient with

pressure, but rather the ability to determine the spectral location of the absorption line used for excitation of NO. For the turbulent flame measurements, the single-shot detection limit appears to be ~2 ppm in an atmospheric-pressure $\phi=0.80$ flame.

Another important result of this work is the identification of a shift in the peak NO concentration towards stoichiometric conditions with increasing pressure for the low-temperature flames. This behavior was noticed in both the ethane and ethylene flames, indicating that the phenomenon is probably universal for low temperature, hydrocarbon combustion. An analysis of the chemical kinetics for these flames suggests that this shift is caused by the effects of pressure and equivalence ratio on the reaction $CH_2 + OH \rightarrow CH + H_2O$. Thus, more CH is formed in near-stoichiometric flames at higher pressures due to a greater relative concentration of the hydroxyl radical. Since these flames are dominated by prompt-NO production so that the amount of NO formed is directly related to the CH level, the above reaction causes a shift in the peak NO concentration towards leaner conditions with increasing pressure.

The selected chemical kinetics schemes had different degrees of success at predicting the NO concentrations in these flames. Use of the energy solution of the GMK-DB mechanism was, in general, accurate both quantitatively and qualitatively when predicting the NO formed in both the low-temperature and high-temperature ethane flames. For the high-temperature flames, the energy solution tended to slightly underpredict the actual temperature, and to also underpredict the NO formed in the flame front; however, the solution was often still adequate. The MB mechanism gives accurate qualitative predictions for the [NO] in the low-temperature ethane flames, but grossly underpredicted the actual [NO] levels in these flames. This was due primarily to the rate parameters used for the primary prompt-NO reaction, i.e., $CH + N_2 \leftrightarrow HCN + N$, and the inclusion of the reaction $CH + H_2O \leftrightarrow CH_2O + H$. The latter removes CH from the flame, which then reduces production of NO. Neither the GMK-DB nor the MIME-DB mechanisms were

particularly accurate for the ethylene flames. The two mechanisms were adequate at equivalence ratios less than $\phi \approx 1.2$, but then underpredicted the NO concentrations at higher equivalence ratios. This caused poor predictions of the equivalence ratio corresponding to the peak [NO], particularly at lower pressures. The MIME-DB mechanism also tended to greatly underpredict the NO concentrations quantitatively in these flames. Thus, in summary, the proposed reaction mechanisms are adequate for the ethane flames, and inadequate for the ethylene flames at lower pressures. In addition, the good agreement for the ethane flames may be more fortuitous than an indication of a well-defined chemical kinetics model.

Analysis of the chemical kinetics suggests that improvement of the predictions for the ethylene flames will require a better understanding of the initial breakdown of C_2H_4. The basic scheme for the small hydrocarbon kinetics for all three mechanisms was developed primarily for methane combustion. As seen in this work, these kinetics for methane combustion appear to be adequate for the ethane flames. However, the kinetics do not appear adequate for the rich ethylene flames of Chapter 5. As suggested in Chapter 5, inaccurate predictions of the CH profiles in rich flames by the MIME-DB mechanism may be the cause of the poor NO predictions. The work of Miller *et al.* [1991], which showed that the CH profiles are peaking closer to the burner for the predictions as compared to the measurements for rich flames, suggests that further refinement of the fuel oxidation models is needed for non-paraffinic fuels. If these models can be improved, the predictions of [NO] in the low-temperature flames may correspondingly improve as well.

The Rayleigh scattering temperature measurement technique was found to be useful for accurately measuring temperatures for the low-temperature, atmospheric-pressure flames. However, the difficulty with obtaining accurate temperatures near the burner surface (due to the large amount of background scattering) and the poor precision of the technique (~5%) limits its utility for high-temperature flame measurements. The large

dependence of thermal-NO production on temperature requires more precise measurements than can be obtained with the Rayleigh scattering technique before proper evaluation can be made of the chemical kinetics controlling high-temperature NO formation.

Finally, it was found that it is best to calibrate the LIF measurements of NO concentration as close to the flame conditions as possible. It is very important to calibrate at the same pressure, due both to the effects of pressure broadening on the spectral lines and the changes in quenching environment with pressure. While it is generally not possible to easily apply a calibration found at one pressure to a measurement at another pressure, calibration can frequently be performed in a flame with a different temperature at the same pressure.

10.2 Recommendations for Future Work

This work has shown the feasibility of performing LIF measurements of NO concentration in high-pressure flames and in turbulent flames. Therefore, there are many possible ways in which the LIF method can be applied to practical environments. First, LIF measurements should be obtained in more high-temperature flames, both at atmospheric and high pressure. The limiting factor in this study was the burner used for these measurements. Burners designed using a capillary tube configuration will not be particularly successful at producing premixed flames at high-pressure, for the flame tends to be either pushed into the burner or to be extinguished by the small tube diameter of the burner assembly. These problems could possibly be overcome with an uncooled McKenna type, sintered ceramic burner. This type of burner could generate higher-temperature flames by avoiding water-cooling; moreover, the flame would not be able to propagate back into the burner at higher pressures.

A second area which should be pursued using LIF is the measurement of pdfs of NO concentration under turbulent flame conditions. The feasibility of such measurements was shown in this study, but little was found in the way of useful results. The best

approach would be to use a jet burner, such as that used in this experiment. However, this is only appropriate if the Reynolds number of the flow can be made large enough to obtain high levels of turbulence. This would require a flow system with a larger available range for the fuel flow. A second option here would be to use a burner design similar to that of Goix and Shephard [1993]. This burner contains a grid to generate turbulence within the burner, above a partially premixed flow configuration. Such a burner may allow for turbulent premixed combustion without the need for very high flow rates.

The method of LIF for NO can also be extended to planar LIF (PLIF). PLIF measurements allow for the measurement of NO concentrations from an entire flow field. This could be useful for determining NO production mechanisms in practical combustors with different combustor geometries. It would also be useful for studying thermal-NO production, for the entire flow field above the burner could be monitored simultaneously. PLIF imaging would be especially useful for turbulent flames, as the fluctuations of the [NO] over an entire flow field could be captured instantaneously, providing a better picture of the turbulence within the flame.

Another possible application for the LIF method would be simultaneous point measurements of temperature and NO concentration in turbulent flames. This could be done with Rayleigh scattering for the temperature measurements and LIF for the [NO] measurements. One of two approaches could be taken for such measurements. First, a second monochromator could be used for the detection of Rayleigh scattering, with the scattering monitored via the optical port opposite the LIF signal monitoring port. This measurement scheme would require precise optical alignment so that the NO concentrations and temperature are measured from the same location in the flame. The second option would be to use a beam splitter to divide the fluorescence signal obtained from only one optical port into two parts and direct each part to different monochromators. However, this approach may reduce the fluorescence signal substantially, and could therefore

only be used successfully in flames with large NO concentrations.

It is also desirable to obtain OH and CH profiles in some high-pressure flames to ascertain the correctness of the hypotheses proposed in Chapters 4 and 5. The OH measurements would be useful for determining if the postulate for the shift in NO concentration with pressure is correct, and the CH profiles could be used to evaluate the ability of the chemical kinetics models to predict the CH profiles in ethylene flames. Due to the rapid decrease in OH and CH concentrations in the post-flame zone, the highest pressure at which these measurements could be usefully performed may be limited. However, some high-pressure measurements of OH and CH should be feasible with LIF.

Finally, it would be desirable to develop reduced chemical kinetics mechanisms which could accurately predict NO concentrations in high-pressure hydrocarbon flames. The size of the current mechanisms does not permit them to be used in turbulent combustion models. The mechanisms must be reduced to contain only a few species with a limited number of controlling elementary reactions [Frenklach, 1991]. This will not be an easy task, for as shown in this study, the prompt-NO mechanism is important for low-temperature production of NO. Therefore, the hydrocarbon kinetics will need to be reduced into a form which contains many fewer species, but still provides accurate predictions of the CH and NO concentrations.

LIST OF REFERENCES

Bachmaier, F., Eberius, K.H., and Just, Th. [1973]. The formation of nitric oxide and detection of HCN in premixed hydrocarbon-air flames at 1 atmosphere. *Combust. Sci. and Tech.* **7**, 77.

Bartok, W., Engleman, V.S., Goldstein, R., and del Valle, E.G. [1972]. Basic kinetic studies and modeling of nitrogen oxide formation in combustion processes. *AIChE Symp. Ser. 126* **68**, 30.

Battles, B.E., Seitzman, J.M., and Hanson, R.K. [1994]. Quantitative planar laser-induced fluorescence imaging of radical species in high pressure flames. AIAA paper 94-0229. Thirty-second Aerospace Sciences Meeting, Reno, NV.

Bernstein, J.S., Fein, A., Choi, J.B., Cool, T.A., Sausa, R.C., Howard, S.L., Locke, R.J., and Miziolek, A.W. [1993]. Laser-based flame species profile measurements: a comparison with flame model predictions. *Combust. Flame* **92**, 85.

Blint, R.J. [1986]. Calculated dependence of flame speed and flame width on pressure, In *Complex Chemical Reaction Systems*, J. Warnatz and W. Jager, eds., Springer-Verlag, New York, p. 253.

Bozzelli, J.W., Ul Karim, M.H., and Dean, A.M. [1993]. Reactions of CH_2 and CH with N_2 and CH with NO. In *Turbulence and Molecular Processes in Combustion*, Takeno, T., ed., Elsevier, p. 101.

Bradley, D. and Matthews, K.J. [1968]. Measurement of high gas temperatures with fine wire thermocouples. *J. Mech. Eng. Sci.* **10**, 299.

Carter, C.D., King, G.B., and Laurendeau, N.M. [1989]. A combustion facility for high-pressure flame studies by spectroscopic methods. *Rev. Sci. Instrum.* **60**, 2606.

Carter, C.D., King, G.B., and Laurendeau, N.M. [1992]. Saturated fluoresence measurements of the hydroxyl radical in laminar high-pressure $C_2H_6/O_2/N_2$ flames. *Appl. Opt.* **31**, 1511.

Carter, C.D. [1992]. Personal Communication.

Carter, C.D. and Barlow, R.S. [1994]. Simultaneous measurements of NO, OH, and the major species in turbulent flames. *Opt. Lett.* (in press).

Carter, C.D. and Laurendeau, N.M. [1994]. Wide- and narrow-band saturated fluorescence measurements of hydroxyl concentration in premixed flames from 1 to 10 bar. *Appl. Phys. B* (accepted for publication).

Cattolica, R.J., Cavolowsky, J.A., and Mataga, T.G. [1989]. Laser-fluorescence measurements of nitric oxide in low-pressure $H_2/O_2/NO$ flames. *Twenty-second Symposium (International) on Combustion*, The Combustion Institute, Pittsburgh, PA, 1165.

Chang, A.Y., DiRosa, M.D., and Hanson, R.K. [1992]. Temperature dependence of collision broadening and shift in the NO A ← X (0,0) band in the presence of argon and nitrogen. *J. Quant. Spectroc. Radiat. Transfer* **47**, 375.

Chou, M.-S., Dean, A.M., and Stern, D. [1983]. Laser induced fluorescence measurements of NO in NH_3/O_2 and CH_4/air flames. *J. Chem. Phys.* **78**, 5962.

Corr, R.A., Malte, P.C., and Marinov, N.M. [1992]. Evaluation of NO_x Mechanisms for Lean, Premixed Combustion. *ASME Journal of Engineering for Gas Turbines and Power* **114**, 425.

Crosley, D.R. [1992]. Personal Communication.

Daily, J.W. [1977]. Saturation effects in laser induced fluorescence spectroscopy. *Appl. Opt.* **16**, 568.

Dean, A.J., Davidson, D.F., Hanson, R.K., and Bowman, C.T., [1988]. Development and application of CH laser absorption diagnostic for shock tube kinetic studies. Western States Section/The Combustion Institute, Paper 88-91.

Dean, A.J., Hanson, R.K., and Bowman, C.T., [1991]. High temperature shock tube study of reactions of CH and C-atoms with N_2. *Twenty-Third Symposium (International) on Combustion*, The Combustion Institute, Pittsburgh, PA, 259.

Deézsi, I. [1958]. A recent rotational analysis of the γ bands of the NO molecule. *Acta Phys. Acad. Sci. Hung.* **9**, 125.

Dibble, R.W. and Hollenbach, R.E. [1981]. Laser Rayleigh thermometry in turbulent flames. *Eighteenth Symposium (International) on Combustion*, The Combustion Institute, Pittsburgh, PA, 1489.

DiRosa, M.D. and Hanson, R.K. [1994]. Collision-broadening and -shift of NO γ(0,0) absorption lines by H_2O, O_2, and NO at 295 K. *J. Molec. Spectrosc.* **164**, 97.

Drake, M.C. and Pitz, R.W. [1985]. Comparison of turbulent diffusion flame measurements of OH by planar fluorescence and saturated fluorescence. *Exp. in Fluids.* **3**, 283.

Drake, M.C. and Blint, R.J. [1991]. Calculations of NO_x formation pathways in propagating laminar, high pressure premixed CH_4/air flames. *Combust. Sci. and Tech.*, **75**, 261.

Drake, M.C., Ratcliffe, J.W., Blint, R.J., Carter C.D., and Laurendeau N.M. [1991]. Measurements and modelling of flamefront NO formation and superequilibrium radical concentrations in laminar high-pressure premixed flames. *Twenty-third Symposium (International) on Combustion*, The Combustion Institute, Pittsburgh, PA, 387.

Drake, M.C., and Blint, R.J. [1992]. Personal Communication.

Drake, M.C. [1993]. "High pressure nitric oxide formation: kinetics modeling and laser experiments." Joint Central and Eastern States Section/The Combustion Institute, Spring Technical Meeting, New Orleans.

Drake, M.C., and Ratcliffe, J.W. [1993]. High temperature quenching cross sections for nitric oxide laser-induced fluorescence measurements. *J. Chem. Phys.* **98**, 3850.

Dreier, T. and Rakestraw, D.J. [1990]. Measurement of OH rotational temperatures in a flame using degenerate four-wave mixing. *Opt. Lett.* **15**, 72.

Duterque, J., Avezard, N., and Borghi, R. [1981]. Further results on nitrogen oxides produced in combustion zones. *Combust. Sci. and Tech.* **25**, 85.

Eckbreth, A.C., Bonczyk, P.A., and Verdieck, J.F. [1979]. Combustion diagnostics by laser Raman and fluorescence techniques. *Prog. Energy Combust. Sci.* **5**, 253.

Fenimore, C.P. [1971]. Formation of nitric oxide in premixed hydrocarbon flames. *Thirteenth Symposium (International) on Combustion*, The Combustion Institute, Pittsburgh, PA, 373.

Ferguson, C.R. and Keck, J.C. [1979]. Stand-off distances on a flat flame burner. *Combust. Flame* **34**, 85.

Fontijn, A., Sabadell, A.J., and Ronco, R.J. [1970]. Homogeneous chemiluminescent measurement of nitric oxide with ozone. *Anal. Chem.* **42**, 575.

Freedman, R. and Nicholls, R.W. [1980]. Molecular constants for the $v'' = 0$ ($X^2\Pi$) and $v' = 0, 1$ ($A^2\Sigma^+$) levels of the NO molecule and its isotopes. *J. Molec. Spectrosc.* **83**, 223.

Frenklach, M. [1991]. Reduction of Chemical Reaction Models, In *Numerical Approaches to Combustion Modeling*. E.S. Oran and J.P. Boris, eds., AIAA, Washington.

Fristrom, R.M.,and Westenberg, A.A. [1965]. *Flame Structure*, McGraw-Hill, New York.

Gardiner, W.C., Jr., Hidaka, Y., and Tanzawa, T. [1981]. Refractivity of combustion gases. *Combust. Flame* **40**, 213.

Gardiner, W.C., Jr., and Troe, J. [1984]. Rate coefficients of thermal dissociation, isomerization, and recombination reactions, In *Combustion Chemistry*, W.C. Gardiner Jr., ed., Springer-Verlag, New York.

Garo, A., Hilaire, C., and Puechberty, D. [1992]. Experimental study of methanol-oxygen flames doped with nitrogen oxide or ammonia. Comparison with modeling. *Combust. Sci. and Tech.* **86**, 87.

Glarborg, P., Miller, J.A., and Kee, R.J. [1986]. Kinetic modeling and sensitivity analysis of nitrogen oxide formation in well-stirred reactors. *Combust. Flame* **65**, 177.

Goix, P.J. and Shepherd, I.G. [1993]. Lewis number effects on turbulent premixed flame structure. *Combust. Sci. and Tech.* **91**, 191.

Hanson, R.K., and Salimian, S. [1984]. Survey of rate constants in the N/H/O system, In *Combustion Chemistry*, W.C. Gardiner Jr., ed., Springer-Verlag, New York.

Harris, J.M., Lytle, F.E., and McCain, T.C. [1976]. Squirrel-cage photomultiplier base design for measurement of nanosecond fluorescence decays. *Anal. Chem.* **48**, 2095.

Heard, D.W., Jeffries, J.B., Smith, G.P., and Crosley, D.R. [1992]. LIF measurements in methane/air flames of radicals important in prompt-NO formation. *Combust. Flame* **88**, 137.

Heberling, P.V. [1977]. "Prompt NO" measurements at high pressure. *Sixteenth Symposium (International) on Combustion*, The Combustion Institute, Pittsburgh, PA, 159.

Hoffman, J.D. [1992]. *Numerical Methods for Engineers and Scientists*, McGraw-Hill, New York.

Howard, S.L., Locke, R.L, Sausa, R.C., Kotlar, A.J., and Miziolek, A.W. [1992]. Laser-based spectroscopic studies of propellant-like low-pressure flames. *Ballistic Research Laboratory Report BRL-TR-3369*.

Humlícek, J. [1979]. An efficient method for the evaluation of the complex probability function: the Voigt function and its derivatives. *J. Quant. Spectroc. Radiat. Transfer* **21**, 309.

Inbody, M.A. [1990]. Personal communication.

Jacobs, D.C. [1986]. Reduction of 1+1 resonance enhanced MPI spectra to population distributions: application to the NO $A^2\Sigma^+$-$X^2\Pi$ system. *J. Chem. Phys.* **85**, 5469.

Johnston, H. [1971]. Reduction of stratospheric ozone by nitrogen oxide catalysts from supersonic transport exhaust. *Science* **173**, 517.

Kee, R.J., Grcar, J.F., Smooke, M.D., and Miller, J.D. [1985]. A Fortran program for modeling steady laminar one-dimensional premixed flames. *Sandia Report SAND85-8240.*

Kee, R.J., Dixon-Lewis Jr., G., Warnatz, J., Coltrin, M.E., and Miller, J.A., [1986]. A Fortran computer code package for the evaluation of gas-phase multicomponent transport properties. *Sandia Report SAND86-8246.*

Kee, R.J., Rupley, F.M., and Miller, J.A., [1987]. A Chemical thermodynamic data base. *Sandia Report SAND87-8215.*

Kee, R.J., Rupley, F.M., and Miller, J.A., [1989]. CHEMKIN-II: A Fortran chemical kinetics package for the analysis of gas-phase chemical kinetics. *Sandia Report SAND89-8009.*

Koechner, W. [1992]. *Solid-State Laser Engineering*, Springer-Verlag, Berlin.

Kohse-Höinghaus, K., Heidenreich, R., and Just, Th. [1984]. Determination of absolute OH and CH concentrations in a low pressure flame by laser-saturated fluorescence. *Twentieth Symposium (International) on Combustion*, The Combustion Institute, Pittsburgh, PA, 1177.

Larson, H.J. [1969]. *Introduction to Probability Theory and Statistical Inference*, John Wiley & Sons, New York.

Laurendeau, N.M. [1988]. Temperature measurements by light-scattering methods. *Prog. Energy Combust. Sci.* 14, 147.

Laurendeau, N.M. and Goldsmith, J.E.M. [1989]. Comparison of hydroxyl concentration profiles using five laser-induced fluorescence methods in a lean subatmospheric-pressure $H_2/O_2/Ar$ flame. *Combust. Sci. and Tech.* 63, 139.

Leonard, G.L. and Correa, S.M. [1990]. NO_x formation in premixed high-pressure lean methane flames. *Fossil Fuel Combustion Symposium 1990*, ASME/PD Vol. 30, Singh, S.N., ed., 69.

Lucht, R.P., Peterson, R.C., and Laurendeau, N.M. [1978]. "Fundamentals of Absorption Spectroscopy fro Selected Diatomic Flame Radicals," *Report PURDU-CL-78-06*, School of Mechanical Engineering, Purdue University, West Lafayette, IN.

Lucht, R.P., Sweeney, D.W., Laurendeau, N.M., Drake, M.C., Lapp, M., and Pitz, R.W. [1984]. Single-pulse, laser-saturated fluorescence measurements of OH in turbulent nonpremixed flames. *Opt. Lett.* 9, 90.

Lucht, R.P., Sweeney, D.W., and Laurendeau, N.M. [1985]. Laser-saturated fluorescence measurements of OH in atmospheric pressure $CH_4/O_2/N_2$ flames under sooting and non-sooting conditions. *Combust. Sci. and Tech.* 42, 259.

Mallard, W.G., Miller, J.H., and Smyth, K.C. [1982]. Resonantly enhanced two-photon photoionization of NO in an atmospheric flame. *J. Chem. Phys.* **76**, 3483.

Malte, P.C. and Pratt, D.T. [1974]. The role of energy-releasing kinetics in NO_x formation: fuel-lean, jet-stirred, CO-air combustion. *Combust. Sci. and Tech.* **9**, 221.

Matheson Gas Products [1990]. 932 Peterson Plank Road, East Rutherford, NJ 07073.

Measures, R.M. [1984]. *Laser Remote Sensing: Fundamentals and Applications*, John Wiley & Sons, New York.

Miller, J.A. and Fisk, G.A. [1987]. Combustion Chemistry. *Chem. Eng. News* **65**, 22.

Miller, J.A. and Bowman, C.T. [1989]. Mechanism and Modelling of Nitrogen Chemistry in Combustion. *Prog. Energy Combust. Sci.* **15**, 287.

Miller, J.A., Volponi, J.V., Durant Jr., J.L., Goldsmith, J.E.M., Fisk, G.A., and Kee, R.J. [1991]. The structure and reaction mechanism of rich, non-sooting $C_2H_2/O_2/Ar$ flames. *Twenty-third Symposium (International) on Combustion*, The Combustion Institute, Pittsburgh, PA, 187.

Miller, J.A. [1992]. Personal Communication.

Miller, J.A. and Melius, C.F. [1992]. Kinetic and thermodynamic issues in the formation of aromatic compounds in flames of aliphatic fuels. *Combust. Flame* **91**, 21.

Morley, C. [1981]. The mechanism of NO formation from nitrogen compounds in hydrogen flames studied by laser fluorescence. *Eighteenth Symposium (International) on Combustion*, The Combustion Institute, Pittsburgh, PA, 23.

Morley, C. [1982]. The application of laser fluorescence to detection of species in atmospheric pressure flames. *Combust. Flame* **47**, 67.

Mortimer, C.E. [1983]. *Chemistry*, Wadsworth Publishing Company, Belmont, CA.

Namer, I. and Schefer, R.W. [1985]. Error estimates for Rayleigh scattering density and temperature measurements in premixed flames. *Exp. in Fluids* **3**, 1.

Norton, T.S., Smyth, K.C., Miller, J.H., and Smooke, M.D. [1993]. Comparison of experimental and computed species concentration and temperature profiles in laminar, two-dimensional methane/air diffusion flames. *Combust. Sci. and Tech.* **90**, 1.

Partridge Jr., W.P. [1994]. Personal Communication

Rajan, S., Smith, J.R., and Rambach, G.D. [1984]. Internal mixing of a turbulent premixed flame using Rayleigh scattering. *Combust. Flame* **57**, 95.

Ramsey, N.F. [1985]. *Molecular Beams*, Oxford Univ. Press, Oxford.

Reisel, J.R. [1991]. Laser-saturated fluorescence measurements of nitric oxide in atmospheric-pressure flames. M.S. Thesis, School of Mechanical Engineering, Purdue University, West Lafayette, IN.

Reisel, J.R., Carter, C.D., and Laurendeau, N.M. [1992]. Einstein coefficients for rotational lines of the (0,0) band of the NO $A^2\Sigma^+$-$X^2\Pi$ system. *J. Quant. Spectroc. Radiat. Transfer*, **47**, 43.

Reisel, J.R., Carter, C.D., Laurendeau, N.M., and Drake, M.C. [1993]. Laser-saturated fluoresence measurements of nitric oxide in laminar, flat, C_2H_6/O_2/N_2 flames at atmospheric pressure. *Combust. Sci. and Tech.* **91**, 271.

Rockney, B.H., Cool, T.A., and Grant, E.R. [1982]. Detection of nascent NO in a methane/air flame by multiphoton ionization. *Chem. Phys. Lett.* **87**, 141.

Rudder, R.R., and Bach, D.R. [1968]. Rayleigh scattering of ruby-laser light by neutral gases. *J. Opt. Soc. Am.* **58**, 1260.

Salmon, J.T., Lucht, R.P., Sweeney, D.W., and Laurendeau, N.M. [1984]. Laser-saturated fluorescence measurements of NH in a premixed subatmospheric CH_4/N_2O/Ar flame. *Twentieth Symposium (International) on Combustion*, The Combustion Institute, Pittsburgh, PA, 1187.

Salmon, J.T. and Laurendeau, N.M. [1985]. Calibration of laser-saturated fluorescence measurements using Rayleigh scattering. *Appl. Opt.* **24**, 65.

Salmon, J.T. and Laurendeau, N.M. [1987]. Absolute concentration measurements of atomic hydrogen in subatmospheric premixed H_2/O_2/N_2 flat flames with photoionization controlled-loss spectroscopy. *Appl. Opt.* **26**, 2881.

Seery, D.J., and Zabielski, M.F. [1981]. Molecular beam sampling-mass spectrometer study of H_2-O_2-N_2 flames. *Eighteenth Symposium (International) on Combustion*, The Combustion Institute, Pittsburgh, PA, 397.

Seitzman, J.M. [1991]. Quantitative Applications of Fluoresence Imaging in Combustion. Ph.D. dissertation, Department of Mechanical Engineering, Stanford University, Palo Alto, California.

Shrader, S.R. [1971]. *Introductory Mass Spectrometry*, Allyn and Bacon Inc., Boston.

Stepowski, D. and Cabot, G. [1992]. Single-shot temperature and mixture fraction profiles by Rayleigh scattering in the development zone of a turbulent diffusion flame. *Combust. Flame* **88**, 296.

Taylor, J.R. [1982]. *An Introduction to Error Analysis*, University Science Books, Mill Valley, CA.

Vaughn, C.B., Sun, W.H., Howard, J.B., and Longwell, J.P. [1991]. Measurements and modeling of light hydrocarbons in rich C_2H_4 combustion in a jet-stirred reactor. *Combust. Flame* **84**, 38.

Wolfrum, J. [1972]. Bildung von Stickstoffoxiden bei der Verbrennung. *Chem. Ing. Tech.* **44**, 656.

Wysong, I.J., Jeffries, J.B., and Crosley, D.R. [1989]. Laser-induced fluorescence of $O(3p^3P)$, O_2, and NO near 226 nm: photolytic interferences and simultaneous excitation in flames. *Opt. Lett.* **14**, 767.

Zabarnick, S. [1992]. A comparison of $CH_4/NO/O_2$ and CH_4/N_2O flames by LIF diagnostics and chemical kinetic modeling. *Combust. Sci. and Tech.* **83**, 115.

Zacharias, H., Schmiedl, R., and Welge, K.H. [1980]. State selective step-wise photoionization of NO with mass spectroscopic ion detection. *Appl. Phys.* **21**, 127.

Zeldovich, J. [1946]. The oxidation of nitrogen in combustion and explosions. *Acta Physiochem. URSS* **21**, 577.

Appendix A - Chemical Kinetics Reaction Mechanisms

This appendix contains the three primary comprehensive chemical kinetics schemes used as input for the computer modeling of the various flames. The first elementary reaction mechanism was compiled by Drake and Blint [1991] (GMK-DB). The mechanism was developed primarily by Glarborg et al. [1986]; however modifications to the mechanism were made using results found by Hanson and Saliman [1984] and by Dean et al. [1988]. In addition, a propane mechanism was added to the GMK scheme, which probably has little effect on the $C_2H_6/O_2/N_2$ flames modeled. The input to the computer model is organized in the following manner. First, the elements considered are listed, followed by the species which are considered, and ending with the elementary reactions in the mechanism. The numbers listed after each reaction represent the constants A, n, and E_a, respectively, in the Arrhenius expression

$$k_f = AT^n \exp\left\{\frac{-E_a}{RT}\right\} \quad , \tag{A.1}$$

where k_f is the rate coefficient for the reaction, T is the temperature (K) and R is the ideal gas constant (cal/gm-mole•K). Some of the reactions containing the third-body species "M" are followed by another line with various species listed. These species represent the "M" in the previous equation, and the numbers represent the third-body enhancement efficiency, which is the amount that the rate coefficients are multiplied by for that species. If this number is 0.0, the above rate coefficient does not apply for that species; rather, the chemical reaction with that species acting as a third-body is located below that line in the mechanism. One reaction is followed by a line containing "DUP"; this indicates that this reaction contains a third-body which is listed later in the mechanism, and the later equation also is followed by "DUP".

The chemical kinetics input for the GMK-DB model can be found below. This mechanism is designed for use at atmospheric pressure. Four reaction rate coefficients are changed at higher pressures, and these values can be found in Chapter 3.

```
ELEMENTS
H C O N
END

SPECIES
N2 CO CO2 O2 H2O H2 OH O H HO2 H2O2
CH4 CH3 CH2 CH C CH2O HCO
C2H6 C2H5 C2H4 C2H3 C2H2 C2H
C3H6 C3H2
CH3O CH2CO HCCO C3H8 C3H7(N) C3H7(I)
NO N NO2 HNO NH3 NH2 NH N2H2 NNH N2O
HCN CN
NCO HNCO HCNO HOCN C2N2
END

REACTIONS
```

H+O2=O+OH	5.10E+16	-0.820	16510.0
H2+O=H+OH	1.80E+10	1.000	8830.0
H2+OH=H2O+H	1.20E+09	1.300	3630.0
OH+OH=H2O+O	6.00E+08	1.300	0.0
H+OH+M=H2O+M	7.50E+23	-2.600	0.0
H2O/20.0/			
O2+M=O+O+M	1.90E+11	0.500	95560.0
H+H+M=H2+M	1.00E+18	-1.000	0.0
H2/0./ H2O/0./ CO2/0./			
H+H+H2=H2+H2	9.20E+16	-0.600	0.0
H+H+H2O=H2+H2O	6.00E+19	-1.250	0.0
H+H+CO2=H2+CO2	5.50E+20	-2.000	0.0
H2+O2=OH+OH	1.70E+13	0.000	47780.0
H+O2+O2=HO2+O2	6.70E+19	-1.420	0.0
H+O2+N2=HO2+N2	6.70E+19	-1.420	0.0
DUP			
HO2+H=H2+O2	2.50E+13	0.000	700.0
HO2+H=OH+OH	2.50E+14	0.000	1900.0
HO2+O=OH+O2	4.80E+13	0.000	1000.0
HO2+OH=H2O+O2	5.00E+13	0.000	1000.0
HO2+HO2=H2O2+O2	2.00E+12	0.000	0.0
H2O2+M=OH+OH+M	1.20E+17	0.000	45500.0
H2O2+H=HO2+H2	1.70E+12	0.000	3750.0
H2O2+OH=H2O+HO2	1.00E+13	0.000	1800.0
CO+O+M=CO2+M	3.20E+13	0.000	-4200.0
CO+O2=CO2+O	2.50E+12	0.000	47700.0
CO+OH=CO2+H	1.50E+07	1.300	-760.0

CO+HO2=CO2+OH	5.80E+13	0.000	22930.0
HCO+M=CO+H+M	1.60E+14	0.000	14700.0
HCO+H=CO+H2	4.00E+13	0.000	0.0
HCO+O=CO+OH	3.00E+13	0.000	0.0
HCO+O=CO2+H	3.00E+13	0.000	0.0
HCO+OH=CO+H2O	5.00E+12	0.000	0.0
HCO+O2=CO+HO2	3.30E+13	-0.400	0.0
CH2O+M=HCO+H+M	3.30E+16	0.000	81000.0
CH2O+H=HCO+H2	2.20E+08	1.770	10500.0
CH2O+O=HCO+OH	1.80E+13	0.000	3080.0
CH2O+OH=HCO+H2O	3.40E+09	1.180	-447.0
CH4+H=CH3+H2	2.20E+04	3.000	8750.0
CH4+O=CH3+OH	1.20E+07	2.080	7630.0
CH4+OH=CH3+H2O	3.50E+03	3.080	2000.0
CH4+CH2=CH3+CH3	1.30E+13	0.000	9500.0
CH3+M=CH2+H+M	1.90E+16	0.000	91600.0
CH3+H=CH2+H2	9.00E+13	0.000	15100.0
CH3+O=CH2O+H	6.80E+13	0.000	0.0
CH3+O=CH2+OH	5.00E+13	0.000	12000.0
CH3+OH=CH2+H2O	1.50E+13	0.000	5000.0
CH3+OH=CH2O+H2	1.00E+12	0.000	0.0
CH3+O2=CH2O+OH	5.20E+13	0.000	34570.0
CH2+H=CH+H2	7.30E+17	-1.560	0.0
CH2+O=CO+H+H	3.00E+13	0.000	0.0
CH2+O=CO+H2	5.00E+13	0.000	0.0
CH2+O=CH+OH	5.00E+13	0.000	12000.0
CH2+OH=CH2O+H	3.00E+13	0.000	0.0
CH2+OH=CH+H2O	4.50E+13	0.000	3000.0
CH2+O2=CO2+H+H	1.60E+12	0.000	1000.0
CH2+O2=CO2+H2	6.90E+11	0.000	500.0
CH2+O2=CO+H2O	1.90E+10	0.000	-1000.0
CH2+O2=CO+OH+H	8.60E+10	0.000	-500.0
CH2+O2=HCO+OH	4.30E+10	0.000	-500.0
CH2+O2=CH2O+O	2.00E+13	0.000	9000.0
CH2+CO2=CO+CH2O	1.10E+11	0.000	1000.0
CH+H=C+H2	1.50E+14	0.000	0.0
CH+O=CO+H	5.70E+13	0.000	0.0
CH+OH=HCO+H	3.00E+13	0.000	0.0
CH+O2=HCO+O	3.30E+13	0.000	0.0
CH+CO2=HCO+CO	3.40E+12	0.000	690.0
C+CH4=CH+CH3	5.00E+13	0.000	24000.0
C+OH=CO+H	5.00E+13	0.000	0.0
C+O2=CO+O	2.00E+13	0.000	0.0
C+CO2=CO+CO	6.00E+08	0.000	0.0
CH3+O2=CH3O+O	7.00E+12	0.000	25650.0
CH3O+M=CH2O+H+M	1.00E+14	0.000	25000.0
CH3O+H=CH2O+H2	2.00E+13	0.000	0.0
CH3O+O=CH2O+OH	1.00E+13	0.000	0.0
CH3O+OH=CH2O+H2O	1.00E+13	0.000	0.0
CH3O+O2=CH2O+HO2	6.30E+10	0.000	2600.0
CH2CO+M=CH2+CO+M	3.60E+15	0.000	59300.0
CH2CO+H=CH3+CO	1.10E+13	0.000	3430.0
CH2CO+H=HCCO+H2	7.50E+13	0.000	8000.0

CH2CO+O=CH2O+CO	2.00E+13	0.000	0.0
CH2CO+O=HCCO+OH	5.00E+13	0.000	8000.0
CH2CO+OH=CH2O+HCO	2.80E+13	0.000	0.0
CH2CO+OH=HCCO+H2O	7.50E+12	0.000	3000.0
HCCO+H=CH2+CO	1.10E+14	0.000	0.0
HCCO+O=CO+CO+H	1.10E+14	0.000	0.0
HCCO+OH=HCO+CO+H	1.00E+13	0.000	0.0
HCCO+O2=CO+CO+OH	1.50E+12	0.000	2500.0
CH2+CH=C2H2+H	4.00E+13	0.000	0.0
CH2+CH2=C2H2+H2	3.20E+13	0.000	0.0
CH+CH3=C2H3+H	3.00E+13	0.000	0.0
CH+CH4=C2H4+H	6.00E+13	0.000	0.0
CH+C2H2=C3H2+H	1.30E+14	0.000	00.0
C+CH3=C2H2+H	5.00E+13	0.000	0.0
C+CH2=C2H+H	5.00E+13	0.000	0.0
CH3+CH2=C2H4+H	3.00E+13	0.000	0.0
C2H6+H=C2H5+H2	5.40E+02	3.500	5200.0
C2H6+O=C2H5+OH	2.50E+13	0.000	6360.0
C2H6+OH=C2H5+H2O	8.70E+09	1.050	1810.0
C2H6+CH3=C2H5+CH4	5.50E-01	4.000	8280.0
C2H6+CH2=CH3+C2H5	2.20E+13	0.000	8660.0
C2H5+O2=C2H4+HO2	3.20E+12	0.000	5020.0
C2H4+H=C2H3+H2	1.10E+14	0.000	8500.0
C2H4+O=HCO+CH3	1.60E+09	1.200	746.0
C2H4+OH=C2H3+H2O	4.80E+12	0.000	1230.0
C2H4+OH=CH2O+CH3	2.00E+12	0.000	960.0
C2H3+H=C2H2+H2	4.00E+13	0.000	0.0
C2H3+O=CH2CO+H	3.30E+13	0.000	00.0
C2H3+OH=C2H2+H2O	5.00E+12	0.000	0.0
C2H3+O2=HCO+CH2O	4.00E+12	0.000	-250.0
C2H3+CH2=C2H2+CH3	3.00E+13	0.000	0.0
C2H3+C2H=C2H2+C2H2	3.00E+13	0.000	0.0
C2H2+M=C2H+H+M	4.20E+16	0.000	107000.0
C2H+H2=C2H2+H	4.10E+05	2.390	860.0
C2H2+O=CH2+CO	2.20E+10	1.000	2580.0
C2H2+O=HCCO+H	3.60E+04	2.700	1390.0
C2H2+O=C2H+OH	3.20E+15	-0.600	15000.0
C2H2+OH=CH2CO+H	3.20E+11	0.000	200.0
C2H2+OH=C2H+H2O	6.00E+12	0.000	7000.0
HCCO+CH2=C2H+CH2O	1.00E+13	0.000	2000.0
HCCO+CH2=C2H3+CO	3.00E+13	0.000	0.0
HCCO+HCCO=C2H2+CO+CO	1.00E+13	0.000	0.0
C2H+O=CH+CO	5.00E+13	0.000	0.0
C2H+OH=HCCO+H	2.00E+13	0.000	0.0
C2H+O2=CO+HCO	2.40E+12	0.000	0.0
C2H+O2=HCCO+O	6.00E+11	0.000	0.0
HNO+M=H+NO+M	1.50E+16	0.000	48680.0
H2O/6.0/ H2/2.0/ O2/2./ N2/2./			
HNO+H=H2+NO	5.00E+12	0.000	0.0
HNO+OH=NO+H2O	3.60E+13	0.000	0.0
NH3+M=NH2+H+M	1.40E+16	0.060	90600.0
NH3+H=NH2+H2	7.00E+06	2.390	10171.0
NH3+O=NH2+OH	2.10E+13	0.000	9000.0

NH3+OH=NH2+H2O	2.04E+06	2.040	566.0
NH2+H=NH+H2	6.90E+13	0.000	3650.0
NH2+O=NH+OH	6.80E+12	0.000	0.0
NH2+O=HNO+H	6.60E+14	-0.500	0.0
NH2+OH=NH+H2O	4.50E+12	0.000	2200.0
NH2+N=N2+H+H	7.20E+13	0.000	0.0
NH2+NO=N2+H2O	3.80E+15	-1.250	0.0
NH+H=N+H2	3.00E+13	0.000	0.0
NH+O=NO+H	2.00E+13	0.000	0.0
NH+OH=HNO+H	2.00E+13	0.000	0.0
NH+OH=N+H2O	5.00E+11	0.500	2000.0
NH+O2=HNO+O	1.00E+13	0.000	12000.0
NH+O2=NO+OH	1.40E+11	0.000	2000.0
NH+N=N2+H	3.00E+13	0.000	0.0
N+O2=NO+O	6.40E+09	1.000	6280.0
N+OH=NO+H	3.80E+13	0.000	0.0
N+CO2=NO+CO	1.90E+11	0.000	3400.0
NO+HO2=NO2+OH	2.10E+12	0.000	-480.0
NO2+M=NO+O+M	1.10E+16	0.000	66000.0
NO2+H=NO+OH	3.50E+14	0.000	1500.0
NO2+O=NO+O2	1.00E+13	0.000	600.0
N2H2+M=NNH+H+M	5.00E+16	0.000	50000.0
N2H2+H=NNH+H2	5.00E+13	0.000	1000.0
NNH+M=N2+H+M	2.00E+14	0.000	20000.0
NNH+H=N2+H2	3.70E+13	0.000	3000.0
NNH+NO=N2+HNO	5.00E+13	0.000	0.0
NH2+NH=N2H2+H	5.00E+13	0.000	0.0
NH2+NO=NNH+OH	8.80E+15	-1.250	0.0
NH+NO=N2O+H	4.30E+14	-0.500	0.0
N2O+H=N2+OH	7.60E+13	0.000	15200.0
N2O+O=NO+NO	1.00E+14	0.000	28200.0
N2O+O=N2+O2	1.00E+14	0.000	28200.0
CH+NO=HCN+O	1.10E+14	0.000	0.0
CH2+N2=HCN+NH	1.00E+13	0.000	74000.0
CH+NH2=HCN+H+H	3.00E+13	0.000	0.0
CH+NH=HCN+H	5.00E+13	0.000	0.0
CH2+NH=HCN+H+H	3.00E+13	0.000	0.0
CH+N=CN+H	1.30E+13	0.000	0.0
CH2+N=HCN+H	5.00E+13	0.000	0.0
CH3+N=HCN+H+H	5.00E+13	0.000	0.0
CH4+N=NH+CH3	1.00E+13	0.000	24000.0
HCN+O=CN+OH	2.70E+09	1.580	26600.0
HCN+O=NH+CO	3.50E+03	2.640	4980.0
HCN+OH=CN+H2O	1.50E+13	0.000	10929.0
CN+O=CO+N	1.80E+13	0.000	0.0
CN+H2=HCN+H	3.00E+05	2.450	2237.0
C+NO=CN+O	6.60E+13	0.000	0.0
C+N2O=CN+NO	1.00E+13	0.000	0.0
N+HCCO=HCN+CO	5.00E+13	0.000	0.0
HCN+OH=HNCO+H	4.80E+11	0.000	11000.0
NCO+H2=HNCO+H	8.60E+12	0.000	9000.0
HOCN+H=HNCO+H	1.00E+13	0.000	0.0
HNCO+H=NH2+CO	2.00E+13	0.000	3000.0

CH2+NO=HCNO+H	1.40E+12	0.000	-1100.0
HCNO+H=HCN+OH	5.00E+13	0.000	12000.0
HCN+OH=HOCN+H	9.20E+12	0.000	15000.0
C2N2+OH=HOCN+CN	1.90E+11	0.000	2900.0
HCN+O=NCO+H	1.40E+04	2.640	4980.0
CN+OH=NCO+H	6.00E+13	0.000	0.0
CN+O2=NCO+O	5.60E+12	0.000	0.0
CN+NO2=NCO+NO	3.00E+13	0.000	0.0
CN+N2O=NCO+N2	1.00E+13	0.000	0.0
NCO+M=N+CO+M	3.10E+16	-0.500	48000.0
NCO+H=NH+CO	5.00E+13	0.000	0.0
NCO+O=NO+CO	5.60E+13	0.000	0.0
NCO+OH=NO+CO+H	1.00E+13	0.000	0.0
NCO+N=N2+CO	2.00E+13	0.000	0.0
NCO+NO=N2O+CO	1.00E+13	0.000	-390.0
HCN+CN=C2N2+H	2.00E+13	0.000	0.0
C2N2+O=NCO+CN	4.60E+12	0.000	8880.0
N+NO=N2+O	3.30E+12	0.300	0.0
N2O=N2+O	2.13E+19	-2.558	63584.0
CH+N2=HCN+N	4.20E+12	0.000	20400.0
C2H5+CH3=C3H8	2.0E+13	0.0	0.0
H+C3H8=H2+C3H7(N)	1.3E+14	0.0	9700.0
H+C3H8=H2+C3H7(I)	1.0E+14	0.0	8360.0
O+C3H8=OH+C3H7(N)	3.0E+13	0.0	5760.0
O+C3H8=OH+C3H7(I)	2.6E+13	0.0	4440.0
OH+C3H8=H2O+C3H7(N)	3.7E+12	0.0	1650.0
OH+C3H8=H2O+C3H7(I)	2.8E+12	0.0	860.0
C3H7(N)=C2H4+CH3	3.0E+14	0.0	33030.0
C3H7(I)=C3H6+H	2.0E+14	0.0	38740.0
C3H7(N)=C3H6+H	1.0E+14	0.0	37330.0
C3H8+HO2=C3H7(N)+H2O2	5.00E+12	0.0	18000.0
C3H8+HO2=C3H7(I)+H2O2	5.00E+12	0.0	18000.0
H+O2+M=HO2+M	2.10E+18	-1.000	0.0

H2O/21.0/ CO2/5./ H2/3.3/ CO/2./ O2/0./ N2/0./
DUP

C2H5+H=CH3+CH3	4.00E+13	0.000	0.0
CH3+CH3=C2H4+H2	2.10E+14	0.000	19200.0
CH4=CH3+H	4.4E+30	-5.158	104290.0
C2H6=CH3+CH3	3.9E+31	-4.810	91908.0
C2H5=C2H4+H	3.1E+23	-3.384	42121.0
C2H3+M=C2H2+H+M	3.0E+15	0.000	32027.0
C2H4+M=C2H2+H2+M	2.60E+17	0.000	79350.0
C2H4+M=C2H3+H+M	2.60E+17	0.000	96600.0

END

The next chemical kinetics model used is that of Miller and Bowman [1989]. This mechanism has a similar format to the GMK-DB mechanism. However, the pressure dependencies of several reactions are handled by directly including the curve-fitting parameters for the Troe, SRI, or Lindemann-Hinshelwood corrections. A common feature of these fits is the parameter "LOW", which represents the low-pressure limit of the reaction rate coefficient. The details of these corrections can be found in Kee *et al.* [1989]. The MB model is listed below.

```
ELEMENTS
 H C O N
END
SPECIES
  CH4 CH3 CH2 CH C CH2(S) CH3O CH2O CH2OH
  CO2 CO C CH2CO
  C2H6 C2H5 C2H4 C2H3 C2H2 C2H C2N2
  C3H2 C4H2
  H HO2 H2 H2O H2O2 HCO HCCO HCCOH
  O2 OH O N2
  N NH NO NCO NO2 N2O NH2 NH3 NNH
  HCN H2CN HCNO HOCN HNCO HNO CN
  H2CCCH H2CCCCH
END
```

REACTIONS

Reaction	A	n	E
CH3+CH3(+M)=C2H6(+M)	9.03E+16	-1.200	654.0
LOW/3.18E+41 -7.0 2762./			
TROE/ .604 6927. 132./			
H2/2.0/ CO/2.0/ CO2/3.0/ H2O/5.0/			
CH3+H(+M)=CH4(+M)	6.00E+16	-1.000	0.0
LOW/8.0E+26 -3.0 0.0/			
SRI/0.45 797.0 979./			
H2/2.0/ CO/2.0/ CO2/3.0/ H2O/5.0/			
CH4+O2=CH3+HO2	7.90E+13	0.000	56000.0
CH4+H=CH3+H2	2.20E+04	3.000	8750.0
CH4+OH=CH3+H2O	1.60E+06	2.100	2460.0
CH4+O=CH3+OH	1.02E+09	1.500	8604.0
CH4+HO2=CH3+H2O2	1.80E+11	0.000	18700.0
CH3+HO2=CH3O+OH	2.00E+13	0.000	0.0
CH3+O2=CH3O+O	2.05E+18	-1.570	29229.0
CH3+O=CH2O+H	8.00E+13	0.000	0.0
CH2OH+H=CH3+OH	1.00E+14	0.000	0.0
CH3O+H=CH3+OH	1.00E+14	0.000	0.0
CH3+OH=CH2+H2O	7.50E+06	2.000	5000.0
CH3+H=CH2+H2	9.00E+13	0.000	15100.0

CH3O+M=CH2O+H+M	1.00E+14	0.000	25000.0
CH2OH+M=CH2O+H+M	1.00E+14	0.000	25000.0
CH3O+H=CH2O+H2	2.00E+13	0.000	0.0
CH2OH+H=CH2O+H2	2.00E+13	0.000	0.0
CH3O+OH=CH2O+H2O	1.00E+13	0.000	0.0
CH2OH+OH=CH2O+H2O	1.00E+13	0.000	0.0
CH3O+O=CH2O+OH	1.00E+13	0.000	0.0
CH2OH+O=CH2O+OH	1.00E+13	0.000	0.0
CH3O+O2=CH2O+HO2	6.30E+10	0.000	2600.0
CH2OH+O2=CH2O+HO2	1.48E+13	0.000	1500.0
CH2+H=CH+H2	1.00E+18	-1.560	0.0
CH2+OH=CH+H2O	1.13E+07	2.000	3000.0
CH2+OH=CH2O+H	2.50E+13	0.000	0.0
CH+O2=HCO+O	3.30E+13	0.000	0.0
CH+O=CO+H	5.70E+13	0.000	0.0
CH+OH=HCO+H	3.00E+13	0.000	0.0
CH+CO2=HCO+CO	3.40E+12	0.000	690.0
CH+H=C+H2	1.50E+14	0.000	0.0
CH+H2O=CH2O+H	1.17E+15	-0.750	0.0
CH+CH2O=CH2CO+H	9.46E+13	0.000	-515.0
CH+C2H2=C3H2+H	1.00E+14	0.000	0.0
CH+CH2=C2H2+H	4.00E+13	0.000	0.0
CH+CH3=C2H3+H	3.00E+13	0.000	0.0
CH+CH4=C2H4+H	6.00E+13	0.000	0.0
C+O2=CO+O	2.00E+13	0.000	0.0
C+OH=CO+H	5.00E+13	0.000	0.0
C+CH3=C2H2+H	5.00E+13	0.000	0.0
C+CH2=C2H+H	5.00E+13	0.000	0.0
CH2+CO2=CH2O+CO	1.10E+11	0.000	1000.0
CH2+O=CO+2H	5.00E+13	0.000	0.0
CH2+O=CO+H2	3.00E+13	0.000	0.0
CH2+O2=CO2+2H	1.60E+12	0.000	1000.0
CH2+O2=CH2O+O	5.00E+13	0.000	9000.0
CH2+O2=CO2+H2	6.90E+11	0.000	500.0
CH2+O2=CO+H2O	1.90E+10	0.000	-1000.0
CH2+O2=CO+OH+H	8.60E+10	0.000	-500.0
CH2+O2=HCO+OH	4.30E+10	0.000	-500.0
CH2O+OH=HCO+H2O	3.43E+09	1.180	-447.0
CH2O+H=HCO+H2	2.19E+08	1.770	3000.0
CH2O+M=HCO+H+M	3.31E+16	0.000	81000.0
CH2O+O=HCO+OH	1.80E+13	0.000	3080.0
HCO+OH=H2O+CO	1.00E+14	0.000	0.0
HCO+M=H+CO+M	2.50E+14	0.000	16802.0
H2/1.9/ CO/1.9/ CH4/2.8/ CO2/3.0/ H2O/5.0/			
HCO+H=CO+H2	1.19E+13	0.250	0.0
HCO+O=CO+OH	3.00E+13	0.000	0.0
HCO+O=CO2+H	3.00E+13	0.000	0.0
HCO+O2=HO2+CO	3.30E+13	-0.400	0.0
CO+O+M=CO2+M	6.17E+14	0.000	3000.0
CO+OH=CO2+H	1.51E+07	1.300	-758.0
CO+O2=CO2+O	1.60E+13	0.000	41000.0
HO2+CO=CO2+OH	5.80E+13	0.000	22934.0
C2H6+CH3=C2H5+CH4	5.50E-01	4.000	8300.0

C2H6+H=C2H5+H2	5.40E+02	3.500	5210.0
C2H6+O=C2H5+OH	3.00E+07	2.000	5115.0
C2H6+OH=C2H5+H2O	8.70E+09	1.050	1810.0
C2H4+H=C2H3+H2	1.10E+14	0.000	8500.0
C2H4+O=CH3+HCO	1.60E+09	1.200	746.0
C2H4+OH=C2H3+H2O	2.02E+13	0.000	5955.0
CH2+CH3=C2H4+H	3.00E+13	0.000	0.0
H+C2H4(+M)=C2H5(+M)	2.21E+13	0.000	2066.0
LOW/6.37E+27 -2.8 -54.0/			
H2/2.0/ CO/2.0/ CO2/3.0/ H2O/5.0/			
C2H5+H=2CH3	1.00E+14	0.000	0.0
C2H5+O2=C2H4+HO2	8.43E+11	0.000	3875.0
C2H2+O=CH2+CO	1.02E+07	2.000	1900.0
C2H2+O=HCCO+H	1.02E+07	2.000	1900.0
H2+C2H=C2H2+H	4.09E+05	2.390	864.0
H+C2H2(+M)=C2H3(+M)	5.54E+12	0.000	2410.0
LOW/2.67E+27 -3.5 2410.0/			
H2/2.0/ CO/2.0/ CO2/3.0/ H2O/5.0/			
C2H3+H=C2H2+H2	4.00E+13	0.000	0.0
C2H3+O=CH2CO+H	3.00E+13	0.000	0.0
C2H3+O2=CH2O+HCO	4.00E+12	0.000	-250.0
C2H3+OH=C2H2+H2O	5.00E+12	0.000	0.0
C2H3+CH2=C2H2+CH3	3.00E+13	0.000	0.0
C2H3+C2H=2C2H2	3.00E+13	0.000	0.0
C2H3+CH=CH2+C2H2	5.00E+13	0.000	0.0
OH+C2H2=C2H+H2O	3.37E+07	2.000	14000.0
OH+C2H2=HCCOH+H	5.04E+05	2.300	13500.0
OH+C2H2=CH2CO+H	2.18E-04	4.500	-1000.0
OH+C2H2=CH3+CO	4.83E-04	4.000	-2000.0
HCCOH+H=CH2CO+H	1.00E+13	0.000	0.0
C2H2+O=C2H+OH	3.16E+15	-0.600	15000.0
CH2CO+O=CO2+CH2	1.75E+12	0.000	1350.0
CH2CO+H=CH3+CO	1.13E+13	0.000	3428.0
CH2CO+H=HCCO+H2	5.00E+13	0.000	8000.0
CH2CO+O=HCCO+OH	1.00E+13	0.000	8000.0
CH2CO+OH=HCCO+H2O	7.50E+12	0.000	2000.0
CH2CO(+M)=CH2+CO(+M)	3.00E+14	0.000	70980.0
LOW/3.60E+15 0.0 59270.0/			
C2H+O2=2CO+H	5.00E+13	0.000	1500.0
C2H+C2H2=C4H2+H	3.00E+13	0.000	0.0
H+HCCO=CH2(S)+CO	1.00E+14	0.000	0.0
O+HCCO=H+2CO	1.00E+14	0.000	0.0
HCCO+O2=2CO+OH	1.60E+12	0.000	854.0
CH+HCCO=C2H2+CO	5.00E+13	0.000	0.0
2HCCO=C2H2+2CO	1.00E+13	0.000	0.0
CH2(S)+M=CH2+M	1.00E+13	0.000	0.0
H/0.0/			
CH2(S)+CH4=2CH3	4.00E+13	0.000	0.0
CH2(S)+C2H6=CH3+C2H5	1.20E+14	0.000	0.0
CH2(S)+O2=CO+OH+H	3.00E+13	0.000	0.0
CH2(S)+H2=CH3+H	7.00E+13	0.000	0.0
CH2(S)+H=CH2+H	2.00E+14	0.000	0.0
C2H+O=CH+CO	5.00E+13	0.000	0.0

C2H+OH=HCCO+H	2.00E+13	0.000	0.0
2CH2=C2H2+H2	4.00E+13	0.000	0.0
CH2+HCCO=C2H3+CO	3.00E+13	0.000	0.0
C4H2+OH=C3H2+HCO	6.66E+12	0.000	-410.0
C3H2+O2=HCO+HCCO	1.00E+13	0.000	0.0
C4H2+O=C3H2+CO	1.20E+12	0.000	0.0
C2H2+O2=HCCO+OH	2.00E+08	1.500	30100.0
C2H2+M=C2H+H+M	4.20E+16	0.000	107000.0
C2H4+M=C2H2+H2+M	1.50E+15	0.000	55800.0
C2H4+M=C2H3+H+M	1.40E+16	0.000	82360.0
H2+O2=2OH	1.70E+13	0.000	47780.0
OH+H2=H2O+H	1.17E+09	1.300	3626.0
O+OH=O2+H	4.00E+14	-0.500	0.0
O+H2=OH+H	5.06E+04	2.670	6290.0
H+O2+M=HO2+M	3.61E+17	-0.720	0.0
H2O/18.6/ CO2/4.2/ H2/2.9/ CO/2.1/ N2/1.3/			
OH+HO2=H2O+O2	7.50E+12	0.000	0.0
H+HO2=2OH	1.40E+14	0.000	1073.0
O+HO2=O2+OH	1.40E+13	0.000	1073.0
2OH=O+H2O	6.00E+08	1.300	0.0
2H+M=H2+M	1.00E+18	-1.000	0.0
H2/0.0/ H2O/0.0/ CO2/0.0/			
2H+H2=2H2	9.20E+16	-0.600	0.0
2H+H2O=H2+H2O	6.00E+19	-1.250	0.0
2H+CO2=H2+CO2	5.49E+20	-2.000	0.0
H+OH+M=H2O+M	1.60E+22	-2.000	0.0
H2O/5.0/			
H+O+M=OH+M	6.20E+16	-0.600	0.0
H2O/5.0/			
2O+M=O2+M	1.89E+13	0.000	-1788.0
H+HO2=H2+O2	1.25E+13	0.000	0.0
2HO2=H2O2+O2	2.00E+12	0.000	0.0
H2O2+M=2OH+M	1.30E+17	0.000	45500.0
H2O2+H=HO2+H2	1.60E+12	0.000	3800.0
H2O2+OH=H2O+HO2	1.00E+13	0.000	1800.0
CH+N2=HCN+N	3.00E+11	0.000	13600.0
CN+N=C+N2	1.04E+15	-0.500	0.0
CH2+N2=HCN+NH	1.00E+13	0.000	74000.0
H2CN+N=N2+CH2	2.00E+13	0.000	0.0
H2CN+M=HCN+H+M	3.00E+14	0.000	22000.0
C+NO=CN+O	6.60E+13	0.000	0.0
CH+NO=HCN+O	1.10E+14	0.000	0.0
CH2+NO=HCNO+H	1.39E+12	0.000	-1100.0
CH3+NO=HCN+H2O	1.00E+11	0.000	15000.0
CH3+NO=H2CN+OH	1.00E+11	0.000	15000.0
HCCO+NO=HCNO+CO	2.00E+13	0.000	0.0
CH2(S)+NO=HCN+OH	2.00E+13	0.000	0.0
HCNO+H=HCN+OH	1.00E+14	0.000	12000.0
CH2+N=HCN+H	5.00E+13	0.000	0.0
CH+N=CN+H	1.30E+13	0.000	0.0
CO2+N=NO+CO	1.90E+11	0.000	3400.0
HCCO+N=HCN+CO	5.00E+13	0.000	0.0
CH3+N=H2CN+H	3.00E+13	0.000	0.0

C2H3+N=HCN+CH2	2.00E+13	0.000	0.0
HCN+OH=CN+H2O	1.45E+13	0.000	10929.0
OH+HCN=HOCN+H	5.85E+04	2.400	12500.0
OH+HCN=HNCO+H	1.98E-03	4.000	1000.0
OH+HCN=NH2+CO	7.83E-04	4.000	4000.0
HOCN+H=HNCO+H	1.00E+13	0.000	0.0
HCN+O=NCO+H	1.38E+04	2.640	4980.0
HCN+O=NH+CO	3.45E+03	2.640	4980.0
HCN+O=CN+OH	2.70E+09	1.580	26600.0
CN+H2=HCN+H	2.95E+05	2.450	2237.0
CN+O=CO+N	1.80E+13	0.000	0.0
CN+O2=NCO+O	5.60E+12	0.000	0.0
CN+OH=NCO+H	6.00E+13	0.000	0.0
CN+HCN=C2N2+H	2.00E+13	0.000	0.0
CN+NO2=NCO+NO	3.00E+13	0.000	0.0
CN+N2O=NCO+N2	1.00E+13	0.000	0.0
C2N2+O=NCO+CN	4.57E+12	0.000	8880.0
C2N2+OH=HOCN+CN	1.86E+11	0.000	2900.0
HO2+NO=NO2+OH	2.11E+12	0.000	-479.0
NO2+H=NO+OH	3.50E+14	0.000	1500.0
NO2+O=NO+O2	1.00E+13	0.000	600.0
NO2+M=NO+O+M	1.10E+16	0.000	66000.0
NCO+H=NH+CO	5.00E+13	0.000	0.0
NCO+O=NO+CO	2.00E+13	0.000	0.0
NCO+N=N2+CO	2.00E+13	0.000	0.0
NCO+OH=NO+CO+H	1.00E+13	0.000	0.0
NCO+M=N+CO+M	3.10E+16	-0.500	48000.0
NCO+NO=N2O+CO	1.00E+13	0.000	-390.0
NCO+H2=HNCO+H	8.58E+12	0.000	9000.0
HNCO+H=NH2+CO	2.00E+13	0.000	3000.0
NH+O2=HNO+O	1.00E+13	0.000	12000.0
NH+O2=NO+OH	7.60E+10	0.000	1530.0
NH+NO=N2O+H	2.40E+15	-0.800	0.0
N2O+OH=N2+HO2	2.00E+12	0.000	10000.0
N2O+H=N2+OH	7.60E+13	0.000	15200.0
N2O+M=N2+O+M	1.60E+14	0.000	51600.0
N2O+O=N2+O2	1.00E+14	0.000	28200.0
N2O+O=2NO	1.00E+14	0.000	28200.0
NH+OH=HNO+H	2.00E+13	0.000	0.0
NH+OH=N+H2O	5.00E+11	0.500	2000.0
NH+N=N2+H	3.00E+13	0.000	0.0
NH+H=N+H2	1.00E+14	0.000	0.0
NH2+O=HNO+H	6.63E+14	-0.500	0.0
NH2+O=NH+OH	6.75E+12	0.000	0.0
NH2+OH=NH+H2O	4.00E+06	2.000	1000.0
NH2+H=NH+H2	6.92E+13	0.000	3650.0
NH2+NO=NNH+OH	6.40E+15	-1.250	0.0
NH2+NO=N2+H2O	6.20E+15	-1.250	0.0
NH3+OH=NH2+H2O	2.04E+06	2.040	566.0
NH3+H=NH2+H2	6.36E+05	2.390	10171.0
NH3+O=NH2+OH	2.10E+13	0.000	9000.0
NNH=N2+H	1.00E+04	0.000	0.0
NNH+NO=N2+HNO	5.00E+13	0.000	0.0

NNH+H=N2+H2	1.00E+14	0.000	0.0
NNH+OH=N2+H2O	5.00E+13	0.000	0.0
NNH+NH2=N2+NH3	5.00E+13	0.000	0.0
NNH+NH=N2+NH2	5.00E+13	0.000	0.0
NNH+O=N2O+H	1.00E+14	0.000	0.0
HNO+M=H+NO+M	1.50E+16	0.000	48680.0
H2O/10.0/ O2/2.0/ N2/2.0/ H2/2.0/			
HNO+OH=NO+H2O	3.60E+13	0.000	0.0
HNO+H=H2+NO	5.00E+12	0.000	0.0
HNO+NH2=NH3+NO	2.00E+13	0.000	1000.0
N+NO=N2+O	3.27E+12	0.300	0.0
N+O2=NO+O	6.40E+09	1.000	6280.0
N+OH=NO+H	3.80E+13	0.000	0.0
CH2+C2H2=H2CCCH+H	1.20E+13	0.000	6600.0
H2CCCH+O2=CH2CO+HCO	3.00E+10	0.000	2868.0
H2CCCH+O=CH2O+C2H	2.00E+13	0.000	0.0
H2CCCH+OH=C3H2+H2O	2.00E+13	0.000	0.0
C2H2+C2H2=H2CCCCH+H	2.00E+12	0.000	45900.0
H2CCCCH+M=C4H2+H+M	1.00E+16	0.000	59700.0
CH2(S)+C2H2=H2CCCH+H	3.00E+13	0.000	0.0
H2CCCH+N=HCN+C2H2	1.00E+13	0.000	0.0

END

The final chemical kinetics model used is the combined mechanism of the hydrocarbon kinetics of Miller and Melius [1992], and the nitrogen kinetics of Drake and Blint [1991] (MIME-DB). The MIME-DB mechanism has a similar format to the MB mechanism, and is listed below.

ELEMENTS
 H   O   C   N
END

SPECIES
 O2 H2 H2O H O OH HO2 H2O2
 CO2 CO
 CH2O HCO CH2CO HCCO
 CH4 CH3 CH2 CH2(S) CH C
 CH2OH CH3O
 C2H6 C2H5 C2H4 C2H3 C2H2 C2H C2
 HCCOH C2O
 C3H4 C3H4P H2CCCH C3H2
 CH2CHCHCH2 CH2CHCHCH CH2CHCCH2 CH2CHCCH HCCHCCH
 H2CCCCH C4H2 H2C4O
 C5H2 C5H3
 C6H6 C6H5 C6H5O C6H2
 N2 NO N NO2 HNO NH3 NH2 NH N2H2 NNH N2O HCN CN NCO
 HNCO HCNO HOCN C2N2
END

REACTIONS

H2+O2=2OH	0.170E+14	0.000	47780.0
OH+H2=H2O+H	0.117E+10	1.300	3626.0
O+OH=O2+H	0.400E+15	-0.500	0.0
O+H2=OH+H	0.506E+05	2.670	6290.0
H+O2+M=HO2+M	0.361E+18	-0.720	0.0
H2O/18.6/ CO2/4.2/ H2/2.86/ CO/2.11/			
OH+HO2=H2O+O2	0.750E+13	0.000	0.0
H+HO2=2OH	0.140E+15	0.000	1073.0
O+HO2=O2+OH	0.140E+14	0.000	1073.0
2OH=O+H2O	0.600E+09	1.300	0.0
H+H+M=H2+M	0.100E+19	-1.000	0.0
H2O/0.0/ H2/0.0/ CO2/0.0/			
H+H+H2=H2+H2	0.920E+17	-0.600	0.0
H+H+H2O=H2+H2O	0.600E+20	-1.250	0.0
H+H+CO2=H2+CO2	0.549E+21	-2.000	0.0
H+OH+M=H2O+M	0.160E+23	-2.000	0.0
H2O/5/			
H+O+M=OH+M	0.620E+17	-0.600	0.0

```
     H2O/5/
O+O+M=O2+M                              0.189E+14      0.000       -1788.0
H+HO2=H2+O2                             0.125E+14      0.000          0.0
HO2+HO2=H2O2+O2                         0.200E+13      0.000          0.0
H2O2+M=OH+OH+M                          0.130E+18      0.000      45500.0
H2O2+H=HO2+H2                           0.160E+13      0.000       3800.0
H2O2+OH=H2O+HO2                         0.100E+14      0.000       1800.0

CH3+CH3(+M)=C2H6(+M)                    9.220E+16     -1.174        635.8
    LOW/1.135E36  -5.246 1704.8/
    TROE/0.405 1120. 69.6/
     H2/2/ CO/2/ CO2/3/ H2O/5/
CH3+H(+M)=CH4(+M)                       6.000E+16     -1.000          0.0
    LOW/8.0E26  -3.0 0.0/
     SRI/0.45 797. 979./
     H2/2/ CO/2/ CO2/3/ H2O/5/
CH4+O2=CH3+HO2                          0.790E+14      0.000      56000.0
CH4+H=CH3+H2                            0.220E+05      3.000       8750.0
CH4+OH=CH3+H2O                          0.160E+07      2.100       2460.0
CH4+O=CH3+OH                            1.020E+09      1.500       8604.0
CH4+HO2=CH3+H2O2                        0.180E+12      0.000      18700.0
CH3+HO2=CH3O+OH                         0.200E+14      0.000          0.0
CH3+O=CH2O+H                            8.000E+13      0.000          0.0
CH3+O2=CH3O+O                           0.205E+19     -1.570      29229.0
CH2OH+H=CH3+OH                          0.100E+15      0.000          0.0
CH3O+H=CH3+OH                           0.100E+15      0.000          0.0
CH3+OH=CH2+H2O                          0.750E+07      2.000       5000.0
CH3+H=CH2+H2                            0.900E+14      0.000      15100.0
CH3O+M=CH2O+H+M                         0.100E+15      0.000      25000.0
CH2OH+M=CH2O+H+M                        0.100E+15      0.000      25000.0
CH3O+H=CH2O+H2                          0.200E+14      0.000          0.0
CH2OH+H=CH2O+H2                         0.200E+14      0.000          0.0
CH3O+OH=CH2O+H2O                        0.100E+14      0.000          0.0
CH2OH+OH=CH2O+H2O                       0.100E+14      0.000          0.0
CH3O+O=CH2O+OH                          0.100E+14      0.000          0.0
CH2OH+O=CH2O+OH                         0.100E+14      0.000          0.0
CH3O+O2=CH2O+HO2                        0.630E+11      0.000       2600.0
CH2OH+O2=CH2O+HO2                       0.148E+14      0.000       1500.0
CH2+H=CH+H2                             0.100E+19     -1.560          0.0
CH2+OH=CH+H2O                           0.113E+08      2.000       3000.0
CH2+OH=CH2O+H                           0.250E+14      0.000          0.0
CH+O2=HCO+O                             0.330E+14      0.000          0.0
CH+O=CO+H                               0.570E+14      0.000          0.0
CH+OH=HCO+H                             0.300E+14      0.000          0.0
CH+OH=C+H2O                             4.000E+07      2.000       3000.0
CH+CO2=HCO+CO                           0.340E+13      0.000        690.0
CH+H=C+H2                               0.150E+15      0.000          0.0
CH+H2O=CH2O+H                           1.170E+15     -0.750          0.0
CH+CH2O=CH2CO+H                         0.946E+14      0.000       -515.0
CH+C2H2=C3H2+H                          0.100E+15      0.000          0.0
CH+CH2=C2H2+H                           0.400E+14      0.000          0.0
CH+CH3=C2H3+H                           0.300E+14      0.000          0.0
CH+CH4=C2H4+H                           0.600E+14      0.000          0.0
```

C+O2=CO+O	0.200E+14	0.000	0.0
C+OH=CO+H	0.500E+14	0.000	0.0
C+CH3=C2H2+H	0.500E+14	0.000	0.0
C+CH2=C2H+H	0.500E+14	0.000	0.0
CH2+CO2=CH2O+CO	0.110E+12	0.000	1000.0
CH2+O=CO+H+H	0.500E+14	0.000	0.0
CH2+O=CO+H2	0.300E+14	0.000	0.0
CH2+O2=CO2+H+H	0.160E+13	0.000	1000.0
CH2+O2=CH2O+O	0.500E+14	0.000	9000.0
CH2+O2=CO2+H2	0.690E+12	0.000	500.0
CH2+O2=CO+H2O	0.190E+11	0.000	-1000.0
CH2+O2=CO+OH+H	0.860E+11	0.000	-500.0
CH2+O2=HCO +OH	0.430E+11	0.000	-500.0
CH2O+OH=HCO+H2O	0.343E+10	1.180	-447.0
CH2O+H=HCO+H2	0.219E+09	1.770	3000.0
CH2O+M=HCO+H+M	0.331E+17	0.000	81000.0
CH2O+O=HCO+OH	0.180E+14	0.000	3080.0
HCO+OH=H2O+CO	0.100E+15	0.000	0.0
HCO+M=H+CO+M	0.250E+15	0.000	16802.0
CO/1.87/ H2/1.87/ CH4/2.81/ CO2/3./ H2O/5./			
HCO+H=CO+H2	0.119E+14	0.250	0.0
HCO+O=CO+OH	0.300E+14	0.000	0.0
HCO+O=CO2+H	0.300E+14	0.000	0.0
HCO+O2=HO2+CO	0.330E+14	-0.400	0.0
CO+O+M=CO2+M	0.617E+15	0.000	3000.0
CO+OH=CO2+H	0.151E+08	1.300	-758.0
CO+O2=CO2+O	2.530E+12	0.000	47688.0
HO2+CO=CO2+OH	0.580E+14	0.000	22934.0
C2H6+CH3=C2H5+CH4	0.550E+00	4.000	8300.0
C2H6+H=C2H5+H2	0.540E+03	3.500	5210.0
C2H6+O=C2H5+OH	0.300E+08	2.000	5115.0
C2H6+OH=C2H5+H2O	0.870E+10	1.050	1810.0
C2H4+H=C2H3+H2	0.110E+15	0.000	8500.0
C2H4+O=CH3+HCO	0.160E+10	1.200	746.0
C2H4+OH=C2H3+H2O	0.202E+14	0.000	5955.0
CH2+CH3=C2H4+H	0.400E+14	0.000	0.0
H+C2H4(+M)=C2H5(+M)	0.221E+14	0.000	2066.0
LOW/6.369E27 -2.76 -54.0/			
H2/2/ CO/2/ CO2/3/ H2O/5/			
C2H5+H=CH3+CH3	1.000E+14	0.000	0.0
C2H5+O2=C2H4+HO2	0.843E+12	0.000	3875.0
C2H2+O=CH2+CO	0.102E+08	2.000	1900.0
C2H2+O=HCCO+H	0.102E+08	2.000	1900.0
H2+C2H=C2H2+H	0.409E+06	2.390	864.3
H+C2H2(+M)=C2H3(+M)	0.554E+13	0.000	2410.0
LOW/2.67E27 -3.5 2410./			
H2/2/ CO/2/ CO2/3/ H2O/5/			
C2H3+H=C2H2+H2	0.400E+14	0.000	0.0
C2H3+O=CH2CO+H	0.300E+14	0.000	0.0

C2H3+O2=CH2O+HCO	0.400E+13	0.000	-250.0
C2H3+OH=C2H2+H2O	2.000E+13	0.000	0.0
C2H3+CH2=C3H4+H	3.000E+13	0.000	0.0
C2H3+C2H=C2H2+C2H2	0.300E+14	0.000	0.0
C2H3+C2H3=CH2CHCCH2+H	4.000E+13	0.000	0.0
C2H3+CH=CH2+C2H2	0.500E+14	0.000	0.0
OH+C2H2=C2H+H2O	3.370E+07	2.000	14000.0
OH+C2H2=HCCOH+H	5.040E+05	2.300	13500.0
OH+C2H2=CH2CO+H	2.180E-04	4.500	-1000.0
OH+C2H2=CH3+CO	4.830E-04	4.000	-2000.0
HCCOH+H=CH2CO+H	0.100E+14	0.000	0.0
C2H2+O=C2H+OH	0.316E+16	-0.600	15000.0
CH2CO+O=CO2+CH2	0.175E+13	0.000	1350.0
CH2CO+H=CH3+CO	0.113E+14	0.000	3428.0
CH2CO+H=HCCO+H2	0.500E+14	0.000	8000.0
CH2CO+O=HCCO+OH	0.100E+14	0.000	8000.0
CH2CO+OH=HCCO+H2O	0.750E+13	0.000	2000.0
CH2CO(+M)=CH2+CO(+M)	0.300E+15	0.000	70980.0
LOW/3.6E15 0.0 59270./			
C2H+O2=CO+CO+H	3.520E+13	0.000	0.0
C2H+C2H2=C4H2+H	0.300E+14	0.000	0.0
HCCO+C2H2=H2CCCH+CO	1.000E+11	0.000	3000.0
H+HCCO=CH2(S)+CO	0.100E+15	0.000	0.0
O+HCCO=H+CO+CO	0.100E+15	0.000	0.0
HCCO+O2=CO2+CO+H	1.400E+09	1.000	0.0
CH+HCCO=C2H2+CO	0.500E+14	0.000	0.0
HCCO+HCCO=C2H2+CO+CO	0.100E+14	0.000	0.0
HCCO+OH=C2O+H2O	3.000E+13	0.000	0.0
C2O+H=CH+CO	1.000E+13	0.000	0.0
C2O+O=CO+CO	5.000E+13	0.000	0.0
C2O+OH=CO+CO+H	2.000E+13	0.000	0.0
C2O+O2=CO+CO+O	2.000E+13	0.000	0.0
CH2(S)+M=CH2+M	0.100E+14	0.000	0.0
H/0.0/ H2O/0.0/ C2H2/0.0/			
CH2(S)+CH4=CH3+CH3	0.400E+14	0.000	0.0
CH2(S)+C2H6=CH3+C2H5	0.120E+15	0.000	0.0
CH2(S)+O2=CO+OH+H	7.000E+13	0.000	0.0
CH2(S)+H2=CH3+H	0.700E+14	0.000	0.0
CH2(S)+H2O=CH3+OH	1.000E+14	0.000	0.0
CH2(S)+H2O=CH2+H2O	3.000E+13	0.000	0.0
CH2(S)+C2H2=H2CCCH+H	1.800E+14	0.000	0.0
CH2(S)+C2H2=CH2+C2H2	4.000E+13	0.000	0.0
CH2(S)+H=CH2+H	0.200E+15	0.000	0.0
CH2(S)+O=CO+H+H	3.000E+13	0.000	0.0
CH2(S)+OH=CH2O+H	3.000E+13	0.000	0.0
CH2(S)+H=CH+H2	3.000E+13	0.000	0.0
CH2(S)+CO2=CH2O+CO	3.000E+12	0.000	0.0
CH2(S)+CH3=C2H4+H	2.000E+13	0.000	0.0
CH2(S)+CH2CO=C2H4+CO	1.600E+14	0.000	0.0
C2H+O=CH+CO	0.500E+14	0.000	0.0
C2H+OH=HCCO+H	0.200E+14	0.000	0.0
C2H+OH=C2+H2O	4.000E+07	2.000	8000.0
C2+H2=C2H+H	4.000E+05	2.400	1000.0

C2+O2=CO+CO	5.000E+13	0.000	0.0
C2+OH=C2O+H	5.000E+13	0.000	0.0
CH2+CH2=C2H2+H+H	0.400E+14	0.000	0.0
CH2+HCCO=C2H3+CO	0.300E+14	0.000	0.0
CH2+C2H2=H2CCCH+H	0.120E+14	0.000	6600.0
C4H2+OH=H2C4O+H	0.666E+13	0.000	-410.0
C3H2+O2=HCCO+CO+H	5.000E+13	0.000	0.0
C3H2+OH=C2H2+HCO	5.000E+13	0.000	0.0
C3H2+CH2=H2CCCCH+H	3.000E+13	0.000	0.0
H2C4O+H=C2H2+HCCO	5.000E+13	0.000	3000.0
H2C4O+OH=CH2CO+HCCO	1.000E+07	2.000	2000.0
H2CCCH+O2=CH2CO+HCO	0.300E+11	0.000	2868.0
H2CCCH+O=CH2O+C2H	0.200E+14	0.000	0.0
H2CCCH+H=C3H2+H2	5.000E+13	0.000	3000.0
H2CCCH+OH=C3H2+H2O	0.200E+14	0.000	0.0
H2CCCH+CH2=CH2CHCCH+H	4.000E+13	0.000	0.0
H2CCCH+CH=HCCHCCH+H	7.000E+13	0.000	0.0
H2CCCH+CH=H2CCCCH+H	7.000E+13	0.000	0.0
CH2CHCCH+OH=HCCHCCH+H2O	7.500E+06	2.000	5000.0
CH2CHCCH+H=HCCHCCH+H2	2.000E+07	2.000	15000.0
CH2CHCCH+OH=H2CCCCH+H2O	1.000E+07	2.000	2000.0
H+HCCHCCH=H2CCCCH+H	1.000E+14	0.000	0.0
H2CCCCH+O2=CH2CO+HCCO	1.000E+12	0.000	0.0
H2CCCCH+OH=C4H2+H2O	3.000E+13	0.000	0.0
H2CCCCH+O=CH2CO+C2H	2.000E+13	0.000	0.0
H2CCCCH+O=H2C4O+H	2.000E+13	0.000	0.0
H2CCCCH+H=C4H2+H2	5.000E+13	0.000	0.0
H2CCCCH+CH2=C3H4+C2H	2.000E+13	0.000	0.0
CH2CHCCH+H=H2CCCCH+H2	3.000E+07	2.000	5000.0
CH2CHCHCH+OH=CH2CHCCH+H2O	2.000E+07	2.000	1000.0
CH2CHCHCH+H=CH2CHCCH + H2	3.000E+07	2.000	1000.0
C6H6+H=C6H5+H2	3.000E+07	2.000	5000.0
C6H6+OH=C6H5+H2O	7.500E+06	2.000	5000.0
C2H3+C2H2=CH2CHCCH+H	2.000E+12	0.000	5000.0
C2H2+CH2CHCHCH=C6H6+H	2.800E+03	2.900	1400.0
HCCHCCH+C2H2=C6H5	2.800E+03	2.900	1400.0
C3H4+H=H2CCCH+H2	5.000E+07	2.000	5000.0
C3H4+OH=H2CCCH+H2O	2.000E+07	2.000	1000.0
C3H4P+H=H2CCCH+H2	5.000E+07	2.000	5000.0
C3H4P+H=CH3+C2H2	1.000E+14	0.000	4000.0
C3H4P+OH=H2CCCH+H2O	2.000E+07	2.000	1000.0
C6H5+OH=C6H5O+H	5.000E+13	0.000	0.0
C6H5+O2=C6H5O+O	1.000E+13	0.000	0.0
CH2+C4H2=C5H3+H	0.130E+14	0.000	4326.0
CH+C4H2=C5H2+H	0.100E+15	0.000	0.0
CH2(S)+C4H2=C5H3+H	0.300E+14	0.000	0.0
C4H2+O=C3H2+CO	0.120E+13	0.000	0.0
C4H2+C2H=C6H2+H	0.400E+14	0.000	0.0
C2H2+O2=HCCO+OH	0.200E+09	1.500	30100.0
C2H2+M=C2H+H+M	0.420E+17	0.000	107000.0
C2H4+M=C2H2+H2+M	0.150E+16	0.000	55800.0
C2H4+M=C2H3+H+M	0.140E+17	0.000	82360.0
C2H3+C2H4=CH2CHCHCH2+H	3.000E+12	0.000	1000.0

Reaction	A	n	E
CH2CHCHCH2+H=CH2CHCHCH+H2	3.000E+07	2.000	13000.0
CH2CHCHCH2+H=CH2CHCCH2+H2	3.000E+07	2.000	6000.0
CH2CHCHCH2+OH=CH2CHCHCH+H2O	2.000E+07	2.000	5000.0
CH2CHCHCH2+OH=CH2CHCCH2+H2O	2.000E+07	2.000	2000.0
CH2CHCHCH+H=CH2CHCCH2 + H	1.000E+14	0.000	0.0
H2CCCCH(+M)=C4H2+H(+M)	1.000E+14	0.000	55000.0
LOW/ 2.0E15 0.0 48000./			
HCCHCCH(+M)=C4H2+H(+M)	1.000E+14	0.000	36000.0
LOW/ 1.0E14 0.0 30000./			
CH2CHCCH2(+M)=CH2CHCCH+H(+M)	1.000E+14	0.000	50000.0
LOW/2.0E15 0.0 42000./			
CH2CHCHCH(+M)=CH2CHCCH+H(+M)	1.000E+14	0.000	37000.0
LOW/1.0E14 0.0 30000./			
H+C6H5=C6H6	5.000E+13	0.000	0.0
H2CCCH+H(+M)=C3H4(+M)	6.000E+16	-1.000	0.0
LOW/8.0E26 -3.0 0.0/			
H2O/5/ H2/2/ CO2/3/ CO/2/ O2/2/ C2H2/2/			
H2CCCH+H(+M)=C3H4P(+M)	6.000E+16	-1.000	0.0
LOW/8.0E26 -3.0 0.0/			
H2O/5/ H2/2/ CO2/3/ CO/2/ O2/2/ C2H2/2/			
H2CCCH+H2CCCH=C6H5+H	1.000E+13	0.000	0.0
HNO+M=H+NO+M	1.50E+16	0.000	48680.0
H2O/6.0/ H2/2.0/ O2/2./ N2/2./			
HNO+H=H2+NO	5.00E+12	0.000	0.0
HNO+OH=NO+H2O	3.60E+13	0.000	0.0
NH3+M=NH2+H+M	1.40E+16	0.060	90600.0
NH3+H=NH2+H2	7.00E+06	2.390	10171.0
NH3+O=NH2+OH	2.10E+13	0.000	9000.0
NH3+OH=NH2+H2O	2.04E+06	2.040	566.0
NH2+H=NH+H2	6.90E+13	0.000	3650.0
NH2+O=NH+OH	6.80E+12	0.000	0.0
NH2+O=HNO+H	6.60E+14	-0.500	0.0
NH2+OH=NH+H2O	4.50E+12	0.000	2200.0
NH2+N=N2+H+H	7.20E+13	0.000	0.0
NH2+NO=N2+H2O	3.80E+15	-1.250	0.0
NH+H=N+H2	3.00E+13	0.000	0.0
NH+O=NO+H	2.00E+13	0.000	0.0
NH+OH=HNO+H	2.00E+13	0.000	0.0
NH+OH=N+H2O	5.00E+11	0.500	2000.0
NH+O2=HNO+O	1.00E+13	0.000	12000.0
NH+O2=NO+OH	1.40E+11	0.000	2000.0
NH+N=N2+H	3.00E+13	0.000	0.0
N+O2=NO+O	6.40E+09	1.000	6280.0
N+OH=NO+H	3.80E+13	0.000	0.0
N+CO2=NO+CO	1.90E+11	0.000	3400.0
NO+HO2=NO2+OH	2.10E+12	0.000	-480.0
NO2+M=NO+O+M	1.10E+16	0.000	66000.0
NO2+H=NO+OH	3.50E+14	0.000	1500.0
NO2+O=NO+O2	1.00E+13	0.000	600.0
N2H2+M=NNH+H+M	5.00E+16	0.000	50000.0
N2H2+H=NNH+H2	5.00E+13	0.000	1000.0
NNH+M=N2+H+M	2.00E+14	0.000	20000.0
NNH+H=N2+H2	3.70E+13	0.000	3000.0

NNH+NO=N2+HNO	5.00E+13	0.000	0.0
NH2+NH=N2H2+H	5.00E+13	0.000	0.0
NH2+NO=NNH+OH	8.80E+15	-1.250	0.0
NH+NO=N2O+H	4.30E+14	-0.500	0.0
N2O+H=N2+OH	7.60E+13	0.000	15200.0
N2O+O=NO+NO	1.00E+14	0.000	28200.0
N2O+O=N2+O2	1.00E+14	0.000	28200.0
CH+NO=HCN+O	1.10E+14	0.000	0.0
CH2+N2=HCN+NH	1.00E+13	0.000	74000.0
CH+NH2=HCN+H+H	3.00E+13	0.000	0.0
CH+NH=HCN+H	5.00E+13	0.000	0.0
CH2+NH=HCN+H+H	3.00E+13	0.000	0.0
CH+N=CN+H	1.30E+13	0.000	0.0
CH2+N=HCN+H	5.00E+13	0.000	0.0
CH3+N=HCN+H+H	5.00E+13	0.000	0.0
CH4+N=NH+CH3	1.00E+13	0.000	24000.0
HCN+O=CN+OH	2.70E+09	1.580	26600.0
HCN+O=NH+CO	3.50E+03	2.640	4980.0
HCN+OH=CN+H2O	1.50E+13	0.000	10929.0
CN+O=CO+N	1.80E+13	0.000	0.0
CN+H2=HCN+H	3.00E+05	2.450	2237.0
C+NO=CN+O	6.60E+13	0.000	0.0
C+N2O=CN+NO	1.00E+13	0.000	0.0
N+HCCO=HCN+CO	5.00E+13	0.000	0.0
HCN+OH=HNCO+H	4.80E+11	0.000	11000.0
NCO+H2=HNCO+H	8.60E+12	0.000	9000.0
HOCN+H=HNCO+H	1.00E+13	0.000	0.0
HNCO+H=NH2+CO	2.00E+13	0.000	3000.0
CH2+NO=HCNO+H	1.40E+12	0.000	-1100.0
HCNO+H=HCN+OH	5.00E+13	0.000	12000.0
HCN+OH=HOCN+H	9.20E+12	0.000	15000.0
C2N2+OH=HOCN+CN	1.90E+11	0.000	2900.0
HCN+O=NCO+H	1.40E+04	2.640	4980.0
CN+OH=NCO+H	6.00E+13	0.000	0.0
CN+O2=NCO+O	5.60E+12	0.000	0.0
CN+NO2=NCO+NO	3.00E+13	0.000	0.0
CN+N2O=NCO+N2	1.00E+13	0.000	0.0
NCO+M=N+CO+M	3.10E+16	-0.500	48000.0
NCO+H=NH+CO	5.00E+13	0.000	0.0
NCO+O=NO+CO	5.60E+13	0.000	0.0
NCO+OH=NO+CO+H	1.00E+13	0.000	0.0
NCO+N=N2+CO	2.00E+13	0.000	0.0
NCO+NO=N2O+CO	1.00E+13	0.000	-390.0
HCN+CN=C2N2+H	2.00E+13	0.000	0.0
C2N2+O=NCO+CN	4.60E+12	0.000	8880.0
N+NO=N2+O	3.30E+12	0.300	0.0
N2O=N2+O	1.66E+20	-2.880	64115.0
CH+N2=HCN+N	4.20E+12	0.000	20400.0

END

Appendix B - Modeling of Other Flame Species

The chemical kinetics models used to predict NO concentrations in the flames of this study can be used to predict the concentrations of other species as well. The only species measured in this work has been NO. However, there have been several other studies which have performed measurements of other species and compared the results to the predictions of the various chemical kinetics models. Some of this work is reviewed here.

Vaughn et al. [1991] compared measurements of CO, CO_2, H_2, CH_4, C_2H_2, C_2H_4, and C_2H_6 with predictions obtained using the GMK mechanism [Glarborg et al., 1986] for a well-stirred reactor using a premixed C_2H_4/air mixture. The flame temperature was 1750 K, and the combustion was at atmospheric pressure. The nitrogenous species kinetics were eliminated from the mechanism; this had no effect on the predictions from the hydrocarbon kinetics. The model predictions were generally within 20% of the measured concentrations of the species listed above. However, the model severely underpredicted CH_4 concentrations at $\phi > 1.6$. Vaughn et al. [1991] noted that this behavior could be due to an overprediction in the rate of methyl destruction.

Drake et al. [1991] used the GMK-DB scheme to predict OH concentrations, as well as NO concentrations, in high-pressure, lean C_2H_6/O_2/N_2 flames. The flame temperatures were between 1650 and 1750 K. The OH concentrations were measured using laser-saturated fluorescence. The agreement between the measurements and modeling calculations for OH were generally good, and both the measurements and the modeling found large superequilibrium OH concentrations for the various flames. The model predictions did tend to be ~40% higher than the measurements; however, this is not a substantial error for a chemical kinetics evaluation of an intermediate species.

Miller and Bowman [1989] compared the MB model predictions to several experimentally measured species concentrations. One flame studied was a lean ($\phi = 0.97$),

low-pressure (18.5 torr) $C_2H_4/O_2/N_2$ flame; for this flame, comparisons were made between measured and predicted C, CH, and CH_2 profiles. The model was fairly accurate at predicting the heights above the burner corresponding to the maximum concentration for the different species, but underpredicted the CH_2 and C concentrations by ~50%, and overpredicted the CH concentration by ~30%; this agreement is adequate for many purposes. Comparisons between measurements and predictions were also made for CO, CO_2, N_2, and HCN in low-pressure (25 torr) $H_2/O_2/Ar/HCN$ flames ($0.5<\phi<1.5$). Agreement between the measurements and modeling was found to be within ~10% for these four species. Finally, comparisons were made between the predictions and measurements of CN, N_2, and HCN concentrations in rich ($\phi=1.5$), low-pressure $H_2/O_2/Ar/C_2H_2/HCN$ and $H_2/O_2/Ar/C_2H_2/NO$ flames. Again, the same level of agreement was found between the measurements and the MB modeling.

Zabarnick [1992] compared results of the MB model with measured concentrations in low-pressure (63 torr), premixed, laminar $CH_4/NO/O_2$ and CH_4/N_2O flames. The peak flame temperature, as determined by OH rotational temperature measurements, was ~2400 K for the former and ~2700 K for the latter. LIF measurements were obtained for OH, NH, CH, and CN concentrations. Comparisons between the measurements and predictions were generally better for the CH_4/N_2O flame. The OH and CN concentrations are overpredicted by a factor of 2 - 3 for the $CH_4/NO/O_2$ flame, while the OH and NH concentrations are overpredicted by a similar amount for the CH_4/N_2O flame. The model also predicts the CH profile to peak at a lower height than found in the measurements for the $CH_4/NO/O_2$ flame.

Garo et al. [1992] compared measurements in low-pressure (25 torr) $CH_4/O_2/NH_3$ and $CH_4/O_2/NO$ flames with predictions from the MB model. Comparisons were made between the predictions and measurements for H_2O, CO_2, CO, O_2, and NH_3. In general, the predictions of the profiles of these species as a function of height above the burner

were within 20% of the measurements. Measurements of O and H were made using mass spectrometry, and OH was measured using absorption. Comparisons were made of the concentrations of these species, and it was found that the concentrations predicted by the MB model tended to be too high in comparison to the measurements by a factor of two. The predictions of CH_3 and HCN were somewhat inaccurate both qualitatively and quantitatively. Garo *et al.* [1992] concluded that the MB model gave accurate predictions of the major species profiles, but possessed some inaccuracies for flame radicals.

Bernstein *et al.* [1993] compared concentration measurements of O, H, OH, CH, CO, HCO, and CH_3 to predictions from the mechanism of Miller and Melius [1992] (MIME). The flames considered were low-pressure (17-20 torr), stoichiometric $CH_4/O_2/Ar$, C_2H_4 $/O_2/Ar$, and $C_2H_6/O_2/Ar$ flames. The temperatures of these flames were less than 2000 K. The predicted HCO profiles were in good agreement (within 10%) for the methane flame, but the other flames suffered from overprediction by a factor of two. The CH_3 predictions were good for the methane and ethane flames, but tended to be too low (by a factor of 2) for the ethylene flames and the peak locations were several millimeters in error. The CH profile was well predicted for the methane and ethane flames, but were a factor of two low for the ethylene flames. The O and OH profiles were accurately predicted in all four flames. The predicted H profiles tended to have the correct magnitude, but the qualitative agreement was not good; the predictions suggest an increase in [H] far above the burner, while the measurements indicate a decrease. Bernstein *et al.* [1993] suggest that this error could be due to the one-dimensional nature of the model which neglects such effects as the increase in cross-sectional area of the flow with increasing distance above the burner. Finally, the agreement between the measurements and predictions was within 20% for the CO profiles in the various flames.

Miller *et al.* [1991] compared three low-pressure (25 torr), rich, non-sooting C_2H_2 $/O_2/Ar$ flames to predictions from the MIME model. The species compared were CO_2,

C_4H_2, H_2O, CO, O_2, C_2H_2, OH, H, and CH. The stable species are generally well predicted by the MIME model, although the C_4H_2 concentration is overpredicted by a factor of 3. The radical concentrations are well-predicted for the near stoichiometric flame, although the CH tends to be overpredicted by a factor of two. However, at higher equivalence ratios, the agreement between the measurements and predictions for the radical profiles becomes substantially poorer, both in quantitative agreement and in the qualitative shape of the profiles.

Miller and Melius [1992] compared measured and MIME predicted concentrations for C_2H_2, O_2, CO_2, H_2O, H, CO_2, H_2, C_2H, C_2H_3, OH, C_4H_2, C_4H_4, C_4H_3, C_4H_5, and C_6H_6 for a lightly sooting $C_2H_2/O_2/Ar$ flame. Here the model did, in general, a good job at predicting the concentrations. The radical species concentrations were generally within a factor of two of the measurements. The largest errors are in the underprediction of the H and the C_4H_4 concentrations. The agreement tends to be better for all species in the flame region, although some discrepancies arise in the post-flame zone. For instance, the predicted H_2O concentration drops more slowly in the post-flame zone than the measured concentration.

In this appendix, a brief review has been presented of several studies which have compared experimentally measured species concentrations (other than [NO]) with predictions from the various chemical kinetics schemes used in this study. The agreement between the measurements and modeling varies for different flame conditions. However, in general, the predictions of the models are within 20% of measurements for the stable species concentrations, and often improvement is needed in the predictions of flame radical concentrations.

Appendix C - Uncertainty Analysis for Measurements

Measurements of every type have a certain amount of uncertainty associated with them. This uncertainty can take various forms, including the uncertainty in reading a gauge, and the uncertainty stemming from random deviations in consecutive measurements of the same quantity. For instance, if the length of an object is to be found from a series of measurements using an ordinary ruler, uncertainty in the length will come from two main sources. There would be a contribution to the uncertainty for each measurement due to the required interpolation between the markings on the ruler. The other main source of uncertainty would arise from the different values of length that would be found during successive measurements. Similar uncertainties can be found for all types of measurements, and presentation of the uncertainties in measurements enables others to know the accuracy of the measurement.

One way to determine the uncertainty in a measurement is to use the method of propagation of errors. In this method, it is assumed that there are a series of measurements, $x, \dots, z$, which contribute to the final measured quantity, q; q can be written as a function of the other measurements. Each of the measurements $x, \dots, z$ has an associated uncertainty, $\delta x, \dots, \delta z$. If the uncertainties $\delta x, \dots, \delta z$ are random and independent, the uncertainty in q, δq, can be written [Taylor, 1982]

$$\delta q = \sqrt{\left(\frac{\partial q}{\partial x}\delta x\right)^2 + \left(\frac{\partial q}{\partial y}\delta y\right)^2 + \dots + \left(\frac{\partial q}{\partial z}\delta z\right)^2} \ . \qquad (C.1)$$

An uncertainty analysis has been performed for the measurements of nitric oxide number density in the $C_2H_6/O_2/N_2$ flames and the $C_2H_4/O_2/N_2$ flames (see Chapters 4, 5, and 8) and the Rayleigh scattering temperature measurements in the $C_2H_6/O_2/N_2$ flames (see Chapters 7 and 8). The uncertainty analyses for both the LIF measurements and the

Rayleigh scattering measurements employ a 2σ confidence interval (95%). The uncertainty in the fluorescence signal can be determined from the following procedure. For a linear fluorescence measurement, the NO number density in each flame can be found from

$$[NO]_{flame} = [NO]_{cal} \frac{V_{flame}}{V_{cal}} \frac{I_{L,cal}}{I_{L,flame}} \quad , \tag{C.2}$$

where $[NO]_{flame}$ is the NO number density in the flame of interest, $[NO]_{cal}$ is the calibration NO number density, V_{flame} is the fluorescence signal in the flame of interest, V_{cal} is the fluorescence signal in the calibration flame, and $I_{L,flame}$ and $I_{L,cal}$ are the respective laser intensities for the measurements. For each flame, the uncertainty in the calibration carries over to that in each flame. However, the precision of the measurement can be found by neglecting the uncertainty in the calibration (which affects the accuracy) and calculating

$$\frac{\delta [NO]_{flame}}{[NO]_{flame}} = \sqrt{\left(\frac{\delta V_{cal}}{V_{cal}}\right)^2 + \left(\frac{\delta V_{flame}}{V_{flame}}\right)^2 + \left(\frac{\delta I_{L,cal}}{I_{L,cal}}\right)^2 + \left(\frac{\delta I_{L,flame}}{I_{L,flame}}\right)^2} \quad . \tag{C.3}$$

Using Eq. (C.3), the precision of the LIF measurements is typically found to be about $\pm 5\%$. However, a few measurements did have uncertainties of $\pm 7\%$; therefore, the precision of the LIF measurements can be conservatively taken as $\pm 7\%$. As an example, Table C.1 lists the intermediate values for the calculation of the precision of the [NO] measurement for four of the 9.15 atm $C_2H_4/O_2/N_2$ flames from Chapter 5.

The calibration number density can be calculated from

$$[NO]_{cal} = \frac{X_{NO}P}{kT} \quad , \tag{C.4}$$

where NO_{cal} is the NO number density for the calibration flame, X_{NO} is the NO mole fraction of the calibration flame, P is the pressure, k is Boltzmann's constant, and T is the temperature. For the calibration, it will be assumed that the pressure is accurately known.

Table C.1:   Intermediate quantities in the uncertainty analysis of LIF data for some of the 9.15 atm $C_2H_4/O_2/N_2$ flames of Chapter 5.

Quantity	Flame Equivalence Ratio			
	0.80	1.10	1.25	1.50
$\delta V_{cal}/V_{cal}$	2.80E-2	2.80E-2	2.80E-2	2.80E-2
$\delta V_{flame}/V_{flame}$	3.20E-2	2.06E-2	3.08E-2	4.93E-2
$\delta I_{L,cal}/I_{L,cal}$	1.06E-2	1.06E-2	1.06E-2	1.06E-2
$\delta I_{L,flame}/I_{L,flame}$	1.06E-2	0.98E-2	0.88E-2	0.77E-2
$\delta[NO]_{flame}/[NO]_{flame}$	4.82E-2	3.76E-2	4.38E-2	5.82E-2

To determine the uncertainty in the calibration, one must be concerned with the uncertainties in the temperature, the day-to-day repeatability of the calibration (X_{NO}), and the accuracy of the NO/N_2 mixture used to calibrate the flames. The day-to-day repeatability of the NO concentration of the calibration flame was found to be ±20% for the calibration of the ethylene flames at 3.05 atm; this value is typical of the measurements. The uncertainty in the loss of the doped NO through the flamefront is ±5%. The quoted uncertainty in the accuracy of the NO concentration in the NO/N_2 cylinder used for doping NO into the flame for the calibration is ±4% [Matheson Gas Products, 1990]. An uncertainty of ±5% was placed on the thermocouple-measured temperature [Norton et al., 1993]. As found above, the precision of the [NO] measurements was ±7%. Using a propagation of errors analysis, the overall accuracy of the [NO] measurements is ~25%. This uncertainty is dominated by the day-to-day repeatability of the calibration. The repeatability could most likely be improved by implementing a better flow system for doping NO into the flame; i.e., the current high-pressure flowmeter which is used for the

NO flow could be replaced with another mass flowmeter. On the other hand, the accuracy of the NO measurement is comparable to the uncertainty found in previous LSF measurements of OH concentration [Lucht et al., 1985].

Determining the uncertainty of the Rayleigh scattering temperature measurements follows a similar procedure, but involves considerably more measurements. For this procedure, it was assumed that the uncertainty in the background measurement is equal to that of the helium scattering measurement. Because the background was determined by fitting a line to two data points, the uncertainty in the background is not directly determinable. The background, however, closely follows the helium measurement, and is not as greatly affected by the nitrogen measurement. In addition, it can be assumed that there is no uncertainty in the temperature of the calibration gas, and that the differential cross-sections also have no uncertainty. The temperature as measured with Rayleigh scattering is given by

$$T_f = T_{cal} \frac{\hat{S}_{cal} I_f (d\sigma_{eff}/d\Omega)}{\hat{S}_f I_{cal} (d\sigma_{cal}/d\Omega)} \quad , \tag{C.5}$$

where the calibration and flame Rayleigh scattering signals are given by

$$S = S_{RS} - S_{BG} \quad . \tag{C.6}$$

In Eq. (C.6), S is the true Rayleigh scattering signal, S_{RS} is the signal measured in the experiment, and S_{BG} is the background signal. All of these Rayleigh scattering signals are found by dividing the photomultiplier voltage by the laser power monitoring photodiode voltage: $S = \hat{S}/I$. Therefore, two measurements are used to obtain S_{RS} and S_{BG}. The first step in calculating the uncertainty is to determine the uncertainty in S_{RS}:

$$\frac{\delta S_{RS}}{S_{RS}} = \sqrt{\left(\frac{\delta V_{PMT}}{V_{PMT}}\right)^2 + \left(\frac{\delta V_{PD}}{V_{PD}}\right)^2} \quad , \tag{C.7}$$

where V_{PMT} and V_{PD} are the photomultiplier tube and photodiode voltages. Values of $\delta S_{RS}/S_{RS}$ need to be calculated for the N_2 calibration measurement, the helium measurement (which will then be considered the background uncertainty), and for each of the flame Rayleigh scattering signals.

The uncertainty in the calibration and flame Rayleigh scattering signals can be found from

$$\delta S = \sqrt{(\delta S_{RS})^2 + (\delta S_{BG})^2} \quad . \tag{C.8}$$

The total temperature uncertainty is then

$$\frac{\delta T}{T} = \sqrt{\left(\frac{\delta S_{cal}}{S_{cal}}\right)^2 + \left(\frac{\delta S_{flame}}{S_{flame}}\right)^2} \quad , \tag{C.9}$$

where δS_{cal} and δS_{flame} are found from their respective measurements using Eqs. (C.7) and (C.8).

This procedure has been used to find the uncertainty in the Rayleigh scattering measurements. Example intermediate results are presented in Table C.2 for the three flames of Chapter 7. Typically, the total uncertainty in the temperature measurements is ~5%.

Table C.2: Intermediate quantities in the uncertainty analysis of the Rayleigh scattering temperature measurements for the data obtained 7 mm above the burner surface for the $C_2H_6/O_2/N_2$ flames of Chapter 7.

Quantity	Flame Equivalence Ratio		
	0.8	1.0	1.3
$\delta S_{He} = \delta S_{BG}$ (V)	7.04E-3	7.04E-3	7.04E-3
S_{BG} (V)	1.73E-2	1.73E-2	1.73E-2
δS_{N2} (V)	6.29E-2	6.29E-2	6.29E-2
S_{N2} (V)	3.19E+0	3.19E+0	3.19E+0
δS_{flame} (V)	2.46E-2	2.36E-2	2.55E-2
S_{flame} (V)	6.13E-1	5.66E-1	5.70E-2
$\delta(S_{N2}-S_{BG})$ (V)	6.33E-2	6.33E-2	6.33E-2
$S_{N2}-S_{BG}$ (V)	3.17E+0	3.17E+0	3.17E+0
$\delta(S_{flame}-S_{BG})$ (V)	2.56E-2	2.38E-2	2.58E-2
$S_{flame}-S_{BG}$	5.96E-1	5.49E-1	5.53E-1
$\delta T/T$	4.74E-2	4.78E-2	5.06E-2
T (K)	1.76E+3	1.96E+3	1.82E+3
δT (K)	8.34E+1	9.34E+1	9.21E+1

REPORT DOCUMENTATION PAGE

1. AGENCY USE ONLY (Leave blank)	2. REPORT DATE	3. REPORT TYPE AND DATES COVERED
	December 1994	Final Contractor Report

4. TITLE AND SUBTITLE

Laser Induced Fluorescence Measurements and Modeling of Nitric Oxide in High-Pressure Premixed Flames

5. FUNDING NUMBERS

WU-537-02-20
G-NAG3-1038

6. AUTHOR(S)

John R. Reisel and Normand M. Laurendeau

7. PERFORMING ORGANIZATION NAME(S) AND ADDRESS(ES)

Purdue University
West Lafayette, Indiana 47907

8. PERFORMING ORGANIZATION REPORT NUMBER

E-9248

9. SPONSORING/MONITORING AGENCY NAME(S) AND ADDRESS(ES)

National Aeronautics and Space Administration
Lewis Research Center
Cleveland, Ohio 44135-3191

10. SPONSORING/MONITORING AGENCY REPORT NUMBER

NASA CR-195404

11. SUPPLEMENTARY NOTES

Project manager, Yolanda R. Hicks, Propulsion Systems Division, NASA Lewis Research Center, organization code 2710, (216) 433-3410.

12a. DISTRIBUTION/AVAILABILITY STATEMENT

Unclassified - Unlimited
Subject Categories 07, 23, 34 and 35

12b. DISTRIBUTION CODE

13. ABSTRACT (Maximum 200 words)

Laser-induced fluorescence (LIF) has been applied to the quantitative measurement of nitric oxide (NO) in premixed, laminar, high-pressure flames. Their chemistry was also studied using three current kinetics schemes to determine the predictive capabilities of each mechanism with respect to NO concentrations. The flames studied were low-temperature (1600<T<1850K) $C_2H_6/O_2/N_2$ and $C_2H_4/O_2/N_2$ flames, and high temperature (2100<T<2300K) $C_2H_6/O_2/N_2$ flames. Laser-saturated fluorescence (LSF) was initially used to measure the NO concentrations. However, while the excitation transition was well saturated at atmospheric pressure, the fluorescence behavior was basically linear with respect to laser power at pressures above 6 atm. Measurements and calculations demonstrated that the fluorescence quenching rate variation is negligible for LIF measurements of NO at a given pressure. Therefore, linear LIF was used to perform quantitative measurements of NO concentration in these high-pressure flames. The transportability of a calibration factor from one set of flame conditions to another also was investigated by considering changes in the absorption and quenching environment for different flame conditions. The feasibility of performing LIF measurements of [NO] in turbulent flames was studied; the single-shot detection limit was determined to be 2 ppm.

14. SUBJECT TERMS

Laser-induced fluorescence; High pressure flames; Nitric oxide; Modeling

15. NUMBER OF PAGES

240

16. PRICE CODE

A11

17. SECURITY CLASSIFICATION OF REPORT	18. SECURITY CLASSIFICATION OF THIS PAGE	19. SECURITY CLASSIFICATION OF ABSTRACT	20. LIMITATION OF ABSTRACT
Unclassified	Unclassified	Unclassified	

National Aeronautics and
Space Administration

Lewis Research Center
21000 Brookpark Rd.
Cleveland, OH 44135-3191